UNIVERSITY OF SOUTHAMPTON

Spectroscopic Studies of the Optical and Structural Properties of Nano-Engineered Polymer Opals

by

Otto Lauri Juhana Pursiainen

A thesis submitted in partial fulfillment for the degree of Doctor of Philosophy

in the

Faculty of Engineering, Science and Mathematics

School of Physics and Astronomy

June 2008

UNIVERSITY OF SOUTHAMPTON

ABSTRACT

FACULTY OF ENGINEERING, SCIENCE AND MATHEMATICS
SCHOOL OF PHYSICS AND ASTRONOMY

Doctor of Philosophy

by Otto Lauri Juhana Pursiainen

The results of the spectroscopic studies of the optical and structural properties of polymer-based thin film photonic crystals are presented in this thesis. The 3D polymer opal material system is created through the shear-induced self-assembly of core-shell polymer particles leading to the ordering of the polymer spheres into an *fcc*-lattice. The polymer sphere size can be tuned in the precursor manufacturing polymerization process so that these opals have their optical response in the visible wavelength range. Furthermore, the polymer opal can be straightforwardly doped with nanoparticles enabling the tailoring of the optical features. The structural ordering of the polymer opal was studied using UV-laser diffraction revealing opal superdomains extending over tens of square-centimetres. UV-diffraction was also used to analyze the unit cell changes of the opal under strain and the results show significant anisotropy depending on the mutual orientation of the opal director and the strain vector. The reflection, transmission and scattering characteristics in the visible wavelength range were studied both by simulations and in experiments. Angle-, strain-, and wavelength-dependent characteristics were measured for both undoped and doped opals. The results show that the reflectivity is minimized at the bandgap conditions and at the same time the scattering is maximized. The opals also show colour-scattering features that can be tuned with the inclusion of nanoparticles. The effect of the nanoparticles is to widen the bandgap colour viewing angle and to prune the non-resonant scattering from the opals. Thus the overall colour appearance of the opals is enhanced significantly. These features cannot be understood in the traditional Bragg scattering regime, but new models combining nanoparticle-induced multiple scattering and the underlying low-refractive index contrast opal have to be developed. Coherent backscattering studies reveal that the scattering mean free path length is maximized in the vicinity of the bandgap and can be tuned with the nanoparticle doping level. Furthermore, the coherent backscattering spectroscopy results suggest that the opal scattering is most likely a combination of Mie and Rayleigh type contributions and their balance can be affected by the nanoparticle doping level. Finally, the polymer opal thin film photonic crystal shows substantial industrial potential in decorative, sensing, and security applications.

Contents

List of Figures

List of Tables

Publications

Compact strain-sensitive flexible photonic crystals for sensors
Pursiainen, O.L.J.; Baumberg, J.J.; Ryan, K.; Bauer, J.; Winkler, H.; Viel, B.; Ruhl, T.
Appl. Phys. Lett., **87**,101902 (2005).

Nanoparticle-tuned structural colour from polymer opals
Pursiainen, O.L.J.; Baumberg, J.J.; Winkler, H.; Viel, B.; Spahn, P.; Ruhl, T.
Opt. Exp. **15**, 9553 (2007).

Shear-induced organization in flexible polymer opals
Pursiainen, O.L.J.; Baumberg, J.J.; Winkler, H.; Viel, B.; Spahn, P.; Ruhl, T.
Adv. Mat. **20**, 1484 (2008).

Acknowledgements

Firstly I would like to express my gratitude to my supervisor Prof. Jeremy J. Baumberg for the opportunity to pursue the PhD degree in the funkadelic world of polymer opals. Also I would like to thank Jeremy for the help and the ideas as well as the ability to point out interesting things in what to a normal post-grad looks like useless data.

I wish also to thank Dr. Tilmann Ruhl, Dr. Benjamin Viel and Dr. Peter Spahn at the Deutsches Kunststoff-Institut DKI for providing the polymer opal samples. Huge thanks also go out to the guys in our post-grad/post-doc office; Alastair for the interesting discussions and help in all technical aspects, Nic for the jointly-conducted three year study of rock-appreciation, and Giorgio for being always available for discussions on physics or on any other aspects of life.

Furthermore, I would like to thank the different funding parties who have helped me financially during the thesis; EPSRC, Merck KgaA, Wiipurilainen Osakunta WiO, Finnish Foundation of Technology TES, and Helsingin Sanomat Centennial Foundation.

I would also like to say "Kiitos!" to my parents and my brother who have always supported me during the course of my education.

Finally, I would like to thank Riina for the support, love and encouragement throughout this PhD-project.

Nomenclature

$\vec{D}$	Electric displacement vector
$\vec{B}$	Magnetic induction vector
$\vec{E}$	Electric field vector
$\vec{H}$	Magnetic vector
$\vec{r} = [x\ y\ z]^T$	Spatial vector
μ	Magnetic permeability
μ_0	Free space magnetic permeability
ϵ_0	Dielectric constant of free space
ϵ_r	Relative dielectric constant
i	Imaginary number
ω	Angular frequency
c	Speed of light
t	Time
$\vec{a}$	Elementary real lattice vector
$\vec{b}$	Elementary reciprocal lattice vector
$\vec{k}$	Wave vector
λ	Wavelength
$\vec{G}$	Reciprocal lattice vector
δ_{ij}	Kronecker delta
v	Velocity
n	Refractive index
v_g	Group velocity
d_{hkl}	Interplanar distance
ϕ	Diameter
β	Angle between lattice planes
ν	Packing fraction
$\vec{n}_d$	Director vector
$\vec{r}^{\circ}$	Radial unit vector
δ	Diffraction angle
$\vec{n}$	Surface normal vector
$\vec{k}_{in}$	Incident wave vector
$\vec{k}_R$	Reflected wave vector

$\vec{k}_d$	Diffracted wave vector
θ	Scan angle
d	Sample-screen distance
$\vec{s}$	Strain vector
d	Sphere row spacing
$N = 1/d$	Sphere row density
γ	Surface diffraction angle
k	Diffraction order
ϕ_{sn}	Strain-director angle
A_ϕ	Aperture function
A_δ	Delta-function array
d	Cavity length
n_{eff}	Effective refractive index
a	Cubic unit cell side length
θ	Incident angle
ν	Poisson ratio
I	Intensity
l_α	Absorption length
L_B	Bragg length
$\overline{n}$	Complex refractive index
κ	Extinction coefficient
α_{NP}	Nanoparticle cross-section
η	Enhancement factor
Λ	Phase difference
r_p	Fresnel p-polarized reflection coefficient
r_s	Fresnel s-polarized reflection coefficient
t_p	Fresnel p-polarized transmission coefficient
t_s	Fresnel s-polarized transmission coefficient
ϑ_S	Angular scattering width
l_{mfp}	Scattering mean free path
l^*	Transport mean free path
θ	Backscattering angle
$\vec{p}_i$	Initial photon direction
$\vec{p}_f$	Final photon direction
$\Delta\phi$	Phase difference
R	Scatterer separation
θ_{is}	Angle between incident and scattered photon
$\Delta\theta_{CBS}$	CBS cone FWHM angle
r_{eff}	Effective scatterer radius
σ_R	Rayleigh scattering cross-section
σ	Scattering strength

fcc	Face-centered cubic
RIC	Refractive index contrast
R	Reflection
T	Transmission
S	Scattering
DOS	Density of states
MDOS	Mutual density of states
LDOS	Local density of states
SDOS	Spectral density of states
CBS	Coherent backscattering
vv	Polarization conserving channel
vh	Polarization flipping channel
N_{scatt}	Number of scattering events

I believe that a scientist looking at non-scientific problems is just as dumb as the next guy.

Richard P. Feynman

Chapter 1

Introduction

Photonic crystals are periodic material systems that interact with photons in very much the same way as the atomic crystals affect the motion of electrons. In a photonic crystal a periodic variation of the refractive index replaces the electronic potential of an atomic crystal thus creating a barrier for the photons entering the structure. Through inducing this periodic variation in 3 dimensions it is possible to design materials that selectively reflect all polarizations of light for a certain wavelength range or, alternatively, by inducing a defect into the structure create a 3D waveguide for photons of a certain wavelength range. Traditionally the birth of the photonic crystal research field is associated with the simultaneous publications by Yablonovitch [1] and John [2] in 1987 about the possibility of creating a photonic band gap (PBG). The photonic band gap is a frequency range where it is forbidden for photons to travel. John and Yablonovitch also proposed the idea of the suppression of spontaneous emission in certain periodic structures even though Bykov [3] already discussed similar findings in 1972. The findings of John and Yablonovitch sparked a huge photonic crystal research boom with future visions of light speed computers and photonic information technology [4].

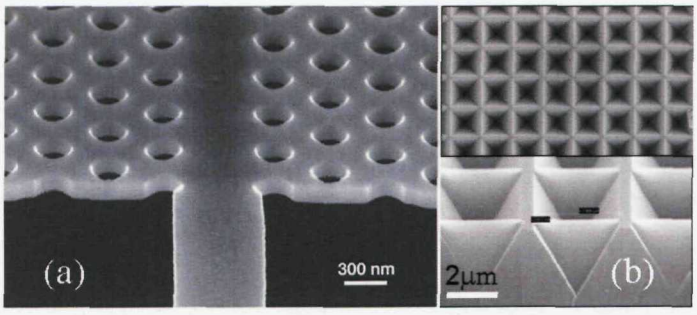

FIGURE 1.1: (a) 2D silicon photonic crystal waveguide. Taken from [5]. (b) 2D pyramidal pit nanopatterned Si substrate before gold coating used in surface enhanced Raman spectroscopy. Taken from [6].

The wildest predictions of the photonic crystal revolution have, however, been subdued by the realization of the manufacturing difficulties especially related to the 3D technology. Polydispersity in size and position of the photonic crystal structural components result in light scattering and extinction of coherent beams [7] especially in 3D systems limiting their use in optical integrated circuits. The photonic crystal technology in 2D is somewhat more advanced and is already producing applications such as 2D silicon light guides for group velocity control [5], Fig. 1.1 (a), and 2D nanostructured surfaces for surface-enhanced Raman spectroscopy [6], Fig. 1.1 (b). Furthermore, photonic crystal fibres, where the light guiding is based on a two-dimensional photonic crystal [8], are commercially available and routinely used e.g. in super-continuum generation [9] and are being currently researched for a platform for fibre-integrated optoelectronic devices [10].

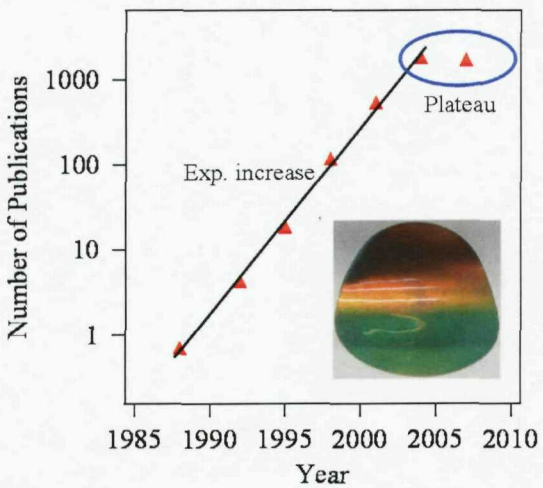

FIGURE 1.2: Amount of photonic crystal publications vs time. Inset: Polymer opal showing structural colour features.

The evolution of the scientific photonic crystal publications versus the year is shown in Fig. 1.2. We see that the trend is exponential between years 1987 and 2004 revealing the huge scientific interest in these periodic materials. However, in the recent years the technological difficulties in 3D have become more evident possibly causing the plateau level in the trace of Fig. 1.2. This is a clear indication of the reality kicking in and the initial "hype" wearing out with the realization of the manufacturing difficulties. On the other hand it calls for photonic crystals that have additional functionality and that are not too sensitive to possible structural imperfections but also manufacturing techniques enabling mass-producing of these materials. Photonic crystals are still very much in search of technological applications, but in recent years photonic crystal systems fulfilling (at least partially) the above mentioned requirements have been reported e.g. by Arsenault et al. [11] and Tian et al. [12].

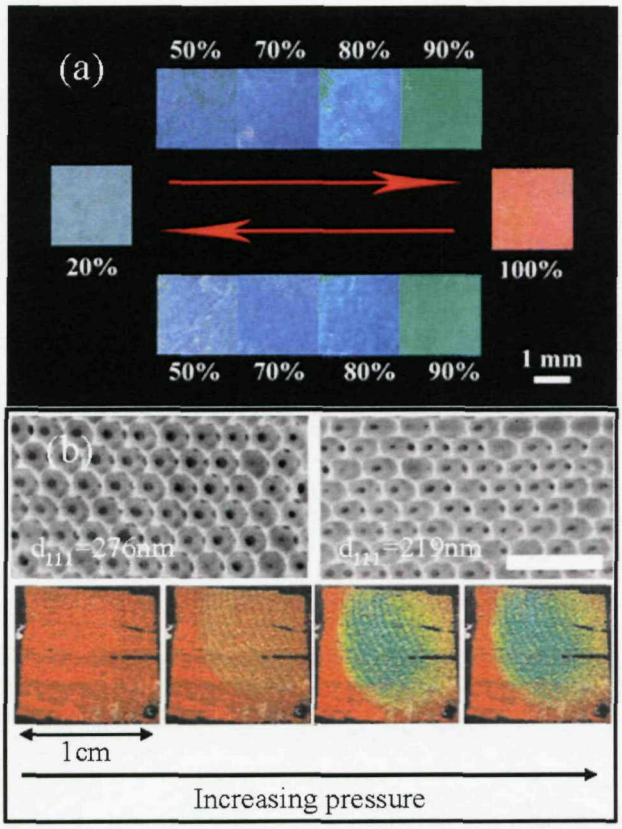

FIGURE 1.3: (a) A hydrogel photonic crystal changes its colour from violet to red with ambient relative humidity change from 20% to 100%, respectively. Taken from [12]. (b) Top: Compression-induced changes in the polymer-based elastomeric photonic crystal with the corresponding (111) -lattice plane spacings. Bottom: Colour images of the photonic crystal based finger-printing sensor. Taken from [11].

Tian et al. have developed a humidity sensitive photonic crystal hydrogel that can change its colour reversibly from violet to red (over 240nm) with the ambient relative humidity change from 20% to 100%. The colour changing photonic crystal together with the corresponding humidity scale is presented in Fig. 1.3 (a). Arsenault et al. manufacture large-area elastomeric porous photonic crystals from polymers and suggest their use in e.g. colour fingerprint sensing claiming them to be able to distinguish between a real print and a rubber replica. SEM images of the relaxed and strained state photonic crystal together with the different (111) -plane spacings are presented in Fig. 1.3 (b) top left and right, respectively. Colour images of the backlit fingerprint sensing system based on their elastomeric photonic crystal are presented in Fig. 1.3 (b), bottom.

This thesis deals with a new kind of photonic crystal system called a polymer opal. This material is composed of polymer spheres in a polymer matrix thus resulting in a low refractive-index contrast. The polymer opal manufacturing technique relies on self-assembly through shear-ordering processes and enables the mass-production as well as nanoparticle doping of these photonic crystals. Fig. 1.4 (a-c) displays pictures of

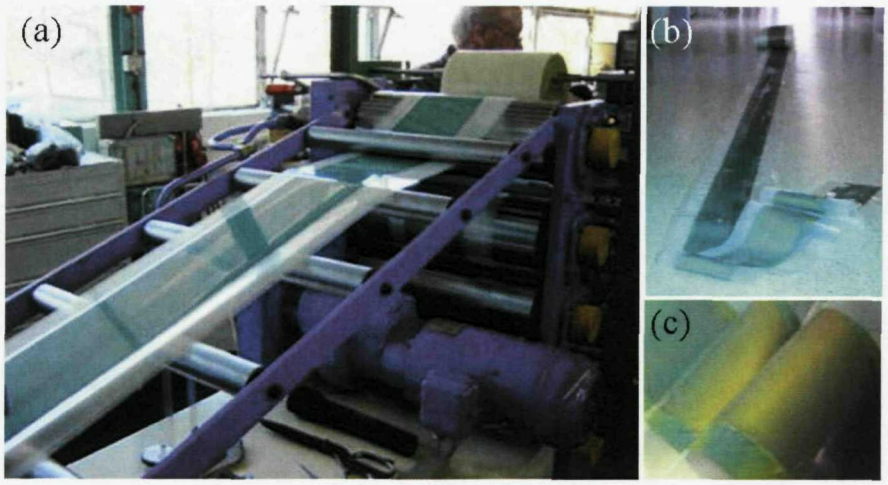

FIGURE 1.4: Polymer opals being manufactured in large quantities in (a) extrusion-to-roll manufacturing sequence. (b) Several meters of polymer opal sheet on a roll, with structural colour features in (c).

extrusion-produced polymer opal sheets and clearly demonstrates the industrial potential of this material. The main emphasis of this thesis is on the experimental research of the optical properties of these polymer opals. The structural ordering has been studied by UV-diffraction and reveals large-area superdomain ordering. Furthermore, these opals display brilliant structural colour features through scattering in the periodical photonic crystal environment which can be tuned by nano-particle doping [13]. We have studied the scattering features both by concentrating on the colour-scattering characteristics in front of the opal and monitoring the multiple scattering events inside the opal through coherent backscattering measurements. While the study presented here sheds light on many of the scattering features of the polymer opals it also raises the point that there is genuine need for more thorough theoretical understanding of scattering in periodic systems. Moreover, the polymer opals show real potential for industrial applications in e.g. security, sensing, and decorative applications.

1.1 The Thesis Outline

Chapter 2 first introduces the concept of a photonic crystal in 1D, 2D, and 3D before reviewing the mathematical concepts based on Maxwell's equations used to treat the periodic systems. The photon dispersion relations are then discussed in one and three-dimensional cases together with some remarks on the group velocity and the optical density of states. Finally a few important properties of the face-centered-cubic lattices are highlighted anticipating their importance when considering opal-based systems in the later chapters.

In Chapter 3 different manufacturing techniques used for opaline photonic crystals are considered. Main emphasis is given to the polymer opal manufacturing technique developed at the Deutsches Kunststoff Institut (DKI) in Darmstadt, Germany. First the precursor particle synthesis is introduced before presenting the manufacturing sequence for the thin film polymer opal photonic crystals enabling the doping of these crystals by nanoparticles.

Chapter 4 deals with the structural order of the thin film polymer opals. Different aspects of the shear-induced ordering are studied using UV-laser diffraction from both unstrained and strained polymer opal films.

Chapter 5 presents both experimental and simulated results for the photonic crystal reflection, transmission and scattering features. Angle- and strain-dependent optical characteristics are also discussed. Furthermore different nanoparticle dopants are considered as well as their interaction with the photonic crystal bandgap.

In Chapter 6 the structural colour characteristics from nanoparticle-doped polymer opals is discussed. It is shown that the colour features can be tuned with the inclusion of the dopants and that the structural colour features cannot be understood by any conventional Bragg-type diffraction model. Theoretical ideas combining the photonic crystal band gap and scattering are discussed with relation to the existing theoretical framework.

Coherent Backscattering characteristics of the polymer opals are presented in Chapter 7. This photon self-interference effect in these polymer opals is measured using both single-line laser and broadband sources. The results are discussed relating them to the existing theories concerning multiple scattering in disordered structures and differences due to the periodic nature of our system are outlined.

Finally, Chapter 8 presents an overview on the major findings of the previous chapters and provides a future outlook on the polymer opal material experiments and applications.

Chapter 2

Photonic Crystal Theory

The behaviour of electromagnetic waves in periodic materials has been the subject of intense theoretical and experimental research during the last two decades. Analogies can be drawn from solid state physics and the study of atomic crystals and their effect on the electron motion. The discovery of the diffraction of X-rays in atomic crystals by Max van Laue in 1912 and the subsequent studies by W.H. and W.L. Bragg as well as Leon Brillouin's [14] studies of wave propagation in periodic structures have provided a sound foundation for the studies of electromagnetic radiation in periodic structures. As was mentioned previously the first studies of suppression of spontaneous emission due to 1D periodicity was published by Bykov [3, 15] and more general discussion in 2D and 3D was later provided by Yablonovitch [1] and John [2]. In this chapter the basic theory of photonic crystals as well as examples of 1D, 2D, and 3D periodic structures are presented. Properties of face-centered cubic (*fcc*) crystals are also discussed in more detail to provide some groundwork for the following chapters.

2.1 Examples of Photonic Crystals in 1D, 2D, and 3D

The essence of photonic crystals is the fact that they provide some means of manipulating (e.g. reflecting, transmitting, guiding) light at a certain wavelength range through having a periodic structure at a similar size scale as light. A photonic band gap is a range of wavelengths (or frequencies) where light incident on a periodic structure is reflected. The bandgap can be complete, i.e. for all polarizations and directions in the lattice the reflectivity is 100%, or partial thus only partially reflecting the incident light at some directions or light of a certain polarization. Examples of periodic structures in three different dimension are presented in Fig. 2.1. In (a) a simple dielectric multilayer structure is depicted, which can be used for example as a high reflectivity mirror for a certain wavelength range determined by the layer thicknesses and refractive indices [16]. The high reflectivity perpendicular to the layer sequence is the equivalence of the

band gap in 1D. Two dimensional photonic crystal in Fig. 2.1 (b) consisting of rods in a rectangular lattice possesses band gaps in directions perpendicular to the rods. The details of the reflectivities depend on the ratio of the rod diameter to the lattice constant and the rod and surrounding material refractive indices. Two-dimensional photonic crystals are promising for industrial use e.g. in LEDs to enhance the light extraction from the high refractive index semiconductor [17]. An example of 3D photonic crystal is depicted in (c) where a simple cubic lattice of dielectric spheres is presented. These kind of structures are the synthetic equivalent of the natural opals and potentially have use in structural colour applications [13] or as inverted structures in complete band gap materials and photon localization [18]. The common factor of all these structure in Fig. 2.1 (a-c) is the periodicity size scale which is in the range of the photon wavelength.

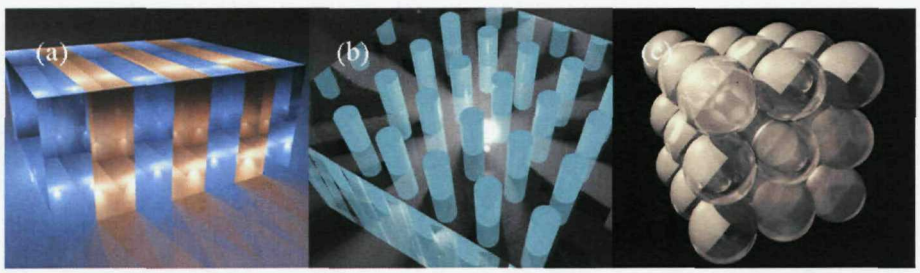

FIGURE 2.1: Examples of photonic crystals in (a) 1D, (b) 2D, and (c) 3D. © N. Perney 2007.

2.2 Mathematical Theory of Photonic Crystals

The mathematical theory outlined here is based on the concise treatment by Sakoda [19] and Joannopoulos et al. [20]. This treatment relies on the Maxwell equations in the case where there are no sources present and the media are non-dissipative dielectrics. Thus we have:

$$\vec{\nabla} \cdot \vec{D}(\vec{r}, t) = 0 \tag{2.1}$$

$$\vec{\nabla} \cdot \vec{B}(\vec{r}, t) = 0 \tag{2.2}$$

$$\vec{\nabla} \times \vec{E}(\vec{r}, t) = -\frac{\partial \vec{B}(\vec{r}, t)}{\partial t} \tag{2.3}$$

$$\vec{\nabla} \times \vec{H}(\vec{r}, t) = \frac{\partial \vec{D}(\vec{r}, t)}{\partial t}, \tag{2.4}$$

where $\vec{D}(\vec{r}, t)$ stands for electric displacement field, $\vec{B}(\vec{r}, t)$ for magnetic induction, $\vec{E}(\vec{r}, t)$ for electric field, and $\vec{H}(\vec{r}, t)$ for magnetic field. Assuming that magnetic permeability equals that of free space, i.e. $\mu = \mu_0$ we have:

$$\vec{B}(\vec{r},t) = \mu_0 \vec{H}(\vec{r},t). \tag{2.5}$$

Further assuming that the dielectric constant is real (no absorption) and perfectly periodic with the spatial coordinate $\vec{r}$ we can set:

$$\vec{D}(\vec{r},t) = \epsilon_0 \epsilon_r(\vec{r},t)\, \vec{E}(\vec{r},t), \tag{2.6}$$

where ϵ_0 is the dielectric constant of free space and $\epsilon_r(\vec{r})$ the relative dielectric constant of the photonic crystal material. Substituting (2.5-2.6) into (2.2-2.4) we get:

$$\vec{\nabla} \cdot \left[\epsilon_r(\vec{r})\, \vec{E}(\vec{r},t)\right] = 0 \tag{2.7}$$

$$\vec{\nabla} \cdot \vec{B}(\vec{r},t) = 0 \tag{2.8}$$

$$\vec{\nabla} \times \vec{E}(\vec{r},t) = -\mu_0 \frac{\partial \vec{H}(\vec{r},t)}{\partial t} \tag{2.9}$$

$$\vec{\nabla} \times \vec{H}(\vec{r},t) = \epsilon_0 \epsilon_r(\vec{r}) \frac{\partial \vec{E}(\vec{r},t)}{\partial t}. \tag{2.10}$$

Dividing (2.10) by $\epsilon_r(\vec{r})$ and subsequently taking the curl ($\vec{\nabla}\times$) of both sides yields:

$$\vec{\nabla} \times \left[\frac{1}{\epsilon_r(\vec{r})} \vec{\nabla} \times \vec{H}(\vec{r},t)\right] = -\frac{1}{c^2} \frac{\partial^2}{\partial t^2} \vec{H}(\vec{r},t), \tag{2.11}$$

where we have used the identity for the speed of light $c = \frac{1}{\sqrt{\epsilon_0 \mu_0}}$. Next we'll seek the harmonic solutions in the form of:

$$\vec{H}(\vec{r},t) = \vec{H}(\vec{r})\, \mathrm{e}^{-i\omega t}, \tag{2.12}$$

where ω is the eigen-angular frequency and substituting (2.12) into (2.11) finally results in:

$$\vec{\nabla} \times \left[\frac{1}{\epsilon_r(\vec{r})} \vec{\nabla} \times \vec{H}(\vec{r})\right] = \frac{\omega^2}{c^2} \vec{H}(\vec{r}), \tag{2.13}$$

which is an eigenvalue equation for $\vec{H}(\vec{r})$. In other words in (2.13) $\vec{H}(\vec{r})$ is an eigenfunction with an eigenvalue $\frac{\omega^2}{c^2}$. The operator $\vec{\nabla} \times \left[\frac{1}{\epsilon_r(\vec{r})} \vec{\nabla}\times\right]$ in (2.13) is Hermitian and thus its eigenvalues are real and positive [20]. Furthermore the periodicity of $\epsilon_r(\vec{r})$ plays an extremely important part here. The periodicity implies:

$$\epsilon_r\left(\vec{r}+\vec{a}_i\right)=\epsilon_r\left(\vec{r}\right), \tag{2.14}$$

where $\vec{a}_i$ is the lattice vector (i=1,2,3). Due to this periodicity in the system Bloch's theorem can be applied to solve for the eigenfunctions $\vec{H}\left(\vec{r}\right)$ in (2.13). The Bloch theorem states that the solutions can be sought in the form of:

$$\vec{H}\left(\vec{r}\right)=\vec{H}_{\vec{k}n}\left(\vec{r}\right)=\vec{u}_{\vec{k}n}\left(\vec{r}\right)\mathrm{e}^{i\vec{k}\cdot\vec{r}}. \tag{2.15}$$

Moreover, the functions $\vec{u}_{\vec{k}n}\left(\vec{r}\right)$ in (2.15) have the same periodicity as the dielectric function in (2.14) and thus:

$$\vec{u}_{\vec{k}n}\left(\vec{r}+\vec{a}_i\right)=\vec{u}_{\vec{k}n}\left(\vec{r}\right). \tag{2.16}$$

In (2.15) $\vec{k}$ is confined to the first Brillouin zone (1st B.z.) and n is an index needed for the solution indexing in the 1st B.z. The 1st B.z. is a primitive cell in the reciprocal space into which all $\vec{k}$-values can be folded back by subtracting or adding an integer multiple of the reciprocal lattice vector $\vec{G}$. The very existence of the 1st B.z. stems from the periodicity of the original real lattice, cf. (2.14). The reciprocal lattice vectors $\vec{G}$ are defined by the elementary reciprocal lattice vectors $\vec{b}_i$ (i=1...3) through the following identities:

$$\vec{a}_i\cdot\vec{b}_j=2\pi\delta_{ij}, \tag{2.17}$$

$$\vec{G}=l_1\vec{b}_1+l_1\vec{b}_2+l_1\vec{b}_3, \tag{2.18}$$

where l_i are integers and δ_{ij} is the Kronecker delta. The essence of the Bloch theorem is that the eigenvalue equation (2.13) can be solved in the 1st B.z. due to symmetry. A graphical interpretation of the Bloch wave (2.15) is given in Fig. 2.2. The plane wave $e^{i\vec{k}\cdot\vec{r}}$ is modulated by a function with periodicity $\vec{a}_i$ of the dielectric function yielding a periodic Bloch wave.

Furthermore the periodic $\vec{u}_{\vec{k}n}$ in(2.16) and $\epsilon_r\left(\vec{r}\right)^{-1}$ can be expanded into Fourier series in terms of the reciprocal lattice vector $\vec{G}$:

$$\vec{u}_{\vec{k}n}\left(\vec{r}\right)=\sum_{\vec{G}}\vec{u}_{\vec{k}n}(\vec{G})\mathrm{e}^{i\vec{k}\cdot\vec{r}},\quad\frac{1}{\epsilon_r\left(\vec{r}\right)}=\sum_{\vec{G}}\epsilon_r(\vec{G})\mathrm{e}^{i\vec{k}\cdot\vec{r}}. \tag{2.19}$$

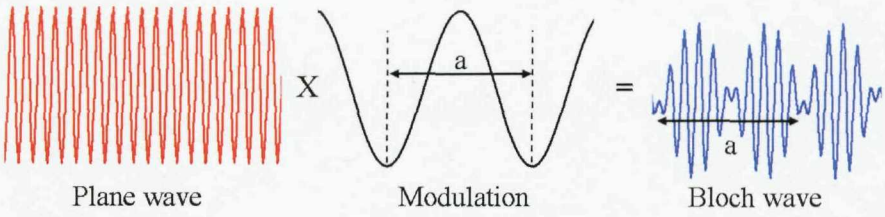

FIGURE 2.2: Bloch wave composed from a plane wave and a modulating function.

The insertions of (2.15) and (2.19) into (2.13) yields a system of equations for each $\vec{k}$ in the 1st B.z. relating the wave vectors to energy. The numerical solution of this system (also known as the plane wave solution) yields a relationship between the allowed $\vec{k}$ values in the crystal and energy (or angular frequency ω) and is referred to as the band diagram. The numerical solution for the plane wave system solution of (2.13) was first demonstrated by Leung et al. [21] and Zhang et al. [22] in *fcc* lattices and by Ho et al. [23] for diamond lattices. Eq. (2.13) can also be solved by scalar-wave-approximation (SWA), i.e. not taking into account the vectorial nature (polarizations) of light. This was demonstrated by Satpathy et al. [24] and Shung et al. [25] who were able to obtain analytical solution in the SWA. The major difficulties in this approach are related to its use in describing the wave motion inside the crystal in any arbitrary direction. However, it can be used in describing the behaviour in the high-symmetry directions [26] such as the [111] direction.

2.3 Photonic Crystal Band Diagrams

2.3.1 1D Multilayer System

It is very informative to look at the photonic crystal band diagrams first in the 1D case, i.e. in case of the multilayer system of Fig. 2.1 (a). The solution of (2.13) in 1D leads to the band diagram qualitatively presented Fig. 2.3.

The multilayer system with layer periodicity a is presented as the blue stack with the different refractive indices n_1 and n_2, $n_2 > n_1$. The blue dashed line corresponds to the light dispersion line in a non-dispersive material with a constant refractive index of $n = n_{eff} = \frac{n_1+n_2}{2}$ (assuming equal layer thicknesses), i.e. $\omega = vk = \frac{c}{n_{eff}}k$. The 1st B.z. extends from $-\pi/a$ to π/a in the k-space. Due to the periodicity the allowed light bands (in red) bend away from the light line when moving closer to the 1st B.z. edge. Thus a gap $\Delta\omega$ in frequency is created around the central gap frequency ω_{gap} such that in this $\Delta\omega$ range there are no available k values in the periodic system. The bands bend back towards the light line moving away from the 1st B.z. edge to greater k-values. Due to the periodicity we can use the reciprocal lattice vectors $\vec{G}$ to map the bands outside

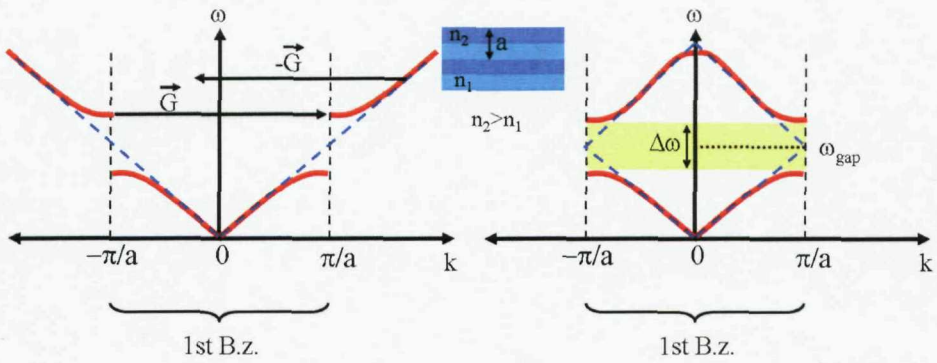

FIGURE 2.3: 1D band structure ω vs k showing the full reciprocal space (left) and the reduced scheme in the 1st Brillouin zone (right). The allowed bands are depicted in red, light dispersion line $\omega = vk$ in blue, the reciprocal lattice vectors $\vec{G}$ in black, and the bandgap in light yellow. Also shown is the multilayer system with layer period a and the refractive indices n_1 and n_2.

the 1st B.z. back to the 1st B.z. resulting in the band diagram in Fig. 2.3, right. A bandgap extending through the entire 1st B.z. is highlighted in yellow. Mathematically the bandgap is a result of the non-existent purely real value solutions to (2.13) at the 1st B.z. edge. The solution has an imaginary part resulting in an evanescent wave, i.e. an attenuating wave extending to the structure but not propagating through a thick structure.

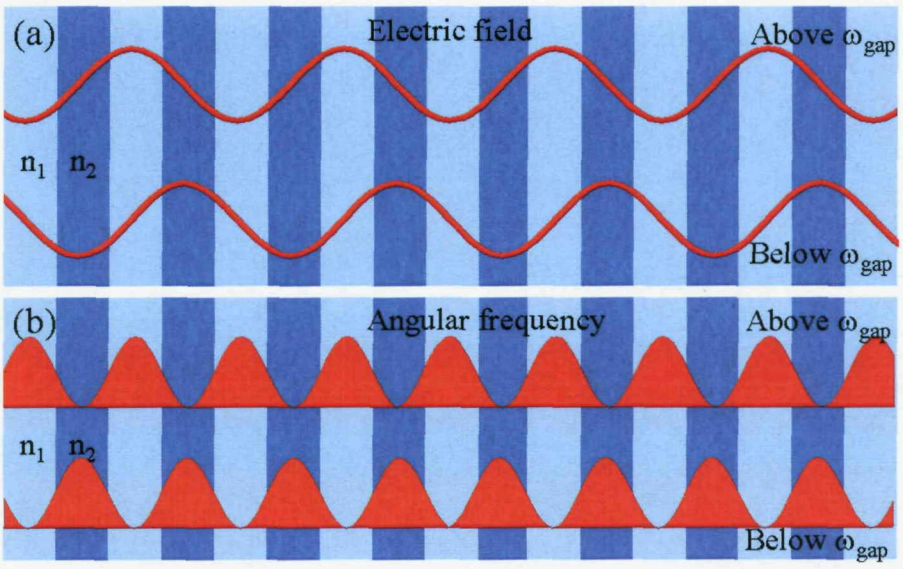

FIGURE 2.4: (a) Electric field and (b) energy/frequency distributions above and below the bandgap ω_{gap} in a multilayer materials with refractive indices n_1 and n_2, $n_2 > n_1$.

In 1D systems an energy gap opens up as soon as the refractive index contrast (RIC) between the layers is non-zero, i.e. $\frac{n_1}{n_2} \neq 1$. The bandgap formation in 1D can be

understood by considering the frequencies (i.e. energies) immediately below and above the mid-bandgap frequency ω_{gap} (cf. Fig. 2.3). The electric fields and energies are depicted in Fig. 2.4 (a-b), respectively, in the 1D multilayer system where dark (light) blue corresponds to high (low) refractive index. The solutions above and below the bandgap are standing wave solutions with the same k-vector but different frequency ω (i.e. different energy). Due to symmetry reasons these standing wave patterns can be positioned in the multilayer system in two ways, either the wave maxima in high or low refractive index materials. The electromagnetic field stores more energy if it has its extrema in the high-refractive index material[1]. Thus in order for the system energy to be minimized the high energy mode is predominantly localized in the low-refractive index material and low energy mode is localized more in the high refractive index material. This physical separation of the electric fields leads to the generation of the bandgap. As was already mentioned, any RIC in 1D leads to the opening of the bandgap, the larger the contrast the larger the bandgap. For small refractive index modulation, e.g. where $n_2 = n_1 + \Delta n$ and when $\Delta n/n_1 \ll 1$, the following approximation has been proposed [27]:

$$\frac{\Delta\omega}{\omega_{gap}} \cong \frac{1}{2}\frac{\Delta n}{n_1}. \tag{2.20}$$

2.3.2 3D System

Adding more dimensionality to the bandstructure consideration complicates the matter. The relative dielectric constant $\epsilon_r(\vec{r})$ is considered to be a scalar value function of a vector $\vec{r} = [x, y, z]^T$ and the reciprocal has the same dimensionality as the real space. For a complete photonic bandgap to be created the individual bandgaps in every direction in the lattice need to overlap suitably. The bandstructure calculation is still based on (2.13) but now yields different (ω, k) solutions for different polarizations and directions in the lattice, hence the different directions in the cubic lattice have to be considered carefully.

The cubic lattice directions are traditionally expressed in terms of the Miller indices hkl, which are obtained by considering the intersection coordinates (in lattice constants a) of the different planes with the coordinates axes. The reciprocal of each number is then determined and all the indices obtained this way are multiplied by a suitable number to reduce them to smallest integers. This is depicted in Fig. 2.5 (a) and (b). In (a) the intersection of the blue plane is at (1,∞,∞) and thus the reciprocals are (100) which are the Miller indices (hkl) of this cubic system plane. The direction perpendicular to this plane is indicated by [100]. Similar treatment applies for (b) where the intersection coordinates are (1,1,1) yielding the Miller indices (hkl)=(111) and the

[1]The time averaged Poynting vector magnitude describing the energy flux is equal to $\langle S\rangle = \frac{1}{2}E_0^2 c\epsilon_0 n$, where E_0 is the electric field amplitude and n is the refractive index $(= \sqrt{\epsilon})$

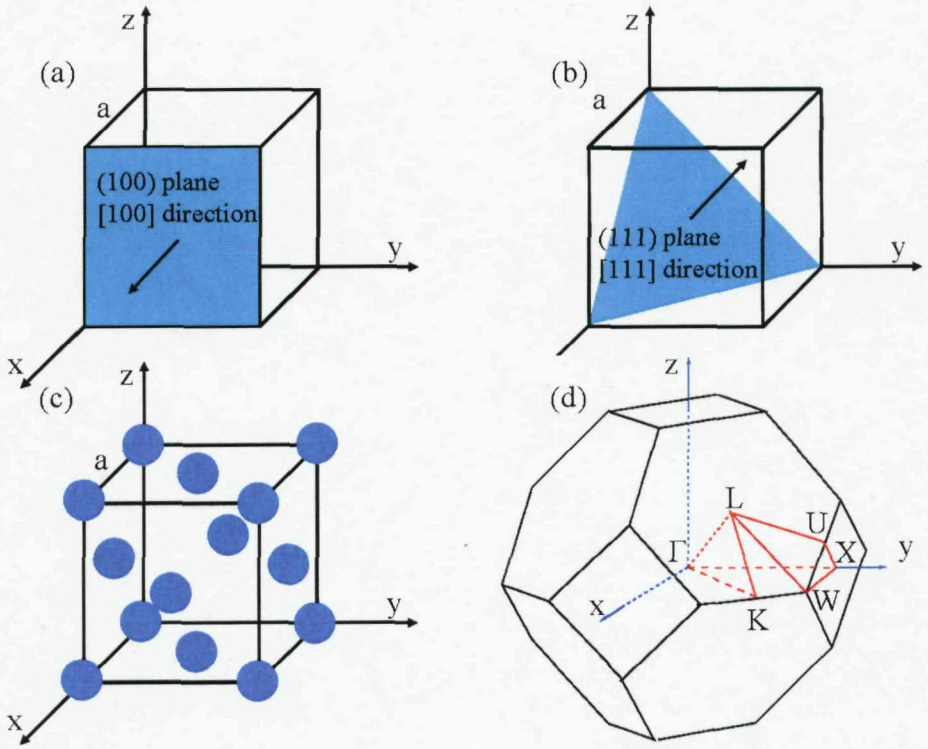

FIGURE 2.5: The Miller indices for plane (a) (100) and (b) (111) together with the corresponding directions. (c) Face-centered-cubic (*fcc*) lattice with lattice constant a. (d) Reciprocal space of the *fcc* -lattice showing some important symmetry points.

corresponding perpendicular direction [111]. It is interesting to look at the 3D *fcc*-lattice and the corresponding reciprocal lattice in detail. These are depicted in Fig. 2.5 (c-d), respectively. In the *fcc*-lattice there is an elementary component (e.g. atom, nanosphere) in each corner of the cube (side length a). Furthermore, there are components in the middle of each face of the cube. The reciprocal space, and more exactly the 1st B.z. can be calculated defining first primitive translation vectors[2] for the real lattice and subsequently calculating the reciprocal vectors through (2.17). Finally, the 1st B.z. can be formed by the volume inside of the intersections of the planes perpendicular to the reciprocal lattice vectors $\vec{G}$ defined by (2.21-2.22) and located at the midpoints of these vectors [28]:

$$\left(\frac{2\pi}{a}\right)\left(\pm\vec{i}\pm\vec{j}\pm\vec{k}\right) \text{ and} \tag{2.21}$$

$$\left(\frac{2\pi}{a}\right)\left(\pm 2\vec{i}\right);\ \left(\frac{2\pi}{a}\right)\left(\pm 2\vec{j}\right);\ \left(\frac{2\pi}{a}\right)\left(\pm 2\vec{k}\right) \tag{2.22}$$

The 1st B.z. of an *fcc* lattice is thus observed to be a truncated octahedron, Fig. 2.5 d). Important reciprocal lattice directions are labeled in the image with the Γ -point taken

[2]Coordinates of every lattice point can be expressed as a linear combination of these vectors.

to be the origin. The ΓL direction corresponds to the lattice direction perpendicular to the (111) planes, i.e. direction [111]. Similarly, the direction ΓX is the direction [010] and ΓK corresponds to direction [110]. The symbols Γ, L, U, X, W, K are traditionally used for indicating the different points and directions in the fcc -lattice.

The band structure is usually calculated with reference to the different lattice directions outlined above. Fig. 2.6 presents the bandstructure obtained by solving (2.13) by the plane-wave method for different symmetry directions. This bandstructure was calculated by Pavarini et al. [29] for a close-packed *fcc*-lattice consisting of dielectric spheres ($n = 1.59$) in air. The frequencies in the vertical axis are expressed in terms of the reduced frequency $\frac{\omega a}{2\pi c}$ where ω is the angular frequency and a the *fcc*-lattice constant.

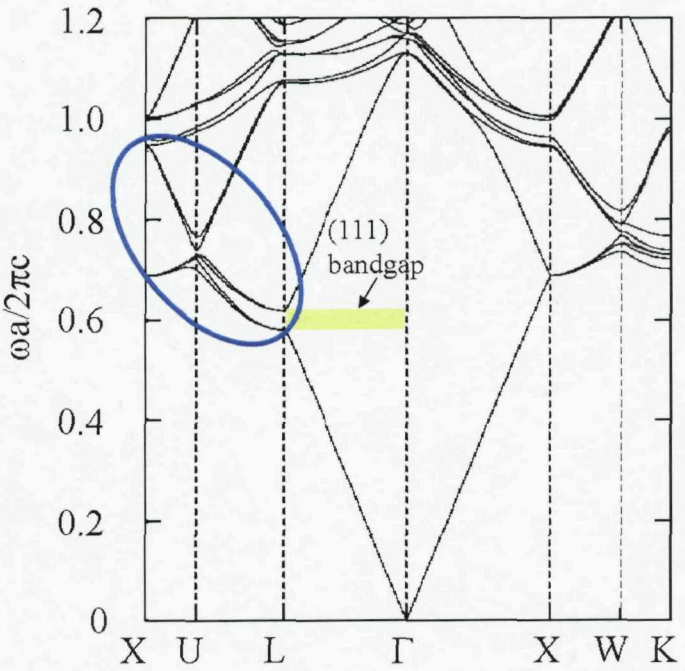

FIGURE 2.6: Bandstructure with reduced frequency $\frac{\omega a}{2\pi c}$ vs. k calculated for an *fcc*-lattice consisting of dielectric spheres ($n = 1.59$) in air. The (111) bandgap around $\frac{\omega a}{2\pi c} = 0.6$ is highlighted in yellow. Blue circle highlights the area where the bandgap angular-tuning is observed. Taken from [29].

The bandstructure of the lattice in question is seen to be a relatively complicated collection of lines corresponding to different energies and directions. The bandgap corresponding to set of (111) planes is highlighted in Fig. 2.6 in yellow. This is the bandgap that we have been mostly interested in this work and is seen to be located at the reduced frequency value of $\frac{\omega a}{2\pi c} = 0.6$. Furthermore, the bandstructure in Fig. 2.6 can be used to analyze the angle-dependence of the (111) bandgap. As the incoming angle is changed from the ΓL towards the X (through U), one is changing the angle of incidence from the [111] direction to more in-plane, and the bandgap is tuned into higher energies. This is highlighted with a blue circle in Fig. 2.6. This feature is further discussed in Chapter

5. The crossing of the (200) and (111) bandgaps is seen at point U which has also been experimentally observed by van Driel et al. [30] and Romanov et al. [31].

It is also observed that in the material system of Fig. 2.6 no complete band gaps exist. Complete band gap would manifest itself as an energy range where there are no allowed k-vector values across the whole horizontal axis of the band diagram. In fact, it has been shown [23] that no complete photonic bandgaps exist for purely *fcc* crystals for any refractive index ratio, but an inverted *diamond* lattice is needed for the complete bandgap. Interestingly, in another theoretical publication [32] some years later (partially by the same authors) this is contradicted and it is argued that a complete photonic bandgap is achieved in an inverted *fcc*-structure with air spheres in a dielectric ($n = 3.1$) host at the frequency $\frac{\omega a}{2\pi c} = 0.6$. The conclusion is that in order to achieve a photonic bandgap a high RIC is needed. However, this does not make the study of low RIC *fcc* photonic crystals any less interesting, which will be shown later on in this thesis. In the very intense search for the complete bandgap systems the study of moderate or low refractive index photonic crystals has been widely neglected, even though many features of the polymer opals considered in this thesis are due to the low RIC.

2.4 Group Velocity and the Density of States

Group velocity v_g is a measure of the energy velocity in a material. Here the photonic crystal effect on the group velocity is considered. It is again very informative to consider the 1D situation here. The group velocity is defined by (2.23) [19]:

$$v_g = \frac{\partial \omega}{\partial k}. \tag{2.23}$$

Close to the band gap the group velocity is affected by the band bending when compared to the vacuum light line in Fig. 2.3. Whereas the group velocity for the vacuum case stays constant (constant slope) the group velocity in the photonic crystal decreases due to the decreasing derivative in (2.23) (i.e. the light slows down) towards the 1st B.z. edge. When $k = \pi/a$ the band is horizontal and the group velocity vanishes completely. As described earlier the modes at the edge of the 1st B.z. are standing waves and do not propagate to the left or right, i.e. $v_g = 0$.

Photon density of states (DOS) $D(\omega)$ is another interesting feature in photonic crystals. Basically the rate of spontaneous emission from an excited state of an atom is proportional to $\omega D(\omega)$ and for vacuum conditions the DOS can be calculated by considering that in a cube (side length L) there is one allowed photon mode per reciprocal space volume $\left(\frac{2\pi}{L}\right)^3 = \frac{8\pi^3}{V}$ [19, 28], where V is the real space volume. In k-space an increase of dk increases the sphere volume of radius k by $4\pi k^2 dk$. Photon dispersion $\omega = ck$ yields

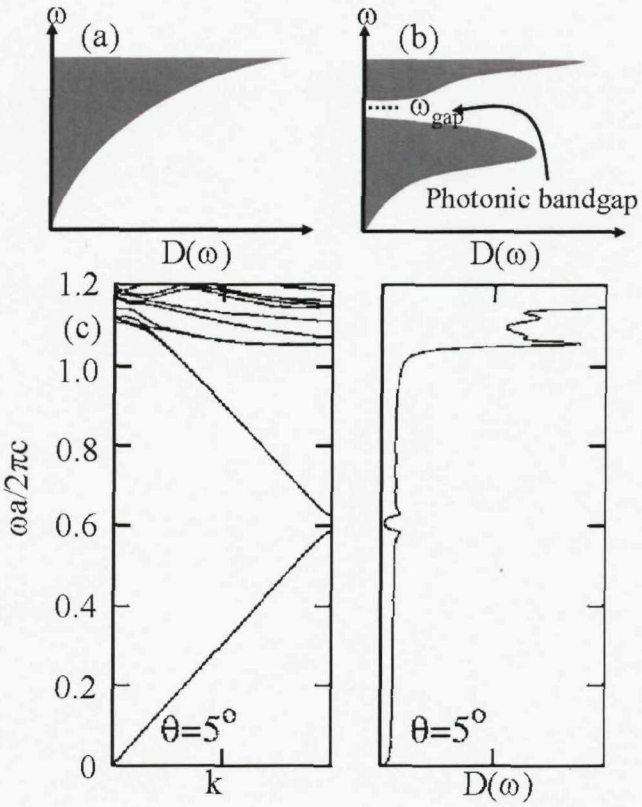

FIGURE 2.7: Schematic illustrations of (a) the photon vacuum density of states (DOS) $D(\omega)$ and (b) the density of states showing the bandgap where $D(\omega) = 0$. (c) Calculated bandstructure (left) and the density of states (right) for an *fcc* -packing of dielectric spheres ($n = 1.59$) in air at near normal incidence to (111) planes ($\theta = 5°$). Taken from [29].

$d\omega = cdk$, and thus the increase in the number of photon modes $N(\omega)$ for the increase dk of the wavevector equals:

$$dN(\omega) = \frac{4\pi(\omega/c)^2 d\omega/c}{(2\pi)^3} V \cdot 2 = \frac{\omega^2 d\omega}{\pi^2 c^3}, \tag{2.24}$$

where we have taken into account the two possible photon polarizations per mode. Finally the photon density of states can be calculated by normalizing (2.24) with the volume V:

$$D(\omega) = \frac{dN(\omega)}{d\omega}\frac{1}{V} = \frac{\omega^2}{\pi^2 c^3}. \tag{2.25}$$

The key point here is that in a photonic crystal the density of states is greatly modified and thus provides a method of suppressing the rate of spontaneous emission or enhancing the light extraction e.g. in LEDs [17, 33]. Some basic key features of the DOS and the bandgap are outlined in Fig. 2.7. In Fig. 2.7 (a) a schematic description of the density of

states $D(\omega)$ (bottom axis) against photon frequency ω is provided. This is an increasing function of ω as (2.25) also indicates. The DOS of a photonic crystal in Fig. 2.7 (b) however is drastically different. At a certain energy ω_{gap} there is a gap in the DOS indicating that at this energy the $D(\omega) = 0$, i.e. there are no available states in the crystal for the photons at this energy. In (c, right panel) the results for a theoretically calculated values [29] of $D(\omega)$ are shown for an *fcc* system of close-packed dielectric ($n = 1.59$) spheres in air for the bandstructure (left) at near normal incidence to (111) planes ($\theta = 5°$). Although for most parts $D(\omega)$ is featureless we see that there is a definite drop in the DOS values at the bandgap at $\frac{\omega a}{2\pi c} = 0.6$. This drop would manifest itself in a reflection peak and a transmission drop in a photonic crystal. It should be mentioned that usually in the DOS calculations the $D(\omega)$ is averaged over different directions in 3D whereas it is of utmost importance for the low RIC polymer opals to calculate the DOS as a function of different directions in the lattice. This will be further discussed in Chapter 6.

2.5 Important Features of the *fcc*-lattice

In this section a few important properties of the *fcc*-lattice will be outlined. For a thorough discussion of the *fcc*-lattices the reader is referred to Ref. [28]. Miller indices are a very useful approach to treating cubic lattices. A description of forming them was given earlier and one of their useful properties is that they can be use to calculate the interplanar distances in the *fcc* -lattice. Consider a group of lattice planes parallel to the plane (hkl). The interplanar distance d_{hkl} can be calculated by (2.26):

$$d_{hkl} = \frac{a}{\sqrt{h^2 + k^2 + l^2}}, \tag{2.26}$$

where a is the lattice constant (cf. Fig. 2.5). Furthermore, since in the cubic crystals the vector $[hkl]$ is perpendicular to the (hkl) plane[3] the angle β between the different lattice planes $(h_1k_1l_1)$ and $(h_2k_2l_2)$ can be calculated by the dot product relationship of (2.27):

$$\cos\beta = \frac{h_1h_2 + k_1k_2 + l_1l_2}{\sqrt{h_1^2 + k_1^2 + l_1^2}\sqrt{h_2^2 + k_2^2 + l_2^2}}. \tag{2.27}$$

Finally, the close-packed packing fraction ν, i.e. the fraction of the sphere volume to the unit cell in Fig. 2.5 (c), can be calculated by considering that the closest-packed face of the cube is the one with a sphere in the middle and in the corners relating the sphere diameter ϕ and the unit cell side length a through (cf. Fig 2.8):

[3] This is not generally true for non-cubic system.

$$a^2 + a^2 = (2\phi)^2 \Rightarrow a = \sqrt{2}\phi. \tag{2.28}$$

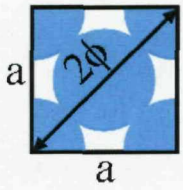

FIGURE 2.8: Closest packed face of the *fcc* -lattice showing the lattice constant a and the sphere diameter ϕ.

In the unit cell of *fcc* -lattice we have contributions from spheres in the eight corners and on the six faces. Thus there is $8 \cdot 1/8 + 6 \cdot 1/2 = 4$ spheres in the unit cell and by virtue of (2.28) the packing fraction ν in a close-packed *fcc* -lattice therefore reads:

$$\nu = \frac{4 \cdot \frac{4}{3}\pi \left(\frac{a}{2\sqrt{2}}\right)^3}{a^3} = \frac{\pi}{3\sqrt{2}} \approx 74\%. \tag{2.29}$$

Chapter 3

Opaline Photonic Crystal

The fabrication of 3D photonic crystals has proven very difficult during the last two decades. At the moment one of the most promising routes seems to be the use of the self-assembly of nanospheres. These systems are analogous to the precious opal gemstones found in the nature. The origin of the natural opals and their properties is an active research area [34, 35, 36, 37, 38]. The general consensus is that opals are formed in sedimentary or volcanic environments when nanosize amorphous silica spheres are self-assembled into a regular lattice [34, 39]. During the last ten years several research groups have developed methods of producing self-assembled systems similar to the natural opals using different nanospheres (e.g. silica [37, 40], polymer [41, 42]) as building blocks thus creating synthetic opals. The self-assembled nanosphere systems do not generally exhibit complete band gaps, which is why they are often used as templates for creating inverse opals. This is achieved through depositing high-refractive index material in the lattice interstitial sites and subsequently removing the nanospheres creating an inverse opal structure [37, 18]. In the following the most common methods of creating synthetic opals through sedimentation, vertical deposition, spin coating, shearing of colloidal solutions as well as possible subsequent inversion steps and characterization are briefly reviewed. Also the route to create polymer opals through compression induced shear-ordering is described.

3.1 Common Manufacturing Techniques for Synthetic Opals

3.1.1 Sedimentation and Vertical Deposition Methods

The two methods of sedimentation and vertical deposition are illustrated in Fig. 3.1. In the sedimentation method of Fig. 3.1 (a) the precursor colloid consists of a solvent (e.g. water) within which the nanospheres are dispersed [43, 44, 45]. Controlled layer-by-layer growth is achieved by slow sedimentation of the spheres due to gravity. The result is

a sedimented region forming the opal in the bottom of the vessel; typical evaporation times range from days to a couple of months. During the sedimentation different regions in the sedimentation vessel can be distinguished, cf. Fig. 3.1 (a), after [45]. To avoid nanosphere clusters (characteristic of regions 2-3) and thereby resulting deterioration of the opal the sedimentation procedure can be optimized by first separating the single spheres of layer 1 and subsequently proceeding with the sedimentation with these these spheres only [45]. After the evaporation the opal can also be sintered in order to increase its mechanical robustness.

Another popular manufacturing route based on colloidal nanosphere solutions is the vertical deposition method, Fig. 3.1 (b). In this self-assembly technique capillary forces are used to organize colloids into crystal multilayers. These arrays are ordered over long (~1cm) length scales and can be fabricated with thicknesses ranging from two layers to several hundred layers. A substrate slide is placed vertically in the deposition vessel containing the colloidal solution of the nanospheres to be deposited and suitable solvent, see inset of Fig. 3.1 (b). As the solvent evaporates, the nanospheres self-assemble into a close-packed crystal where the meniscus meets the slide surface. A thin crystal film is formed over a large area of the slide surface with the dropping liquid level, [40, 46]. In addition the the substrate can also be slowly lifted allowing for the adjustment of deposition rates and crystal thickness [47]. Vertical deposition is a fairly powerful fabrication route especially for non-aqueous colloids, where the evaporation rate is reasonably high.

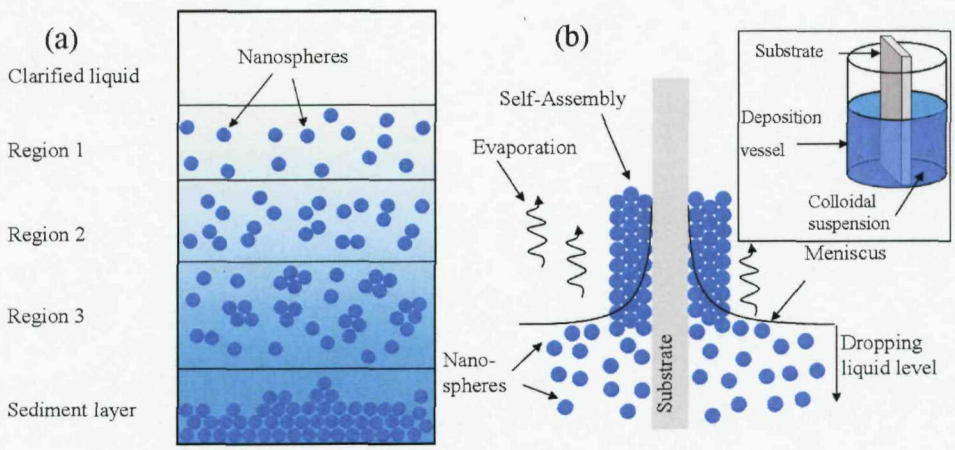

FIGURE 3.1: (a) Sedimentation fabrication of opals. Different regions with varying contents of microsphere clusters can be distinguished [45]. The opal is sedimented in the bottom of the vessel due to gravity. (b) Vertical sedimentation of opals. The nanospheres self-assemble onto the substrate in the vicinity of the meniscus as the liquid level drops. Inset: Deposition vessel with the vertically placed substrate and colloidal solution, after [46, 48].

Both the sedimentation and vertical deposition methods yield crystals of thicknesses up to 50μm and areas of around cm^2 but suffer from relative slowness of the preparation method. The fabrication of a few cm^2 area opal can take up to months and furthermore, the excellent crystalline order is often shadowed by possible cracking during sintering or drying [49].

3.1.2 Spincoating Technique

In the spin coating technique the precursor nanospheres (e.g. SiO_2) used for the opal are dispersed in a monomer and subsequently spincoated on a wafer (e.g. glass or Si) [50]. The resulting colloidal crystal thickness can be controlled through the spinning speed and the result is a hexagonally close packed lattice of the nanospheres in a monomer matrix. Finally the monomer can be photo-polymerized and subsequently removed through oxygen plasma etching. Alternatively the silica spheres can be removed through wet etching creating macroporous polymers. The resulting crystals show large scale ordering but with a moderate concentration of defects [51].

3.1.3 Colloidal Crystals

The method of creating crystal structures through shearing of colloids containing nanospheres (e.g. PMMA) has been studied among others by Ackerson et al. [52, 53], Haw et al. [54, 55] and Amos et al. [56]. In these types of crystals the ordering is brought about by shear which is induced in the material in either steady state or oscillatory form. Two straightforward methods of creating shear in colloidal suspensions are presented in Fig. 3.2.

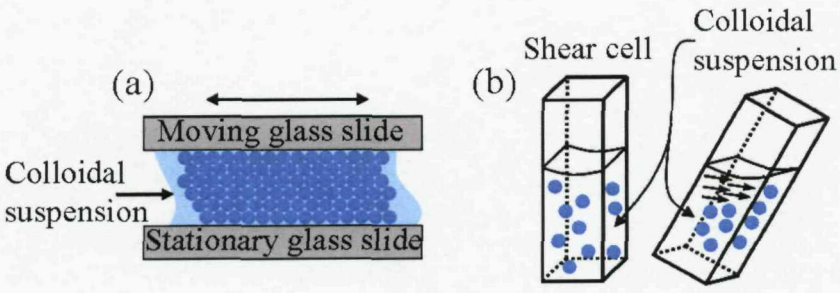

FIGURE 3.2: (a) Shearing of colloidal suspension between a stationary and a moving glass slide. Move direction indicated by an arrow. (b) Shearing of colloidal suspension by rocking the shear cell. The rocking creates the motion in the suspension indicated by the arrows.

Fig. 3.2 (a) shows how the shear is created in the colloidal suspension sandwiched between the two glass plates by keeping the bottom plate stationary while the top plate is under either steady or oscillatory motion. Fig. 3.2 (b) demonstrates how the shear

can be created by simply rocking the shear cell containing the colloidal suspension. The shearing motion creates crystal ordering in the colloid and often the best ordering is achieved at the glass plates or walls of the shear cell. These shear cell systems are especially well suited for studying the effect of different volume fractions to the crystallization but the resulting crystals suffer from the fact that the crystals often form only on the opposite faces of the cell with the middle of the colloid remaining disordered [57].

3.2 Further Functionalization Steps for Opaline Photonic Crystals

As mentioned previously several steps for further functionalization of the photonic crystals can be taken once the synthetic opals have first been created through one of the methods described above. One approach is to use the polymer opal as a template to create inverse structures where the interstitial pores of an opal are filled with a high refractive index solid and the original opal is subsequently removed. These high RIC inverse systems can be used to study the existence of the complete bandgap in 3D. A schematic of the manufacturing sequence of an inverted opal is given in Fig. 3.3 (a) with a TEM image of TiO_2 inverse opal in (b) [58].

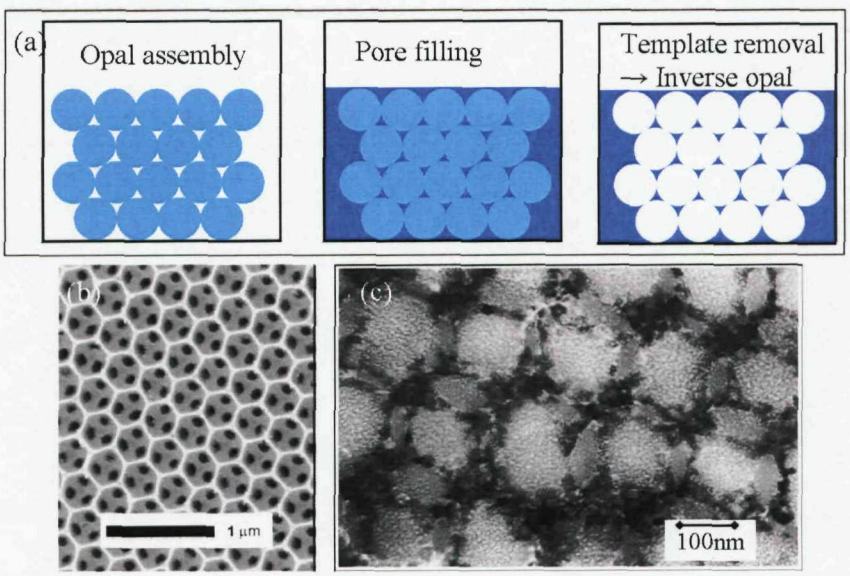

FIGURE 3.3: (a) Inverse opal fabrication sequence. After creation of the opal (light blue spheres, left), the interstities are filled usually with a high refractive index material (dark blue, middle) after which the original opal template is removed. (b) TiO_2 inverse opal, taken from [58]. (c) CdSe nanocrystal impregnated SiO_2 opal where the CdSe is observed as the dark aggregates between the larger lighter colour SiO_2 spheres, taken from [59].

Fig. 3.3 (a) shows the opal template being fabricated through self-assembly of e.g. PS spheres. Subsequently the pores are filled by a high refractive index material (e.g. TiO_2) and finally the opal template is removed through calcination yielding an inverse opal structure, see Fig. 3.3 (b). Another example of inverse opals was demonstrated by Arsenault et al. [11] who created a flexible polymer inverse opal through a process similar to the one described in Fig. 3.3 (a). They used SiO_2 to create the opal, after which the interstities were filled by a monomer, crosslinker agent and a photoinititator. Finally, the interstitial monomer was polymerized through UV-exposure and subsequently the SiO_2 opal template is removed through HF-etching. The resulting flexible inverse polymer opal has possible applications e.g. in sensing.

A further technique used for functionalization of synthetic opals is the impregnation or infiltration of the interstities with nanoparticles without removing the opal template. This has been done e.g. by Vlasov et al. [59] who used a SiO_2 opal filled with CdSe nanocrystals to study the effects of the presence of high refractive index semiconductor to the photonic crystal bandstructure. The impregnation was achieved though chemical vapor deposition of CdSe [60]. Example structure of SiO_2 opal with CdSe nanocrystals is given in Fig. 3.3 (c) where the nanocrystals can be seen as the dark aggregates between the lighter silica spheres. This type of doping of the original crystal is also used extensively in this thesis but with a completely different manufacturing technique, as will be described in the following sections.

3.3 Artificial Opals by Melt Compression

Totally different approach to the opal manufacturing has been presented by Ruhl et al. [49, 61]. This technique relies on the shear-ordering of core-shell polymer nanospheres through rapid uniaxial compression. This is the method of sample preparation for opals studied in this thesis. One of the most critical manufacturing steps in the compression technique is the precursor fabrication. The monodispersity of these precursor particles is of utmost importance to ensure the optimal shear-profile and thus ordering in the latter stages of the manufacturing [49]. In the following the process of emulsion polymerization is first outlined, before introducing the detailed precursor particle synthesis. Finally, the actual opal compression process is presented.

3.3.1 Polymer Precursor Fabrication

The theory of emulsion polymerization was developed by Harkins [62] and Smith et al. [63]. The idea is schematically outlined in Fig. 3.4 (a). The monomer (e.g. styrol) is stabilized by emulsifier molecules in water forming large monomer droplets. Excess emulsifiers in the solution form micelles into which small amounts of monomer diffuse.

Initiator radical is introduced into the solution, which then initiates the polymerization of the monomers inside the micelles thus turning the micelle into a polymer particle. More monomers diffuse out of the monomer droplets into the growing particle and eventually most of the monomers are located in the resulting polymer particles [64].

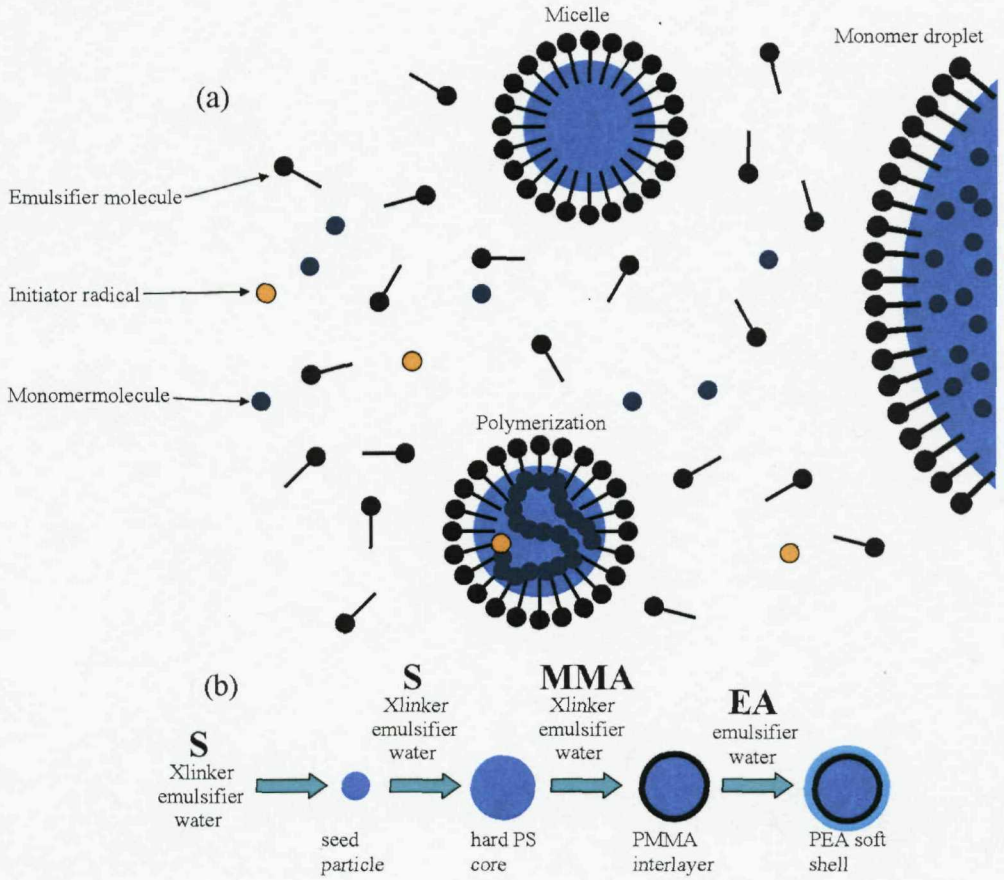

FIGURE 3.4: (a) Emulsion polymerization. Polymer particles a grown through the use of emulsifier molecules forming micelles and monomer droplets. Initiator radical is used to kick-off the polymerization. (b) Sequential growth of multi-shelled polymer particles starting form styrene (S), thereafter methylmethacrylate (MMA) and finishing in ethylacrylate (EA). Crosslinkers (Xlinker) are used in different stages to crosslink the polymer structures.

This technique can be further refined by the use of seed particles. This is basically an initialization step creating seed particles (through the mechanism described above) which have been stabilized by the emulsifier molecule. When more monomer emulsion containing water, styrene, crosslinker chemical and emulsifier is added to the seed particle solution the seed particles continue to grow. This is achieved through carefully balancing the amount of the monomer and the emulsifier molecules such that no new micelles (and thereby polymer) are formed but rather the existing particles continue to grow. The size of the PS particles is controlled by the amount of the emulsifier molecule in the seed particle growth; bigger particles result from lower emulsifier concentration. The crosslinking chemical can be activated (e.g. thermally) making the spheres hard, and

also enhancing the monodispersity by preventing further swelling by monomers. A typical polydispersity value, defined through the standard deviation of the nanosphere diameter is 5% [64], about the same as typical values of 4% for commercially available SiO_2 nanospheres [65].

This manufacturing procedure can be applied in sequence to create core-shell particles. These types of particles are the core innovation for producing artificial opals by polymer melt compression. By applying the emulsion polymerization for different monomers one can create a whole range of polymer mixtures and architectures. The opal precursor spheres considered in this thesis consist of a polystyrene (PS) hard core coated with a polymethylmethacrylate (PMMA) interlayer followed by a polyethylacrylate (PEA) shell. These multi-shelled spheres are synthesized using the emulsion polymerization reaction according to Fig. 3.4 (b). First the PS seed particle is formed using styrene (S) monomer after which the actual core PS particle is grown using the same monomer. Subsequently the monomer is switched to MMA which polymerizes forming an interlayer between PS and the final shell consisting of PEA. The PMMA layer is needed between the PS and PEA to ensure complete grafting of the PEA to the underlying structure. Note that PS and PMMA are crosslinked whereas the PEA is left uncrosslinked leaving it soft and flowing at room temperature. The PEA shell thickness is chosen such that it will be enough to produce good elasticity in the opal manufacturing stage later on. The PEA shell must be thick enough to permit flow in the compression later on but thin enough to be efficiently grafted on to the PMMA interlayer [49]. Typically the material composition of the polymers has volume fractions of 30:13:57 of PS:PMMA:PEA [64], respectively. The PS-PMMA sphere radii can be varied between 190-350nm in a straightforward manner by varying the emulsifier content during the seed particle growth.

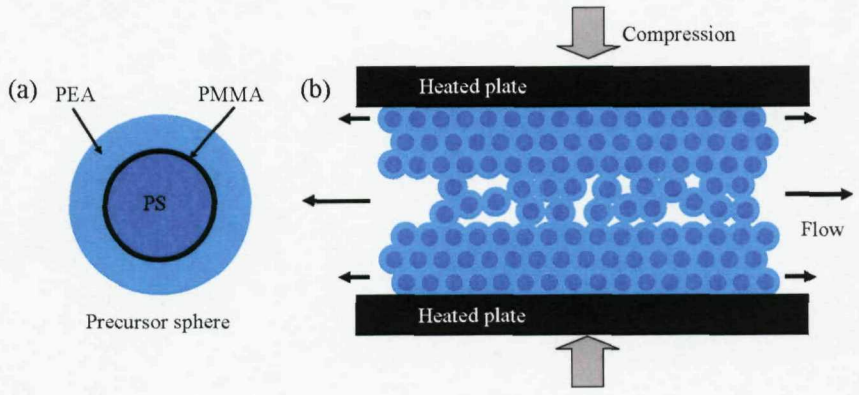

FIGURE 3.5: (a) Precursor polymer nanosphere consisting of PS hard core, PMMA interlayer, and PEA shell. (b) Uniaxial compression between two heated plates resulting in the crystallization of the PS-PMMA spheres with the soft PEA material flowing to fill the interstitial sites

3.3.2 Compression Manufacturing of Polymer Photonic Crystals

The polymer core-shell nanospheres, cf. Fig. 3.5 (a), can now be used as building blocks for the artificial polymer opal. The opal manufacturing process is depicted in Fig. 3.5 (b). The core-shell latex emulsion is first coagulated or spray-dried and thereafter the polymer mass is subjected to uniaxial compression between two heated plates as depicted in Fig. 3.5 (b). The compression lasts for ~1min with a maximum pressure of 50 bars and the plate temperature of 150°C. During compression the polymer melt flows sideways and the PS-PMMA cores self-assemble into a quasi-close-packed lattice and the soft non-crosslinked PEA fills the lattice interstitial sites. The compression-induced flow is at its maximum in the middle of the melt, but at the same time the shear is maximized at the plates. The maximized shear results in the colloidal crystal growing from the plates towards the center of the film. The resulting film has, for the ordered part, face-centered-cubic (*fcc*) lattice with the [111]-direction perpendicular to the compression plates. The quality of the crystal can readily be verified from Fig. 3.6 (a) where the TEM picture reveals the hexagonal ordering of the (111)-planes. Also the characteristic ABC-packing is observed in Fig. 3.6 (b) with only the very tops of the third sphere layer showing [49]. However, studies done at DKI, Darmstadt, show that ratio of ordered to disordered parts in the film is roughly $\frac{1}{3} : \frac{1}{3} : \frac{1}{3}$, with the ordered parts situated against the compression plates with the disorder in between [66]. The engineering of the flow-profile and the resulting degree of ordering is a very challenging and interesting issue and work is being done at the moment to examine this feature further.

The photonic properties of these films are determined by the precursor sphere size, refractive index contrast in the lattice as well as possible dopants or infiltrated materials. The refractive indices for PS, PMMA and PEA are 1.59, 1.49 and 1.46 [64], respectively. This means that the refractive index of the core-polymers at the *fcc*-lattice sites is 1.56 (volume average of PS:PMMA) yielding an effective refractive index of 1.51 for the entire structure. Note that this composition assumes that the structure spheres are not touching; in the case of close-packed PS-PMMA spheres (packing fraction 0.74 [67]) this effective refractive index would be 1.53. In other words the material has a very low refractive index contrast within the *fcc*-lattice and thus exhibits no complete photonic bandgap [68].

In order to optimize the flow in the compression manufacturing the PS-PMMA particles need to be monodisperse but also crosslinked to retain their shape. The compression manufacturing results in a soft and flexible film with a thickness between 200-500μm depending on the amount of the precursor material and compression pressure. Furthermore, UV-activated crosslinking chemicals (such as Benzophenone) can be mixed into the polymer melt during compression. This crosslinker can then be activated afterwards by exposing the film to UV light creating thus an elastomeric thin film photonic crystal.

A realization of the film is given in Fig. 3.6 (c-d) with the color changing due to strain-induced lattice change. The colour change is not very pronounced due to non-ideal lighting conditions.

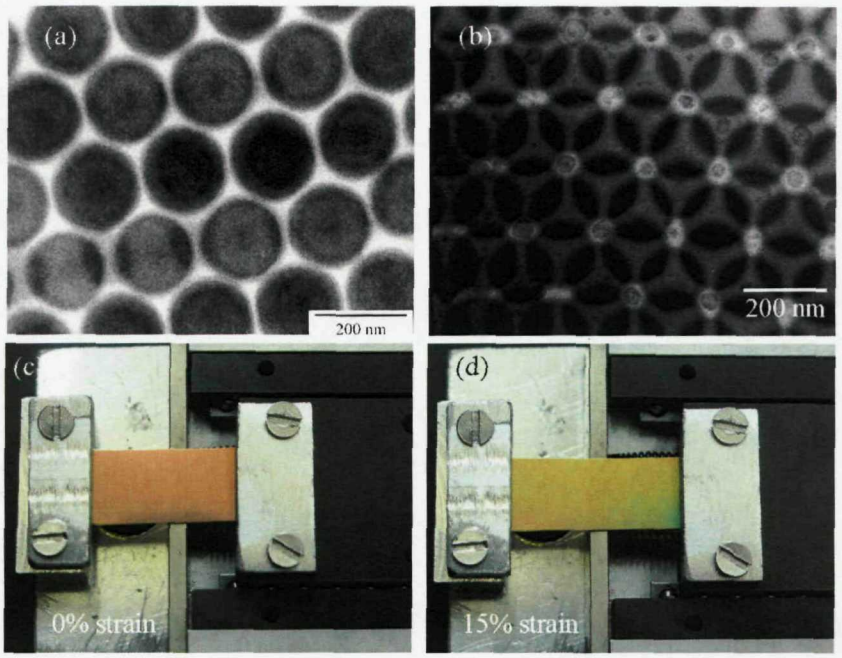

FIGURE 3.6: (a) TEM image of the 111-lattice plane, PS-PMMA spheres in black, PEA in white. (b) ABC -packing of the PS-PMMA spheres. Color changes due to strain induced lattice change from (c) reddish-orange (0% strain) towards (d) greenish (15% strain).

3.3.3 Brief Comparison of Sedimented and Polymer Opal

Fig. 3.7 shows digital images of a natural sedimented opal (left) and a bent polymer opal (right). The separate domains in the natural opal are clearly visible through discrete colouration of the opal. The absence of polycrystallinity is observed in the polymer opal, with a colour continuum produced by the changing angle of incidence on the bent polymer opal surface. The scale bar also shows the magnitude of the uniform appearance of the polymer. This is, of course, not an extensive proof of the long range ordering but gives visual evidence of the pronounced difference in the appearance of these two very different systems.

3.3.4 Nanoparticle Mixing

Another very attractive feature of this manufacturing technique is the easy incorporation of additional nanomaterials into the periodic structure. This can be achieved either by introducing these nano-dopants directly into the polymer precursor prior to compression

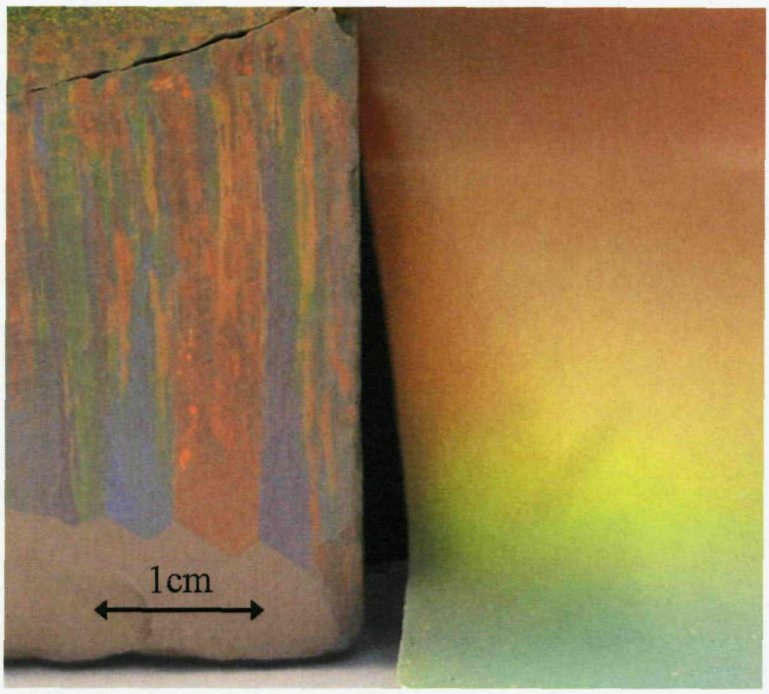

FIGURE 3.7: Digital image showing a natural compressed opal (left) and a bent polymer opal (right).

or by running an additional mixing phase with the polymer and dopants. This mixing is carried out by using a twin screw extruder, such as the one prsented in Fig. 3.8 (a).

The precursor polymer particles can be mixed together with the nanoparticle dopant powder in an extrusion process with a twin-screw extruder. The polymer-dopant mix is fed into the extruder with a plunger through the opening indicated by the blue arrow in Fig. 3.8 (a). The twin screws force the mix down towards the lower end of the extruder (blue path) until the point labeled as "by-pass valve". This valve can be operated to either feed the mix back to the input end of the screw to improve mixing (red path) or to steer the mix into the output dye (blue dashed path). At higher temperatures (150° C) the soft PEA shells merge into a continuous matrix that embeds the rigid PS-PMMA -cores. These latex spheres flow at high temperatures practically like a regular polymer melt. This extrusion process is carried out to homogenise the dopant distribution, e.g. carbon nanoparticles (known as carbon black) or semiconductor quantum dots (QD), within the precursor PEA matrix material (Fig. 3.8 (b)) using the shearing forces present in the twin-screw extruder. The extruder output in room temperature is a spaghetti-like rope, which is then chopped up before opal compression. During the compression the PS-PMMA cores form the lattice while the nanoparticles occupy the interstitial lattice sites in the PEA rather homogeneously. The nanoparticle dopant distribution is controlled through the extrusion but also through the compression sequence. As was previously mentioned it is possible to manufacture the opal film directly by placing all the ingredients (precursor polymer and the nano-dopants) into the compression method but the pre-compression extrusion ensures better mixing. Obviously the shear force

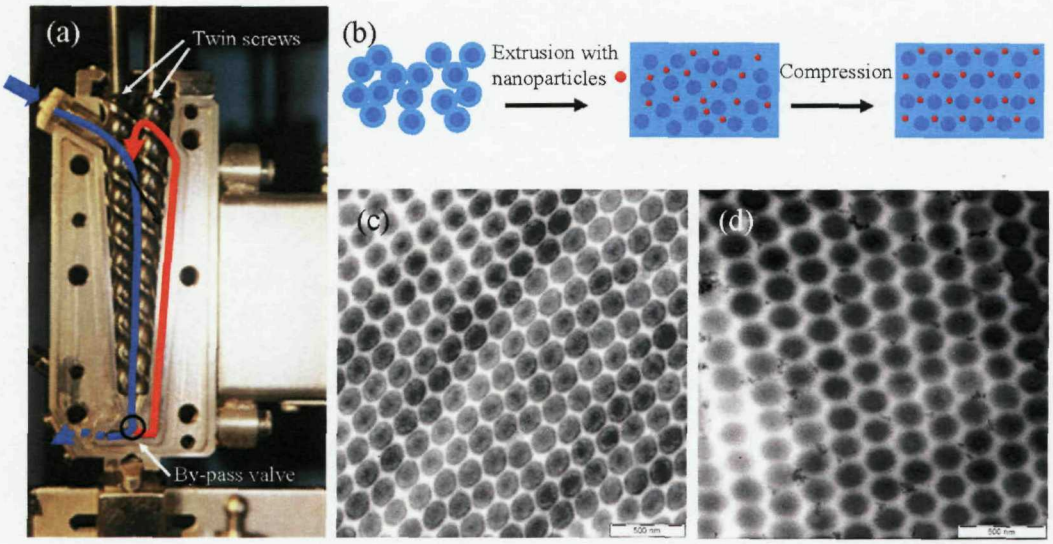

FIGURE 3.8: (a) Twin-screw extruder showing the input path of the precursor-nanoparticle mix starting from the blue arrow and following the blue solid line. By-pass valve can be operated to either feed the mix back to the input end of the screw to improve mixing (red path) or to steer the mix into the output dye (blue dashed path). (b) Schematic view of the effect of mixing starting from precursor mix (left), using the extruder to create the mix of PS-PMMA (dark blue) spheres in the PEA melt (lighter blue) and nanoparticles (red dots) and finally creating a relatively homogeneous mixing of the nanoparticles into the PS-PMMA lattice in the PEA surrounding. (c-d) TEM images of a polymer opal. The images are of the same sample, but (c) has been stained with rutheniumtetroxide for a better contrast of the polystyrene polyacrylate system, (d) has not been stained, and thus shows the black interstitial carbon nanoparticles. The skew in the images is created by the microtoming process and thus not present in the actual lattice.

profile (and thus the nanoparticle mixing) can be controlled through different pressure and temperature sequences in the extrusion and the compression and research into the optimisation of the fabrication parameters is ongoing. Furthermore, the film can also be fabricated by continuous extrusion which takes places through a thin slit forcing the shear flow resulting in the self-assembly of the precursor particles. However, all the opal samples considered in this thesis are compression assembled unless otherwise mentioned.

The mixing of the dopants can be observed in Fig. 3.8 (c-d), which are two TEM images of the doped polymer opal. The dopant used is carbon black and the opal in Fig. 3.8 (c) has been stained with ruthenium-tetroxide for a better contrast of the polystyrene polyacrylate system, whereas Fig. 3.8 (d) has not been stained, and thus shows the black interstitial carbon nanoparticles. The skew in the images is created by the microtoming process and thus is not present in the actual lattice. We see from the TEM images that the mixing is rather homogeneous and even though in case of C-black, cf. Fig. 3.8 (d), some coagulation of the dopant is observed the nanoparticles are not greatly disturbing the lattice ordering. One of the most interesting problems that is discussed in this thesis is the complicated interplay between the polymer opal lattice, possible intrinsic lattice defects and the additional dopants.

3.3.4.1 Nanoparticle Dopants

A great variety of dopants can be mixed into the polymer opal structure. The dopants in different forms can be mixed into the precursor in the extrusion phase. Throughout the most of this thesis the samples have been doped with carbon black (C-black) nanoparticles. Carbon black [C.A.S. NO. 1333-86-4] is a colloidal form of carbon particles that are produced by e.g. incomplete combustion of gaseous or liquid hydrocarbons [69]. Most carbon blacks contain over 97% of elemental carbon and are widely used in rubber and plastic products, tires, inks and as pigment. Carbon black is introduced into the precursor mix as black powder.

Other types of nanodopants that can be used are semiconductor quantum dots, metallic (e.g. gold) nanoparticles, molecular dyes or magnetic nanoparticles. In the course of this work these type of dopants have been briefly experimented with and they are normally introduced into the extrusion-mixing process in the form of colloidal solution. It should be pointed out that the nanoparticles disperse in the manufacturing process in the PEA interstitial material since they cannot penetrate the hard crosslinked PS-PMMA cores.

3.4 Polymer Opal Sample Introduction

Digital images of different polymer opal samples are presented in Figs. 3.9 - 3.10. These images have been taken in different geometries so no direct comparison as to the different colors vs. (111)-plane distances can be made. However, they do illustrate the effect of the nanoparticle dopant to bring out the colour. From left to right in Fig. 3.9 the polymer opals are doped with Au, Carbon black and no dopants. In Fig. 3.10 we see the effect of doping with carbon black at different levels. From (a) to (d): 0 wt-%, 0.05 wt-%, 0.1 wt-%, and 0.2 wt-%. The images of Fig. 3.10 have been recorded in exactly the same forward-scattering (near reflection) geometry, thus allowing for comparison of visual appearance between the images.

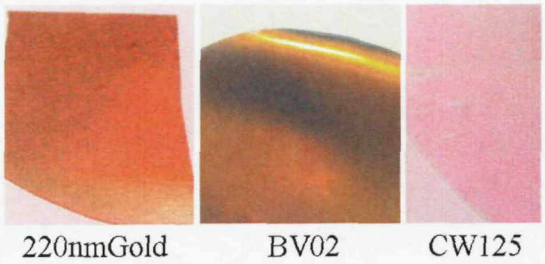

FIGURE 3.9: Images of Polymer opal pieces doped with (from left to right): Au, carbon black and no dopants.

The different polymer opal samples studied in this thesis are summarised in Table 3.4. The table shows the sample name, the perpendicular incidence resonance wavelength

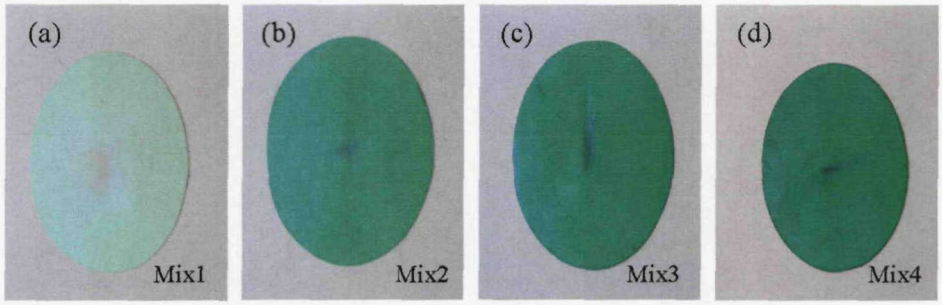

FIGURE 3.10: Images of polymer opal discs doped with carbon black nanoparticles by the amounts (a) 0 wt-% , (b) 0.05 wt-%, (c) 0.1 wt-%, and (d) 0.2 wt-%.

TABLE 3.1: Polymer opal samples used in this thesis. Samples marked with $^+$ were prepared by the author.

Name	λ_{111}(nm)	d_{111}(nm)	Dopant (size)	Conc. (wt-%)
LS02	901	290	C-black ($\sim$ 10nm)	0.1
BV02	635	206	C-black ($\sim$ 10nm)	0.2
Au	629	204	Au (8nm)	not known
CW125	560	182	undoped	0
QD	567	184	CdSe quantum dots (4 nm)	2mg
MD	567	184	molecular dye	0.1
Mix1$^+$	601	195	C-black	0
Mix2$^+$	601	195	C-black ($\sim$ 10nm)	0.05
Mix3$^+$	601	195	C-black ($\sim$ 10nm)	0.1
Mix4$^+$	601	195	C-black ($\sim$ 10nm)	0.2

λ_{111} corresponding to the (111) -plane resonance, the (111) plane distance d_{111}, the type and the size of dopants and their concentration. The samples Mix1-Mix4 were manufactured by the author while visiting the DKI in Darmstadt in 2006, while all the other samples were maufactured by the DKI staff during the course of this thesis.

3.5 Chapter Summary

In this chapter the different opal manufacturing routes were discussed. Sedimentation and the vertical deposition methods and the pros (excellent lattice quality) and cons (slow method, small scale crystals due to cracking) of each method were outlined. The polymer opal fabrication was detailed starting from the precursor synthesis also presenting the compression fabrication route. Different nanoparticle dopants include e.g. carbon black, semiconductor quantum dots and gold nanoparticles and they are dispersed in the intrestitial PEA rather homogeneously. The major benefits of this technique are the straightforward, scalable manufacturability yielding well ordered opals that can be nanoparticle-doped. Finally, the different polymer opal samples used in this thesis were described through structural details and optical images.

Chapter 4

Flow-Induced Shear Ordering of Polymer Opals

The polymer opal manufacturing technique used for samples in this thesis was presented in Chapter 3. The idea of flow-induced ordering has been experimented with quite extensively in the last two decades [52, 53, 57, 54, 70, 56]. Ackerson et al. [52, 53, 57] have conducted extensive research on colloidal solutions showing long-range ordering in oscillatory shear conditions. Haw et al. [54] experimented with different oscillatory shear rates on colloidal suspensions showing regimes of ordering depending on the amount of strain. In their steady shear experiments Amos et al. [56] reported the finding of large-area single crystals with twinned *fcc*-structure. The technique here and their findings resemble those of ours, with the main difference being the way the shear is introduced into the system, which in our case is through uniaxial-compression (Fig. 3.5 (b)), and the viscosity and components of the system (colloids in solvents vs. viscous polymer melt). In this chapter a key analysis of the 3D rheologically-derived properties of the shear-ordered opaline thin-film photonic crystals is presented using optical tracking of the strain-induced anisotropy. Probing UV-surface diffraction combined with band gap measurements reveal a complete picture of the unit cell changes under strain.

4.1 Flow and Shear Profile

The polymer opal manufacturing process was outlined in Chapter 3 with the very straightforward compression sequence given in Fig. 3.5 (b). Intuitively the resulting flow profile due to the compression has two distinct features. First it is predicted to have a distribution function along the compression plates, possibly defined by a radial flow field, and secondly the thickness direction (vertical x-direction in Fig. 3.5 (a)) experiences a flow which is defined by the viscosity of the polymer melt. Roughly speaking one can distinguish two processes related to the creation of the opal. Hexagonally-

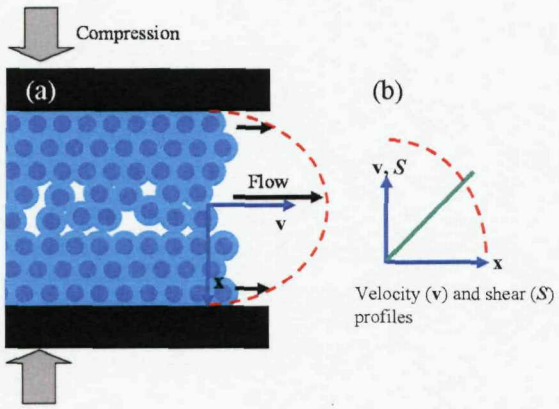

FIGURE 4.1: (a) Compression manufacturing of polymer opals with the flow indicating arrows (black), Poiseuille flow profile (red) and the coordinate system definition (blue). (b) Clearer view of the coordinate system with the flow (red) and shear (green) profiles.

(quasi)-close-packed layers are needed by energy minimization principle to accommodate the PS-PMMA cores in the (111) plane family but also thereby created layers need to be ordered in the thickness direction for the opal structure.

4.2 Vertical Flow Profile

The vertical flow profile is indicated in Fig 4.1 (a) by black arrows and is thought to be Poiseuille type [57, 71] with the maximum velocity of the flow at the middle of the polymer melt. This type of flow is characteristic of incompressible viscous fluids flowing between two parallel plates or in a pipe. The flow profile is achieved by solving the Navier-Stokes equation yielding a parabolic flow velocity field [72]. This is indicated in Fig. 4.1 (a) by the red dashed line having its minima at the plate surfaces due to the drag of the plates experienced by the fluid and maximum in the center of the melt. We define a (v,x) -coordinate system as in Fig. 4.1 (a) and rotate it by 90° to get the view in Fig. 4.1 (b). In the view of Fig. 4.1 (b) one can define the velocity v according to (4.1):

$$v = v_0 + ax^2, \tag{4.1}$$

where v_0 and $a(>0)$ are zero-velocity and geometry parameters, respectively. From this flow field it is straightforward to define a shear parameter S by:

$$S = \frac{dv}{dx} = 2ax. \tag{4.2}$$

Eq. (4.2) shows that shear is an increasing function of x i.e. the distance from the center of the melt. This is also indicated in Fig. 4.1 (b) by the green line. We can thus expect

the shear to be at its maximum at the plates which in turn leads to maximized ordering as has been witnessed also previously [49, 52, 57]. The physical processes occurring during the compression are far more complicated than outlined above, but clearly, in order to maximize the ordering in the polymer structures one has to carefully engineer the shear-profile in the compression. This is a very challenging task for many reasons. The melt flow in the lateral direction (perpendicular to the plane of the paper) has to be taken into account and it has some very interesting properties as will be outlined in the following sections.

As already described in Chapter 3, one of the characteristics of the ordering in the thickness direction during the compression manufacturing is that the resulting film has three distinct regions. We observe that about one third of the film close to the top compression plate is well ordered, followed by a one third of less ordered center region, and finally a ordered third close to the bottom plate. This is also shown in the TEM image in Fig. 4.2 below revealing the ordered region closer to the top surface of the film and the increased disorder towards the middle of the film. Similar findings in shear-ordered materials have been reported before [57] indicating that the decreasing shear leads to decreasing order. This is one of the big challenges remaining in the compression induced shear-ordering. On the other hand, with the polymer opal materials we have been mostly interested in reflection and scattering properties at bandgap. These properties depend strongly on the penetration depth of the light in to the structure and this depth is expected to be $\leq 10\mu$m (cf. Chapter 6 for further discussion). Thus the reflection and scattering take place within the first ordered third of the opal film because the typical film thickness ranges from 100μm to 400μm.

4.2.1 Twinned fcc-structures

Shear-ordering can lead to very satisfactory crystal quality in the depth direction. Evidence of the ABC-type layer stacking leading to an *fcc*-type crystal ordering has been given, cf. Fig. 3.6 (a), but due to the local nature of the TEM imaging this is by no means a decisive proof of flawless *fcc*-packing. In fact, it is not entirely clear why the packing should obey the ABC-type sequence. This could be due to vibrational states of the structure being formed which then lead to the favoring of ABC -packing over ABAB or completely random packing sequence. There is evidence in the literature of self-assembled colloidal crystal showing a behavior called twinning [57, 56]. This means that somewhere in the crystal the packing changes from being ABCABC... to ACBACB... which changes the diffraction behavior of the crystal. This feature has not been extensively studied in this thesis but it is pointed out in earlier studies that shear-ordered polymer opals also show evidence of twinning. In Fig. 4.3 (a) the different packing sequences are schematically depicted, whereas Fig. 4.3 (b) shows the schematic of the near grazing-incidence diffraction from (220) planes. The resulting diffraction pattern from

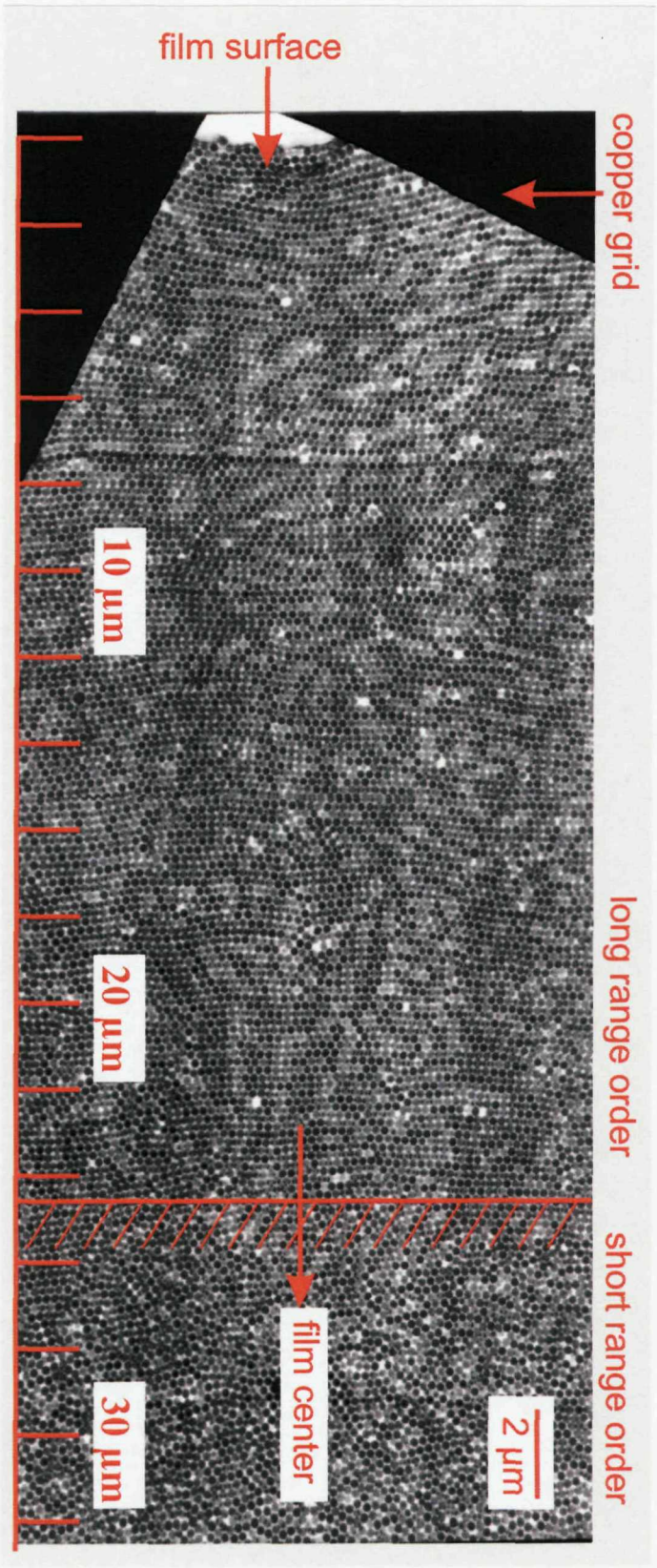

FIGURE 4.2: Ordering of the polymer opal film in the thickness direction from top (left) to bottom (right) showing the well-ordered first third of the film becoming less ordered towards the middle of the film. Taken from [49].

a polymer opal showing six-armed reflection from the twinned (220)-plane structure is presented in Fig. 4.3 (c) [61].

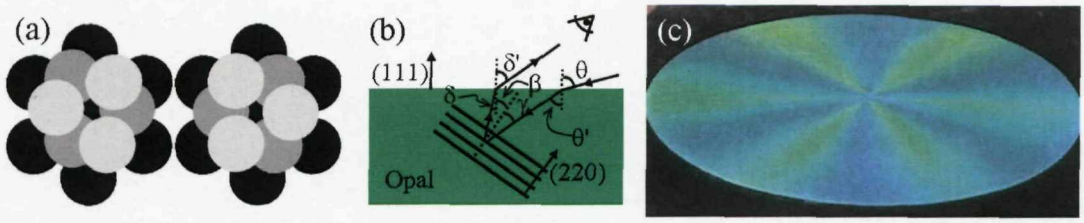

FIGURE 4.3: (a) Schematic picture showing the origins of twinning due to ABC (left) and ACB packing. (b) A schematic picture showing the near grazing incidence diffraction from (220) planes. (c) Diffraction from a twinned structure at near grazing incidence due to (220) crystal plane family. Taken from [61].

The possible diffraction angles δ' from (220) planes can be calculated by considering the incident angle θ, the effective refractive index of the opal n_{eff}=1.56 and the angle β between the (111) planes (parallel to the opal surface) and (220) planes. This angle can be calculated through (2.27) to be $\beta = 35.2°$. Geometrical analysis from Fig. 4.3 (b) yields $\delta = 2\beta - \theta'$. This diffraction can only be seen at the angle range $\delta = [30.6°, 35.2°]$. The presence of one of the twins would yield the diffraction from (220), (202) and (022) planes and would thus be a 3-fold diffraction pattern but the presence of both twins manifests itself as the 6-fold diffraction presented in Fig. 4.3 (c) [61, 73].

4.3 (111)-Layer Flow Profile

In the previous section a brief overview of the shear flow was given. It is clear that the shearing affects the order in the thickness direction (between the compression plates) leading to ordering of consecutive (111) layers in the structure. However it is interesting to consider how such compression affects the organization within a (111) layer and how the flow is organised. We studied the compression-induced intra-layer order using a frequency doubled Ar-ion laser (Coherent Innova 90C FRED). The fundamental line of 496nm was doubled to yield 248nm UV-radiation. At this wavelength the penetration length into polystyrene is ~1.0 μm [74]. Moreover taking into consideration that the LS02 sample studied here is doped by absorbing C-black effectively we are probing the *surface* layer of the opal. This pattern cannot originate from twinned (220) planes because the measured diffraction angles for the sixfold pattern (cf. Fig. 4.4 (a)) are approximately 48° compared and the expected twinned (220) plane volume diffraction angles would be $\approx 63°$. Thus by looking at the diffraction pattern are able to draw conclusions on the surface layer ordering and flow. Typical *surface*-diffraction pattern from a 355nm diameter PS-PMMA sphere sample LS02 (cf. Table 3.4) can be seen in Fig. 4.4 (a) and shows the 6-fold nature which corresponds to 6-fold symmetry of the single layer of PS-PMMA spheres in PEA polymer.

In these systems the crystal ordering is dependent on both the applied shear profile and the strength of shear, and with suitable conditions long range ordering is achieved, possibly with some dislocations or stacking faults. In both steady-state shear and oscillatory shear between a stationary and a moving plate, two different regimes have been distinguished [54]. It has been suggested that in the low shear regime the lines of quasi-touching spheres ($\vec{n}_d$) are perpendicular to the velocity flow $\vec{v}$, Fig. 4.4 (b), whereas in the high strain regime these lines are parallel to the velocity vector, Fig. 4.4 (c). Two different scenarios of how local hexagonal geometry produced by shear-flow ordering can be pictured. Firstly, ordered regions can independently nucleate depending on the shear, with formation of poly-crystalline domains across the film, Fig. 4.4 (d), which is characteristic of opal systems prepared by sedimentation or drying of colloidal suspensions [42, 75, 76]. In the other scenario the radially-symmetric material flow during compression forces domain alignment, resulting in a "super-domain" as large as the entire 15cm diameter sample with a macroscopic radial director profile, $\vec{n}_d$ outwards in Fig. 4.4 (e). While it is clear that slip line dislocations or point vacancies are needed in this structure to accommodate the local hexagonal packing, the super-domain is characterised by a spatially-coherent director vector, $\vec{n}_d(r, \theta) = n_d \vec{r}^{\circ}$. [1]

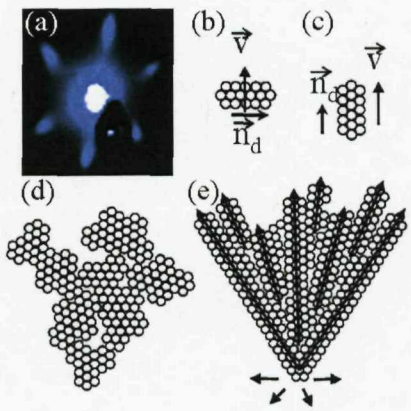

FIGURE 4.4: (a) The hexagonal surface diffraction pattern from sample LS2 measured in reflection with a 248nm laser. (b) Low-shear and (c) high-shear regime. (d) Multi-domain ordering vs. (e) radially-oriented large scale hexagonal ordering of the polymer opal into a super-domain during compression.

The idea of this director $\vec{n}_d$ measurement setup lies in testing the intuitive assumption that when compressing an amount of polymer uniaxially the material flow is basically radially directed. We aim to test the hypothesis that the the compression works in the high shear regime and thus the polymer flow velocity $\vec{v}$ would be parallel to the director $\vec{n}_d$ pointing outwards from the film center. This would lead to a macroscopic lattice director vector which is oriented everywhere on the circular sample film collinear with radial unit vector (see Fig. 4.4 (e)).

[1] This would be true everywhere except at the middle region of the film which is the origin of the polymer material flow.

A schematic of the measurement setup is given in Fig. 4.5 (a) with the laser light horizontally polarized along the x-axis. The laser beam was directed through the aperture (A) to be incident at approximately $\delta = 23°$ on the sample located at a distance of 52 mm from the screen and 24mm left along the scanline of the inset in Fig. 4.5 (a). The resulting front-side diffraction pattern was recorded using a CCD camera (square pixels of 6.45μm x 6.45μm) and a camera lens viewing the screen at an angle of 67°. The bright reflection spot (R) was attenuated using a ND2 filter. Then the spot was moved 1mm right and the diffraction pattern was re-recorded. This repeated for a number of times always moving the spot across the centerline as depicted in Fig. 4.5 (a), inset. An angular range of about 57° was covered. The angle of incidence was chosen such that the diffracted photons were detected within the camera angle of view but also such that diffraction from the sample was possible. Note that the diffracted contribution consisted only of a single beam since the probing wavelength was relatively long in comparison to the structure being probed (PS-PMMA sphere diameter of around 235nm). This is due to the effect which the diffracting lattice has on the incident wavevector $\vec{k}_{in}$. This is illustrated in Fig. 4.5 (b) in a 1D case. The incoming beam defines the diffraction circle of radius $\left|\vec{k}_{in}\right| = 2\pi/\lambda$. The reflected beam is indicated by $\vec{k}_R$. The effect of the lattice is to change the parallel momentum by a multiple of $\vec{G}$, which is the lattice vector (red dashed vector). We see from the illustrations that only one of the possible diffractions fullfils the energy conservation $\left|\vec{k}_D\right| = \left|\vec{k}_{in}\right|$. Only by fixing the angle of incidence such that the sum of the parallel component of the incident momentum $\vec{k}_{in}$ and the lattice vector $\vec{G}$ can still be projected onto the circle defined by the length of the incident wavevector $\left|\vec{k}_{in}\right|$ can diffraction be observed. Fig. 4.5 (c) shows a typical diffraction pattern with the reflected beam (R) (attenuated by an ND2 filter), the aperture (A) and the diffracted beam (D).

From the diffraction patterns the polymer opal grating vector $\vec{G}$ can be calculated using the following procedure. Firstly, we find from the image the reflection point coordinates $R = (R_x, R_y, -d)$, where d is the distance from the screen and R_x (R_y) are the x (y) coordinates of the reflection spot on the screen. Similarly the diffraction point coordinates are extracted, $D = (D_x, D_y, -d)$. Now the surface normal $\vec{n}$ is calculated in this geometry (the incoming beam hits the sample at the origin and $\vec{k}_{in}$ is always perpendicular to the screen) using the help of the dashed triangle drawn on the screen in Fig. 4.5 (a). With the help of the dashed line triangle on the screen we can calculate: $\tan\alpha = 1/d\sqrt{{R_x}^2 + {R_y}^2}$, and that $\alpha/2 = \delta$ (angle of incidence), $\tan\phi = R_x/R_y$ and $s = d\tan\delta$. Finally this allows for us to write the normal vector $\vec{n}$ in its component form: $n_x = -s\cos\phi$, $n_y = -s\sin\phi$ and $n_z = -d$. Next we normalize the normal vector by its length to get the normal unit vector $\vec{n}°$. We use this technique to incorporate any surface corrugation or possible tilt of the sample to the calculation of the surface normal vector. For the diffracted beam we write:

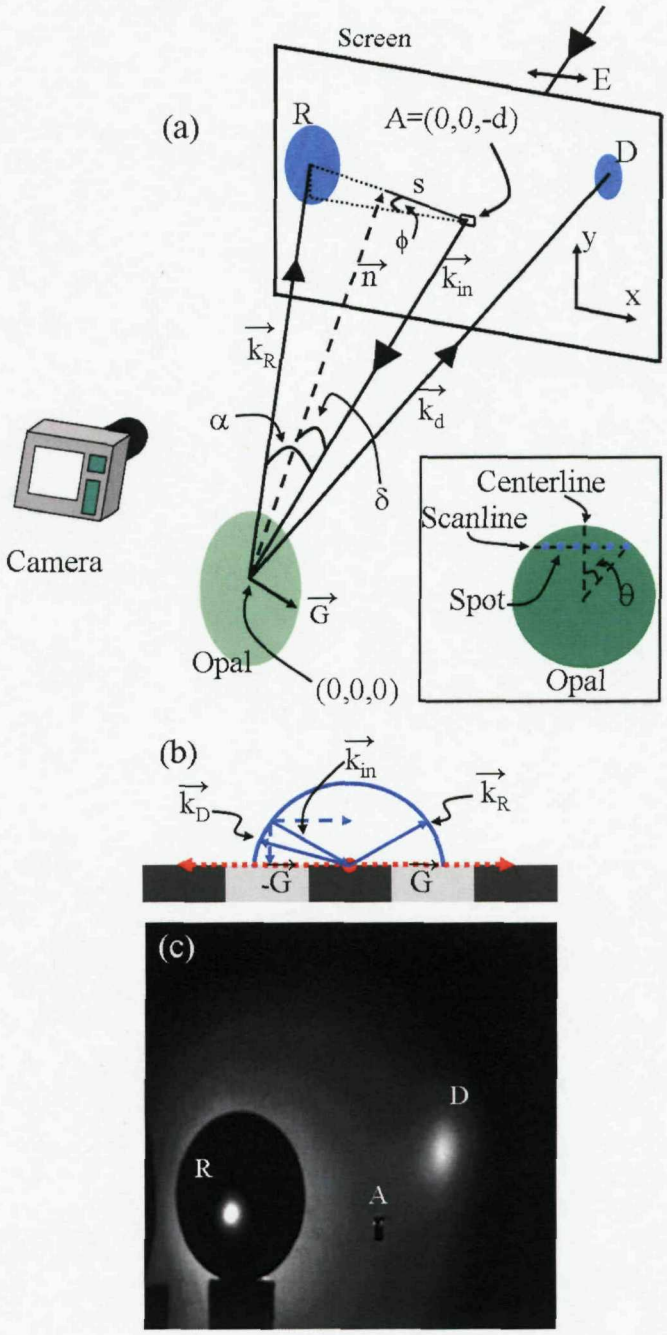

FIGURE 4.5: (a) Director measurement setup with the symbols used to calculate the diffraction geometry. Inset: Scan sequence to measure the director. (b) Dependence of the allowed diffraction on the incident wavevector $\vec{k}_{in}$, lattice vector $\vec{G}$ and the diffracted wavevector $\vec{k}_D$, reflected wavevector $\vec{k}_R$ also shown. (c) Digital image of the diffraction with reflection (R) (attenuated by an ND2 filter), aperture (A) and the diffracted spot (D).

$$\vec{k}_d = \vec{k}_{d_\parallel} + \vec{k}_{d_\perp} = \vec{k}_{in_\parallel} + \vec{G} + \vec{k}_{d_\perp} = \vec{k}_{in_\parallel} + \vec{G} + (\vec{k}_d \cdot \vec{n}^\circ)\vec{n}^\circ. \tag{4.3}$$

Now regrouping (4.3) yields:

$$\vec{G} = \vec{k}_d - \vec{k}_{in} + \vec{n}^\circ \left[\vec{n}^\circ \cdot \left(\vec{k}_{in} - \vec{k}_d\right)\right]. \tag{4.4}$$

Setting $\vec{k}_{in} = 2\pi/\lambda\,(0, 0, d)$ and the previously determined $\vec{n}^\circ$ (4.4) allow us to determine $\vec{G}$. The position where the y-component of $\vec{G}$ equals zero corresponds to the position on the sample where the lattice vector is horizontal, and this lattice vector is defined as $\vec{G}_0$.

FIGURE 4.6: Evolution of the diffraction spot (bright spot on the right) around the reflected direction (bright spot on the left) with the changing angular position of the laser spot on the sample. Scan positions between θ=40° (left), θ=-15° (right).

The images recorded for one scan are given as a sequence in Fig. 4.6. The sample is scanned in front of the beam from right to left (as is depicted in the inset of Fig. 4.5 (a) and the diffracted spot scans around the reflected beam which indicates that the grating vector direction is changing over the surface. Note also that the reflected beam position is changing slightly on the ND2 filter due to the surface imperfections which was accounted for in the procedure described above. Fig. 4.5 shows only 5 of the total 45 image frames. In reality the change of the lattice vector was measured with an angular resolution of ~1.0°.

Finally we calculate the rotation angle of the lattice vector $\vec{G}$ with comparison to $\vec{G}_0$ through the dot product of these two vectors. This can be compared directly to the scanned angle across the sample of the surface (indicated as θ in Fig. 4.7 (a), inset). If the lattice vector is indeed determined by the flow direction one would then expect a one-to-one mapping between the lattice vector rotation and the scanned angle θ.

While we find the lattice pitch to be independent of position on the sample, the orientation of the director precisely tracks the radial velocity flow in the melt (Fig. 4.7 (a)). In all cases we find the high-shear regime operates in which the director is parallel to the velocity flow, Fig. 4.4 (c). Hence these polymeric photonic crystals form super-domains on macroscopic length scales of many cm, in complete contrast to other types of opals [42, 75, 76].

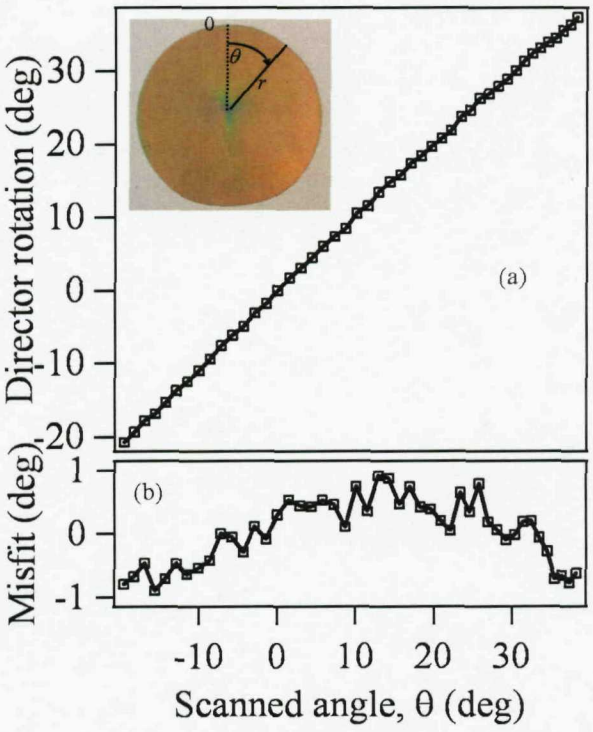

FIGURE 4.7: (a) Extracted orientation of lattice director as a function of the angular position θ of the laser spot on the sample (inset shows scan of laser spot). (b) Misfit between the lattice director orientation and the angular position θ.

This radial orientation of the director is found to be insensitive to its radial distance in the outflow (once out of the central region). Similar scans at different distances from the sample center agree very well with the data of Fig. 4.7 (a). However, deviations in alignment of $\vec{n}_d$ and $\vec{v}$, Fig.4.7 (b), are seen on the scale of 1° across a sector, and 0.4° between points. This can, at least partially, be attributed to the fact that the sample shape deviates from being perfectly circular. Moreover, the images were not calibrated for camera distortion which might affect the misfit of Fig. 4.7 (b). In addition, we only ever observe a single diffraction spot showing the lack of polycrystallinity. Clearly dislocations are needed to accommodate the radially oriented local hexagonal ordering as is indicated in Fig. 4.4 (e). This measurement does not give information about the dislocations, other than that their presence does not create a multidomain crystal and that they are fairly uniformly distributed. In conclusion, we can say the results show that the opal film disc is characterised by the radial flow director originating from the center of the disc. This is depicted in Fig. 4.8 showing a digital image of an opal film with the radial flow superimposed on top of it schematically. Only a sector of the 2π -symmetric radial flow is depicted for clarity. It should also be pointed out that this type of flow ordering obviously leaves the central region ($\sim$ 1cm^2) disordered, which is observed on the original disc as lack of color.

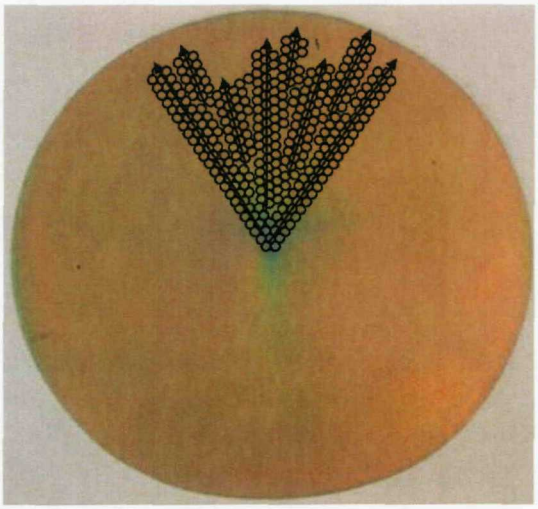

FIGURE 4.8: Schematic radial flow superimposed on a polymer opal disc. Only a sector of the 2π-symmetric radial flow is depicted for clarity.

4.4 Elastomeric Properties of the Unit Cell in Superdomain Polymer Opal

The elastomeric nature of these polymer opals allows the study of how 3D ordered nanocomposites comprised of solid spheres and stretchable filler influence the anisotropic elasto-optic properties. In this section an analysis of the unit cell properties in a strained polymer opal structure is presented. Changes from straining the polymer opal lattice in the film plane (imposing $\vec{s}_x$) were tracked from the changes in the 6-fold surface diffraction of UV light. Also, induced vertical strains ($\vec{s}_z$) were measured from the spectral shift of the reflection Bragg resonance from the (111)-planes (parallel to the surface) at visible wavelengths. Measuring both lateral and vertical strains allows us to track the volume change optically. Furthermore, we can measure the deformation of the unit cell as the strain is applied along different in-plane orientations to the director (where ϕ_{sn} is the angle between strain $\vec{s}_x$ and director $\vec{n}_d$). In order to track the full effect on the different lattice planes in the unit cell, all 6-fold diffracted spots are recorded necessitating the use of the larger-pitch LS02 sample, cf. Fig. 4.5 (b).

A rectangular (2.5cm x 1cm) section of sample was strained using a micrometer while clamped at both ends. The diffraction patterns were recorded according to Fig. 4.9 using a digital camera (Sony CyberShot DSC-S75). In Fig. 4.9 the light is directed through the aperture A and incident *perpendicularly* on the opal sample. The sixfold front UV-diffraction pattern is visible due to fluorescence on a white paper screen. In Fig. 4.9 the central reflection spot is identified with R and the 6 diffraction spots with D. From the diffraction patterns, the spatial distribution of high strain regions within the unit cell, and how they depend on the orientation of the imposed stress, can be identified.

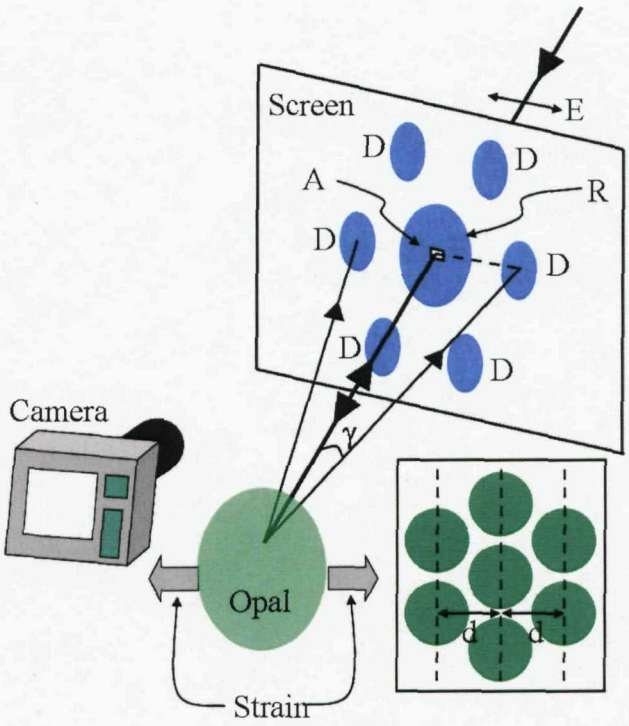

FIGURE 4.9: The setup used for recording the diffraction pattern (D) of the large sphere LS02 sample. Light is directed through the aperture (A) on the screen and hits the opal perpendicularly. The resulting diffraction pattern (visible through the screen fluorescence) is recorded with a digital camera. The sample is clamped to micrometer enabling controlled strain in horizontal direction. Also labeled reflection (R), the six first order diffraction spots and the diffraction angle γ. Inset: The inter-row distance d of the PS-PMMA spheres.

The spacing (d) between the rows of spheres in the hexagonal diffracting PS-PMMA-sphere formation can be calculated from the angle γ in Fig. 4.9, see inset of Fig. 4.9, using the diffraction law [67]:

$$\sin\beta + \sin\gamma = kN\lambda, \tag{4.5}$$

where $\beta(=0)$ is the incident angle, γ the diffracted angle, k the diffraction order ($=\pm 1$), λ the diffraction wavelength and N the density of diffracting sphere rows (i.e. $1/d$). The angle γ is extracted from the diffraction spot position. On the other hand, the real lattice vectors for the spheres can be determined by using (4.6) for determining the relationship between real and reciprocal lattices and symmetry. The diffraction pattern reveals the reciprocal lattice directions [67].

$$\vec{a}_i \cdot \vec{b}_j = 2\pi\delta_{ij}, \text{for } i,j = 1...2, \tag{4.6}$$

where $\vec{a}_i$ ($\vec{b}_j$) is the real (reciprocal) lattice vector, and δ_{ij} is the Kronecker delta. Now the reciprocal lattice vectors can be determined from the diffraction pattern by considering the diffraction spot location in the recorded images of Fig. 4.10. In Fig. 4.10 the bright green circles correspond to PS-PMMA spheres in the lattice (i.e. the real space) and the blue spots to the diffraction pattern. These two geometries are both sixfold symmetric and rotated by 30° with respect to each other. In order to examine the real space lattice changes we define the reciprocal space lattice vectors matching the diffraction spots as depicted in Fig. 4.10 (a-b). The difference between these two geometries is the rotation of the opal director vector $\vec{n}_d$ with respect to the strain direction $\vec{s}_x$ such that in Fig. 4.10 (a) they are parallel,ϕ_{sn}=0°, and in (b) they differ by ϕ_{sn}=30°.

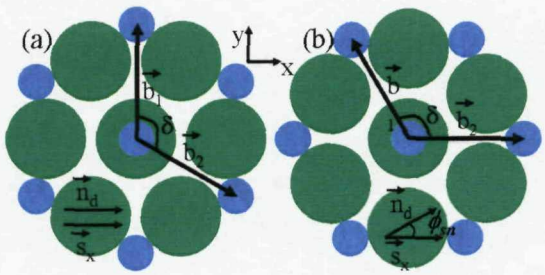

FIGURE 4.10: The real lattice of PS-PMMA spheres (green) and the reciprocal lattice formed by the diffraction spots (blue) in case of the strain ($\vec{s}_x$ parallel to the director ($\vec{n}_d$ (a) and at 30° angle to it (b). The reciprocal lattice vectors $\vec{b}_1$ and $\vec{b}_2$ at the angle δ to each other.

To form the diffraction (reciprocal lattice) vectors for the case when $\phi_{sn} = 0$ we set:

$$\vec{b}_1 = \frac{2\pi}{d}\begin{bmatrix} 0 \\ 1 \end{bmatrix} \tag{4.7}$$

$$\vec{b}_2 = \frac{2\pi}{d}\begin{bmatrix} \cos\delta \\ \sin\delta \end{bmatrix} \tag{4.8}$$

For the $\phi_{sn} = 30°$ we set:

$$\vec{b}_1 = \frac{2\pi}{d}\begin{bmatrix} \cos\delta \\ \sin\delta \end{bmatrix} \tag{4.9}$$

$$\vec{b}_2 = \frac{2\pi}{d}\begin{bmatrix} 1 \\ 0 \end{bmatrix} \tag{4.10}$$

When strain is applied across the sample the diffraction pattern (i.e. the reciprocal lattice) changes and the change can be expressed through (4.7-4.10). The typical changes in the diffraction patterns due to in-plane strain for $\phi_{sn} = 0°$ are depicted in Fig. 4.11.

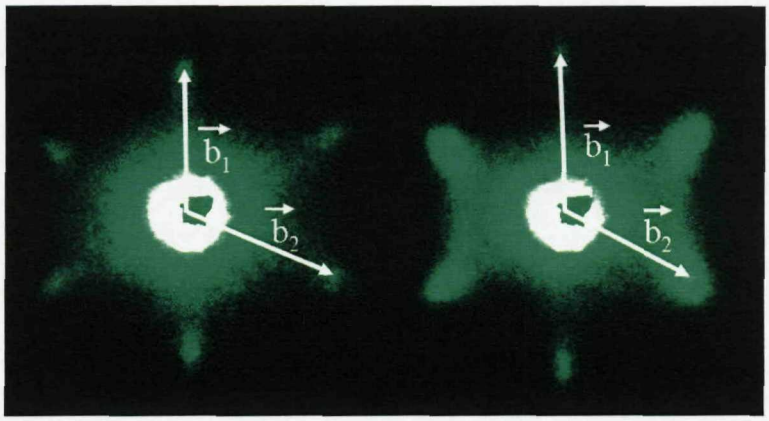

FIGURE 4.11: Changes in the diffraction pattern when $\phi_{sn} = 0°$ with the corresponding reciprocal lattice vectors $\vec{b}_1$ and $\vec{b}_2$ also shown. Letf: strain $s_x = 0$, right strain $s_x = 10\%$.

Thus by first calculating the distance between the sphere rows using (4.5) and subsequently (4.6) together with (4.7 - 4.10) with the δ extracted from the geometry-calibrated images of strained diffraction (Fig. 4.11) the strain-induced lattice deformations can be calculated. The changes in the in-plane sphere separation for the case of $\phi_{sn} = 0$ are shown in Fig. 4.12 below for the two spots corresponding to the reciprocal lattice vectors $\vec{b}_1$ and $\vec{b}_2$. These values can then be used to calculate the real lattice vectors indicating the PS-PMMA sphere movements. Furthermore, we measured the (111)-plane resonance shift due to strain in order to fully analyze the 3D unit cell change.

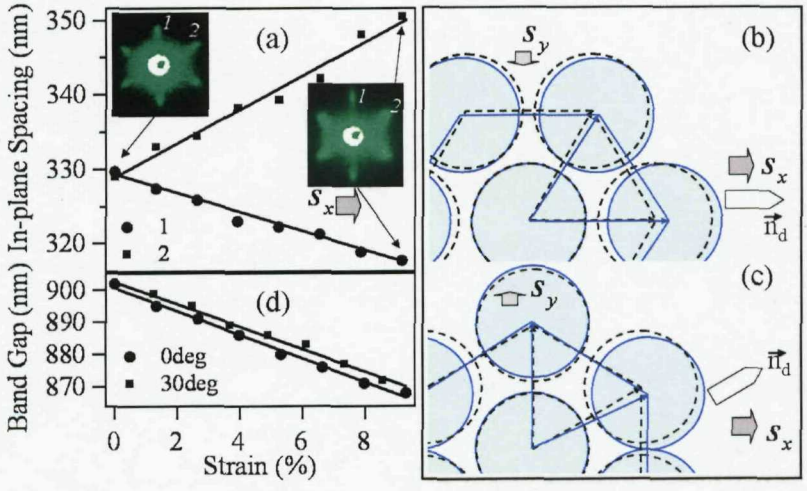

FIGURE 4.12: (a) Changes in the in-plane spacing of the diffracting sphere rows on the opal surface as function of strain. Insets: corresponding diffraction patterns when probing the surface with 248 nm laser. Geometric changes in the unit cell of the PS spheres with zero (black dashed lines) and 10% in-plane strain along x (blue solid lines) when ϕ_{sn} equals 0° (b) 30° (c). (d) Change in (111) lattice spacing with strain in the same conditions.

For uniaxial strains s_x parallel to the lattice director $\vec{n}_d$, the change in the plane spacings corresponding to the two diffraction spots (labeled as 1 and 2) are shown in Fig. 4.12 (a). Initially the planes (which are at 60° to each other) are both 330nm apart, but the strain modifies them differently with the 10% imposed strain in the x-direction leading to a +6.9% increase in the separation of spheres in plane 2, while a -4.0% decrease in the separation of spheres in plane 1. On the other hand, when this measurement is repeated for the case of $\phi_{sn} = 30°$ the results show that both plane spacings 1 and 2 increase by +2.8% showing how structural anisotropy can be used to impose specific optical anisotropy. In all cases we find that the actual radial velocity flow direction gives identical results to those in the nominally symmetric directions at 60° to it, implying that surface packing is indeed hexagonal and initially unstrained.

We compare the two geometries of $\vec{n}_d$ vs. $\vec{s}$ (for $s_x = 0, +10\%$) in Fig. 4.12 (b-c), showing the movement of the individual spheres relative to each other. The behaviour when $\phi_{sn} = 0°$ is intuitively clear: as the structure is elongated the horizontal planes move closer to each other ($s_y < 0$, Fig. 4.12 (b). In contrast for $\phi_{sn} = 30°$, the lattice expands in every direction when strained along x. In the collinear case the surface unit cell area increases by +7.1% whereas for the case where the strain is 30° to the director, the area increases by +11.0%. We note that this strain is not uniformly distributed within the unit cell since the cross-linked PS spheres do not deform. We estimate that the increase in the PEA area is 29% (45%) for the 0° (30°) angle between the strain s_x and director $\vec{n}_d$ and thus the elastic limit is also anisotropic. The principal orientations here already reveal the clear influence of elastically-heterogeneous photonically-active composites. The imposition of the director alignment during radial material flow from uniaxial-compression generates specific anisotropic elasto-optic properties.

Finally, to investigate the 3D nature of the strain-induced change in the polymer opal fcc-lattice we combine the unit cell area changes with the changes in the (111)-plane direction perpendicular to the surface. The results for the $\phi_{sn} = 0, 30°$ (Fig. 4.12 (d) show only 5% difference in the strain-induced changes in the (111)-plane spacing between the two experimental geometries. Combining this information with the unit cell areas calculated earlier reveal that the for +10% strain, the unit cell volume increases by +2.7% for $\phi_{sn} = 0°$, while by +6.7% for $\phi_{sn} = 30°$ (over twice as much). We conclude that the anisotropy of the unit cell expansion is mostly due to the 2D surface morphology which depends strongly on the angle between the director and the strain vectors.

4.4.1 Diffraction Intensities and Linehapes

The diffraction spot lineshapes and intensities of the 6-fold patterns of previous section were also studied (Fig. 4.13) in the case of strain parallel to the director i.e. $\phi_{sn} = 0°$. This data also shows some very interesting features presented in Fig. 4.13. Fig. 4.13 panel also shows the changes between the diffraction image appearance from 0% (above)

to 10% strain (below). Also indicated is the spot labelling and the cross-section direction for Fig. 4.13 (b-c). In Figs.4.13 (b-c) the diffraction spot intensities and line widths (respectively) are given as functions of the applied strain.

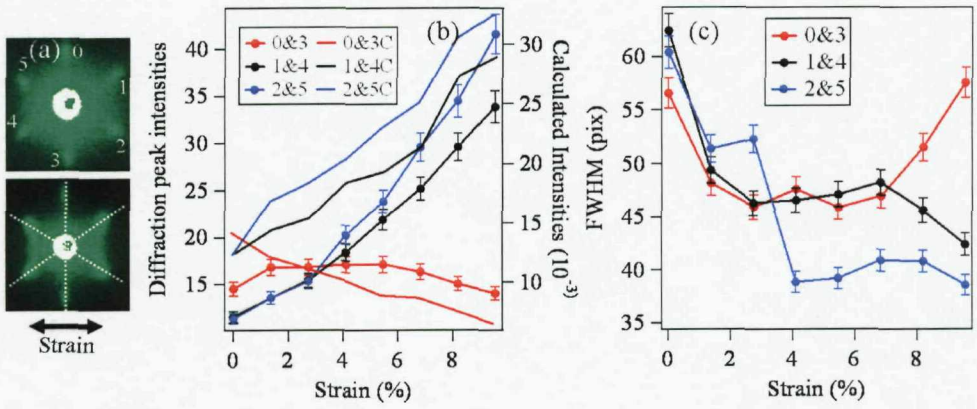

FIGURE 4.13: (a) The diffraction image changes due to horizontal strain (indicated by black arrow) from 0 (above) to 10% below. Spots labeling 0-5 and direction of the spot cross-sections shown. (b) Diffraction intensity versus applied strain for the measured intensities 0&3, 1&4, and 2&5 and the calculated values 0&3C, 1&4C, and 2&5C. Calculations are done using the measured diffracted angles γ and (4.13). (c) Spot FWHM versus applied strain.

The line profiles were taken starting from the spot labeled 0 through the saturated reflection spot in the middle across the spot labeled as 3, and this procedure was repeated for the spot set 1 to 4 and 2 to 5. The diffraction intensity profiles were then fitted with a suitable function to obtain comparable quantities for the comparisons in Fig. 4.13 (b-c). It was found that the best fittings were obtained using Lorentzian line profile of the type $I = A_0 + \frac{A}{B+(x-x_0)^2}$. Here I is the intensity, A_0 background, A intensity parameter, B width parameter, x the variable to be fitted against, and x_0 the peak location. Gaussian profiles were attempted but with far inferior fitting. The intensities on opposite sides of the bright overexposed reflection peak in the middle were averaged to get the data in Fig. 4.13 (b-c).

In Fig. 4.13 (b) we see that the intensity of spots 0&3 first start to increase with the first strain step before leveling and starting to decrease after the strain of about 5%. At the same time the intensities of spots 1&4 and 2&5 grow for all strains. With the increasing strain the sphere rows responsible for diffracting into spots 0&3 move closer to each other (increasing the diffraction angle) as the neighbouring spheres within each row move further from each other. Array theorem [16], Fig. 4.14, can be used to explain the results. The array theorem basically states that the Fraunhofer field distribution of an array of identical apertures equals the Fourier transform of the individual aperture multiplied by the pattern that would result from a set of point sources in an array identical to the diffracting apertures. The mathematical formulation is based on the fact that Fraunhofer field distribution is obtained as the Fourier transform of the diffracting

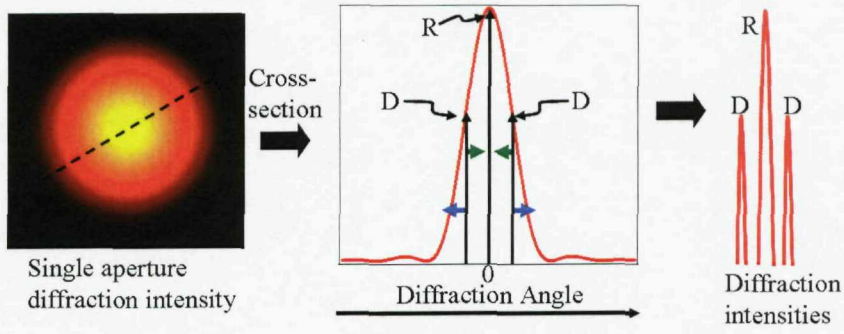

FIGURE 4.14: (a) Diffraction intensity from a circular aperture is described by squared jinc-function. (b) Cross section of the intensity distribution. Array theorem states that the diffraction intensities for an array are obtained by sampling the single diffraction distribution by the Fourier transform of the original lattice. Here the Fourier transform of the lattice is represented by delta functions which move closer to the reflection peak R (green arrows) when diffraction angle decreases (diffraction intensity increases) and further away (blue arrows) when the angle increases and thus diffraction D intensity decreases. (c) Schematic of the resulting diffraction pattern.

aperture. Now we have an array A_δ of apertures A_ϕ. Thus the following equation describes the aperture set A_{tot}:

$$A_{tot} = A_\delta \otimes A_\phi, \tag{4.11}$$

where $\otimes$ stands for convolution. From the theory of Fourier transforms it stems that the Fourier transform of a convolution equals the product of the individual Fourier transforms of the functions in the convolution, i.e. from (4.11) we get:

$$\mathbf{F}[A_{tot}] = \mathbf{F}[A_\delta]\mathbf{F}[A_\phi], \tag{4.12}$$

where $\mathbf{F}$ stands for Fourier transform. Basically we have the diffraction pattern from a circular aperture which is being sampled by the array in the Fourier space. The grid of the sampling array in the Fourier space in inverse relation to the sampling in real space such that the single aperture diffraction pattern is sampled at different abscissa values (Fig.4.14) changing the observed diffraction pattern intensities.

With the help of (4.12) and the diffraction angles γ calculated from the diffraction patterns for different strains like the ones presented in Fig. 4.13 (a) we can calculate the diffraction intensity changes for the strained material. From literature [16] we know that the normalised diffraction intensity I_N for a spherical aperture is:

$$I_N = \left[\frac{2J_1\left(k\phi/2\sin\gamma\right)}{k\phi/2\sin\gamma}\right]^2, \tag{4.13}$$

where $J_1(z)$ is the Bessel function of the first kind of order 1, k is the photon wavevector, ϕ is the aperture diameter, and γ the diffraction angle. Using (4.13) and the diffraction angles γ for different spot sets 0&3, 1&4, and 2&5 together with the sample sphere diameter 350nm yields the calculated diffraction values of Fig. 4.13 (b) labeled as 0&3C etc. (right axis). Unfortunately, due to the central reflection spot saturation in the experimental data the experimental intensities cannot be normalised but Fig. 4.13 (b) allows for the comparison of the trend and magnitude in intensity change due to strain between the experimental and semi-theoretical case.

Based on the calculated values for the diffraction intensities in Fig. 4.13 (b) one would expect the experimental intensities of spots 0&3 to decrease with the increasing diffraction angle. Similarly as the diffraction angle for spots 1&4 and 2&5 decreases (cf. Fig. 4.12) the intensities of these spots are expected to increase. This is partially true for the measured spots with the exception of the slightly-increasing intensity for the first strain step for spots 0&3. This increase could be attributed to a possibly increasing ordering due to the initial strain step. This is supported by the decrease in the FWHM during the initial strain in Fig. 4.13 (c). However it is not entirely clear why the intensities for spots 1&4 and 2&5 differ quite a bit at high strains. In Fig. 4.13 (c) the widths are seen to decrease at low strains for all the spot groups which is an indication of increased ordering between the rows responsible for the diffraction into these spots. However, for spots 0&3 the order deteriorates towards high strains whereas it improves for spots 1&4 and 2&5. The stronger decrease in the width parameter for spots 2&5 than for spots 1&4 seems to agree with the different intensity increases. Symmetry would suggest that the changes for these spot groups should agree, but clearly after the strains of about 6% the differences are very visible. It is speculated that the flow symmetry has effect on this but clearly this feature should be verified further with both compression and extrusion manufactured crystals.

4.4.2 Increasing Order with Strain

One mechanism through which small strain could improve ordering is depicted in Fig. 4.15. The PS-PMMA spheres corresponding to different directors $\vec{n}_d$ (black arrows) are in blue. The gap needed to accommodate the local hexagonal packing between the director orientations is indicated by the red block arrow (although exaggerated). The small strain (gray arrow) could have the effect of actually decreasing the gap, indicated in the right panel by the much shortened red arrow, which would then manifest itself as the decreasing spot FWHM seen in the experimental data. This is because the FWHM (essentially Δk) in the diffraction spot corresponds to disorder Δd between adjacent diffracting sphere rows. For large strains the order is expected to deteriorate due to colliding spheres.

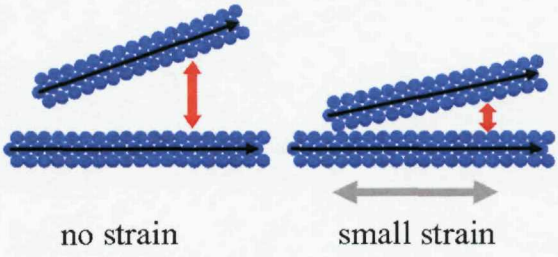

FIGURE 4.15: Possible mechanism for the strain induce ordering for small strains in compression manufactured polymer opals. Left panel shows the local hexagonal ordering of the PS-PMMA spheres (blue) along different adjacent directors (black arrows) and the gap (red block arrow) needed to accommodate the packing. The gap is expected to decrease at small strains thus decreasing the FWHM of the diffraction peak.

While this kind of strain-induced ordering would be inherent for compression manufactured polymer opals due to the radial material flow this hypothesis could be tested with extruded polymer opal films. These structures are not expected to show similar behaviour due to the expected material flow (along the extrusion slit) during extrusion.

4.4.3 Lorentzian vs. Gaussian fits

The fact that the Lorentzian fits performed better than Gaussian is an indication of inherent disorder. This has also been outlined by Avrutsky et al. [77] who studied colloidal crystals also by diffraction. In their statistical model the major finding is that the diffraction lineshape changes from Gaussian to Lorentzian with increasing small defect density in the crystal. This can also be understood by considering the Lorentzian profile which has further reaching "tails" than a Gaussian; a feature that manifests itself as increased scattering from lattice defects. This is hardly a surprise in case of the compression manufactured opals since, as was discussed earlier in this chapter, the radially symmetric superdomain needs point or line defects to accommodate the local hexagonal ordering, cf. Fig. 4.4 (a), (e).

4.5 Chapter Summary

In this chapter we investigated in more detail the ordering process due to compression-flow-induced shear in polymer opals. We clearly show that opals manufactured this way are characterized by a macroscopic director governing the global orientation of the hexagonal lattice. Such polymer photonic crystals have super-domains with characteristic domain sizes over tens of square centimetres. Furthermore, by examining strain-induced changes in the 3D geometry we conclude that the director dictates the anisotropy in the hexagonal lattice planes parallel to the surface but has little effect to

anisotropy in the third dimension of the crystal. Such director-defined anisotropy could be utilized in a number of applications including strain sensing, security tagging, and photonic crystal enhanced birefringence. Furthermore, diffraction line profiles and intensities were discussed. The strain-induced intensity changes can be understood based on the optical array theorem and also a mechanism which could lead to the observed strain-improved order in the opal was presented.

Chapter 5

Optical Properties of Opaline Photonic Crystals

In this chapter the basic optical properties of opaline photonic crystals will be discussed. General features of reflection (R) and transmission (T) of these materials will be discussed together with introductory remarks about the scattering (S) properties. Scattering will be discussed further in the next chapter with relation to the structural colour. Reflection and transmission spectra will be presented for different nanoparticle dopants and analysis of the changes with changing incident angle is also presented. Finally aspects relating to strain induced changes in the R-S-T features are discussed.

5.1 Basic Reflection and Transmission

As was outlined in Chapter 2 the expected reflection and transmission characteristics of an opaline photonic crystal look like the traces presented in Fig. 5.1 (a) in red and blue, respectively. At the stop band (SB), highlighted in yellow, about 60% of the photons cannot enter the material because their frequency lies in the stop band frequency range and are thus reflected [20]. [1]

The photonic band gap manifests itself as a peak in the reflectance (red trace) at λ=600 nm coinciding with a dip in the transmission spectrum (in blue) in Fig. 5.1 (a). Ideally the photons outside the yellow band gap region do not experience the effect of the band gap. We also see that the band gap does not rise to 100% reflection values, i.e. strictly speaking this should be referred to as a partial stop (111) stop band. These R-T spectra are results of 1D multilayer (20 layer pairs) system simulation at normal incidence (see inset of Fig. 5.1 (a)) where the layer thicknesses correspond to the actual

[1] More precisely reflected photons at the stop band do enter the structure but as an evanescent wave and are reflected back within a distance that depends on the refractive index contrast of the crystal [20].

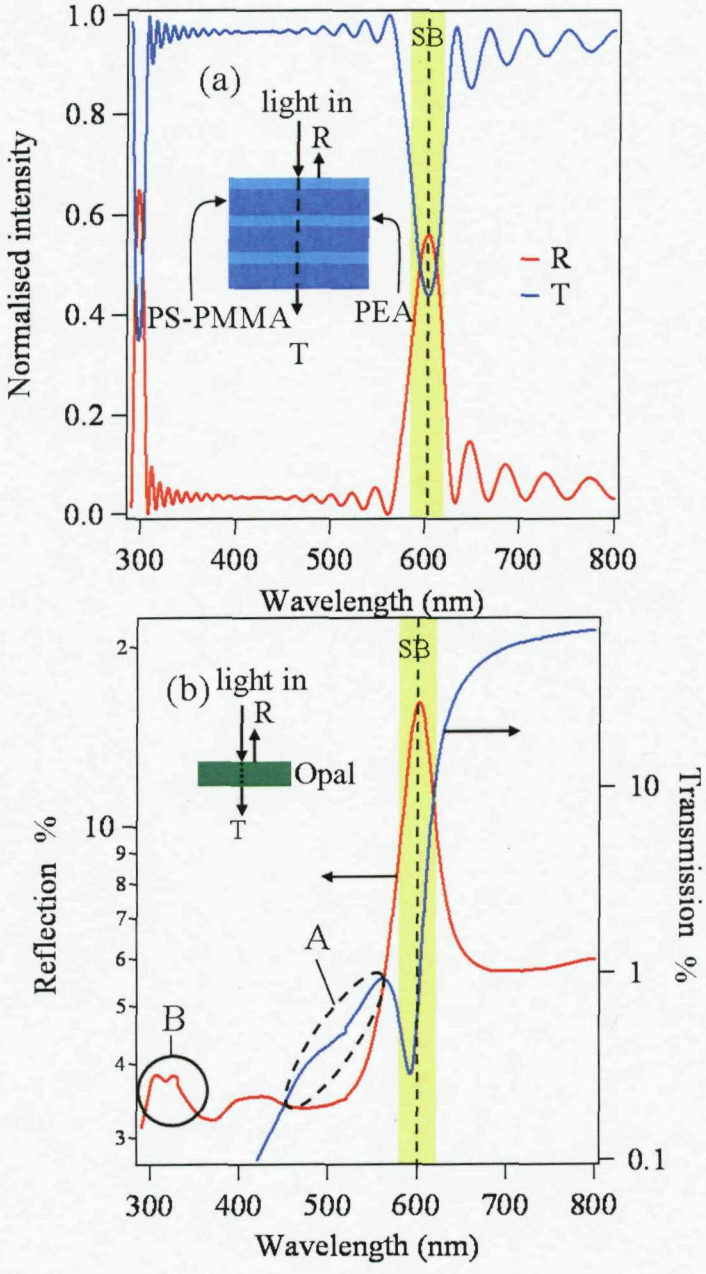

FIGURE 5.1: (a) Theoretical case of photonic crystal reflection (R) and transmission (T) modeled in a planar multilayer system of 20 layer pairs (inset) where the layer thickness ratios correspond to the packing fractions of PS-PMMA and PEA polymer without any dopants in the lattice. (b) Experimental example of undoped opaline photonic crystal reflection (left axis) and transmission (right axis). Inset: Measurement setup showing perpendicular incidence, input (in), reflected (R) and transmitted (T) beams.

packing fractions of PS-PMMA and PEA polymers of the opal structure. Twenty layer pairs were chosen to highlight the fact that the stop band is only partial, but at the same time the photonic crystal characteristics (reflection peak and transmission dip) are clearly observable. The simulation kernel lies in the transfer matrix approach described in great detail in Ref. [78]. Refractive indices are 1.59 and 1.49 for the PS-PMMA and PEA layers, respectively. Also visible in the traces is the second order resonance at around 310nm. Furthermore, the ripples in both T and R traces are a result of Fabry-Perot resonance from the cavity formed by the air-polymer interfaces of the multilayer system.

The experimental picture is seen to be very different from the theoretical case. The experimental traces have been taken in perpendicular incidence, indicated in the inset of Fig. 5.1 (b). The measurements were taken with a commercial spectrophotometer (Jasco UV/VIS 570). We see that at the stop band of about 600nm the reflection trace (in red) indeed shows the characteristic peak and the transmission (in blue) the corresponding band gap dip. At the long wavelength side of the band gap both traces behave as expected i.e. showing a relatively constant plateau. However, at the short wavelength side of the band gap of the transmission trace (region indicated as A) we see that there are some drastic differences between the theoretical and experimental behavior. The transmission does not climb back up to the values of the long-wavelength side but after the band gap increases until 590nm and thereafter rapidly decreases. This is a combined effect of the polymer absorption and scattering possibly due to impurities. The sample studied here has no nanoparticle dopants but the polymers are slightly absorbing and furthermore the flow improvers used in the manufacturing are absorbing at this wavelength regime. The Fabry-Perot interference fringes also are absent due to the combined effect of scattering and absorption losses and finite light input and collection angles which cause averaging over the fringes.

Moreover there is also an interesting shift in the bandgap between the transmission dip and the reflection and the reason to this is not entirely clear at this point. One possibility is that the mismatch results due to slightly different packing close to either surfaces of the opaline film. As was described in Chapter 3 during the compression-initiated self-assembly three different regions are formed in the thickness direction. Close to the compression plates there are the well-ordered *fcc*-packed crystals with the less-ordered region in between. In practice there are no factors in the compression manufacturing that link these two ordered regions together in a way that there is no offset in the crystal ordering between them. Furthermore there could be an angular mismatch between the two ordered layers. These facts combined could lead to a situation where light transmitted in normal incidence by the first ordered layer is partially diffused in the less-ordered middle layer and then hits the second ordered layer at non-normal incidence and thus the transmission band gap lies at slightly lower wavelengths than the reflection bandgap. Similar effects of modified light transmission and diffraction by two distinct

ordered planes in shear-ordered colloidal systems have been reported before in Ref. [57]. This feature of the bandgap tuning with the incident angle will be discussed in detail in Section 5.2. However, if we use (5.4) below we see that in order to explain the difference of 9nm around 600nm bandgap one would need an angular mismatch of around 15° between the two surfaces which is definitely too high. Another possibility is that the shift results from polymer absorption. This has been seen also in samples of higher absorptive nanoparticle doping in experiments as well as simulations and will be discussed further below.

Finally there are some interesting features in the reflection traces in the low-wavelength region indicated as B in Fig. 5.1 (b). It is not entirely clear what all these features correspond especially because transmission counterpart could not be measured due to low signal levels. However, the features around 315nm (the first peak of the double-peak structure) are tentatively attributed to be the first overtone of the 600nm bandgap. This can be understood via considering a simple resonant cavity of Fig. 5.2 where the basic resonance lies at 600nm and (5.1) applies:

$$\frac{\lambda}{2n_{eff}(\lambda)} = d, \tag{5.1}$$

where λ is the resonance wavelength (in vacuum), n_{eff} $(\lambda)(=1.56)$ the effective refractive index of the structure at this wavelength regime and d is the cavity length. Now the cavity length can be solved to be d=192nm. The first overtone corresponds to the situation where $d = \lambda/n_{eff}$, cf. Fig. 5.2. Thereby for λ=315nm yields for the effective refractive index $n_{eff}(\lambda) = 1.64$, which agrees well with the expectations based on the PS refractive index value of $n_{PS} > 1.62$ [79]. The further features in the low-wavelength end of the reflection trace could be speculated to be further resonances but also spectral features of the polymers used due to the very short wavelength.

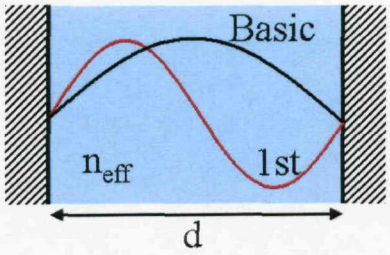

FIGURE 5.2: Cavity (length d, effective refractive index n_{eff}) with the basic resonance (black) and the first overtone (red).

While the basic reflection and transmission properties of the opaline crystal were briefly introduced, with the polymer opals the situation is not so simple. One needs to carefully consider scattering contributions even with as simple experimental setups as depicted in

the inset of Fig. 5.1 (b). In the following section some important optical properties of fcc-crystals are first outlined.

5.2 Angle-Dependent Optical Properties

The angle-dependent properties are dictated by the fact that the crystal exhibits hexagonal close-packing. [2] An *fcc*-lattice is re-presented in Fig. 5.3 (a).

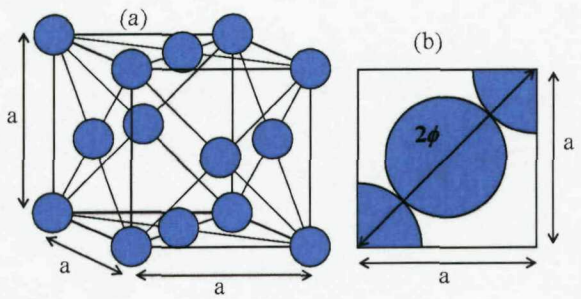

FIGURE 5.3: (a) PS-PMMA spheres (blue) in a face-centered-cubic lattice, a is the lattice constant. (b) Quasi-close-packed face of the lattice showing the dependence of the lattice constant a on the sphere diameter ϕ.

In the polymer opal fcc-lattice there are PS-PMMA spheres in every corner point of the lattice plus additional spheres also on the faces of the cube. The *fcc*-lattice is completely characterized by the lattice constant a. Its dependence on the PS-PMMA sphere size is depicted in Fig. 5.3 (b) as simple geometrical analysis yields $a = \sqrt{2}\phi$ where ϕ is the sphere diameter. Furthermore, as mentioned in Chapter 2 for an *fcc*-lattice the following holds:

$$d_{hkl} = \frac{a}{\sqrt{h^2 + k^2 + l^2}}, \tag{5.2}$$

where d_{hkl} is the interplanar distance for the group of planes characterized by the Miller indices (hkl) [67]. For optical reflectance measurements it is very instructive to derive a relation between the angle of incidence and the resonance inside of the *fcc* -structure. This angular tuning of the stop band energy was already observed in the opal bandstructure in Chapter 2 and here an analytical expression for it is derived. The Laue condition for the resonance inside of a periodic material states that the component of the incident wave vector $\vec{k}$ along the reciprocal lattice vector $\vec{G}_{hkl}$ must be half the length of $\vec{G}_{hkl}$ [67], i.e.:

$$\vec{k} \cdot \vec{G}^{\circ}_{hkl} = \frac{1}{2}|\vec{G}_{hkl}|. \tag{5.3}$$

[2] As outlined in Chapter 4 the ordering is at least locally hexagonal, also cf. Fig. 4.4 (a).

Eq. (5.3) can be simplified using vector relations and geometry of Fig. 5.4 below. First we simplify $\vec{k} \cdot \vec{G}^{\circ}_{hkl} = |\vec{k}| \cos\beta$. Using the identity $|\vec{G}_{hkl}| = 2\pi/d_{hkl}$ and the fact that *inside* the crystal $|\vec{k}| = 2\pi n_{eff}/\lambda_{hkl}$ we get $\lambda_{hkl}/(\cos\beta n_{eff}) = 4d_{hkl}$. Finally Snell's law $n_1 \sin\theta = n_{eff} \sin\beta$ and trigonometric identities allow this to be simplified further into:

$$2d_{hkl}\sqrt{n_{eff}^2 - \sin^2\theta} = \lambda_{hkl}, \tag{5.4}$$

assuming that light is incident from air.

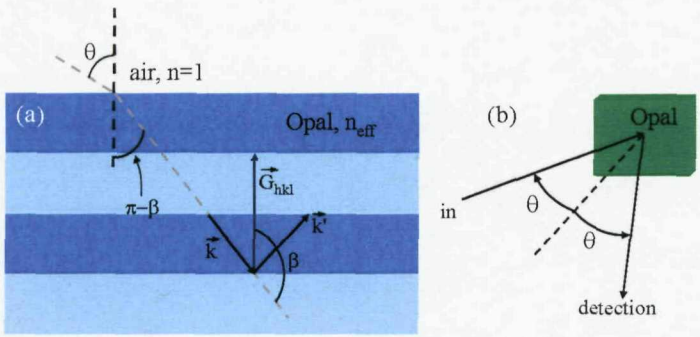

FIGURE 5.4: (a) Geometry used for the calculation of the Bragg scattering law in a polymer opal, Eq.(5.4). Light is incident at angle θ on the air-opal (n_{eff}) interface and undergoes scattering from $\vec{k}$ to $\vec{k}'$ by the reciprocal lattice vector $\vec{G}_{hkl}$, β is the angle between $\vec{k}$ and $\vec{k}'$. For simplicity only the lattice planes parallel to the opal surface are presented. (b) Geometry for measuring the angle-dependent reflectance (primarily) from (111) set of planes, angle of incidence θ equals the angle of detection.

Eq. (5.4) is an extremely useful result describing the dependence between the bandgap wavelength λ_{hkl}, the incident angle θ, effective refractive index n_{eff}, and the inter-planar distance d_{hkl} for the set of lattice planes (hkl). The knowledge of this simple formula allows for the testing of the angle-dependent reflectivity which is measured for the (111) planes in the simple setup of Fig. 5.4. It is also clear that (5.4) is a generalization of the cavity resonance of (5.1) into an angle-varying geometry.

Angle-dependent reflection measurements were carried out to identify the final lattice pitch and average refractive index. Unpolarised monochromatic light was collimated and focused on the sample surface, which was mounted on a rotation stage. The reflection spectra was recorded for incident angles of $\theta = 20° - 60°$ using a photodiode. The sample used here had (111) perpendicular incidence reflection peak at 635nm and it had been doped with carbon black nanoparticles at 0.2 wt-% level. According to (5.4) a decrease of the resonance wavelength with respect to the increasing angle of incidence is expected. The results are presented in Fig. 5.5 (a).

From Fig. 5.5 (a) we see that the evolution of the Bragg reflection peak is according to the expectations set by (5.4) as the peak wavelength decreases with the increasing angle of incidence. This is further verified by extracting the material parameters (n_{eff}

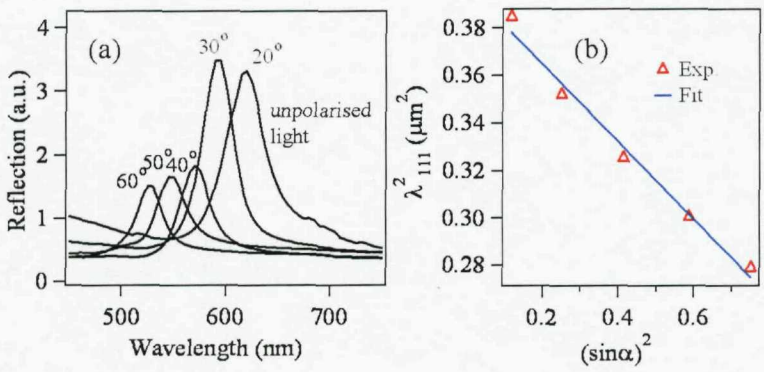

FIGURE 5.5: (a) Reflection peak wavelength λ_{111} vs. the angle of incidence $\theta = 20°...60°$ for unpolarised light. (b) Linear fitting of λ^2_{111} vs. $sin^2\theta$ enabling the extraction of the effective refractive index n_{eff} and (111) plane spacing d_{111} according to (5.4).

and d_{111}) in the following manner based on (5.4). The λ^2_{111} vs. $\sin\theta^2$ values are plotted in Fig. 5.5 (b) and in this configuration we expect a linear depedence between the two. This is readily observed as the red circular symbols in Fig. 5.5 (b). After fitting a linear function $(a + bx)$ to the data we are able to extract the material parameters from the coefficients a and b, i.e: $a = 4d^2_{111}n^2_{eff}$ and $b = -4d^2_{111}$. The fit is given in Fig. 5.5 (b), blue trace. From these fit parameters we extract the following values:

$$\begin{aligned} n_{eff} &= 1.56 \pm 0.05 \\ d_{111} &= 202 \pm 7\text{nm}. \end{aligned}$$

The effective refractive index value is in fair agreement with the value 1.51 determined earlier in Chapter 3 by the volume fractions of different polymers. This refractive index would be gained also by treating the material as PS spheres (instead of PS-PMMA) in PEA in close-packed arrangement. The effective refractive index value of 1.56 will be used throughout the thesis. Moreover, the effective refractive index n_{eff} is assumed to be constant in the visible regime. This is a reasonable assumption because according to Ref. [79] in the visible region of light the PS refractive index varies only around 1% of its average value of 1.59. The (111) plane distance d_{111} would indicate a sphere diameter of 247nm in a close-packed lattice which is very reasonable.

In Fig. 5.5 (a) the peak intensity decreases sharply with the angle of incidence between 30° and 40° which is puzzling. Therefore simulations in the 1D system of Fig. 5.1 were carried out to verify the relationship between the unpolarised reflectivity and the angle of incidence[3]. The results shown in Fig. 5.6.

[3]Small amount of absorption was incorporated in the simulated system in form of complex refractive index in the PEA layer to take into account possible absorption.

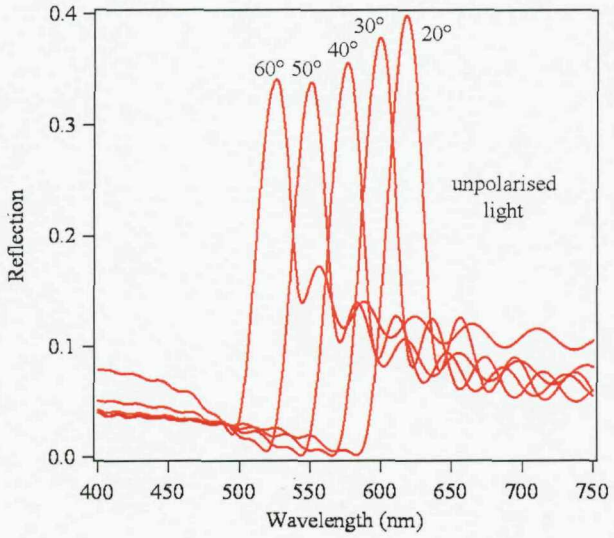

FIGURE 5.6: Simulated unpolarised reflectance results from 1D multilayer system of the type described previously (see Fig. 5.1) for angles of incidence $\theta = 20...60°$.

Comparing the experimental and theoretical reflectivities we see that the intensity trends are somewhat different. In the theoretical traces the intensity seems to decrease from $\theta = 20°$ to $\theta = 50°$ because of the decreasing reflectance of the p-polarised component when approaching the Brewster angle ($\approx 56°$). The intensity increases slightly again at $\theta = 60°$. In the experiment the intensities decrease quite sharply towards the higher angles of incidence. This discrepancy between the experiment and theory is attributed to experimental error such as misalignment. However, it should be emphasized that the 1D model used is an oversimplification of the real-life 3D opal reflector and thus perfect agreement should not be expected.

5.3 Strained Reflection and Transmission

The flexibility of the polymer opals was mentioned in Chapter 3. The crosslinking agent that was mixed in the precursor material can be activated after the compression manufacturing by exposing the polymer opal to UV light. We have experimented on the flexibility and the strain-related optical properties and reported the major findings in Ref. [80]. In bulk material the expected deformation due to strain is depicted in Fig. 5.7 (a).

When the material is elongated from length L to $L + \Delta L$ the perpendicular dimensions change from R to $R + \Delta R$ and from S to $S + \Delta S$. In terms of the volume we have for unstrained volume V_0 and for the strained volume V_1:

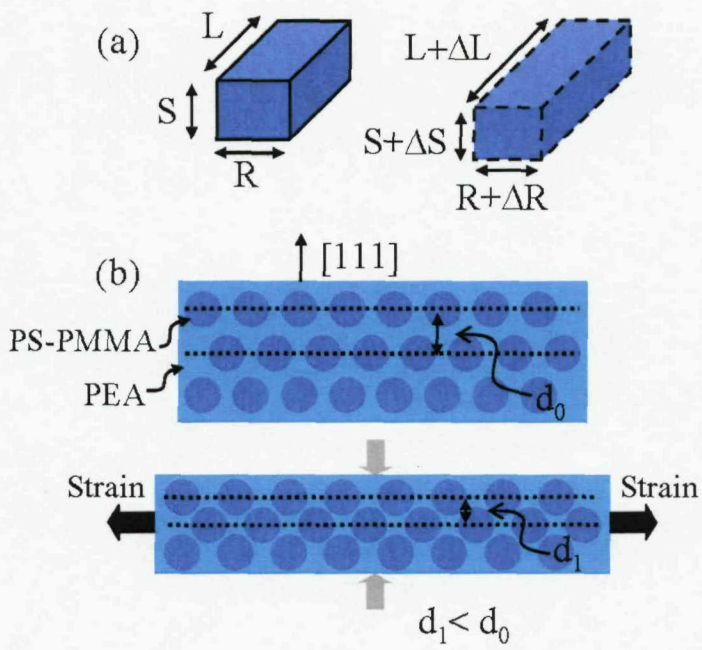

FIGURE 5.7: (a) Schematic illustration of the changes in two perpendicular directions (R,S) when strain is applied in the direction perpendicular to these (L). (b) Schematic of the changes in [111] direction of the polymer opal consisting of hard PS-PMMA spheres in PEA lattice. It is expected that by stretching the opal horizontally the (111) lattice constant decreases from d_0 to d_1.

$$\begin{aligned} V_0 &= LRS \\ V_1 &= (L+\Delta L)(R+\Delta R)(S+\Delta S) \end{aligned}$$

This can be developed further by setting $\Delta V = V_1 - V_0$ and ignoring the terms having higher order Δs than one yielding:

$$\frac{\Delta V}{V_0} = (1 - \frac{\Delta R}{R} - \frac{\Delta S}{S})\frac{\Delta L}{L} = (1-2\nu)\frac{\Delta L}{L}, \tag{5.5}$$

where $\nu = -\frac{\Delta R/R}{\Delta L/L} = -\frac{\Delta S/S}{\Delta L/L}$ is the Poisson ratio. Poisson ratio is thus a dimensionless parameter which describes the relative contraction of a material in one direction when stretch is applied in a perpendicular direction [81]. Using this simple analogy of bulk material we would expect the polymer opal to behave in the cross-sectional view in the manner depicted in Fig. 5.7 (b). When strained longitudinally (horizontally) the (111) lattice planes (indicated by the arrow in Fig. 5.7 (b)) would move closer to each other in accordance to (5.5). This in turn would cause the lattice constant to decrease from d_0 to d_1 shifting the Bragg resonance to shorter wavelengths as a consequence of (5.1). In

other words, with the elastomeric polymer opals it is possible to determine the Poisson ratio ν by optical measurements.

A simple setup for imposing longitudinal strain the polymer film was built and the device depicted in in Fig. 5.8. In the device a micrometer translation stage is attached to a base plate. The sample is attached to the system by clamping it between two clamps, one on the base plate and another on the translation stage. Longitudinal (horizontal in Fig. 5.8) strain is applied across the sample by turning the micrometer actuator screw indicated by the red arrow in the schematic. The system can be combined with a commercial spectrometer or custom made measuring system and enables the measuring of the strain-dependent reflectivity or the transmission through the hole in the base plate.

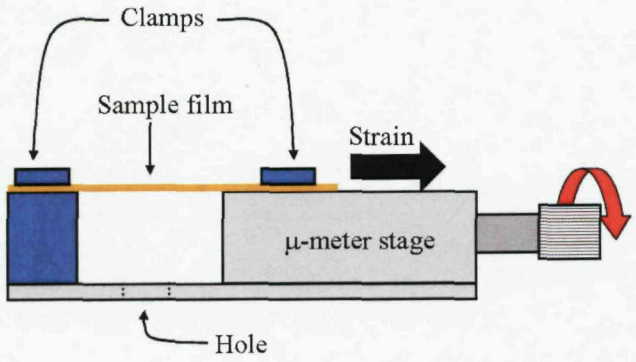

FIGURE 5.8: Simple device for straining the polymer opal film horizontally. A micrometer translation stage was attached to a base plate. The polymer opal film can be clamped on one end to the base plate clamps and on the other end to the micrometer. Turning the micrometer knob (indicated by the red arrow) imposes horizontal strain on the film. The optical response can be measured from the top for reflection or through the hole in the base plate for transmission.

The strain-dependent reflection and transmission results measured with the straining device of Fig. 5.8 used together with a spectrophotometer (Jasco UV/VIS 570) are presented in Fig. 5.9 (a-b). The reflectivity and transmission traces for imposed strains of 0, 2, 5.8, 7.8, 10.4, and 13% are presented in Fig. 5.9 (a) and (b), respectively. Increasing strain is indicated by the arrows.

From Fig. 5.9 (a-b) we see that the (111) -plane resonance is shifted to shorter wavelengths with increasing strain. This is in accordance with the expectations based on Fig. 5.7 (b) and (5.1-5.4) and can be attributed to the decreasing lattice constant d_{111} when longitudinal strain is applied across the polymer opal. From the peak wavelength shifts of Fig. 5.9 (b) we can extract the Poisson ratio ν using the with the symbols of Fig. 5.7 (a) by considering:

$$\Delta S = \Delta d_{111} = \frac{\Delta \lambda_{111}}{2 n_{eff}}, \tag{5.6}$$

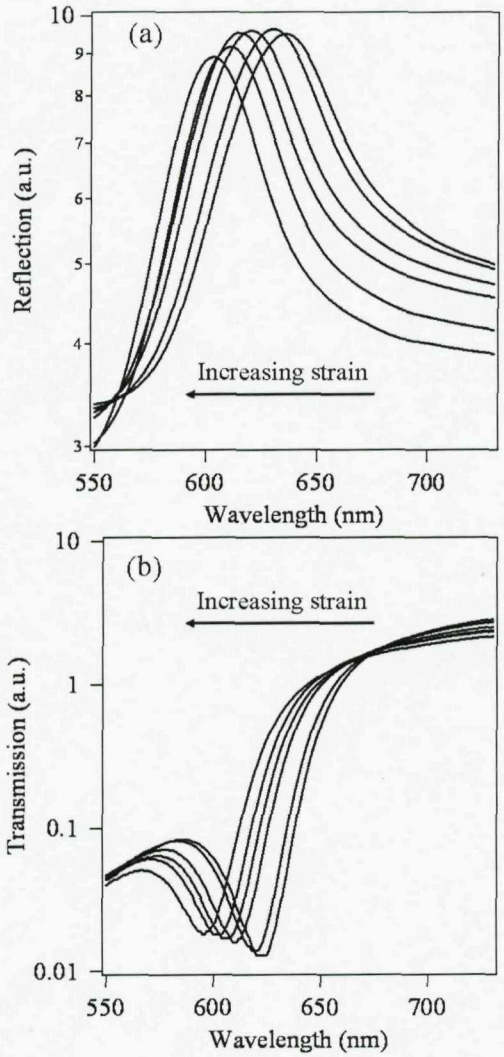

FIGURE 5.9: Strain induced changes in the (a) reflectivity and (b) transmission for strains of 0, 2, 5.8, 7.8, 10.4, and 13%. Increasing strain is indicated by arrows.

when longitudinal strain of ΔL is applied and we have used equation 5.4 at normal incidence and the assumption of isotropic stress in directions perpendicular to the strain and constant refractive index n_{eff}. Eq. 5.6 can be developed further by virtue of (5.5) yielding:

$$\frac{\Delta d_{111}}{d_{111}} = \frac{\Delta \lambda_{111}}{\lambda_{111}} = -\nu \frac{\Delta L}{L}. \tag{5.7}$$

According to (5.7) if the relative change in the (111) peak position is plotted against the relative strain, the Poisson ration ν can be extracted as the slope of this linear dependence. This is done in Fig. 5.10. In this figure we have fitted a linear dependence between the relative strain and relative wavelength shift between the strains 0 and 13% (indicated by the arrow in Fig. 5.10). The linear dependence fits relatively well for

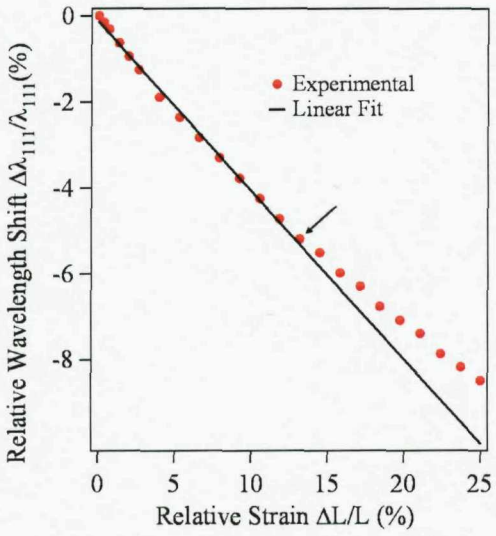

FIGURE 5.10: Poisson ratio extracted as the slope of a linear fit between the relative (111) -peak wavelength change and relative longitudinal strain. Data fitted between 0 and 13% strain (indicated by the arrow).

moderate strains but the deviations between the fit and the experimental data are clear after 13% strain. Eq. 5.5 is only valid for small strains so the deviations are not surprising. In fact the fitted Poisson ratio $\nu = 0.39 \pm 0.006$ is surprisingly close to the literature value for polystyrene which is $\nu = 0.34$ [82]. It is not at all obvious that the polymer opal material consisting of hard spheres in an elastomeric matrix should display the same mechanical characterisics as bulk polymer. However, in this case we conclude that the small lattice changes due to mechanical strain can relatively well be understood within the framework defined for bulk material, at least in the [111] direction of the lattice.

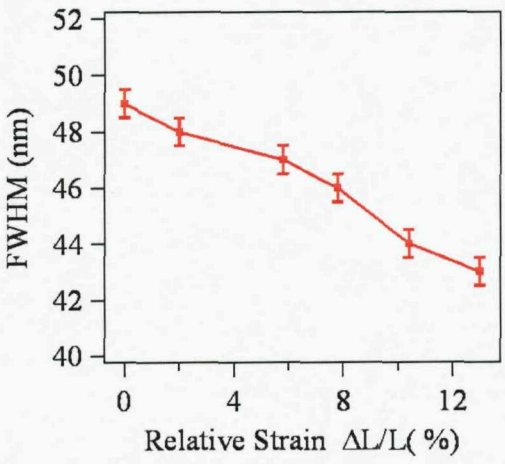

FIGURE 5.11: Full width at half maximum values extracted from the reflection peaks of Fig. 5.9 as a function of relative strain.

It is also interesting to look at the differences in the reflection peak widths for different strains. The FWHM of the peak is an indicator of the degree of ordering and monodispersity in the crystal [83, 84]. These values are presented for the reflection traces of Fig. 5.9 (a) in Fig. 5.11. We see that the FWHM values actually decrease as a function of the imposed strain. This would in fact mean that the ordering is improving inside of the crystal due to the strain. It could be understood by considering an initial state of slight disorder which gets improved by the applied strain, i.e. the PS-PMMA spheres actually find their correct location thanks to the strain. Ruhl et al. [49] discuss a related mechanism and argue that the PEA matrix exhibits entropic coil elasticity which results in a driving force which push the PS-PMMA cores to their correct positions. It is conceivable that the starting position is characterised by slight disorder which then due to the strain and the presence of these above mentioned elastic forces turns to better ordering thus improving the FWHM values. Strain-induced order improvement was also reported in the results of the previous chapter and the arguments of Section 4.4.2 apply here as well. Finally, it is clear that the opal has its definite elastic limit after which it cannot be returned to its original shape. It is argued that strains in the excess of 13% tend to result in permanent deformations in the opal. This relatively low limit is due to the very exclusive nature of the strain distribution into the PEA matrix since the PS-PMMA spheres are crosslinked and not deforming. Therefore the elastic limit is reached at relatively low strain value of 13%.

5.4 Doped Opal Photonic Crystals

The idea and implementation of doping the polymer opals was discussed in Chapter 3. During this thesis polymer opals doped with varying amounts of carbon black has been the material system most experimented with. Also some initial experiments have been conducted with opals doped with other nanoparticles, such as gold or CdSe quantum dots. In this section an overview of the dopant-modified optical characteristics of polymer opals will be given. Also the band gap interaction with the dopant will be discussed.

To study the effect of different amount of carbon black in the opal four samples were manufactured differing only in the amount of dopant. The normal incidence reflectivity and transmission spectra were measured using a commercial UV-VIS spectrometer. The results are shown in Fig. 5.12.

The results of Fig. 5.12 correspond to the carbon black doping of 0, 0.05, 0.1, and 0.2 wt-% in traces (a-d), respectively. The red traces are for reflectance and blue for transmission. Each one of the systems clearly has an incomplete photonic band gap as was already explained in Section 5.1. As a general trend a decrease in reflected and transmitted light for increasing level of doping is observed. The reflection values

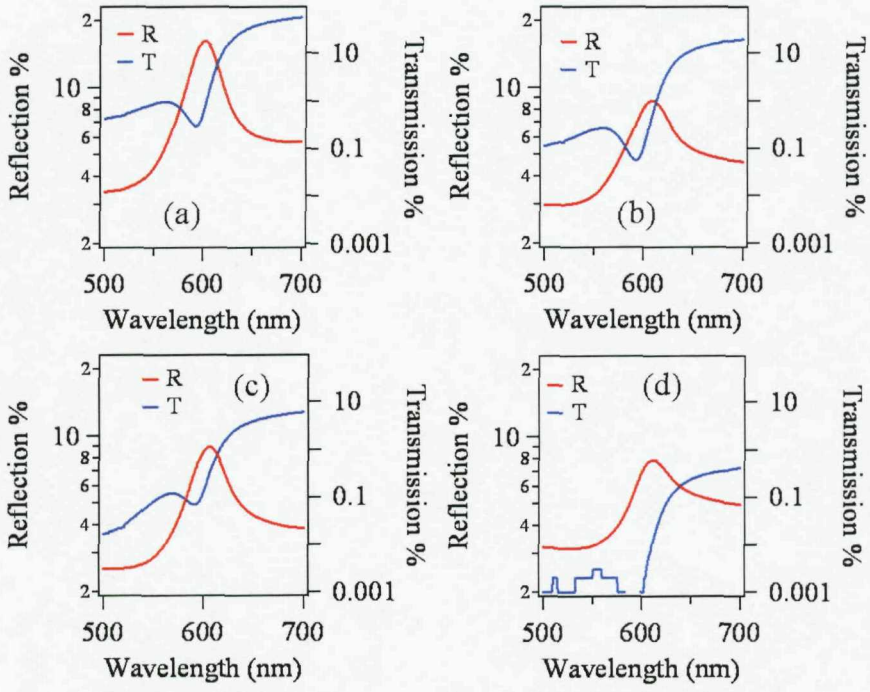

FIGURE 5.12: Measured reflectivity (R, red) and transmission (T, blue) values for opals doped with carbon black nanoparticles. Amount of dopant: (a) 0, (b) 0.05 wt-%, (c) 0.1 wt-%, and (d) 0.2 wt-%.

drop form around 17% (0 doping) to 7% (0.2 wt-% doping) and the lowest point of the transmission spectrum decreases from 0.2% (0 doping) to 0.08% (0.1 wt-% doping) while finally in Fig. 5.12 (d) it is already outside the experimental sensitivity of the instrument. We can further extract interesting data from these traces, and Fig. 5.13 (a) shows the evolution of the reflection peak intensity (in red) and the bulk absorption (L_α, black) as function of the Carbon black (C-black) content.

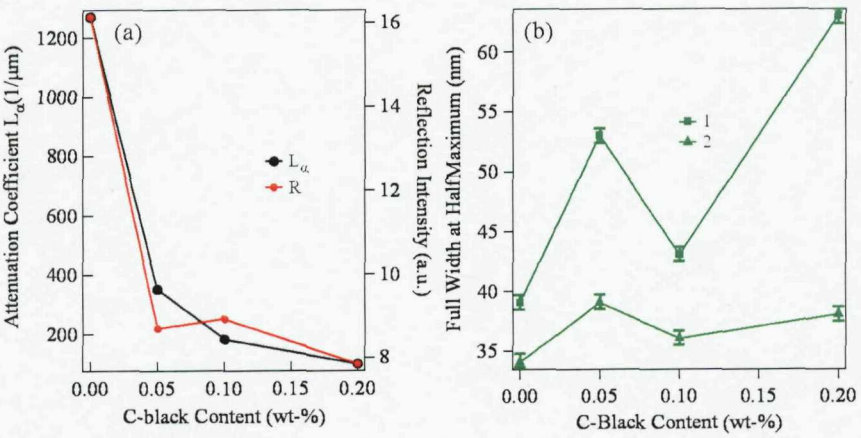

FIGURE 5.13: (a) Reflection (R) peak intensity and bulk attenuation coefficient (L_α, black) as functions of Carbon black (C-black) content. (b) FWHM of the reflection peak measured

The bulk absorption coefficient was extracted from the relative transmission data using the Beer law [16] between transmission (T), bulk attenuation coefficient (L_α) and material thickness L:

$$T = I_{out}/I_{in} = e^{-L/L_\alpha}.$$

The above formula was applied to the transmission values at 800nm and the individual sample thicknesses. At 800nm we are 200nm higher than the bandgap so that it is reasonable to assume negligible influence for this coefficient from the band gap related effects and the light uniformly irradiates the opal interior. From Fig. 5.13 (a) black trace we see that the absorption length scales with the C-black content as expected, while the reflection peak intensity is showing similar trend as well. It is also informative to look at the FWHM values for the reflection traces of Fig. 5.12 (a-d). These are presented in Fig. 5.13 (b). These values have been determined with respect to two different background positions. The trace with triangular symbols has been determined from the background value at 750nm wheres the trace with square symbols was determined using background value at 520nm. These FWHM values describe the "photonic strength" of the material system [85, 86] which has a general interpretation of being the polarizibility per unit cell volume and describes the interaction between light and a photonic crystal.

The trend in both cases is that the doping seems to increase the FWHM, although in the 750nm case this broadening is only about 10% from 0 to 0.2 wt-% doping. When looking at the FWHM in the 520nm case we see that the effect is much more drastic. In either case the "photonic strength" decreases as the doping is increased. The higher decrease for the 520nm case is most likely due to the fact that the absorbing C-black is in the PEA material which has the lower refractive index thus supporting the mode higher energy (i.e. lower wavelength)[20]. Kaliteevski et al. [87] have found that in 2D photonic crystals increasing disorder increases the bandgap FWHM values. Although we have found no obvious evidence in TEM images (cf. Fig. 3.8) that the doping in polymer opals was causing disorder in the lattice the FWHM increase is, at least partially, due to the same mechanism.

Finally we can also look at the bandgap wavelength for transmission and reflection and their difference as a function of C-black dopant content for the nanoparticle doped opals of Fig. 5.12. If we define the reflection peak wavelength as the R-bandgap and the transmission dip wavelength as the T-bandgap we obtain the results of Fig. 5.14. Their difference is indicated as R-T. Furthermore, the reflection trace also has vertical bars indicating the FWHM of the reflection peak.

From the data in Fig. 5.14 we see that that the reflection bandgap location on the wavelength scale seems to have an increasing trend with the increasing C-black content. There is a 9 nm (or 1.4%) increase from 602nm when the C-black doping increases from 0 to 0.2 wt-% level. This is not a very significant increase especially considering the nature of the batch process compression manufacturing. The change could well be due

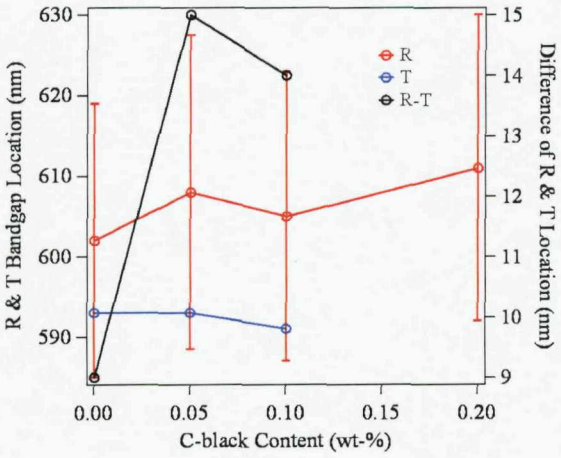

FIGURE 5.14: Bandgap location for reflection (R, red, left axis) and transmission (T, blue, left axis) and their difference (R-T, black, right axis) versus the C-black content. The bandgap location is taken to be the reflection maximum and the transmission minimum. Furthermore the reflection trace has the vertical bars indicating the reflection peak FWHM.

to the difference in the samples, although the measurements were conducted on similar locations on each sample to ensure similar flow-based ordering on these locations. On the other hand the reflection FWHM are quite large and as was mentioned previously Kalitevski reported reflection peak widening in photonic crystals due to increasing disorder which in our case might be caused by doping. The transmission bandgap location seems to stay almost constant with the increasing doping (although unfortunately for the highest doping the extraction of transmission level was impossibe due to very low transmission). Also the transmission bandgap values seem to be withing the range defined by the reflection peak FWHM. Altogether, when looking at the "R-T" difference curve (in black, right axis) we conclude that the increasing doping seems to separate the reflection bandgap from the transmission somewhat. Another factor leading to the separation is likely to be scattering and this is discussed below. Finally it is interesting to note that there is already a 9nm difference in the non-doped sample between the R and T traces. This seems to suggest that the polymers (PS, PMMA, and PEA) exhibit intrinsic absorption which leads to the separation of the bandgaps. As already explained earlier (cf. Section 5.1) the R-T mismatch cannot be due to angled domains on the front and back surfaces of the opal film.

As comparison to the experimental data Fig. 5.15 below presents simulated data for opals with different amount of absorption in them. The absorption is modeled through defining a complex refractive index $\overline{n}(n, \kappa) = n + i\kappa$ where n is the real part and κ the imaginary part. The multilayer structure is the same as the one used in Section 5.1. The main idea here is to match the R and T traces of the measured results of Fig. 5.12 by introducing absorption A in the PEA material in the structure. Furthermore, we are considering the energy balance in the multilayer system through the following equation:

$$R + T + S + A = 1, \tag{5.8}$$

where we are also taking the scattering S into account. Thus we can attribute the mismatch of the measured and simulated systems to scattering S by using (5.8). This is done for the data of samples Mix1-Mix3 in Fig. 5.12 and the results are presented in Fig. 5.15 (a-c). Fig. 5.12 (d) presents the absorption profiles (left) and the simulated and measured R, T and S peak and dip locations.

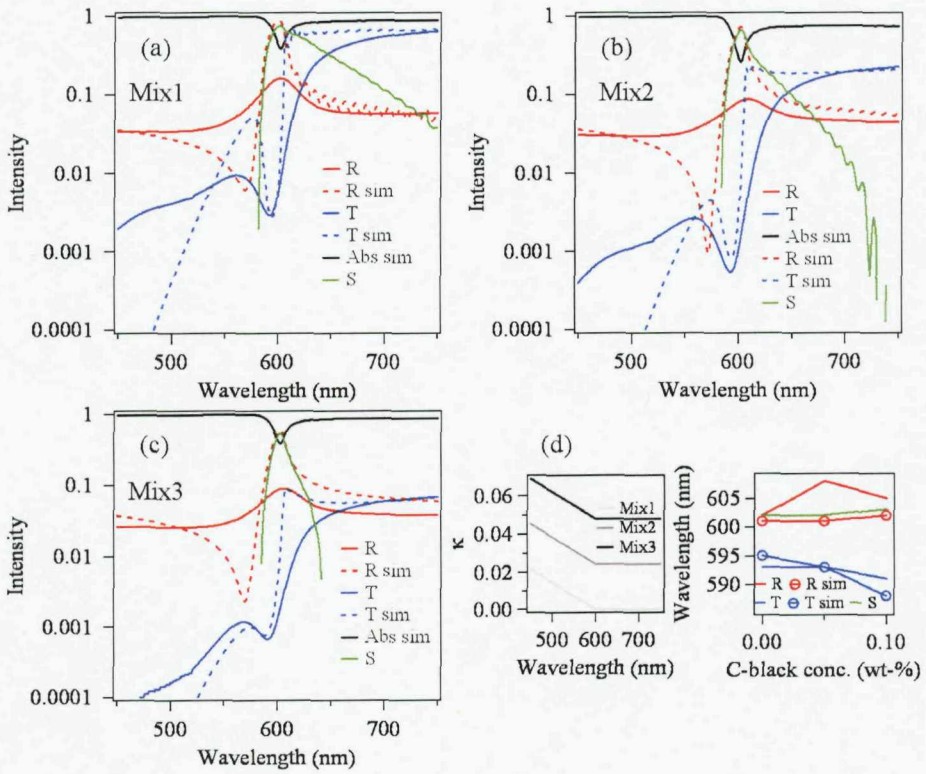

FIGURE 5.15: Simulated (*sim*, dashed lines) and measured (solid lines) reflection (R, red) and transmission (T, blue) and simulated absorption (*Abs sim*, solid black line) for samples Mix1-Mix3 in (a)-(c), respectively. The scattering (S, solid green line) is calculated through (5.8). (d) Transmission minima and reflection and scattering maxima locations for the measured and simulated traces.

It became clear by trial and error that in order to achieve at least a semi-satisfying match between the simulated and measured reflection and transmission traces a wavelength-dependent absorption profile had to be included, cf. Fig. 5.15 (d). The flat non-zero part represents the overall absorption in the polymer whereas the absorption increase towards shorter wavelengths after the stop band of 600nm is needed for the fitting. Also the fitted absorption increases from Mix1-Mix3 to take into account the doping by absorbing C-black. The T-traces were fitted for each sample in the long wavelength regime simulating a bulk-like absorption profile and this also resulted in a decent fit in the long and short wavelength reflection values. The reflection mismatch was attributed

to scattering by virtue of (5.8). We see from that the main disagreements between the simulated and measured results are present in the short wavelength transmission and in the regime from the transmission dip to about 50nm above the dip. The modeled simple absorption profile is not able to reproduce the transmission features in the low wavelength regime or the typical rounding of the transmission shoulder above the stop band. The low and high wavelength end regimes in the reflection are explained quite well with the inclusion of absorption and the mismatch in the stop band region can be attributed to scattering. this simple analysis shows that scattering is an integral part when analysing the optical characteristics of these opals. this will be further discussed in Chapter 6. Finally, Fig. 5.15 (d) shows the locations for the simulated and measured reflection and scattering peaks (maximum intensity wavelengths) and the transmission dips (minimum intensity wavelength) as functions of the C-black doping. We see that the scattering peak follows the reflection peak quite closely. Furthermore the increase in absorption seems to increase the difference in the R and T maxima and minima locations from 6nm (0 wt-% doping) to 14nm (0.1 wt-% doping) and this general trend is present also in the measured results. Most likely this simple 1D simulation is unable the explain all the features in the R, T and S traces, but possibly doping-induced disorder should lso be taken into account [87]. The geometry of the opal scattering is three dimensional and for the future studies it is advisable to resort to 3D radiation transport algorithms, e.g. such as "MULTEM" [88, 89]. As a summary, in order to further quantitatively understand the optical properties of the polymer opals we need to pay very close attention to the opal scattering properties. The next section presents the ideas relating to the high amount of scattering that is characteristic of these opals effecting the spatial distribution of light coming off the opal.

5.4.1 Examples of Nano-Dopants

Due to the versatility of the manufacturing technique it is relatively straightforward to dope the polymer opal with nanoparticles. As discussed in Chapter 3 they are introduced into the polymer mix during the extrusion mixing either in powder form or in a colloidal solution. For the most part this work has concentrated on opals with carbon black nanoparticle doping, but gold nanoparticles, quantum dots and molecular dye were also experimented with briefly. In the following the basic normal incidence reflection and transmission characteristics measured on a spectrophotometer (Jasco UV/VIS 570) are briefly discussed. The reflection and transmission characteristics of polymer opals doped with quantum dots (QD), molecular dye (Mol. dye), and gold nanoparticles (Au) are presented in Fig. 5.17 (a) and (b), respectively.

We first consider the cross sections of the nanoparticles in vacuum. The cross section is an expression for the likelihood for an interaction between two particles to happen. Absorption cross section thus describes a particles tendency to absorb a photon. The

absorption cross sections from C-black, molecular dye, gold nanoparticle, and semiconductor CdSe quantum dot are presented in Fig. 5.16.

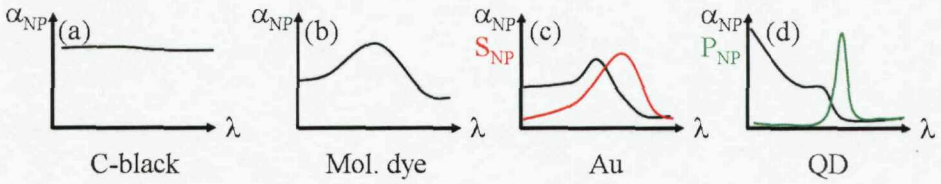

FIGURE 5.16: Absorption (black) cross sections α_{NP} against wavelength λ for (a) carbon black (C-black), (b) molecular dye (mol. dye), (c) gold nanosphere (Au), and (d) CdSe quantum dot from left to right. Also for Au a typical scattering line S_{NP} (red), and for QDs a photoluminescence line P_{NP} line (green) is given.

It is observed from Fig. 5.16 (a) that the absorption resulting from C-black is very flat over the visible spectral range. A molecular dye typically has a very wide absorption spectrum and the peak position depends on the actual dye. In the case of the molecular dye doped polymer opal the dye acts mainly as an absorber without significant emission [90]. The gold nanosphere absorption cross section is given in Fig. 5.16 (c). We see that it typically has fairly constant absorption at short wavelengths until hitting a peak (typically at 500-600nm depending on the sphere size [91]) before decaying into low absorption levels. The Au nanosphere size that was used for doping the polymer opal is 8nm resulting in an absorption maximum at 520nm. Also given is the typical small sphere Rayleigh scattering line (in red) with the broad peak maximised at 550nm [78]. Finally Fig. 5.16 shows the absorption cross section for CdSe quantum dot. The absorption starts at very high values in the low wavelength regime and decays towards the bandgap value of CdSe after which the absorption is negligible. Also depicted is the typical emission line centered around the bandgap. The absorption and the emission line can be tuned with the size of the quantum dot which determines the bandgap location. The bandgap energy is roughly inversely proportional to the square of the size of the quantum dot. The CdSe QDs used in this thesis have the emission maximum at 550nm.

The (111)-plane resonance is observed for each of these opals as the reflection peak in Fig. 5.17 (a). The QD -loaded opal reflection peaks at 567nm as well as the molecular dye -loaded opal. The Au -doped sample has a reflection peak at 629nm due to the different precursor polymer sphere size, cf. Table 3.4. Also the second order features are present for each of these opals around 300nm. The reflection intensities compare relatively well as well as the FWHMs which indicates similar degree of ordering in the opal. In both the reflection and the transmission features the presence of absorption can be observed. Absorption manifests itself in the reflection peaks as the asymmetry such that the short wavelength side of the bandgap is at slightly lower intensities than the long wavelength side. This is very evident especially in the transmission traces. At the short wavelength side of the bandgap the transmission values do not recover back to the same values than at the high wavelength mainly due to the fact that the absorbing

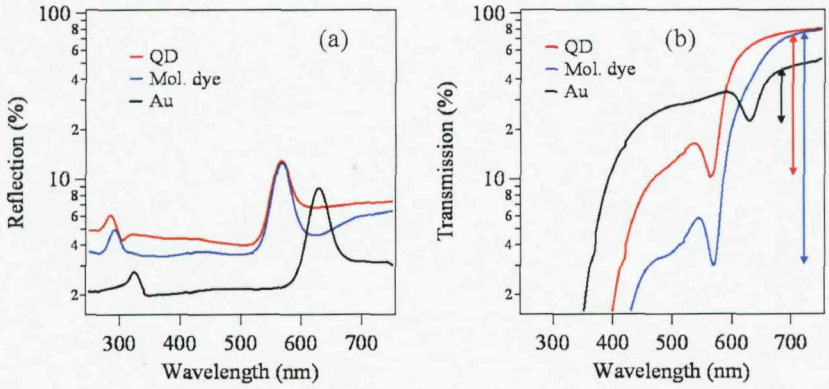

FIGURE 5.17: (a) Reflection and (b) transmission characteristics of polymer opals doped with quantum dots (QD, red), molecular dye (mol. dye, blue), and gold nanoparticles (Au, black). Transmission drops indicated by arrows.

nanoparticles are located in the PEA material which supports the short wavelength mode. This will be further discussed in next section. We see that the molecular dye is the strongest absorber on the short wavelength side of the bandgap due to its absorption cross-section being highest there. Finally, all the samples are strong absorbers in the UV.

We also observe that the transmission drop from the values on long wavelength side to the transmission minimum differ quite a bit. These drops are indicated in Fig. 5.17 by arrows. These features are most likely related to disorder in the crystal and can be understood by considering a 1D multilayer system. It is known from literature [78] that the multilayer reflectivity (thus transmission drop) increases as a function of the number of layers. The dopants create some disorder in the lattice thereby effectively reducing the amount of layers in the multilayer structure. We see from Fig. 5.17 that the molecular dye disturbs the lattice order the least resulting in the largest transmission drop.

No evidence of the quantum dot emission is seen, but this is not surprising since the QD photoluminescence is weak and spread over a wide solid angle compared to the reflection contribution. The gold nanoparticle vacuum scattering peak at 550nm is also not visible in the data. However, it is speculated that the nanoparticles act as additional scattering centers in the polymer opal judging by their visual outlook. Without the nanoparticles the opals tend to look whitish and milky if not viewed exactly around the resonance direction which can be verified by considering the images of the polymer opal samples in Figs. 3.9 - 3.10. This effect will be discussed in more detail in Chapter 6.

Finally it is interesting to consider an experiment that could be realized for the quantum dot loaded opal. It was shown in Section 5.3 that by applying strain over the flexible opal structure we are able to shift the bandgap wavelength towards smaller values. By choosing the polymer opal sphere size correctly it would be possible to design a structure where the QD photoluminescence peak and the opal (111) bandgap coincide. Therefore

the QD emission could possibly be suppressed or enhanced by stretching of the opal. This would be similar to the Purcell effect where the emission properties of an emitter can be modified by the presence of a cavity [92]. These kind of effects have already been experimented on [58, 11]. Lodahl et al. measured the angle-dependence of an emitter inside a TiO_2 inverse opal and Arsenault et al. experimented on strain induced changes also in an inverse opal. However, in this case the most interesting feature would be the interaction of the QD with the stopband of a *low* RIC opal and the strain-induced characteristics.

5.5 Band Gap and Nanoparticle Dopants

It is of utmost importance to consider the band gap interaction with the nanoparticle dopants. As was discussed in Section 3.3.4 the inclusion of nanoparticles in the polymer opal is relatively straightforward. The very fundamental fact that needs to be considered here is that the PS-PMMA cores are solid crosslinked hardcore spheres [49] which permit no material exchange (or swelling) between the surroundings and the sphere. Thus the additional dopants in the polymer opal are mixed only *within the PEA* surrounding material. This was already illustrated in Fig. 3.8 and this idea is revisited in Fig. 5.18.

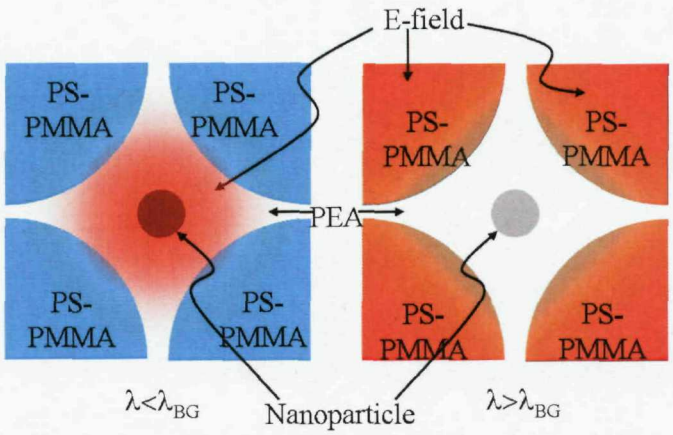

FIGURE 5.18: The electric field (E-field) spatial location (in red) below (left) and above (right) the id stop band wavelength λ_{BG}. The E-field shifts from low-refractive-index PEA (in white) to high-refractive-index PS-PMMA (in blue) when the wavelength λ is scanned across the bandgap affecting the nanoparticle almost solely on the low-refractive-index side of the bandgap.

From the theory of photonic crystals [20] and Chapter 2 we know that the formation of the photonic band gap stems from the physical separation of the electric field locations above and below the band gap. As was discussed previously in Chapter 2 the mode with high frequency tends to concentrate its energy to low-refractive index material while the mode with the low frequency prefers the high-refractive-index material. This fact in term has significant consequences when we consider our material system and doping

in particular. The dopants can not enter the crosslinked PS-PMMA cores and therefore are distributed in the PEA. PEA having the the lower refractive index supports high-frequency mode, and thus there is more interaction between the nanoparticles and the electric field at the low-wavelength side of the bandgap. This mechanism is depicted in Fig. 5.18 where the electric field distribution (in red) is seen to shift from the PS-PMMA spheres (in blue) to the PEA (in white) when the wavelength (λ) is scanned across the bandgap (λ_{BG}). This manifests itself, at least partially, as the asymmetric transmission trace for the quantum-dot and molecular-dye-loaded opals in Fig. 5.17.

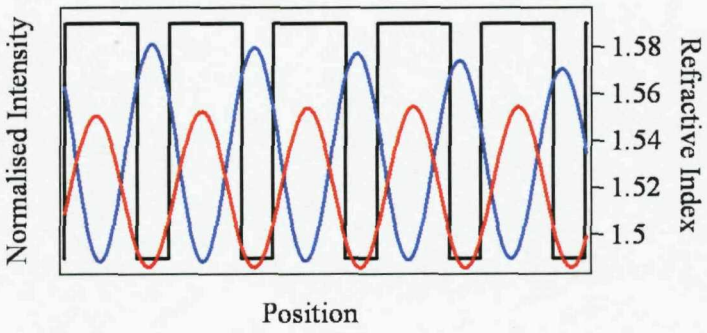

FIGURE 5.19: Five unit cells of a multilayer system consisting of low and high refractive index (right axis) material together with the electric field intensities below (blue) and above (red) the bandgap wavelength. These quantities are plotted against position in the structure.

A 1D model of this field localization is presented in Fig. 5.19 where five primitive cells of the multilayer stack are depicted. The refractive indices are 1.59 and 1.49 and the layer thicknesses 134nm and 58nm, respectively. This structure has a normal incidence bandgap at 600nm and in Fig. 5.19 the electric field intensities at 580nm (blue) and 620nm (red) are presented. We see that the short (long) wavelength mode concentrates its energy at the low (high) refractive index layer. It is now straightforward to integrate the intensity values spatially over the low refractive index structure over 10 unit cells to get a parameter for the energy localization for the different modes. The ratio of the integrated values yields an enhancement factor for the nanoparticle interaction. The enhancement factor η reads:

$$\eta = \frac{\int I_{n_{low}}^{\lambda<\lambda_{BG}}}{\int I_{n_{low}}^{\lambda>\lambda_{BG}}} = 5.7, \tag{5.9}$$

which means that nanoparticle interaction is almost 5 times stronger on the short wavelength side of the bandgap than on the long wavelength side. In 3D the situation is more complicated but (5.9) demonstrates the possibility tailoring the photonic properties of polymer opals by nanoparticle doping.

5.6 Scattering versus Reflection

The images of the polymer opal samples presented in this thesis (cf. Figs. 3.9-3.10) show that these photonic crystals are very colorful when doped with nanomaterials. The colorful appearance can be perceived in a very wide range of angles regardless of the light source position. This is a clear indication of large amounts of wide angular scattering characteristic to these polymer systems. However, at the same time the material shows angular dependence of the interaction wavelength of light which in turn is evidence of the order in the material, as was outlined in Section 5.1. Evidently we have wide angular scattering tuned with structural ordering. These ideas are briefly illustrated in Fig. 5.20.

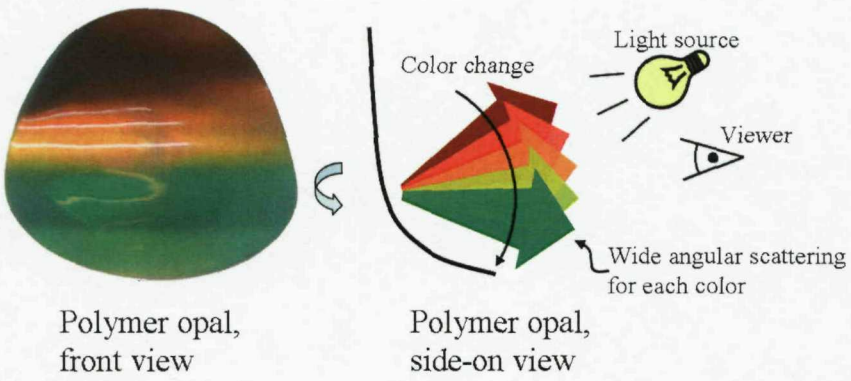

FIGURE 5.20: Left: View of a colorful polymer opal from the front when the light source is located above the viewer. The perceived reflected colors (wavelengths) tune with the angle of incidence and are propagating into a wide range of viewing angles. Right: Side-on view.

Looking at the illustrations of Fig. 5.20 one is left with a very obvious conclusion. Reflection and scattering need to be treated as separate properties with these highly scattering opals. Reflection (R) is the part of the scattered light which is directed into a cone of 3° around the specular reflection direction thus matching the focusing onto the sample. Scattering (S) is defined as the contribution of light outside of the reflection cone. This is illustrated in Fig. 5.21. In the left panel of Fig. 5.21 there is a digital image of the wide angular scattering from a polymer opal when quasi-collimated broadband light is incident on it. The reflection (R) and scattering contributions are indicated as short dashed and long dashed lines respectively. In the right panel the definition of the scattering and reflection is further illustrated. The reflected light is centered around the specular reflection direction, i.e. $\theta_{in} = \theta_{out} = \theta$. The sample normal is indicated with a vertical dashed line. Wide-angular scattered contribution is also indicated in the figure. Note that this definition of reflection and scattering is somewhat in disagreement with the method used for labeling the different traces so far in this chapter. In reality the experimental reflection traces measured with the UV-Vis spectrophotometer (R_{SP}) actually correspond to the reflected plus scattered contributions, i.e. $R_{SP} = R + S$. It

is inevitable that these characteristics are treated separately, and from now on in this thesis we shall take great precaution to indicate whether the discussion is on reflection (i.e. narrow-angle contributions around the specular reflection direction) or scattering (wide-angle contribution excluding reflection). An interesting consequence of the wide-angle scattering with polymer opals is the fact that the measured lineshape depends strongly on the collection aperture. Hence commercial UV-Vis spectrometers for which the adjustment of the collection aperture is not usually possible make the measurement interpretation extremely ambiguous.

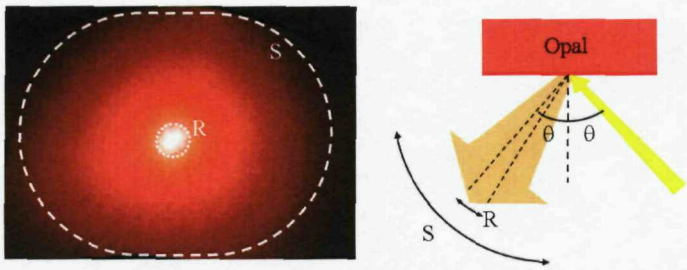

FIGURE 5.21: Left: Digital image of the scattering from polymer opal on a white screen showing the reflected part in the middle (R, short dashed line) and the scattered part (S, long dashed line). Right: Scattering (S) and reflection (R) schematically indicated.

Fig. 5.21 already gives an indication as to how fundamentally different the reflected and scattered distributions are. The reflection spot width is determined by the incoming beam focusing and possible surface fluctuations. The angular width of the scattering can be up to 40°.

5.6.1 Scattering and Reflection Revisited

The measurement setup used for aperture dependent scattering and reflection measurement is presented in Fig. 5.22. This is a goniometer setup which allows us to perform measurements at different angles of incidence and detection independent of each other.

The light source (Source in Fig. 5.22) located at the end of the input arm is a supercontinuum system generating a wavelength continuum from 480nm to 1.8μm. A passively Q-switched JDS Uniphase NanoPulse Nd:YAG solid state laser output (at 1064nm) beam is first let to expand for about 50cm before it is focussed into a photonic crystal supercontinuum fibre (CrystalFibre A/S, length 10m) with a MellesGriot x20 microscope objective. The fibre is dispersion-engineered such that up- and down-conversion in wavelength can occur due to the combined effect of parametric four-wave mixing and stimulated Raman scattering [93, 94]. In the fibre output end we have a MellesGriot x40 microscope objective for the collimation of the continuum light. Typical unpolarised output can be seen in Fig. 5.23.

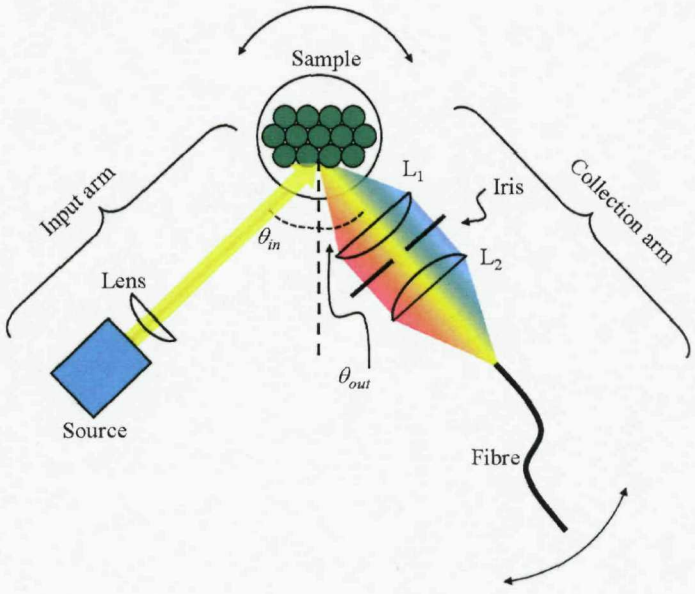

FIGURE 5.22: Goniometer setup. The super-continuum source is directed along the input arm and focused by a lens onto the sample an a rotation stage. Lens L1 collimates the scattered intensity into a quasi-collimated beam, whose width can be controlled through the use of iris. Lens L2 focuses the chosen angular output light into a multi mode fibre connected to a spectrometer. The input arm is fixed, whereas the sample can be rotated in relation to the input and collection arms. The collection arms can also be rotated around the sample rotation stage pivot point.

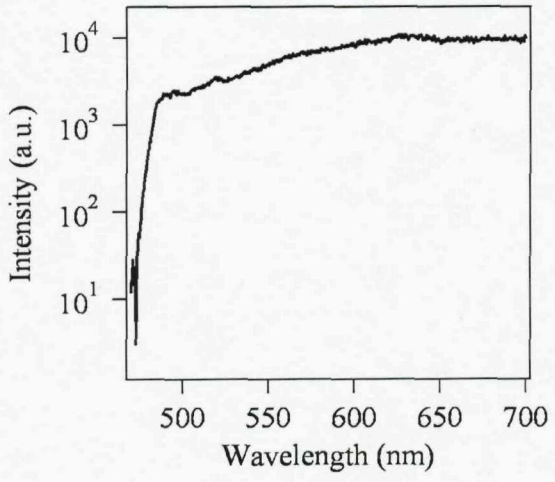

FIGURE 5.23: Typical unpolarised output from a supercontinuum source consisting of a solid-state pulsed pump laser operating at 1064nm and 20m of photonic crystal fibre.

After the collimation the light (yellow beam in Fig. 5.22) is focussed onto the sample to a 500 μm spot by a lens (f=400mm). The sample is mounted on a rotation stage on the pivot point of the two arms (input and collection) of the goniometer setup. The input arm is fixed for mechanical robustness and the angle of incidence can be varied through the rotation of the sample stage. In the collection arm we have a 150mm focal length collimating lens (diameter 25mm) first collimating the angularly divergent light. The semi-collimated beam of light is then incident on a variable iris which enables us to change the collimation angle by varying the iris diameter from sub-millimeter to 25mm. In other words the iris restricts the light throughput in k-space. Following the iris there is a 50mm focal length lens (diameter 25mm) which focuses the light to the end of a multimode fibre at the end of the collection arm coupled to an Ocean Optics USB2000 holographic grating spectrometer. The collection arm can be moved independent of the input arm and of the sample rotation stage such that off-specular reflection scattering (i.e. $\theta_{in} \neq \theta_{out}$) can be collected. All lenses used in the setup are achromats to minimize chromatic aberration of the system.

We used the setup described above to measure angle-dependent scattering and reflection traces from various polymer opal samples. The opal was attached vertically to the rotation stage, an angle of incidence was chosen and the reflection trace was measured at the iris setting such that the collection angle was about 3° collecting most of the specularly reflected light. Subsequently the iris was opened up fully to allow all the collimated light to pass through (collection angle about 40°) and be focussed down to the fibre to yield the total contribution. The scattered contribution is extracted when these two contributions of the total and the reflected light are subtracted. These characteristics were measured for a polymer opal sample BV02 with the normal incidence (111)-resonance at 635nm for angles of incidence $\theta = 10..70°$ (step 10°) for unpolarised light. The results are presented in Fig. 5.24 (a-g). All traces were normalised with the super-continuum spectrum reflected off a Ag mirror. The traces were recorded in a system where neither input polarisers or output analysers were used.

Inspection of the data of Fig. 5.24 (a-g) reveals several interesting features. The black traces correspond to the total output collected (R+S), the red traces to reflection (R) and blue traces to the wide-angle scattering (S). The general feature in all of the plots is that the trace characteristics shift towards shorter wavelengths (higher energies) as the angle of incidence is increased although the features become very undistinguishable at the highest angle of incidence $\theta = 70°$. In other words they seem to obey the Bragg scattering law of (5.4) which is another indication of the fact that the scattering and reflection features are solidly linked together with the underlying symmetry and ordering of the opal structure. Furthermore, all incident angles also show the characteristic behaviour of maximised scattering and minimised reflection at the bandgap. At the angle of incidence 50° and beyond the R+S -trace changes its shape slightly. It is tentatively attributed to difficulties in capturing the whole cone of scattered light at

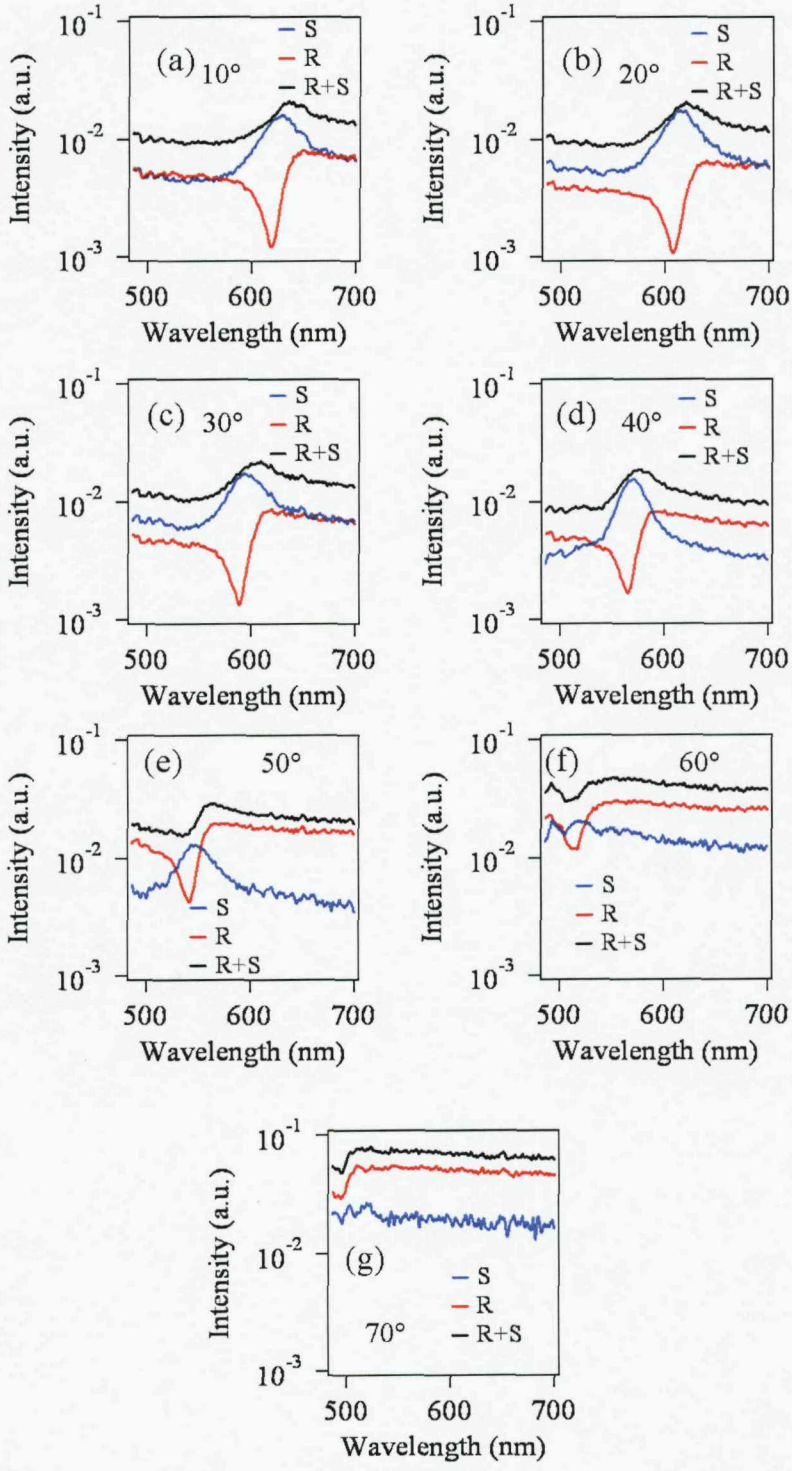

FIGURE 5.24: Total output (R+S), reflection (R), and scattering (S) characteristics of polymer opal sample BV02 collected in the setup of Fig. 5.22 for angles of incidence $\theta = 10..70°$ (step 10°) from (a) to (g), respectively.

high angles of incidence due to setup misalignment issues. However, the reflection trace continues to show its characteristic dip meaning that the energy is removed from this direction possibly into the wide scattering cone. Moreover, it seems from the data of Fig. 5.24 that the long wavelength magnitudes of the R+S and R traces seem to be a monotonically increasing function of the angle of incidence, which would indicate that the material is acting as a bulk reflector at this regime.

The reflection dip can be analysed further by considering its dependence on different polarisations. The angle-dependent results for the reflection measured with the sample BV02 in the setup of Fig. 5.22 for p- and s-polarisations are given in Fig. 5.25 (a-b), respectively, for angles of incidence θ=10...60°. Interestingly we see that the p-polarised trace changes from dip to a peak between incident angles θ=50° and θ=60° whereas the s-polarization trace retains its dip form throughout the different angles of incidence.

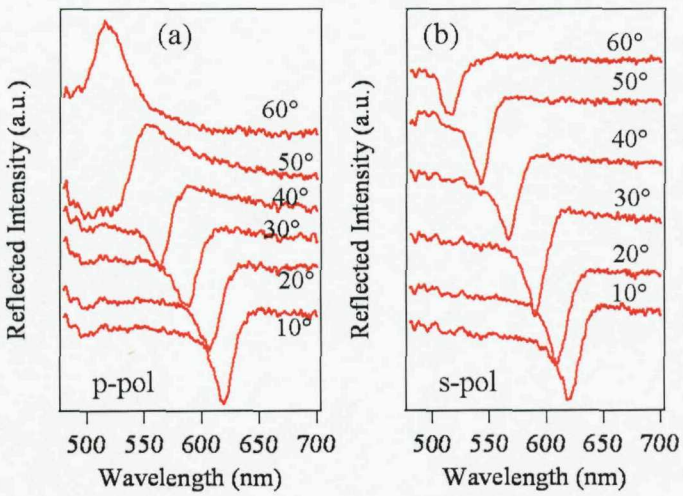

FIGURE 5.25: (a) p and (b) s -polarised reflectivities of sample BV02 incident angles θ=10...60°. The traces have been vertically shifted for clarity. Brewster angle $\approx 56°$.

This polarisation-dependent reflection behaviour can be analysed further by considering the 1D model of a multilayer system with a mismatch layer of thickness d and refractive index n_1 on top depicted in Fig. 5.26. We consider the electric field E_0 incident on the mismatch layer which is partially reflected by the interface and partially transmitted before hitting the multilayer system after thickness d. In order to calculate the total reflected field as a sum of the field reflected by the bulk mismatch layer and the reflection by the multilayer stack $E_{bulk} + E_{multilayer}$ we need to consider the phase evolution of the part of the incident light that gets reflected by the multilayer. We treat the multilayer reflection here through refractive index n_2 and assume $n_2 > n_1 > n_0 = 1$. Thus for the interfering fields we have:

$$E_{tot} = E_{bulk} + E_{multilayer} = r_{ps01}E_0 + t_{ps01}r_{ps12}t_{ps10}e^{ik_0\Lambda}E_0, \tag{5.10}$$

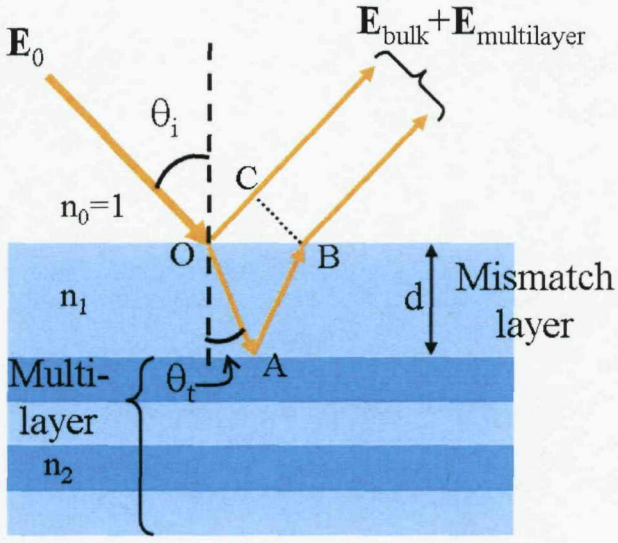

FIGURE 5.26: Multilayer stack with a low refractive index mismatch layer used for modelling the different reflection contributions.

where the r_{ps01} (t_{ps01}) correspond to the Fresnel amplitude reflection (transmission) coefficients (defined in Appendix A) for light travelling from material 0 to 1 (similarly for other indices) and k_0 is the photon wavevector in vacuum. Parameter Λ is the phase difference of the fields that arises through the difference between paths OC and OAB and is defined through [16][4]:

$$\Lambda = 2n_1 d \cos\theta_t, \tag{5.11}$$

where θ_t is the angle of refraction from air to the mismatch layer. Now (5.10) yields for the reflected intensity I:

$$I \sim r_{ps01}^2 + t_{ps01}^2 r_{ps12}^2 t_{ps10}^2 + r_{ps01} t_{ps01} r_{ps12} t_{ps10} 2\cos(k_0\Lambda). \tag{5.12}$$

From (5.12) it is clear that the interference arises from the *cos* -term. The polarisations have to be considered here separately and in Fig. 5.25 (b) we see that all the traces for s-polarisation have a dip which corresponds to destructive interference. The signs for the Fresnel-coefficients in (5.12) for the s -polarisation across the whole angular range are r_{s01}(-), t_{s01}(+), r_{s12}(-), and t_{s10}(+) (cf. graphs in Appendix A) and thus in order to have destructive interference the argument of the cosine should be equal to $(2p+1)\pi$, where p is an integer. If we choose $p = 0$ we have from (5.11-5.12):

[4]We assume here that the net effect of the reflection from the multilayer is the same as for reflection from a higher refractive index layer.

$$\frac{4\pi n_1 d\cos\theta_t}{\lambda} = \pi. \tag{5.13}$$

Eq. (5.13) can be used to calculate the average thickness d based on the dip locations for the s-polarised reflection traces of Fig. 5.25, which yields an average value of $d = \frac{\lambda}{4n_1} = 635nm/5.96 \approx 110nm$, where we have set n_1=1.49 for PEA. Considering the p-polarised traces of Fig. 5.25 (a) wee see that there is something interesting happening between angles $\theta = 50°$ and $\theta = 60°$. Between these incident angles the interference is changing from destructive to constructive and the reflection dip is changing to a reflection peak accordingly. This can be understood via (5.12) and by examining the Fresnel amplitude the reflection and transmission curves of Appendix A. At the Brewster angle of $\theta = 56°$ the coefficient r_{p01} changes its sign from positive to negative with the other coefficients being positive at the angular range. This means that when we keep the condition 5.13 (i.e. $d \approx$110nm) the net effect of the interference term in (5.12) changes from being destructive to constructive and thus we see the change in the measured response from dip to a peak in Fig. 5.25 (a). Altogether this analysis has the following very interesting interpretation. During the manufacturing process described in Chapter 3 the soft and freely flowing PEA not only fills the interstitial sites in the PS-PMMA crystal but also forms a quasi-bulk-like layer of about 110nm on top of the PS-PMMA crystal formation. This layer acts as a mismatch layer between air and the actual crystal creating the reflection dip seen in the measurements. However another possible explanation also exists. The thickness of 110nm would suggest that the relative phase change between the bulk and the multilayer reflections is due to the difference in the first layer with comparison to the rest of the structure. The close packed structure is a sequence of interpenetrating sphere layers with the distinct difference in the surface layer. The phase change could well be also due to the first layer and the rest of the interpenetrating structure. While the 1D multilayer model provides a straightforward way to look at the phenomenon it is possibly too simplified an approach to treat the 3D nature of the sphere packing. Looking at the data of Fig. 5.24 (a-g) the reason for the dip being the prominent feature in the unpolarised measurements is the fact that the s-polarised intensity dominates the reflection traces especially when θ_i >30°.

The reflectivity and scattering changes with respect to the angle of incidence in Fig. 5.24 are further analyzed in Fig. 5.27. In Fig. 5.27 (a) the maximum locations of the S and S+R (blue and black, respectively) traces and the minimum location of the R trace (red) are plotted against the angle of incidence. Additionally the bandgap location according to the (5.4) Bragg law is calculated using the values of $n_{eff} = 1.56$ (average of the extracted value from Section 5.2 and the volume-average value calculated in Section 3.3.2 and $d_{111} = 202$nm. This is plotted in green. From these extracted values we see that they all show the characteristic Bragg-dependence relative to the angle of incidence θ with varying offsets compared to the theoretically computed values. We also see that the total output (black, R+S) shows the best agreement with the theory at least until

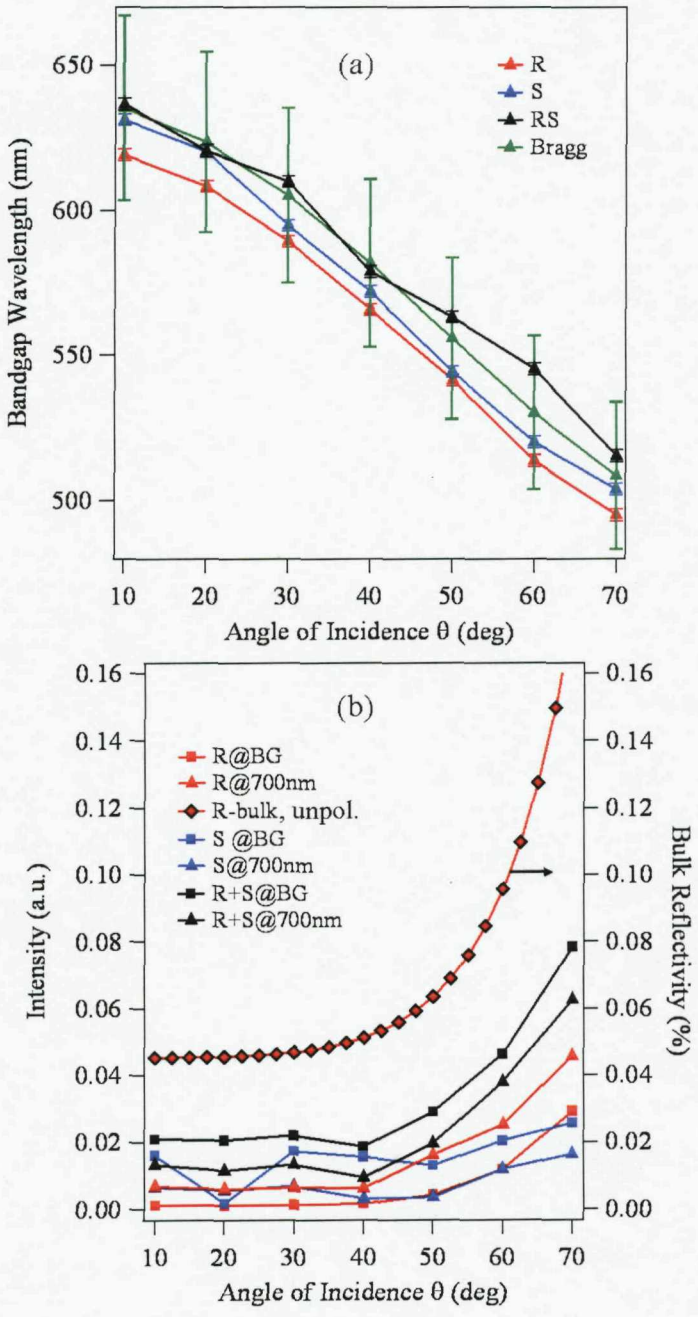

FIGURE 5.27: (a) Reflection minimum and scattering maximum locations extracted from the traces of Fig. 5.24. (b) Scattering, reflection, and total output intensities (left axis) and average bulk reflectivity (right axis). All traces shown as functions of the incident angle for $\theta = 10..70°$.

angles $\theta > 50°$. The reflection trace (red, R) has the largest offset from the theoretical values whereas the scattering maximum location (blue, S) is between these two. At the moment, we have no definite explanation to these offsets, but as was seen in Section 5.4 it probably stems from the doping and/or absorption characteristics.

There has not been much research into the properties of low-contrast opals. The research of Lopez et al. [95, 96, 97, 98, 51, 99] focuses on many aspects on artificial opals ranging from synthesis of polymer inverse opals to disorder in opals and optical responses in different lattice directions. In ref. [97] the aspects of doping a PMMA-opal photonic crystal with larger PS-particle defects is discussed describing it as being a worsening factor to the photonic properties for example in decreasing the reflected peak of incident light. The properties of the defects (size, concentration) are correlated with the different effects seen. Unfortunately, the authors do not go into details in differentiating between the contributions of scattering and reflection. In fact this thesis and the corresponding publications are the only pieces of literature to systematically explore the differences in reflection and scattering.

In a theoretical paper by Kaliteevski et al. [87] the authors investigate the dependence of scattered transmission light and directly transmitted light in a 2D hexagonal photonic crystal with varying amounts of disorder in the form of polydispersity. They find that disorder smoothens and broadens the attenuation dip in transmission spectra and can create an asymmetric shape. This is, at least partially, observed in our samples which can be seen by inspection of the transmission traces of Figs. 5.14 and 5.13 (b). However, it is rather challenging to distinguish between the effect of disorder and absorption in these samples. Kaliteevski et al. further argue that the scattered transmission minimum does not correspond to the center of the photonic band gap but is shifted towards higher energies (i.e. lower wavelengths). Our samples show slight differences in the location of the scattering peak and the reflection dip with respect to the calculated bandgap (cf. Fig. 5.27 (a)). However, we are measuring the scattering *in front* of the sample whereas their findings are for *transmission* scattering and for a system with a relatively high refractive index contrast (3.6:1) in 2D. In transmission we observe no features similar to the results of Kaliteevski et al. The possible connections between our results and their simulations are further complicated by the 3D nature of our system.

Romanov et al. [100, 101] discuss the effects of the side and forward scattering in silica and latex thin film opals. In the side scattering regime a minimum is observed at the band gap due to the removal of the light intensity at this frequency by Bragg reflection. Forward scattering is interpreted as a combination of the original beam of light being diffused and thereafter experiencing the angle-dependent Bragg interaction before escaping the structure. Once again, these results are on one hand close to ours but on the other hand due to the 3D nature of the problem and different refractive index contrasts generalization of their arguments to scattering in front of the sample is impossible. For aspects on theory and discussion of the scattering and reflection

properties of these doped polymer opals together with further comparison on existing works in the literature the reader is referred to Chapter 6.

Stepping back to the data of Fig. 5.27 (b) we have plotted the different intensities of the traces of Fig. 5.24 (a-g) against the incident angle θ. Firstly there are the intensities at the band gap for all the characteristic traces (solid squares, left axis). These intensities are also extracted at the off-bandgap location of 700nm (solid triangles, left axis). Finally, the bulk reflection values (Fresnel reflectivity) for unpolarised light at an interface from air to a material with the refractive index of $n_{eff} = 1.56$ are plotted against the angle of incidence (right axis, red/black diamonds) [78]. It is observed from the data with square symbols that the long-wavelength intensities for R+S and R follow, at least partially, the bulk reflection curve. This would, indeed, indicate that the material has bulk-like properties at this wavelength range. Additionally the R+S trace seems to obey same kind of reflectivity law even at the bandgap wavelength (i.e. at its maximum intensity wavelength). This is maybe somewhat confusing, but one has to remember that the refractive index contrast (and therefore the photonic strength) is quite low for this material, and band gap related properties are thus not very pronounced [85]. However, with the exception of the $\theta = 20°$ value (which is attributed to experimental error) we see that the scattering values at band gap (blue solid squares) are consistently over two-fold with comparison to the off-bandgap long-wavelength values (blue solid triangles) revealing then the characteristic of these materials for intense scattering at the bandgap regardless of the angle of incidence.

5.7 Chapter Summary

Basic optical properties of polymer opals were discussed in this chapter. By far the most important result was that reflection and scattering have to be treated as separate (but linked) entities when discussing the spectroscopy of these materials. The wide-angle scattering from these materials shows maxima whereas the specular reflection contribution is minimised at the bandgap. These reflection minima can be understood by considering an additional PEA mismatch layer on top of the PS-PMMA crystal. The energy minimum of the reflection indicates that this energy is at least partially redirected into scattering at bandgap. These effects tune with the angle of incidence in a way that can be understood by the underlying ordering and the optical Bragg diffraction law. The effect of different nano-dopants was also discussed. The absorption and scattering caused by carbon black nanoparticles lead to separation of the scattering peak and the transmission dip. Other effects include the change in overall colour appearance (to be discussed in detail in next chapter) and overall intensity throughput decrease. The elastomeric nature of these materials allows for the experimenting on the strain-induced changes of the optical characteristics. The strain-induced lattice changes produce predictable effects described by the inter-planar spacing change up to moderate strains.

Also the interaction between the bandgap and the nanoparticles in these polymer opals was discussed and it was shown that the interaction strength is manyfold at the short wavelength side of the bandgap in comparison to the long wavelength side.

Chapter 6

Nanoparticle-Tuned Structural Colour

We have introduced the detailed description of the shear-ordering processes involved in the polymer opal manufacturing in Chapters 4 and 5 and also discussed the basic optical properties of these samples including the reflectivity, transmission and scattering properties. Furthermore, the possibility of nanoparticle doping and the first-order effects were analyzed in these two chapters. In this chapter the analysis is extended towards the scattered colour when light is incident on these highly-scattering materials. We will discuss the topic of structural colour in nature on a very general level and how it is related to the scattering processes present in the polymer opals. A wide range of experiments on the scattering properties in angular and wavelength space has been conducted to shed light into this very challenging problem. It is argued that in order to produce very distinct colour effects in the low-contrast polymer opal one needs to introduce scattering centers and possibly absorption into the periodic structure. The structural colour formation in nature is suggested at least partially to follow a similar process and is thus more complicated than just a Bragg-type scattering mechanism. Furthermore the scattering can not be formulated in terms of the Born approximation[1], as is sometimes done e.g. in the study of index matched photonic crystals, because the refractive index of the scatterer in our case is too high [78]. Finally, shortcomings in the current theories regarding photonic crystals and scattering are outlined and some theoretical considerations covering the opal scattering process are given.

[1]In the Born approximation total field is approximated by the incident field.

6.1 Structural Colour in Nature

Conventional wisdom at the moment seems to be that structural color in nature arises mostly from optical interference of multiple light paths reflected inside periodically-textured materials. According to a plethora of authors, natural opals consisting of stacked silica (SiO_2) spheres acquire their characteristic iridescence due to Bragg interference from the lattice planes [34, 35, 37, 38, 102, 103]. A simple view of such stacked silica opals is given in Fig. 6.1 (a-b). However, another kind of opals exist which are called "fire opals". While the stacked silica opals are quite rare in nature, the "fire opals" are possibly more common and consist of random accumulation of granular particles of hydrated silica of around 20nm size scale [36]. Butterfly wings can change their color with viewing angle due to the grating-like fine structure scales on their surfaces and furthermore hummingbird iridescence is argued to be due to a similar mechanism [103, 104, 105, 106]. The brilliant Morpho butterfly wing color is presented in Fig. 6.2 (a) [103]. The underlying scale nanostructure formed by discrete multilayers of cuticle and air responsible for the colour generation is shown in Fig. 6.2 (b). Some aquatic systems (e.g. some species of the brittlestar) also use photonic nanostructures to collect light. Colours in some species of flora have also been found to be due to photonic band gap structures in 1D through laminations of hydrated cellulose but also due to helical arrangement of cellulose fibrils [103].

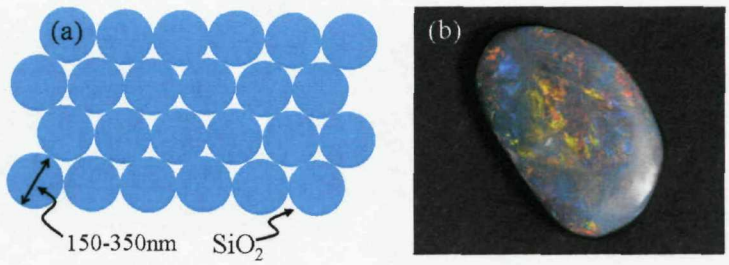

FIGURE 6.1: (a) A schematic view of a stacked silica (SiO_2) sphere opal showing the typical particle diameter for visible response. (b) A digital image showing the colourful interplay of differently oriented domains in a real opal.

In the stacked silica opals the varied and often domained colouring (cf. Fig. 6.1 (b)) is thought to stem from hexagonally packed layers or regions which are then assembled more or less randomly to form the opal gem. From Fig. 6.1 (b) it is also evident that ordering in the natural systems is not perfect. This in turn leads to additional scattering in the opaline system [7, 83, 107, 108] which are losses deteriorating the photonic crystal performance. Very little attention has actually been paid to the process of photonic impurity scattering *inside* the periodic system and its influence on the visual colour appearance of the photonic crystal. We believe that the polymer opals exhibit color features not entirely explained by the conventional Bragg diffraction scheme, which is, as described previously, the normal mechanism invoked for the structural colors of

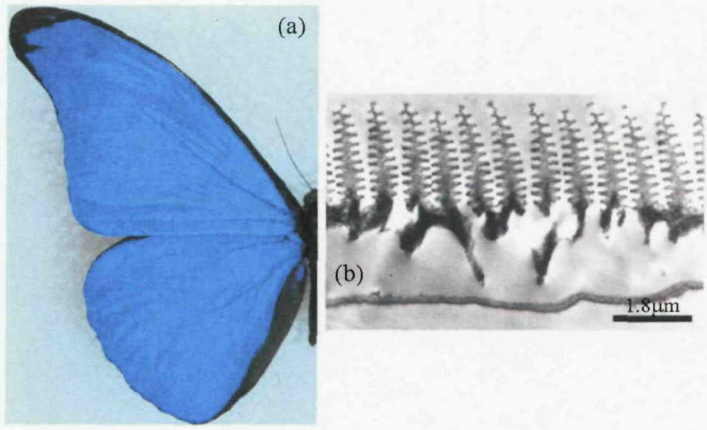

FIGURE 6.2: (a) Dazzling iridescent blue colour of a Morpho Rhetenor butterfly wing. (b) Transmission electron micrograph (TEM) images showing wing-scale cross-sections of Morpho Rhetenor. Taken from [103], ©P. Vukusic.

butterfly wings, iridescent beetles or natural opals. The colour generation in the low-refractive-index polymer photonic crystal relies on a new phenomenon arising from resonant scattering events that take place inside the periodically structured environment. While it is obvious that this mechanism is related to the Bragg diffraction scheme there are distinct differences that need careful consideration. In the polymer opal material system the doping has large effects on the colour appearance and cannot be explained by the existing scattering theories. The resonant scattering from the low-contrast polymer opal should de facto be considered as a feature of the material and not a flaw. We show that this feature can be controlled by nanoparticle doping to some extent and is likely have wide-ranging consequences not only in technological applications but also in understanding the physics of scattering in a photonic band gap material.

6.2 Overview of the Chromatic Scattering from Polymer Opals

In order to understand the need and the means of the analysis of the resonant chromatic scattering from polymer opals some basic characteristic are discussed first. Fig. 6.3 presents the basic features of the chromatic scattering. The images of Fig. 6.3 show the colourful front scattering from the BV02 polymer opal when supercontinuum light is incident on the opal according to the schematic in (a) at the angle of θ_{in} = (b) 10°, (c) 40°, and (d) 70°. The images were recorded with a digital camera located 15cm from the opal sample.

These images show several interesting features. As already pointed out in Section 5.6 the reflection spot and the wide-angle scattering contribution are readily visible in each of the panels in Fig. 6.3 although (d) shows far less scattering than (b) and (c). Also evident is

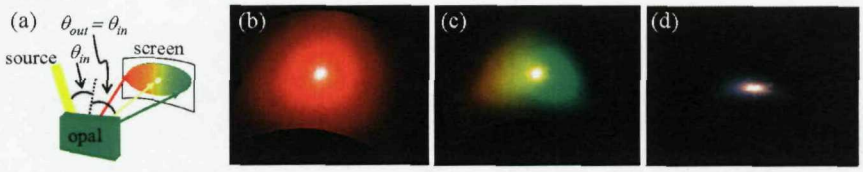

FIGURE 6.3: Digital camera images of the chromatic front scattering from the BV02 opal when the supercontinuum light is incident according to the schematic of (a) at the angle of θ_{in} = (b) 10°, (c) 40°, and (d) 70°.

the fact that the overall or "average" colour changes between each of these images i.e. as a function of the incident angle. Furthermore, on closer inspection it is observed that the colour also changes *within* each of these images when scanning across the image from left to right. For example, in the middle panel (angle of incidence $\theta = 40°$) the colour seems to tune from deep red to bright green. The other two panels also show similar behaviour although less pronounced. The lack of wavelengths (colours) on the right side of the bright reflection spot in Fig. 6.3 (d) is due to the input supercontinuum wavelengths ranging from 480nm upwards (cf. Fig. 5.23), and thus there are no wavelengths to be scattered to the right side of the reflection spot. Summarizing the features of Fig. 6.3 we see that the overall range of the scattered wavelengths depends on the angle of incidence but also that the angular dispersion within a particular angle of incidence has a wavelength dependence. There are some similarities to traditional Bragg scattering (e.g. angle-dependence) but the biggest difference is the fact that in Bragg-type scattering the off-resonance wavelengths should not experience the bandgap but rather be transmitted, especially in the low RIC polymer opal. Furthermore, as was mentioned in Section 5.2 the dispersion of the effective refractive index n_{eff} is ecpected to be very small so prism-like refraction can be ruled out. Evidently, we have scattering events that depend both on the angle of incidence but also have an angular dependence on the scattered wavelength's relation to the bandgap wavelength[2]. Clearly the doped polymer opal is showing evidence of an unusual type of resonant chromatic scattering and furthermore, there is an inescapable need to treat the reflection and scattering separately.

6.2.1 Setup for Measuring the Angular Dependence of Broadband Scattering

The angular properties of the chromatic scattering from polymer opals were measured in the setup of Fig. 6.4. The collimated light from a supercontinuum source (cf. Section 5.6.1) is filtered with a liquid crystal (CRI Varispec) filter into 8nm bandwidths and incident on the polymer opal sample at an angle of θ_{in} through a hole in a hemispherical semitransparent screen (a.k.a. half a pingpong ball). The incident light is scattered

[2]Note that this spatially chromatic scattering was already anticipated in Fig. 5.22 where the scattered contribution was depicted as a cone of spatially varying colours.

to a direction around the specular reflection direction depending on its wavelength and for a fixed incident angle, at each incident wavelength we record the resulting reflection (R) and scattering (S) with a zoom lens imaging the pattern from the hemispherical screen on a Peltier-cooled monochrome CCD-camera (StarlightXpress SXV-H9). The optical axis of the zoom lens is directed towards the sample at an angle $\theta_{out} = \theta_{in}$ and lies in the plane of incidence. The system is set up such that the input photons hit the sample at the center of rotation of the stage onto which the sample is attached to enable the measurement of the scattering dependence at different angles of incidence. This is done by rotating the sample and adjusting the camera position accordingly. Furthermore, the field of view (i.e. the focal length) of the zoom lens must be chosen in such way that the whole pingpong ball is in the image at least in the vertical direction. Knowing the real dimensions of the pingpong ball and the angle of viewing θ_{out} enables the calibration between the image and object coordinates in the recorded images. The spectral response is calibrated by replacing the sample with an aluminium mirror and recording the directly reflected spectrally-filtered laser input, which appears as a small spot in the center of the images - see the whitish highly luminous spot in the center of Fig. 6.3 (b) for example. This compensates for the intensity of each incident wavelength, the luminance of the screen, and the detection efficiency of the CCD. The measurement is repeated for s and p-polarisations and the scattering intensities are averaged to yield the unpolarised output. The experiment is repeated at different angles of incidence θ_{in} to identify scattering that depends on the direction of incoming light.

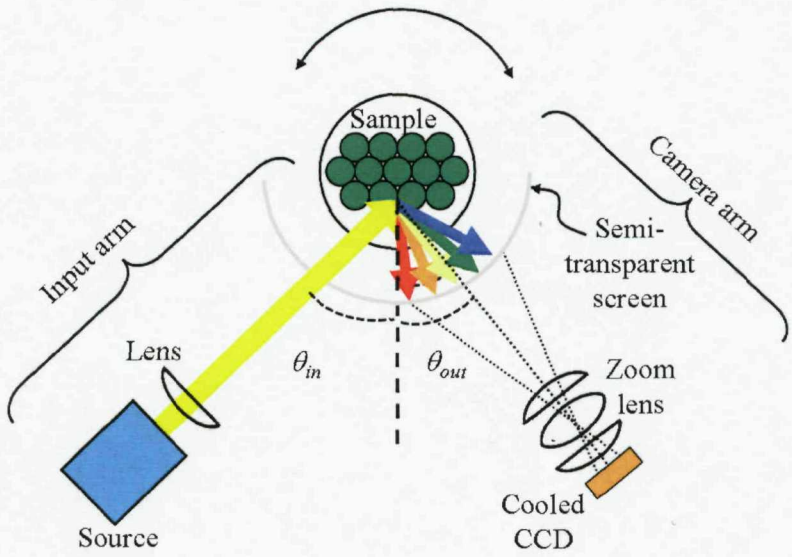

FIGURE 6.4: The measurement setup used to measure the wide-angle scattering dependence on the input wavelength. The light incident form a white continuum source is collimated by and filtered to 8nm bandwidths and incident on a polymer opal at an angle θ_{in} through a hole on the semitransparent screen. The scattering pattern for each input wavelength hitting the screen is recorded with a zoom lens coupled to a cooled CCD viewing the scattering pattern at an angle $\theta_{out} = \theta_{in}$.

6.2.2 Chromatic Angular Scattering for Sample BV02

In this section an overview of the chromatic angular scattering is presented. The sample used for these measurements is BV02 (cf. Table 3.4). The scattering patterns measured in the setup of Fig. 6.4 are shown for angles of incidence $\theta = 10, 33, 50°$.

Fig. 6.5 (a) shows the false-colour digital images for the angular chromatic scattering when the supercontinuum light is incident at $\theta = 10°$. The panels (b) and (c) in Fig. 6.5 show the horizontal and vertical scattering cross-sections on a logarithmic scale for each of the wavelengths in (a), respectively. They are taken at the location of the bright reflection spot in the middle of each wavelength scattering image and shifted vertically for clarity. Thus the horizontal axes show of Fig. 6.5 (b-c) show the angle difference from the reflected direction. Qualitatively it is clear from the images that the closer the incoming wavelength is to the corresponding band gap wavelength for this angle of incidence the stronger the scattering gets. This is readily seen from the width and strength of the halo pattern appearing around the reflection spot in the middle of each image. Also it is observed that the bandap location can visually be extracted from these images by determining where the scattering halo is most symmetric and intense around the reflection spot. In Fig. 6.5 (a) the bandgap is located in the vicinity of 610nm which is in a good agreement with the value of 612nm calculated for the incident angle of 10° according to (5.4). The cross-sections in Fig. 6.5 (b-c) also show some very interesting features and confirm the earlier observation of the enhanced scattering at bandgap. From the horizontal cross-section of Fig. 6.5 (b) it is observed that the scattering contribution moves as a wide cone across the reflection direction which is observed as the narrow contribution. The bandgap trace is highlighted in black and shows a very wide scattering distribution where it is virtually impossible to distinguish between the reflected part and scattered part. Unfortunately, the presence of the input hole in the screen prevents us from showing the scattering cone cross-section for wider angles than $-10°$ in the horizontal direction. In the vertical cross-section of Fig. 6.5 (c) it is once again confirmed that the scattering contribution is maximised at the bandgap (black trace). The lineshape in the vertical direction at the bandgap also seems to be almost linear up to the angular widths of $\pm 20°$.

The angular chromatic scattering is shown as false-colour images and cross-sections of the same sample BV02 for angles of incidence of 33° and 50° in Figs. 6.6 and 6.7, respectively. Similar features as before in Fig. 6.5 are also present in these two figures with the shifting of the bandgap to different wavelengths. The bandgap has shifted to 580nm (550nm) for the incident angle of 33° (50°). These values once again agree reasonably well with the predictions of the Bragg law of (5.4). Also the maximised scattering at bandgap is clearly visible as the symmetric wide angular cone peaked at the angle of 0° (black traces). In Figs. 6.6 and 6.7 the angularly shifting scattering cone is distinctly visible and manifests itself as the shifting "halo" from left to right as the

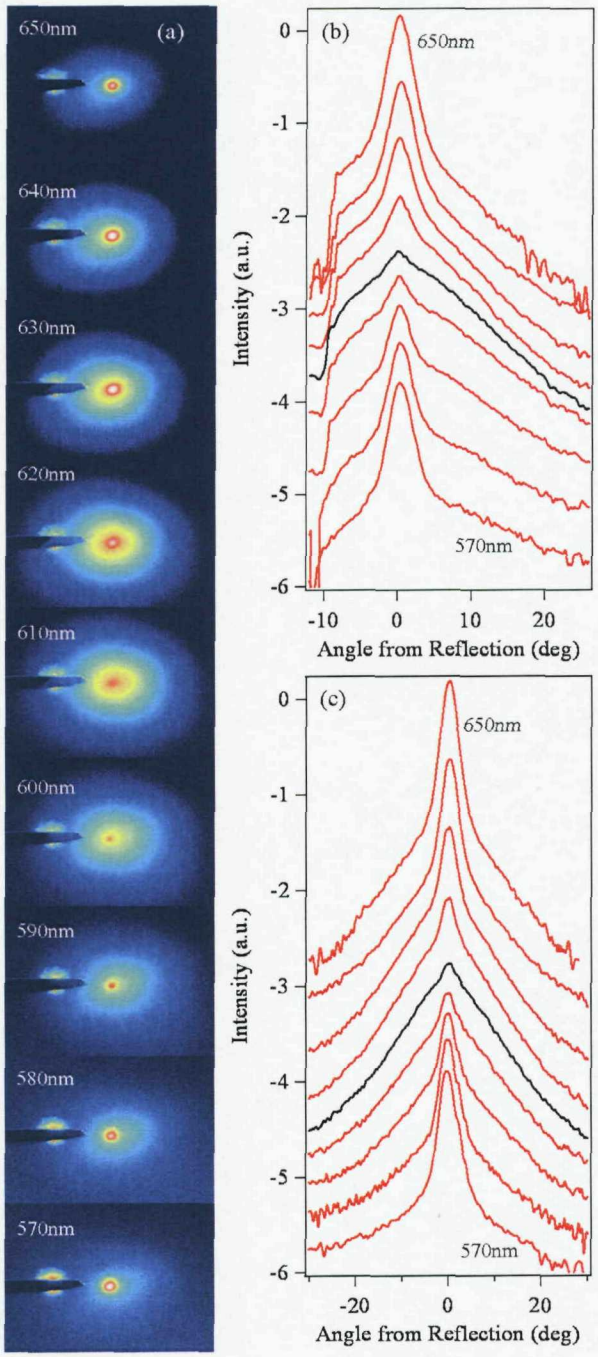

FIGURE 6.5: (a) Chromatic scattering from sample BV02 shown as a false-colour digital image for different incoming wavelengths at 10° incident angle. (b) Horizontal and (c) vertical intensity cross-sections on a logarithmic scale taken across the bright reflection spot in the middle of each scattering image shown against the scattered angle from reflection. In (b) and (c) the scattering cross-sections close to the bandgap (610nm) are highlighted in black. The traces in (b-c) have been shifted vertically for clarity.

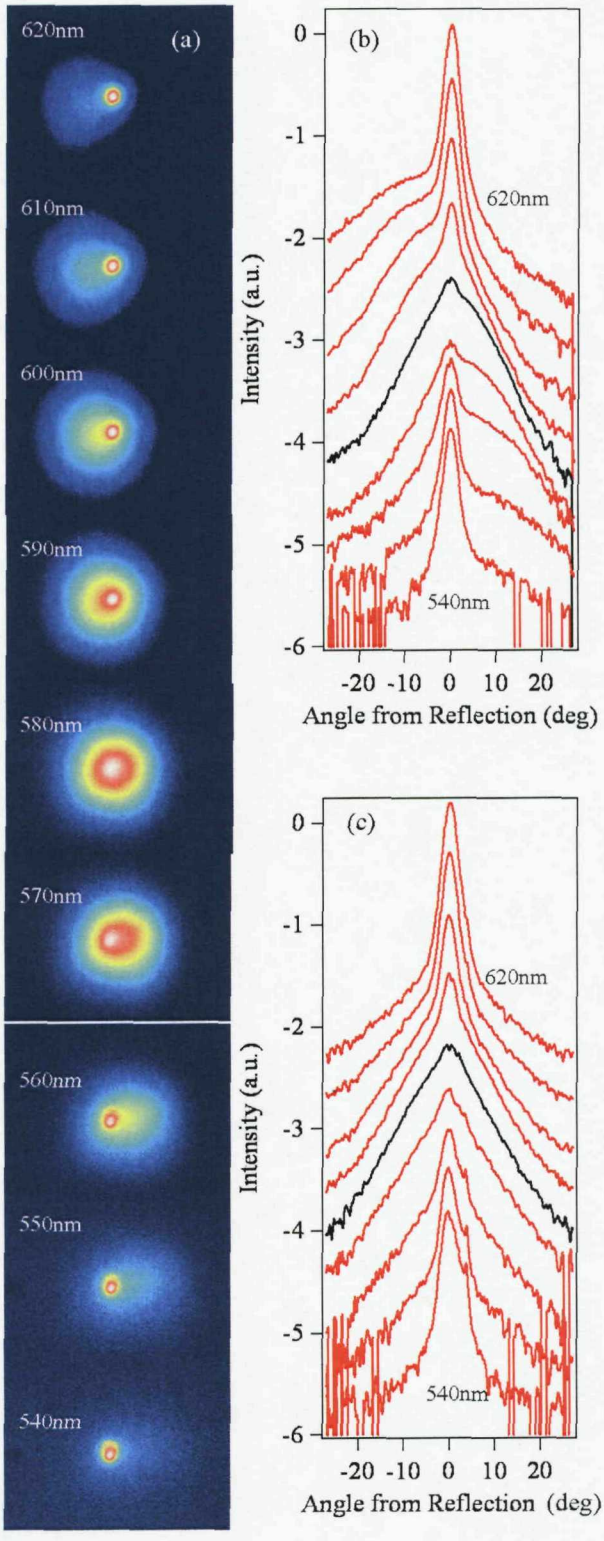

FIGURE 6.6: (a) Chromatic scattering from sample BV02 shown as a false-colour digital image for different incoming wavelengths at 33° incident angle. (b) Horizontal and (c) vertical intensity cross-sections on a logarithmic scale taken across the bright reflection spot in the middle of each scattering image shown against the scattered angle from reflection. In (b) and (c) the scattering cross-sections close to the bandgap (580nm) are highlighted in black. The traces in (b-c) have been shifted vertically for clarity.

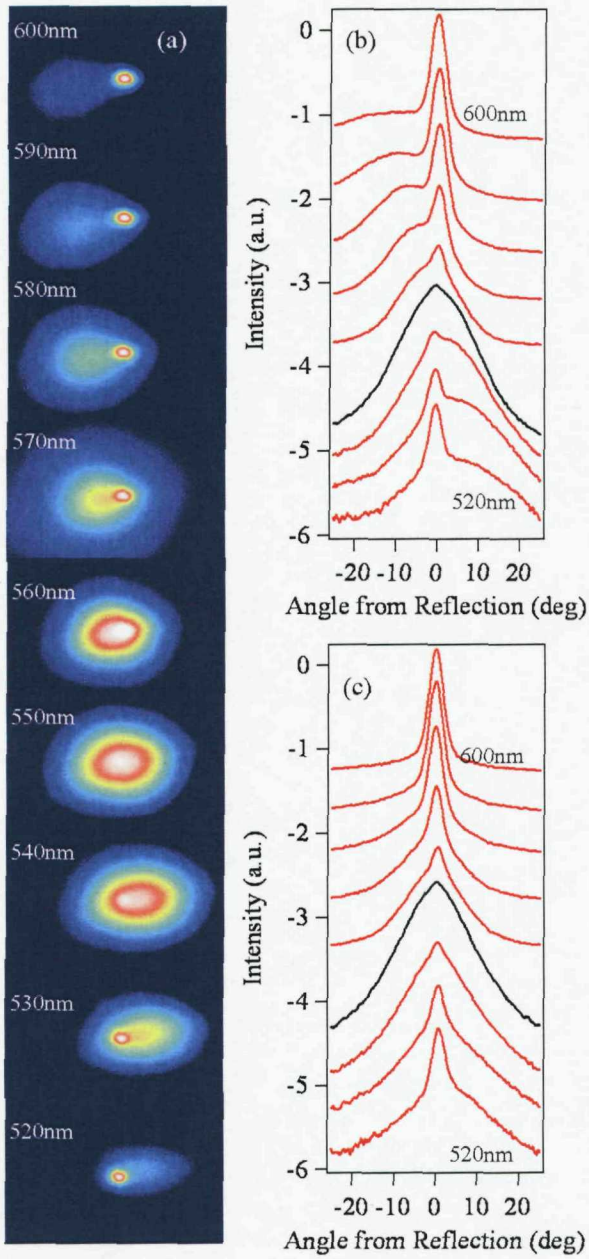

FIGURE 6.7: (a) Chromatic scattering from sample BV02 shown as a false-colour digital image for different incoming wavelengths at 50° incident angle. (b) Horizontal and (c) vertical intensity cross-sections on a logarithmic scale taken across the bright reflection spot in the middle of each scattering image shown against the scattered angle from reflection. In (b) and (c) the scattering cross-sections close to the bandgap (550nm) are highlighted in black. The traces in (b-c) have been shifted vertically for clarity.

wavelength is scanned across the bandgap from long wavelengths to short wavelengths. The horizontal scattering cross-sections in the figures also exhibit this sweep quite clearly. It should also be noted that the scattering pattern in Fig. 6.7 (a) is not exactly horizontal most likely due to an experimental error. The sample was probably skewed by a tiny angle causing the slight angular asymmetry in the pattern.

In the Figs. 6.5, 6.6 and 6.7 it can be seen that two contributions exist in the emerging light. The existence of the reflection outside of the bandgap, which is visible as the bright small spot, is attributed to the bulk Fresnel reflection (cf. Appendix A) which is about 7% at the incident angle 50° for the effective refractive index of $n_{eff} = 1.56$.

6.3 A Closer Look at the Chromatic Scattering from BV02

6.3.1 Scattering Lineshape

As previously mentioned at the bandgap the actual reflection contribution is overwhelmed by the wide angular scattering, i.e. the wide-angle scattering is the dominant interaction of the polymer opal with light. Furthermore, in the logarithmic scale of the cross-sections in Figs. 6.5, 6.6 and 6.7 the lineshape of both horizontal and vertical cross-sections at bandgap is linear on the log-scale (hence exponential in linear scale) versus the angle. The vertical cross-section of the scattering from BV02 at 50° angle of incidence, black trace in Fig. 6.7 (c), is considered here as an example. Firstly the relationship between the k-space and real space needs to be built. The Fourier -space and real space variables are q and x, reciprocally related [109]:

$$q = \frac{2\pi}{\lambda}\sin(\vartheta_S) \approx \frac{2\pi}{\lambda}\vartheta_S, \tag{6.1}$$

where ϑ_S is half of the angular scattering width in radians. From literature [110] it follows that for an exponential distribution in Fourier space the real space distribution is Lorentzian, i.e.:

$$\boldsymbol{F}\left[\frac{1}{a^2+x^2}\right] = \sqrt{\frac{\pi}{2}}\frac{e^{-a|q|}}{a}, \tag{6.2}$$

in other words the Fourier transform (F) of a Lorentzian is exponential. This expression can be manipulated to yield:

$$\boldsymbol{F}^{-1}\left[Ae^{-a|q|}\right] = A\sqrt{\frac{2}{\pi}}\frac{a}{x^2+a^2}, \tag{6.3}$$

where A is an arbitrary constant. The idea here is to relate the q (Fourier) -space scattering to the real space field distribution through the use of a Fourier transform. We fit the k-space scattering cross-section with an exponential function of the variable q and parameters A and a and subsequently relate this distribution to real space through the use of (6.3).

The vertical cross-section of the scattering from BV02 at 50° angle of incidence as a function of q is presented in Fig. 6.8 (red trace). This is fitted with an exponential function where $[A, a] = [0.105, 1005]$. The angular range of the fit is $-30°...30°$ and the dynamic range 17dB.

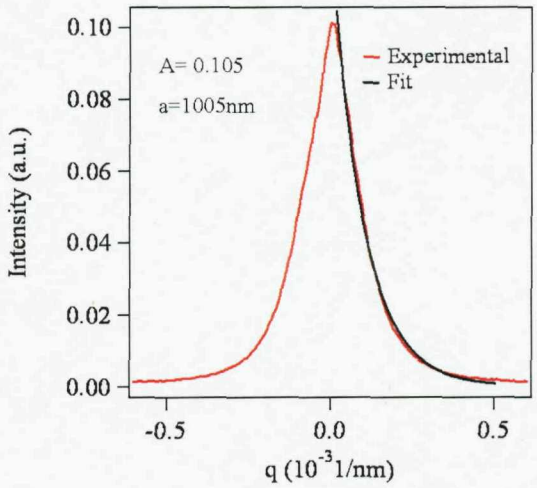

FIGURE 6.8: Experimental trace of the vertical scattering cross-section at band gap (550nm) for BV02 sample at 50° angle of incidence. Exponential fit in black with the fitting parameters shown.

Based on the fit the real space distribution in the opal is roughly characterised by the following function:

$$S(x) = A\sqrt{\frac{2}{\pi}}\frac{a}{x^2 + a^2}.$$

The maximum value (at $x = 0$) for the distribution equals $A\sqrt{\frac{2}{\pi}}1/a$ and thus the normalised distribution $S_n(x)$ reads:

$$S_n(x) = \frac{a^2}{x^2 + a^2}. \tag{6.4}$$

Based on the value from the fit for $a = 1000nm$ we can calculate the FWHM width $s_{FWHM} = 2a = 2000nm$. This gives a rough idea of the distance over which the scattered field distribution is localized inside the opal. It corresponds to a distance of roughly 10 (111) lattice plane separations ($d_{111} = 204nm$). The above methodology can

also be verified by considering the Rayleigh criterion $\Delta\theta = 1.22\lambda/D$ [16], where θ=30° and λ=550nm, yielding $D \approx$1300nm. This is in reasonable agreement with the above figure considering the simplified approach.

Note that this finding is dissimilar to the earlier results about the lineshapes in the surface scattering from opals. In Chapter 4 the diffraction lineshapes were found to be Lorentzian in *k-space* rather than in real space. Lorentzian lineshapes for k-space diffraction have been reported earlier in literature [77, 111] where the authors have found that increasing amounts of defects in a colloidal crystal changes the diffraction lineshape from Gaussian to Lorentzian. The fundamental difference between the Gaussian and Lorentzian lineshapes can be seen in Fig. 6.9 where the most distinct difference is the wider-reaching tails of the Lorentzian distribution. Gaussian diffraction lineshape could indicate wider real space localization of the scattered field in the actual sample and thus possibly lower distribution of the defects. However, in our case it would be reasonable to assume that based on the different lineshapes in *surface* and *volume* - related chromatic scattering the actual mechanisms responsible for the scatterings are somewhat different. The surface diffraction lineshape could possibly be due to slight variations of the PS-PMMA sphere locations whereas the chromatic scattering has most likely many different contributors such as possible sphere dislocations, misalignments and nanoparticle dopants.

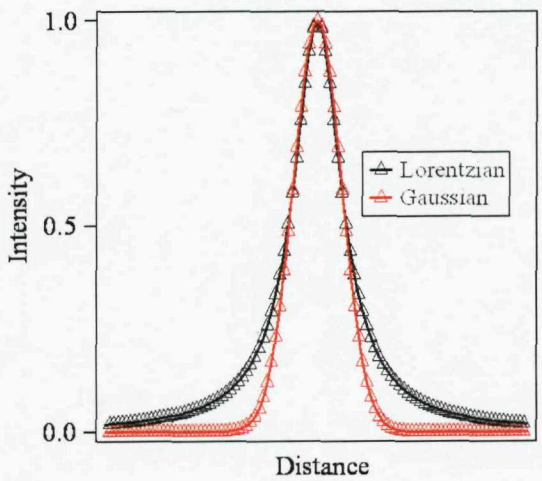

FIGURE 6.9: A Comparison between Lorentzian and Gaussian distributions with equal FWHMs.

6.3.2 Effect of the Varying Angle of Incidence

The chromatic wide-angle scattering measurements were conducted for a large set of incident angles to characterize the effect of the incident angle on the scattering behaviour. The evolution of the scattering cone was then extracted for each incident angle together with the angular widths of the bandgap scattering cones, i.e. at $\lambda = \lambda_{BG}$. First we will

consider the effect of the incident angle on the bandgap scattering cone width. This FWHM at bandgap parameter has been extracted for incident angles of θ=10, 25, 33, 40, and 50° and the data is presented in Fig. 6.10. The inset shows the measurement geometry where the FWHM angular cone width is measured at (or near[3]) the bandgap. The general trend is seen as a slight decrease in the FWHM with increasing incident angle. The deviation at θ=40° could be due to the fact that at θ_{in} we are hitting the exact bandgap wavelength 575nm and the scattering is then maximized wheres with the other incident angles the wavelength is possibly a few nanometers off-bandgap.

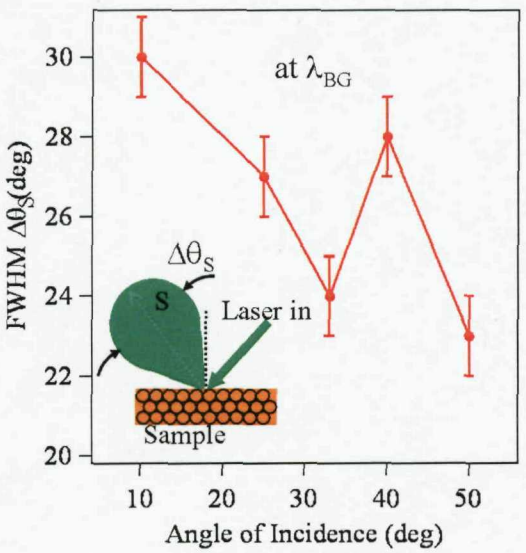

FIGURE 6.10: Bandgap scattering cone FWHM $\Delta\theta_S$ as a function of the incident angle θ. Inset: Measurement geometry.

Secondly we consider the overall angular dispersion evolution for the different angles of incidence. This data is presented in Fig. 6.11 (b). The data was collected in the setup Fig. 6.4 and a further reminder of the setup is given in the inset of Fig. 6.11. On the y-axis there is the angle from sample normal plotted against the incident wavelength on the x-axis. The bandgap wavelength corresponds to the specular reflection angle $\theta_{in} = \theta_{out}$. In Fig. 6.11 (a) the geometry is further described indicating the incident and specular reflection angle θ, the scattering angle θ_S as well as the characteristic behaviour of the scattering cone (S) which moves across the reflection direction (R) with the increasing incident photon wavelength. The scattering traces have slightly different abscissa ranges due to the fact that not all scattered light escapes the sample at all angles of incidence. Moreover, we have also depicted the Bragg law (5.4) (with $n_{eff} = 1.56$ and $d_{111} = 204nm$) dependence of the scattering angle on the incident wavelength. These data have been extracted from considering the angular location of the scattering cone mass center. The general feature of the chromatic angular scattering for different angles of incidence is that the dependence is close to linear (at first approximation). The slope

[3]The exact bandgap location on the wavelength scale was not known a priori, because in the measurement the incident angle was fixed and the incoming wavelength was scanned at 10nm intervals.

of the dependence increases with increasing angle of incidence. While the Bragg law dependence seems to agree relatively well with the scattering directionality for $\theta = 50°$ it is in complete disagreement at lower angles of incidence. Depending on the angle of incidence the different wavelengths are scattered into different directions, e.g. at the photons at 590nm scatter to angles of θ_s=12, 23, 26, 28, and 38°. Similar tendencies are seen for other wavelengths. This is a very interesting feature and clearly reproducible and stable. Currently this characteristic is not understood at all within the current framework of photonic crystal theories as will be discussed in the next section. The deterministic nature of this tuning would suggest that it is not due to random defects or randomly oriented lattice planes inside the polymer opal. We extract the scattering angular dispersion by approximating each of the scattering dependencies of Fig. 6.11 (b) as linear and then calculating the angular spread for a 10nm range using the extracted slope. The dispersion is presented in the inset of Fig. 6.11 (b). It is interesting to see that the dispersion is almost a linearly increasing function of incident angle.

6.3.3 Possible Explanations

Angular chromatic scattering from SiO_2 opals has been previously discussed by Astratov et al. [75]. They witnessed some type of chromatic front scattering from opals with the angle of scattering changing with the incident photon wavelength. The authors argue that this feature is due to the "selective probing of the reflectivity of the appropriately oriented domains at the specular condition represented by an internal angle ϕ of incidence" on the system of (111) planes. The schematic of this model is given in Fig. 6.12. The left panel corresponds to the (111) (parallel to the surface) interaction when light is incident at angle θ. The right panel describes the relationship between the incident light and the scattered direction for a particular wavelength.

This can be understood by considering the following formulas:

$$\begin{aligned} \phi &= \frac{1}{2}\left[\arcsin\left(\frac{\sin\theta}{n_{eff}}\right) + \arcsin\left(\frac{\sin\phi_S}{n_{eff}}\right)\right] \\ \lambda_S &= 2n_{eff}d_{111}\cos(\phi), \end{aligned} \tag{6.5}$$

where ϕ is the average *internal* angle of incidence with respect to two differently oriented (111) plane domains, n_{eff} the effective refractive index, θ the incident angle, ϕ_S the scattering angle, and d_{111} the (111) plane spacing. Their idea is that for the observed scattering direction ϕ_S an average internal angle ϕ is calculated and with this angle the Bragg resonant wavelength is then determined. This model has been implemented to our results in case of 20° ("A 20°") and 50° ("A 50°") incident angles in Fig. 6.11. While this approach seems to fit the results of Astratov et al. very well, in the case

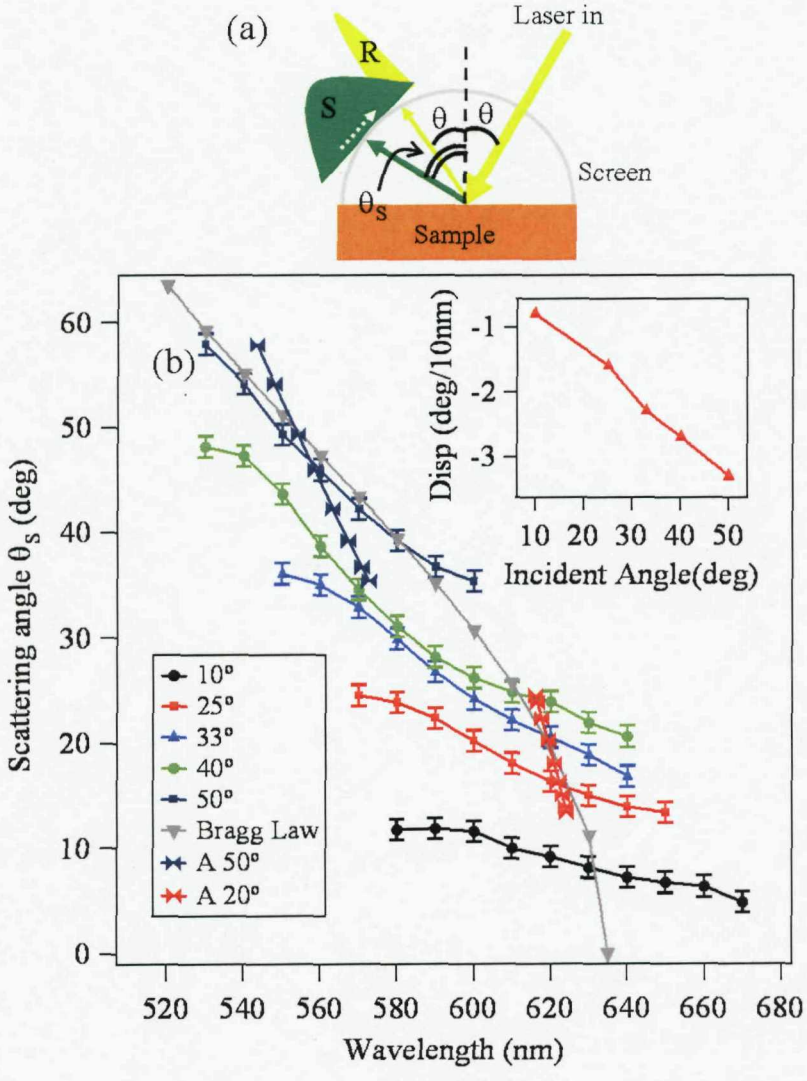

FIGURE 6.11: (a) Measurement geometry showing also the reflection and scattering intensity patterns which scans across the reflection direction as the incident wavelength changes (indicated by the white dashed arrow). (b) Scattering cone angle θ_S as a function of incident photon wavelength for angles of incidence of θ=10, 20, 33, 40, and 50°. Also depicted is the Bragg Law (5.4) dependence of the scattering angle from wavelength. Also results from the model by Astratov et al. [75] for $\theta = 25, 50°$ are shown. Right inset: Scattering dispersion vs. incident angle.

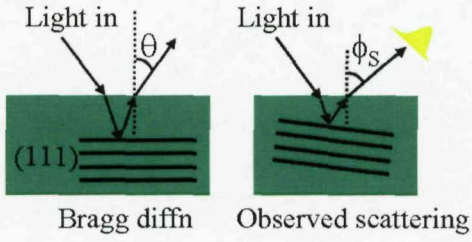

FIGURE 6.12: Left: The light incident on the lattice planes parallel to the surface is reflected into direction θ. Right: Simultaneously some light is reflected by differently oriented planes leading to the scattering at a particular wavelength at the scattering direction ϕ_S.

of the polymer opal scattering the fit is not satisfactory. The angular range for a set range of wavelengths seems to be much higher for polymer opals than for the silica opals studied by Astratov et al. and thus the model proposed yields ill-fitting results. This is possibly due to the fact that their interpretation of the silica opals having many differently-ordered domains and they are basically probing an average orientation. This is contrary to the polymer opals which are more or less monodomained or the possible domain boundaries are not as sharp and well-defined as with sedimented silica opals.

Another interesting interpretation for the chromatic scattering is outlined in the literature by Sanders [112]. This approach relies on the analogies to X-ray scattering theory. The colourful scattering features witnessed by Sanders are explained by interpreting the scattering structures as hexagonal silica sphere layers where the in-plane ordering is well-structured hexagonal but the packing of the layers is close-packed but random. In other words the layer packing sequence could be something like ABACB-CABCABACBABCBCB... In this case it is a well-known fact that the reciprocal space is composed of rods rather than points [109] except for two points corresponding to (111) -plane diffraction. The real space consisting of hexagonally close-packed sphere layers packed at random sequence and the corresponding reciprocal space of lattice rods and two points (P, P') are depicted in Fig. 6.13. In the close-packing of the real lattice the sphere rows are at distance $\frac{\sqrt{3}\phi}{2}$ apart yielding the reciprocal lattice structure spacing of $\frac{4\pi}{\sqrt{3}\phi}$. Since the layers are randomly packed in the thickness direction there is no periodicity in this direction and the points are extended into infinitely long rods in the hexagonal formation. As mentioned above the exception to this is the average spacing of $\sqrt{2/3}\phi$ between (111) layers in real space. This exception in the thickness direction periodicity leads to the existence of the points P and P' which are also located at the distance of $\frac{4\pi}{\sqrt{3}\phi}$ from the lattice rods.

In Ref. [112] the colourful scattering streaks recorded in the experiment are interpreted in terms of these lattice rods and the point P and their interaction with the incoming photon momentum. The illustration from Ref. [112] is reviewed in Fig. 6.14 (a), and the implementation of this technique to our case (assuming random layer packing) is

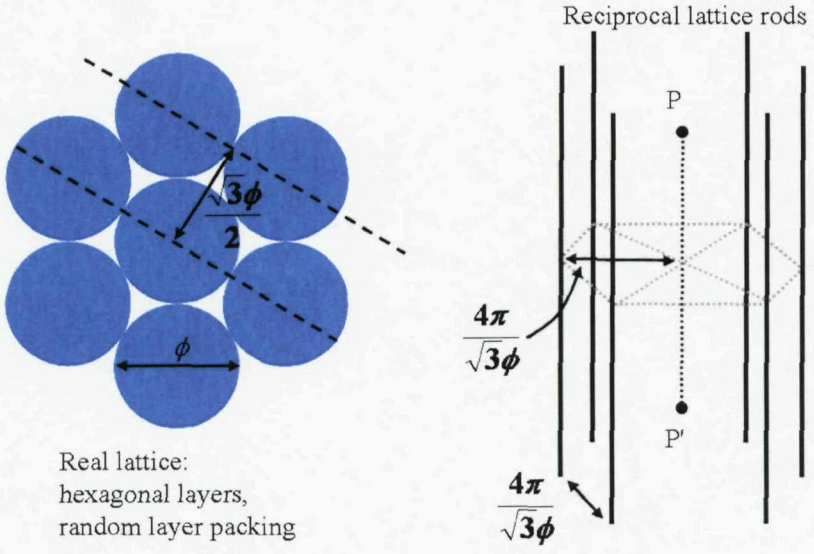

FIGURE 6.13: Left: Real lattice of hexagonal-close packed spheres of diameter ϕ. Right: Reciprocal lattice resulting from the random packing of hexagonally close-packed layers consisting of infinitely long lattice rods and two points P and P' responsible for (111) plane diffraction [109].

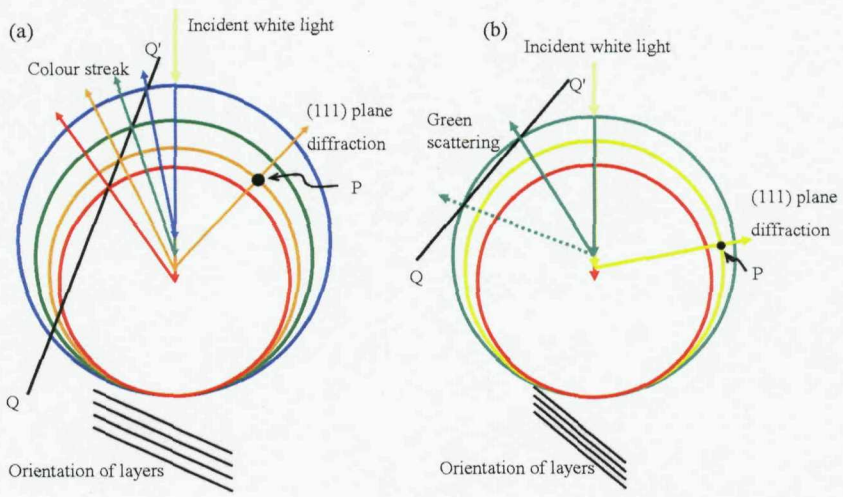

FIGURE 6.14: (a) Ewald sphere arrangement used to interpret colourful scattering from natural opals. After [112]. (b) Similar arrangement for the case of polymer opal scattering at θ=40° form Fig. 6.11.

given in Fig. 6.14 (b). In Fig. 6.14 (a) the different components of the input white light (from above) are shown as the different colour arrows and corresponding Ewald spheres where the sphere radius equals the photon wave vector inside the crystal. Also shown are is the reciprocal lattice rod QQ' and the reciprocal lattice point P. We see that for this particular angle of incidence it is possible to have the (111) plane diffraction (or reflection) in orange (indicated in the schematic) and have colourful scattering streaks produced by the QQ' rod on the other side of the incoming beam. The scattering dependence is dictated by the perpendicular reciprocal lattice distance between the rod and the point P. The colour streak direction is determined by the intersections of the QQ' rod and the Ewald spheres corresponding to different photon momentums. The scattering vector is drawn from the center of each Ewald sphere towards the intersection point. Also indicated in the schematic is the sample layer orientation. Note that the lattice rod responsible for the scattering is oriented perpendicularly to the layers.

The corresponding in-scale geometry is presented for the case of chromatic angular scattering from polymer opal when incident angle θ=40° (cf. Fig. 6.11) in Fig. 6.14 (b). The chromatic scattering in this case ranges from 530nm to 580 nm with the band gap at around 570nm. These three Ewald spheres are depicted in the figure. Also indicated is the direction of the (111) plane bandgap scattering corresponding to the reciprocal lattice point P. According to the calculations shown earlier in this section the distance from point P to the reciprocal lattice rod is $\frac{4\pi}{\sqrt{3}\phi}$, and the corresponding reciprocal lattice rod QQ' (perpendicular to the sample layers) is also drawn on the schematic. At this distance the rod only intersects the Ewald sphere corresponding to the lowest wavelength (green) and the resulting scattering vectors are depicted in the figure. We see that this arrangement seems to suggest green scattering into two directions from which the lower direction (indicated by the dashed green arrow) would most likely not escape the sample. The green scattering which is left is directed at an angle of about 112° off the bandgap direction and about 32° off the incoming direction, but this type of scattering has never been witnessed with the polymer opals. Thus it is concluded that the reciprocal rod analysis is insufficient to explain the chromatic angular scattering. This model requires that the polymer opal layer stacking to be random, but instead it is ordered as was previously suggested in Chapter 3.

6.3.4 Nanoparticle-Doping Effects on the Structural Colour

An overview of the features of the chromatic scattering features presented so far is given in Fig. 6.15. In Fig. 6.15 (a) the imaging geometry for (b) is shown to be the specular reflection setting using white continuum source and a white paper as screen. The characteristic reflection (R) and scattering (S) regions are identified in (b). In (c) there is the reminder of the fact that different colours around the bandgap scatter into different sides of the bandgap direction. The scattering cone width (~40°) is maximised

at the bandgap of 580nm. This fact is shown as horizontal angular cross-sections in (d) centered around the reflection direction of 40°. Inset in (d) shows the vertical cross-section (linear in log-scale) of the scattering cone at bandgap. Finally, (e) is a reminder of the fact that the scattering maxima and the reflection minima tune with the angle of incidence emphasizing their origin from the underlying ordering of the polymer opal.

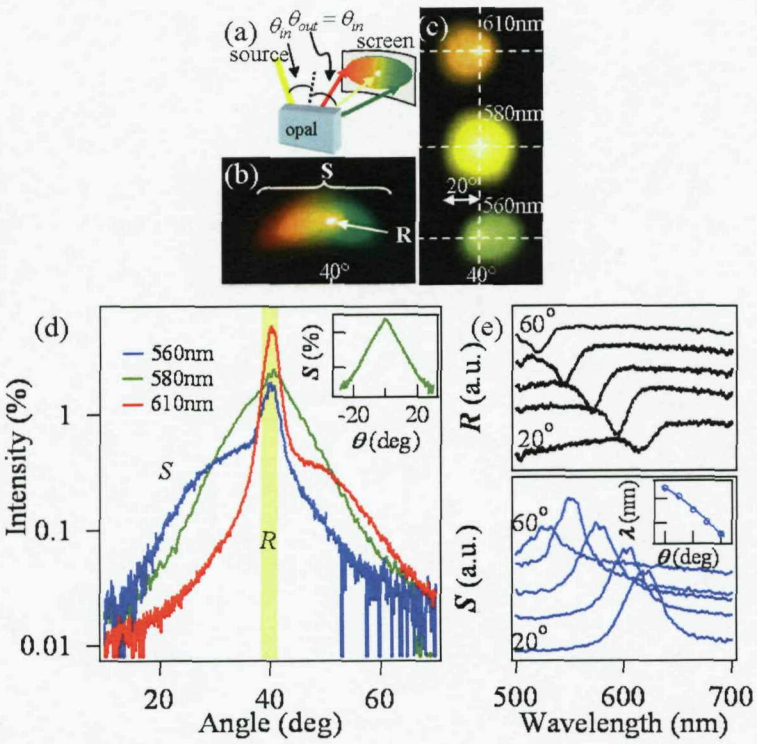

FIGURE 6.15: Summary of the chromatic scattering features for the sample BVO2. (a) The geometry of the imaging for (b). (b) A digital image of the scattering at 40° incident angle showing the scattered (S) and reflected (R) contributions. (c) Images of different wavelengths scattering to different sides of the bandgap direction (middle). Scattering cone width is maximised at band gap to be 40°. (d) Wide angular scattering horizontal cross-sections (log-scale) at bandgap (green trace) and above (red trace) as well as below it (blue trace) shown in the angular regime. Incident angle is 40°, the wide angular scattering is distributed around this direction. Inset: vertical cross-section at the bandgap in log-scale. (e) The angular tuning of the reflection (above) and scattering (below) at bandgap, 10° steps.

The scattering images in Figs. 6.5-6.7 are false-colour images to highlight the scattering cone evolution as a function of the incident wavelength. The actual scattering appears in different colours, in such way that the different colour cones get deviated in different directions around the reflection. In Fig. 6.16 the scattering mechanism is illustrated in colours roughly corresponding to the actual scattered wavelength which results in a clear realization of the scattering. The sample used here is BV02 and the photons are incident on it at an angle of θ=40°. The wavelength ranges from 540nm to 620nm with

10nm steps, and the images have been taken in the setup of Fig. 6.4 and calibrated using the reflection values from silver mirror.

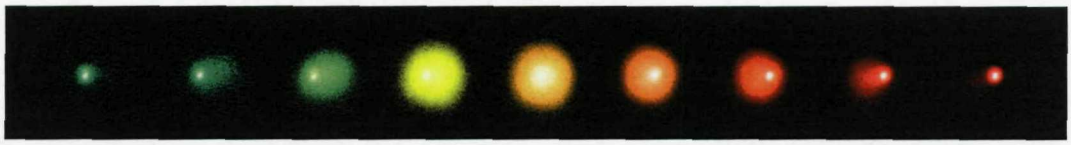

FIGURE 6.16: Evolution of the chromatic scattering from BV02 polymer opal at the incident angle of θ=40°. Images are taken at 10nm steps starting from 540nm (left) and ranging to 620nm (right).

Based on the visual evidence of Figs. 6.5-6.7 it is clear that these polymer opals exhibit very unusual scattering behaviour. The characteristic of this scattering is that it is *maximised* at the bandgap of the opal.

In order to experiment further on the effect of nanoparticles on the chromatic resonant scattering, experiments were conducted on two different samples, Mix1 and Mix2 (cf. Table 3.4). These samples vary only in their doping characteristics: Mix1 is without dopants whereas Mix2 has been doped with C-black at a level 0.05 wt-%. The scattering data was once again collected in the setup of Fig. 6.4 and subsequently normalised with silver reflection intensities. The measured scattering intensities together with the optical images of the samples are presented in Fig. 6.17.

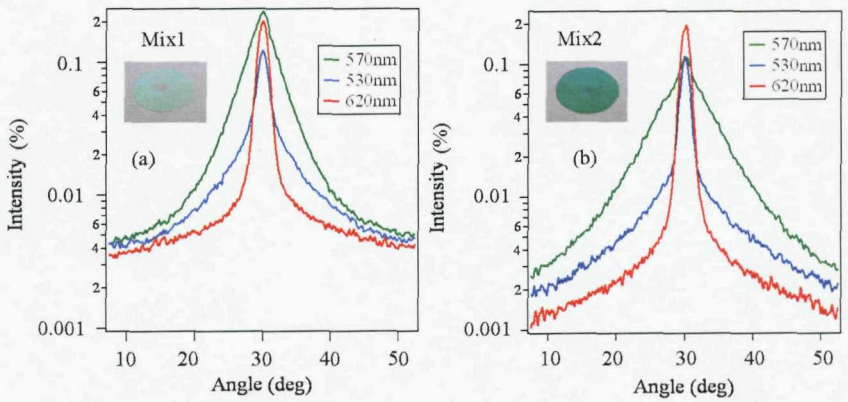

FIGURE 6.17: Scattering cross-sections plotted against scattering angle for (a) undoped and (b) C-black doped (0.05 wt-%) polymer opals at, and either side of, the bandgap at 570nm (samples Mix1 & Mix2). Insets: Images of Mix1 (a) and Mix2 (b).

In Fig. 6.17 (a-b) scattering intensities are presented at the bandgap (green traces) and on each side of the bandgap (red (620nm) and blue (530nm) traces) for Mix1 (undoped) and Mix2 (doped with 0.05 wt-% C-black), respectively. The scattering is plotted against the angle, and because the incident angle $\theta = 30°$ the maxima of the traces are centered around the abscissa value 30°. As was already shown in Chapter 3 we have confirmed by TEM that such low (0.05wt-% for Mix2) loadings of small (<50nm) nanoparticle produces no obvious distortion of the periodic lattice. It can be readily verified from Fig.

6.17 (a-b) that the influence of the nano-dopant is to widen the resonant scattering cone (green trace) to higher scattering angles combined with the pruning of the non-resonant (red and blue traces) scattering contributions. Although the overall scattered intensity is decreased about 25% with the C-black nanoparticle doping the actual perceived resonant colour becomes more pronounced by doping. This can be understood by considering the balance between the on- and off-bandgap scattering values. If we look at the scattered intensities at $\theta = 35°$ in Fig. 6.17 (a-b) wee see that the resonant scattering is at 0.09% (0.06%) for Mix1 (Mix2) whereas it is 0.03% (0.01%) at blue side of the bandgap and 0.01% (0.01%) at the red side of the bandgap. In other words the green-blue contrast ratio is only about 3 for the undoped Mix1 whereas it is about six for the doped Mix2. At higher scattering angles the same trend continues. At $\theta = 50°$ the green-blue contrast is about 1.25 for Mix1 and bout 2.5 for Mix2. In other words without absorbing nanoparticles the scattering is mostly diffuse and hence such samples as Mix1 (like most opals) look milky white with a faint color tinge strongly dependent on their orientation compared to light sources. With the absorbing nanoparticles selectively embedded in the interstices (Mix2), the resonant scattering increases and fills a much larger solid angle (note the overall diffuse light scattered from film also decreases). This characteristic leads to the enhancement in the perceived colour as the bandgap colour dominates over the off-bandgap colours into wider viewing angles.This is also seen in the insets of Fig. 6.17 (a-b).

Another visualisation of the widened scattering cone is given in Fig. 6.18 (b). Here we have calculated the normalised bandgap intensities scattered into a 1° wide annulus around each scattering angle θ for Mix1 (thin trace) and Mix2 (thick trace) according to the schematic in Fig. 6.18 (a). The effect of the nanoparticles is observed as the scattering contribution becoming much wider and thus increased angular range. Without the dopants the scattering contribution is relatively narrowly peaked around $\theta = 35°$ and decreases strongly towards wider scattering angles. The doped contribution instead is much wider extending to angular range of 55° and even further.

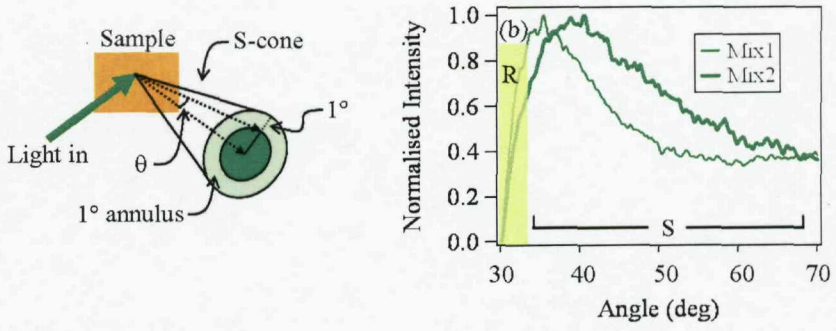

FIGURE 6.18: (a) A schematic presenting the 1° annulus at each scattering angle θ. (b) Scattered optical energy emerging in a 1° annulus around each angle for Mix1 (no dopants) and Mix2 (0.05 wt-% C-black) polymer opal. Reflection (R) and scattering (S) domains indicated, resonant Bragg scattering shaded.

Finally it is very interesting to see the qualitative effect of the nanoparticle doping on the bandgap lineshape of the scattering. By visual inspection we can deduce from Fig. 6.17 (a) that the inclusion of the nanoparticles has somewhat adjusted the lineshape from non-linear (undoped) to almost linear (doped) on the logarithmic scale, i.e. exponential in linear scale. As is described in Section 6.3.1 the linear lineshape on the logarithmic scale implies Lorentzian localization of the scattering field in the opal.

6.4 About the Theory of Polymer Opal Scattering

The scattering in opal photonic structures has been studied quite extensively by several groups [75, 84, 86, 97, 101, 107, 113, 114]. The material systems studied by them are mostly high refractive index contrast (RIC) inverse opals or medium contrast polymer/glass-air opals. The key difference to the system studied in this thesis is that the refractive index contrast of the polymer opal is very low. Using $n_{PS-PMMA} = 1.59$ for the PS-PMMA spheres and $n_{PEA} = 1.49$ [64] for the PEA polymer surrounding the spheres and assuming an *fcc*-packed lattice the RIC can be calculated:

$$\frac{\Delta n}{n_{eff}} = 0.06.$$

As a comparison the *RIC* for PS-air opal is 0.41, 0.34 for SiO_2-air opal (n_{SiO_2}=1.46 [115]), and 1.08 for TiO_2 inverse opals (n_{TiO_2}=2.5 [18]). In other words it is clear that the material systems studied by the above mentioned groups exhibit RICs that are much higher than for the polymer opal. This RIC in turn strongly affects the interaction length (or volume) between the photons and the material and a possible explanation for the observed scattering can be found through considering three very important length scales that affect the scattering in the polymer opal. One of these interaction lengths is called the Bragg attenuation length or the Bragg length L_B [59, 116, 117], and the higher the contrast Δn, the shorter the Bragg length. The Bragg length is thus a measure of the field penetration into the material at the bandgap and is usually defined as the length during which the electric field intensity decays to $1/e$ -value of the original. Another important length scale when dealing with scattering is the scattering mean free path l_{mfp}. This is a measure of the average path of photons between two consecutive scattering events [118]. Thirdly, we must consider the photon absorption path length in the opal i.e. l_α defined as the length over which the intensity inside the opal decreases to the relative value $1/e$ of its original value. While the scattering mean free path will be dealt in greater detail later in Chapter 7 a qualitative theory will be outlined here using the three length measures.

Based on the above given contrasts for TiO_2 inverse opals and for the polymer opal one would expect quite a large difference in their Bragg lengths. The effect of the refractive

index has been simulated using a multilayer program similar to the one used already in Chapter 5 with one important difference. The simple 1D multilayer refractive index sequence has been replaced with an average refractive index as a function of the depth along the [111] direction through the close-packed sphere layers. Here the refractive index has been averaged over the two lateral dimensions leaving only the dependence on the third i.e. [111] direction. The method has been outlined in [113] and can be scaled according to the sphere diameter in the opal. The typical refractive index profile obtained this way for the polymer opal is given in Fig. 6.19 (a) together with a reminder of the *fcc*-lattice. The refractive index value for spheres (interstitial material) is 1.59 (1.49). The refractive index profile obtained through the same algorithm for an *inverse* TiO_2 opal consisting of air and anatase (TiO_2) with n_{TiO_2}=2.5 is plotted in Fig. 6.19 (b) . This method gives a pseudo-3D approach to the otherwise 1D calculation enabling more accurate determination of the electric fields in the opal structure.

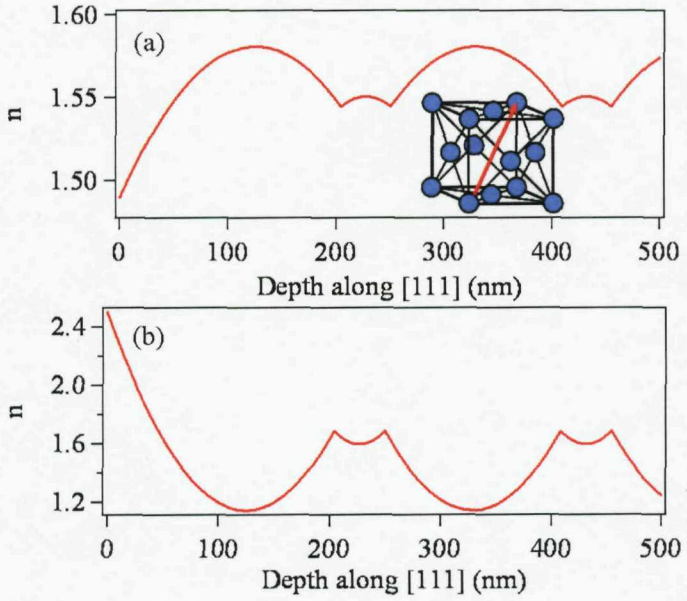

FIGURE 6.19: Refractive index profile versus the depth in an *fcc*-lattice (inset) calculated along the [111] direction indicated by the red arrow in the inset for (a) a polymer and (b) an inverse TiO_2 opal.

When the refractive index profile are modelled this way the electric field Bragg attenuation lengths can be calculated using a multilayer technique. This yields values of L_B=6μm for polymer opal and L_B=0.5μm for an inverse TiO_2 opal. On the other hand the absorption length has been measured for the opals Mix1, Mix2, Mix3, and Mix4, which have exactly the same polymer composition differing only in their C-black doping levels. The absorption was measured in transmission while off-resonance at 800nm and calibrated with the sample thickness using the simple Beer law:

$$\frac{T}{T_0} = e^{-d/l_\alpha}, \tag{6.6}$$

where $\frac{T}{T_0}$ is the normalized transmission, d the sample thickness and l_α the absorption length. The measured absorption lengths and the scattering mean free paths are given in Fig. 6.20 as functions of the C-black doping. The mean free paths are measured at the off-resonance condition with an Ar-ion laser line 515nm. The detailed description of the scattering mean free path measurements will be given in Chapter 7, but here we see that by the inclusion of the nanoparticles we are able to shorten the mean free path from about 30μm (undoped) to about 10 μm (0.2wt-% doping). At the same time the absorption length shows similar behaviour and decreases through the inclusion of absorbing nanoparticles from 1300 μm to 100 μm, but in any case is at least ten times the scattering mean free path.

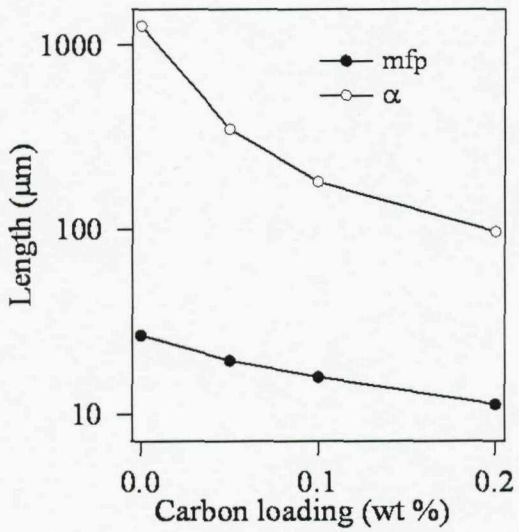

FIGURE 6.20: Measured absorption length (L_α) and scattering mean free path (l_{mfp}) as functions of C-black doping levels.

The key to the theoretical ideas presented here is the comparison of these above presented length scales in case of a high RIC TiO_2 inverse opal and on the other hand the low RIC polymer opal. A very simplistic 1D view of the comparison is given in Fig. 6.21 where the inverse opal (left) and polymer opal (right) are presented as multilayer systems. The photonic strength i.e. the difference in the Bragg attenuation lengths is readily visible; also the average scattering mean free paths are presented. Scattering centres are presented as black dots.

In principle two different regimes of scattering are possible. Typically the high-quality inverse opals exhibit scattering mean free paths $l_{mfp} > 10\mu m$ [119] and thus about 20 times the calculated L_B. This is also indicated in Fig. 6.21, left panel, by the much shorter L_B arrow. If a resonant photon indicated by the green arrow is incident on an inverse opal (left, $L_B \ll l_{mfp}$) it is very likely to get reflected within the first few layers due to the short Bragg attenuation length. On the other hand if a non-resonant photon (orange arrow) is incident on the inverse opal it might travel unaffected for the

length of the l_{mfp} and then undergo scattering. If this photon is then scattered into a resonant direction (green arrow pointing up form scatterer) again it cannot escape the structure due to the strong Bragg attenuation and is re-reflected back into the high RIC structure. This way the scattering in front of the opal is almost completely prohibited due to strong resonance.[4]

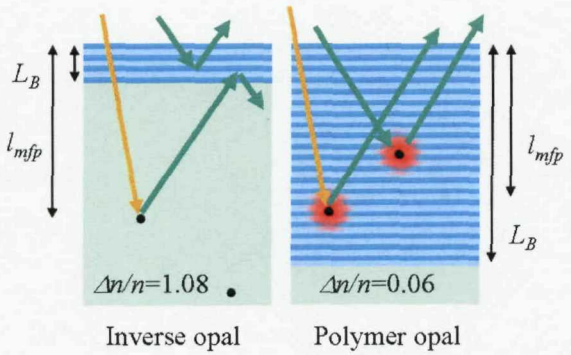

FIGURE 6.21: Left: Scattering form a high RIC inverse opal. Resonant (green arrow) or non-resonant (orange arrow) scattered photons cannot escape the crystal due to strong Bragg interaction and thus short attenuation length L_B. Right: In a polymer opal the scattering is taking place inside the periodical environment and both resonant (green arrow) and non-resonant (orange arrow) can thus escape the crystal.

In contrast to this in the polymer opals a very different scattering regime arises. In the polymer opal we have $L_B \sim l_{mfp}$, which implies that all scattering events take place within the resonant photonic environment. As was already mentioned before $l_{mfp} \sim 27\mu m$ off-resonance in the undoped material (see Fig. 6.20), which decreases on resonance (see Chapter 7) and also as a function of the doping. Basically the cross-section of the scatterer is enhanced at the resonance due to the standing wave pattern inside the crystal. Thus the L_B and l_{mfp} are expected to be similar in the polymer opal. According to Fig. 6.21, right panel, a resonant photon (green arrow) might undergo a scattering event *within* the corresponding Bragg attenuation length. On the other hand, it is also possible for a non-resonant photon (orange arrow) to scatter into a resonant direction and still escape the structure. Furthermore, the absorption lengths of Fig. 6.20 are much greater than the scattering paths so reabsorption is not likely to happen. Scattered photons are thus likely to escape the structure, and the details of the scattering mechanism depend on the density of states inside the polymer opal as well scatterer size. It is reasonable to speculate that the enhanced optical density of states (DOS) inside the photonic crystal resonantly enhances and redirects the scattering for particular wavelengths, as is depicted in Fig. 6.21, left panel, as the enhanced size of the scatterers. This analysis highlights the major differences in the opal scattering that stem from the difference in the RICs. In the following section more insight to the polymer

[4]Note that the different colours in the photon angles in Fig. 6.21 correspond *solely* to the different resonance direction and not to the photon energy. E.g. in the scattering event of the left panel the photon energy is unaltered, only the direction changes from non-resonant to resonant.

opal scattering is given also comparing it to the different mechanisms proposed in the literature.

6.4.1 Polymer Opal Chromatic Scattering vs. Existing Theories

The polymer opal scattering is a very complicated process and only the general principle can be understood via the discussion given in the previous section. As was mentioned this process is highly sensitive to the size and location of the scatterers in the interstitial sites. Hermann et al. [120] have investigated the spontaneous emission rates of an emitter placed inside an inverted photonic crystal with an RIC of $\frac{\Delta n}{n_{eff}} = 1.6$ thus addressing the local density of states (LDOS). They find strong position and polarization dependence of spontaneous emission within the unit cell. While the contrast is much higher than in our system and thus not directly applicable, these results underline the fact that the scattering is dependent on the position of the scatterer within the crystal. They predict enhancement effects at interfaces between the high-index and the low-index material.

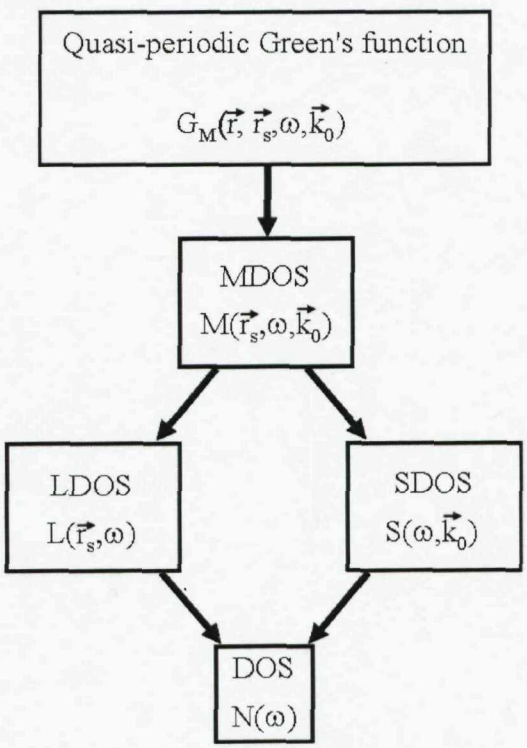

FIGURE 6.22: A flow chart describing the theoretical approach of calculating the mutual, local, spectral and total density of states (MDOS, LDOS, SDOS, DOS, respectively) starting from the quasi-periodic Green's function G_M, after [121].

It is also very important to point out that while the conventional DOS calculations [122, 123, 124] integrate over 3D angles (as needed to calculate the radiative lifetime of an embedded emitter), the resonant scattering here is explicitly angle-dependent. Thus a different measure is required and McPhedran et al. [121] have introduced the Mutual

Density of States (MDOS) to further describe the density of states in more detail. The MDOS is a generalized function that can be used to calculate the LDOS and the spectral density of states (SDOS) which gives angular information on the density of states. The core ideas of their paper are presented in a flow chart of Fig. 6.22. The different densities of state in real space ($\vec{r}$) are discussed in terms of the source location $\vec{r}_s$, photon frequency ω, and wavevector $\vec{k}_0$. They start with the quasi-periodic Green's function $G_M(\vec{r}, \vec{r}_s, \omega, \vec{k}_0)$ whose imaginary part yields the MDOS $M(\vec{r}_s, \omega, \vec{k}_0)$ through correct normalization. The MDOS can then in turn be integrated over the Brillouin zone yielding the LDOS $L(\vec{r}_s, \omega)$. Moreover, the weighted integral of MDOS over the Wigner-Seitz cell gives the SDOS $S(\omega, \vec{k}_0)$. From both the LDOS and SDOS it is possible then to calculate the density of states (DOS) $N(\omega)$ through integrating over the Wigner-Seitz cell or the Brillouin zone, respectively. The DOS is a function of frequency only and thus too simplified an approach to deal with the polymer opal scattering in which the scattering cross-section of defects inside such a low-contrast structure becomes large and anisotropic due to coupling with standing waves produced by multiple reflection. The purpose of this very general review is to highlight a possible route for theoretical scattering models in future projects through the use of the MDOS approach. The fact is that no full theoretical model exists for the scattering, which usually is treated merely as a flaw in the photonic crystal system rather than an interesting feature. In these polymer opals the nanoparticle influenced scattering has to be derived from the angle-dependent local density of states. Currently no theoretical models incorporate 3D scattering and absorption within a photonic crystal environment. Based on discussions with photonic crystal theorists [125] the problematic issue especially with polymer opals doped with absorbing nanoparticles is the break-down of the conventional Green's function approach due to the absorption and this is where the major opposition to the qualitative model presented for the polymer opal scattering arises. However, the straightforward transfer matrix approach (e.g. the one used in this thesis previously) still gives reflection stopbands in the presence of absorption. The dissipation in the photonic crystal and the thereby emerging apparent pitfall of the traditional Green's function approach has actually been dealt with successfully in the literature [126, 127] and leads to a "smoothing" effect where the DOS becomes finite in the bandgap. Absorption is traditionally viewed as very detrimental and unwanted feature in the photonic band gap materials because of its dissipating effect. However, in this work we have shown that it has very interesting features in the framework of polymer opals and thus theoretical models should be adjusted accordingly (like in [126, 127]) to allow the inclusion of absorption.

Naturally, there exists a quite extensive range of research into self-assembled systems (mainly opals) and their optical characteristics. In the following some recent results for opal scattering found in the literature are discussed and also compared to the hypothesis about the polymer opal scattering.

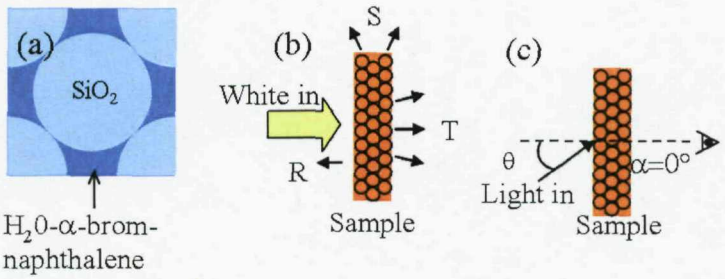

FIGURE 6.23: (a) Tuning the RIC by infiltrating the SiO_2 opal with water α-bromnaphthalene solution. (b-c) Romanov et al. geometry for side scattering and for forward scattering, respectively [100, 101, 31].

In the synthetic opal pioneering works [83, 59, 113] Vlasov et al. investigated the photonic depletion of the density of states using different RICs, but also the effect of defects in the band structure and light localization. In the case of SiO_2 sedimented opals having interstitial pores filled with water solutions of α-bromnaphthalene of varying concentration (enabling the tuning of the RIC, see Fig. 6.23 (a)) they measure the Bragg attenuation length L_B-dependence on the contrast to range from 310 μm ($\Delta n/n_{eff} = 0.007$) to 35μm ($\Delta n/n_{eff} = 0.07$). The latter contrast is close to ours but the L_B shows quite a large difference to the value of 6μm obtained through the simulations. This relatively high value of $L_B = 35\mu m$ does support our hypothesis of the scattering happening resonantly inside the periodic environment and it could well be possible that the quasi 3D -approach of the L_B simulation described previously yields too low values. It is also interesting that in all cases of the RIC the authors witness sharp *reflection* peaks even when they have restricted their collection width to about 0.5°, which is of course completely the opposite of our findings in reflection mode. Furthermore, when investigating the influence of defects in SiO_2 opals Vlasov et al. report on wide angular chromatic scattering in front of the sample which is similar to our findings. Their reasoning is that this colour cone is produced by the incoming highly collimated beam being first diffused by disorder and then this diffuse light scattering back anisotropically according to Bragg diffraction law (5.4). They do not pursue this feature and its origin further. While their measured scattering is similar to ours it is not likely the explanation for our results. This can be readily verified by comparing the angular dependence of the polymer opal scattering traces in Fig. 6.11 with the Bragg scattering dependence in the same figure. They furthermore find that smoothening and broadening of the photonic band gap is due to intrinsic disorder (also argued by Kaliteevski et al. [87] for 2-D) introduced in terms of the precursor sphere diameter polydispersity. Their experimental results when compared with a statistical model introducing deviations to photonic crystal (111) plane stacking lead to a disorder factor of around 30% which they then argue to be stemming not only from precursor spheres but also from stacking etc. faults. This disorder can lead to different levels of light localization in the opal and while a very important finding it has no direct consequence to be drawn for the polymer opal scattering.

As was already mentioned previously (cf. Section 6.3.2 Fig. 6.11) Astratov et. al [75] reported on the chromatic angular scattering from opals which does not seem to fit our findings. Romanov et al. [100, 101, 31] report on the side-scattering of silica opals in the 90°-geometry of Fig. 6.23 (b). They observe a scattering (S) dip at the reflection (R) peak wavelength which they attribute to the Bragg attenuation of the incident wavelength. More interestingly they identify two different scattering mechanisms in transmission (T) mode differing in the interaction range. The long-range scattering mechanism is brought about by the long range lattice periodicity fluctuations whereas the short range resonance scattering has its origin in the wavelength-size defects like missing balls or interstitials. They argue that this mechanism gives rise to strong backscattering but do not pursue this finding further. Furthermore the authors report on the diffraction behaviour of the mixing of the Bragg modes from [111] and [200] lattice directions. They have also studied the "forward-scattering" i.e. scattering of the transmitted light in different directions behind the opal sample, cf. Fig. 6.23 (c). They interpret their results of two different transmission profiles corresponding to individual transmission traces in the directions of α and θ due to the incident light being diffused by multiple scattering events. Furthermore the radial distribution of the forward-scattered light is interpreted through Kossel lines. While these results are very relevant to ours one of their conclusions is that no sufficient theoretical models exist to understand the scattering events in an opal.

In the studies of Baryshev et al. [73, 114] the authors present detailed work on the growth-disorder induced optical characteristics of opal-based photonic crystals. They formulate a theory to treat the diffraction from close-packed (111) planes in a twinned fcc lattice and verify it by experiment. In their experiment they are probing the twinned (111)-planes by light beams propagating in the direction perpendicular to the [111] direction (i.e. in the (111) plane) and find that through angular evolution of the scattering patterns when the sample is rotated around the growth (i.e. [111]) direction it is possible to distinguish between a perfect, twinned and completely disordered fcc -lattices. Their work highlights the method of probing the twinned structures and provides the theory to support it, but it does not provide with insight into the opal scattering in the experimental geometries of this work.

Gajiev et al. [128] have studied the effect of GaP infiltration into SiO_2 opals and effects of deformation of the crystal. This type of deformation may happen during the sintering of the crystal and has been observed before [129]. While reporting on the band-mixing characteristic of high RIC photonic crystal structures [30] their findings do not alleviate the lack of thorough opal scattering theory. Gajiev et al. also formulate a model to treat photonic crystals with deformed spheres. Strain dependent properties have been studied in this thesis although restricted only to the strain-induced inter-planar changes. Deformation is thought to be of a lesser issue with polymer opals due to the crosslinking and thereby the rigid nature of the PS-PMMA spheres [49].

The effect of disorder in colloidal crystals is systematically studied by Rengarajan et al. [84] through the use of the pair-correlation function (PCF). The PCF can be numerically calculated from e.g. an SEM image of the sphere locations and it is a two-dimensional mapping of the distances between the centers of pairs of colloids. By comparing results obtained from colloids with different sphere polydispersity values δ they are able to extract an offset value for δ beyond which the crystal properties start to deteriorate. They argue this value to be $\delta_{\text{offset}} = 6\%$ similar to Vlasov et al. [113] and the primary effect to be the increase of broadband diffuse scattering. Although the expected polydispersity values for the polymer spheres we use are below or at this offset [61] it is very probable that the chromatic scattering exhibited by the polymer opals has effects from the polydispersity-induced diffusion. However, the scattering characteristics are not further discussed in by Rengarajan et al.

6.4.2 Kossel Lines

Since many of the above mentioned reference mention Kossel lines in their analysis this phenomenon is briefly described here. Treatments of this topic can be found in [41, 130, 131]. When a photonic crystal is illuminated by a monochromatic laser beam dark rings and arcs superimposed on a diffuse background can be produced in the back (reflected) or front (transmitted) direction. This generation of Kossel line patterns requires that the original beam is strongly scattered inside the sample and light can be essentially represented as a point source *within* the crystal. The patterns are generated by the Bragg condition being fulfilled at angular cones (cf. (5.4)) forming attenuated bands and thus dark rings and/or arcs. This mechanism is depicted in Fig. 6.24 (a). They key fact is that the incoming beam of light is scattered inside the crystal due to defects or additional scatterers. In Fig. 6.24 (b) there are some simulated angular space Kossel lines at lattice directions ΓL (above) and ΓK (below) for different wavelengths [41]. It is clearly seen that the conical pattern dimensions depend on the wavelength. This can be understood quite clearly for the ring shaped Kossel line for (111) planes by considering the Bragg condition (5.4). In Fig. 6.24 (c) measured colloidal crystal Kossel lines for (111) planes are depicted [130].

Asher et al. have further used the Kossel line technique for identifying twinned crystal structures in colloidal crystals [131]. It is very interesting to examine the measured and simulated Kossel lines of Fig. 6.25 above and below, respectively. The measured pattern shows 6-fold the surface diffraction pattern as the bright spots but also the parabolic dark Kossel lines superimposed on the diffuse background. The wavelength ($\lambda = 488$nm) would suggest the origin of these lines to be from (220) family of planes and the authors conclude the twinning structure on the basis of the actual observed 6-fold symmetry. This is seen as the parabolic traces in Fig. 6.25 (b) where three lines expected from a perfect *fcc* -lattice are labeled as (220), (202), and (022) result in a three-fold symmetric

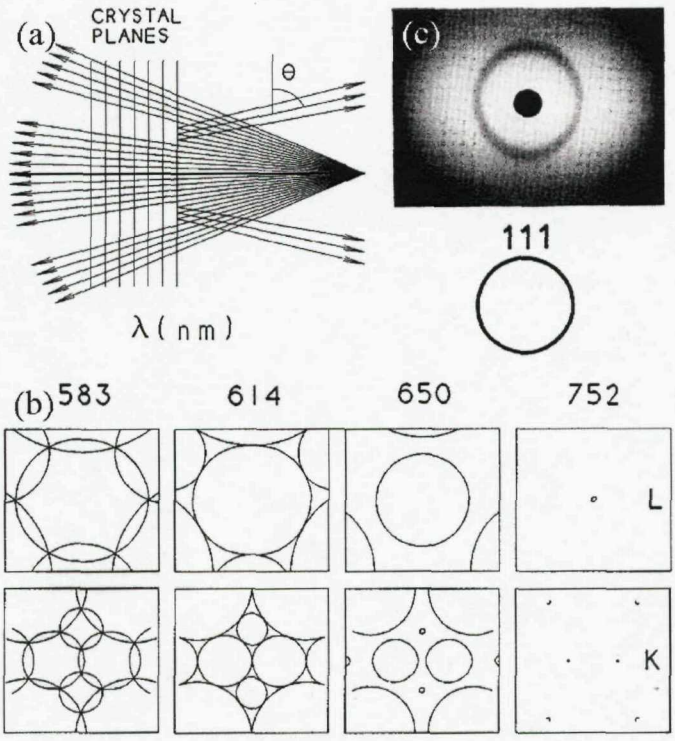

FIGURE 6.24: (a) Schematic description of the origin of Kossel lines. Diverging monochromatic light rays from a source (diffused incoming beam) fulfill the Bragg condition at a certain divergence angle θ and thus a dark circle is observed in forward direction [41]. (b) Simulated Kossel lines for two lattice directions, ΓL above, and ΓK below, for 4 different wavelengths [41]. (c) Observed (above) and calculated Kossel lines from (111) planes [130].

pattern. This pattern is then rotated through 60° to yield the similar pattern from the twin structure. Together these patterns agree very well with the observed Kossel lines of Fig. 6.25 (a).

The Kossel line analysis is very interesting with reference to polymer opal characterization and scattering for several reasons. Firstly, according to Asher et al. it offers a way of characterizing the samples especially in the case of twinning. For example, the possible twinning nature of a polymer opal with its (111) resonance at 700nm could be probed with a laser line below 600nm for the (200) plane family. In order to look at the (220) family planes a laser line below 430nm is needed and polymer absorption might be problematic at this wavelength range [74]. Diffraction from plane families like (210) and (211) is not observed due to zero structure factor at least for perfect crystals [28]. Nevertheless, it could be a powerful characterization tool for IR-polymer opals, especially when they are manufactured through extrusion, which is expected to yield a more cubicly symmetric lattice than compression manufacturing. Another reason why Kossel line analysis is interesting relates to the basic physical principles behind their formation. The Kossel line analysis could prove useful for understanding the scattering

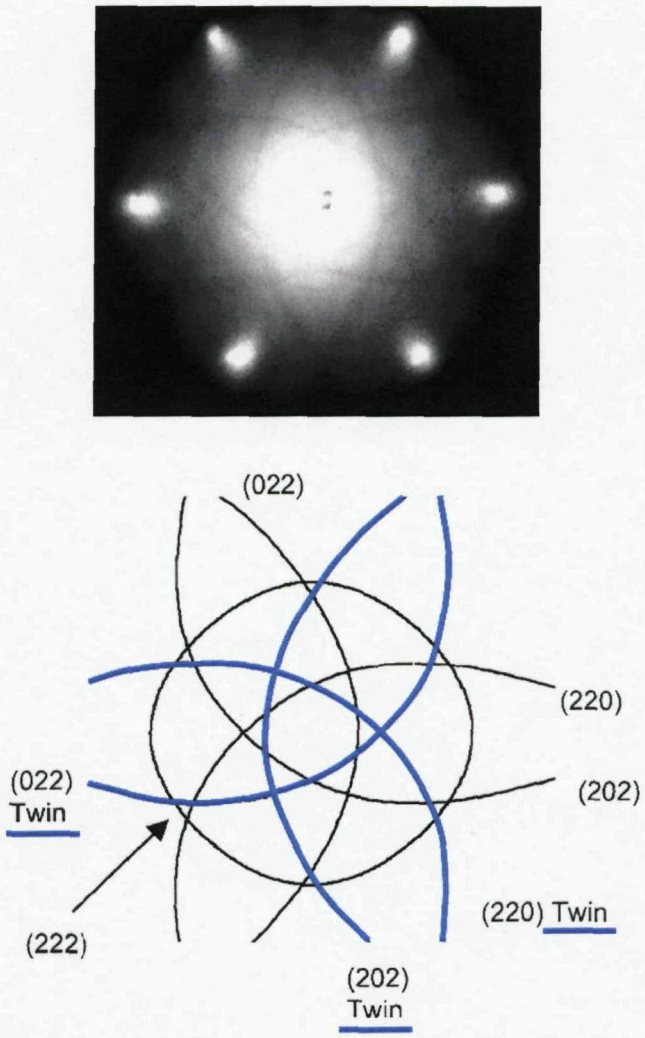

FIGURE 6.25: Measured (above) and simulated (below) Kossel lines resulting from monochromatic ($\lambda = 488$nm) illumination through the plane of the paper of a colloidal crystal with the nearest neighbour distance of 540nm, the lines from the twin structure are highlighted in blue.

and the diffusion process in the opal. After all the scattering hypothesis is based on the fact that on- and off-bandgap photons are more or less diffused by scattering, but the details of the scattering density of states are dictated by the periodic environment. This is after all the reason for the emanation of the Kossel lines when a collimated beam is incident on a photonic crystal. However, we note that in all our scattering experiments we have not observed Kossel line structures possibly due to disorder.

6.5 Chapter Summary

In this chapter the nanoparticle-influenced scattering from a polymer opal was presented and analysed. Angular chromatic scattering where on- and off-bandgap photons

are scattered into directions depending on their wavelength was discussed in detail. The effect of the introduction of nanoparticles was shown to be colour-appearance enhancing through the improvement of contrast and the decrease in viewing-angle dependence. Several proposed models and experimental results available in the literature were discussed and some were proven to be inapplicable whereas other models and results are vaguely related to the polymer opal scattering. It was pointed out that Kossel line analysis could prove useful in the future among other things for structural analysis of extruded samples. One of the most important results of this chapter is that clearly no models exist which treat the scattering inside a periodic environment quantitatively and allow for prediction of results for different nanoparticle doped opals. It is argued that the polymer opal structural colour features cannot be explained by simple Bragg interactions, nor can it be solely attributed to inter- or intra-layer disorder.

Chapter 7

Coherent Backscattering from Polymer Opals

Chapter 6 dealt with the structural colour features of the nanoparticle-doped polymer opals. The characteristic colour is related to the scattering behaviour very closely. A model was proposed where one of the key ingredients was the scattering mean free path (or scattering step) l_{mfp}, which is the characteristic (statistical) average path length between two consecutive scattering events in a material. Thus in order to understand and build the scattering model further, quantitative measures for the scattering path characterization are needed. The aim of this chapter is to introduce a technique called Coherent Backscattering (CBS) which provides the means for the measurement of the l_{mfp} and present results for doped polymer opals. First basic physical insights into the CBS mechanism are presented followed by the detailed description of the measurement setup. Finally results for the CBS measured with a single line laser as well as broadband source are presented.

7.1 Basic Principle of Coherent Backscattering

Coherent backscattering of light is self-interference effect where partial time-reversed (i.e. momentum-reversed) waves emerge from the scattering medium in the exact backscattering direction, i.e. the direction exactly opposite to the incident one. These waves interfere constructively and as a result a bright backscattering intensity distribution is produced and it is centered around the backscattering direction. The idea of the CBS of light is presented in Fig. 7.1 where the incoming photons are scattered into the opposite direction and collected by optical means. When the intensity is plotted against the backscattering angle a cusp-like cross-sectional distribution is found where due to constructive interference the intensity in the exact backscattered direction is two times the

background intensity [132, 133]. When moving away from the exact backscattering direction (i.e. with increasing θ) a phase difference between the the two counter-propagating components is developed and thus the intensity drops finally reaching an "incoherent" background level at large angles. This phenomenon was first demonstrated in optical experiments in [134, 135, 136] for latex spheres in aqueous suspensions. CBS is a representative of phenomena in the *weak localization* regime where $l_{mfp} \gg \lambda$ in contrast to the *strong (Anderson) localization* regime where $l_{mfp} \approx \lambda$ [137].

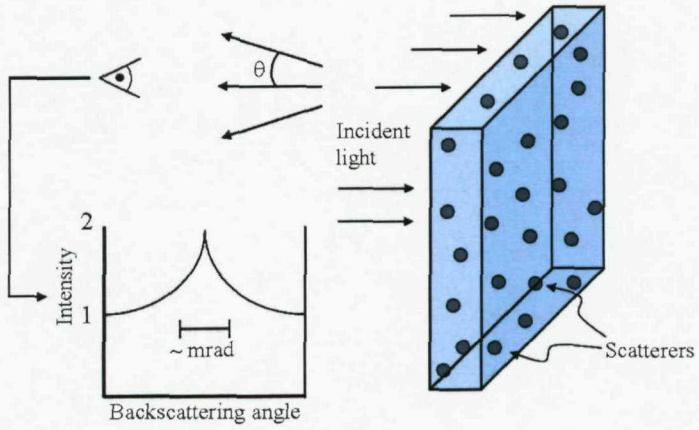

FIGURE 7.1: Schematic of the coherent back scattering phenomenon. Incident light is scattered into the incident direction and through self-interference forms a cone-like intensity distribution around the backscattering direction. The intensity maximum is ideally twice the background intensity and decreases with increasing θ. After Ref. [133].

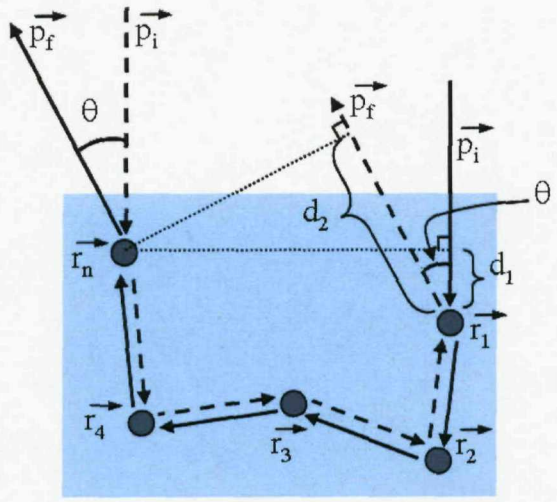

FIGURE 7.2: A prototype scattering path (solid line) and its time-reversed mate (dashed line). The incident photon direction is indicated by $\vec{p_i}$ and it is scattered into direction $\vec{p_f}$ making an angle θ with the incident direction. The intermediate scattering vectors related to scatterings from $\vec{r_1}$ to $\vec{r_n}$ are not labeled for clarity. The path difference between the two time-reversed scattering counterparts is $d_2 - d_1$ as explained in the text. After Ref. [133].

A schematic picture of the different time-reversed scattering paths and their contribution to the backscattered signal is given in Fig. 7.2. Consider the photon with the incident direction $\vec{p_i}$ entering the scattering structure with the scattering centers illustrated as dark circles. This photon may undergo scattering at locations $\vec{r_1}$, $\vec{r_2}$, $\vec{r_3}$, $\vec{r_4}$, and finally at $\vec{r_n}$ before escaping the material into direction $\vec{p_f}$ at an angle of θ. Now its time-reversed mate will undergo the scattering events in the reversed order and escape the structure after the final scattering at $\vec{r_n}$ into direction $\vec{p_f}$ at an angle θ. It is the interference of these two paths that generates the CBS signal and thus their mutual phase difference must be considered here. Their phase difference $\Delta\phi$ is:

$$\Delta\phi = \frac{2\pi}{\lambda}(d_2 - d_1), \tag{7.1}$$

where $d_2 - d_1$ is the geometric path difference of the time-reversed scattering paths[1]. Now d_1 is the projection of a vector that points from $\vec{r_1}$ to $\vec{r_n}$ (i.e. $\vec{r_n} - \vec{r_1}$) onto $-\vec{p_i}$ and d_2 similarly the projection of vector $\vec{r_n} - \vec{r_1}$ onto $\vec{p_f}$. In other words:

$$d_1 = -\vec{p_i} \cdot (\vec{r_n} - \vec{r_1}) \tag{7.2}$$

$$d_2 = \vec{p_f} \cdot (\vec{r_n} - \vec{r_1}), \tag{7.3}$$

and this way the phase difference of (7.1) can be determined as:

$$\Delta\phi = \frac{2\pi}{\lambda}(\vec{p_f} + \vec{p_i}) \cdot (\vec{r_n} - \vec{r_1}). \tag{7.4}$$

From (7.4) it is deduced that for the scattering into the exact back direction, $\vec{p_f} = -\vec{p_i}$, and the phase difference is zero resulting thus in completely constructive interference. This equation can be manipulated further to yield insight into the CBS process and the l_{mfp} vs. the intensity cone width. Setting $R = |\vec{r_n} - \vec{r_1}|$ and using trigonometric identities for obtaining $|\vec{p_f} + \vec{p_i}| = \frac{2\pi}{\lambda} 2\sin(\theta/2)$ we have:

$$\Delta\phi = \frac{2\pi}{\lambda} 2\sin(\theta/2) R\cos(\alpha) \approx \frac{2\pi}{\lambda}\theta R, \tag{7.5}$$

where the dot product of (7.4) has been evaluated and α is the angle between $\vec{p_f} + \vec{p_i}$ and $\vec{r_n} - \vec{r_1}$. Furthermore we have used the fact that θ is small (milliradians) and that we have a dense scatterer with the first and last scatterers being very close to the surface and thus $\vec{r_n} - \vec{r_1}$ is parallel to the surface and to vector $\vec{p_f} + \vec{p_i}$. Using the diffusion approximation we have for the mean square value $\langle R^2 \rangle = 6Dt$, where $D = \frac{cl^*}{3}$, is the

[1]The results only hold for scatterings beyond single scattering, i.e. $n > 1$.

photon diffusion coefficient, l^* is the transport mean free path (the relation to the l_{mfp} will be described later), c the speed of light, and t the time spent during the scattering (i.e the random walk time, cf. Appendix B and [138, 139]). Thus we have for the phase difference:

$$\Delta\phi = \frac{2\pi}{\lambda}\theta\sqrt{2l^*s}, \tag{7.6}$$

where $s = ct$, the total scattering path length. We define a critical angle θ_c for the coherent backscattering for which $\frac{\Delta\phi}{2\pi} \leq 1$, and thus (7.6) yields:

$$\theta_c \leq \frac{\lambda}{\sqrt{2l^*s}}. \tag{7.7}$$

From (7.7) it follows that the critical angle of CBS contribution decreases as the scattering path length s increases. The scattering cone is actually an envelope of different order-N scattering contributions with the higher order scattering (i.e. long scattering paths) contributing in the CBS cone in the very near backscattering direction [140]. This in turn means that any mechanism that extinguishes the long paths will affect the scattering cone top cusp shape by rounding it. These effects include absorption and finite sample size. The scattering cone consists of coherently added contributions of time-reversed path photons travelling different lengths in the scattering material. The idea of the different path length contributions is illustrated in Fig. 7.3. The left panel shows the theoretical CBS intensity around the backscattered direction. We see that the maximum intensity is 2 while the incoherent background intensity approaches 1. The intensity can be calculated by considering that the CBS electric field E is the coherent sum of scattered electric fields E_j [140]:

$$E = \sum_j E_j e^{i\phi_j}, \tag{7.8}$$

and thus the intensity I is defined by:

$$I = \sum_j {E_j}^2 + \sum_{j\neq k} E_j E_k e^{i\phi_j - i\phi_k} = \sum_j {E_j}^2 + \sum_{j\neq k} E_j E_k e^{i\Delta\phi}. \tag{7.9}$$

At its simplest we can treat (7.9) by setting the amplitudes E_j to 1 and using 7.5 for the phase difference yielding:

$$I = 1 + \cos(\frac{2\pi}{\lambda}\theta R), \tag{7.10}$$

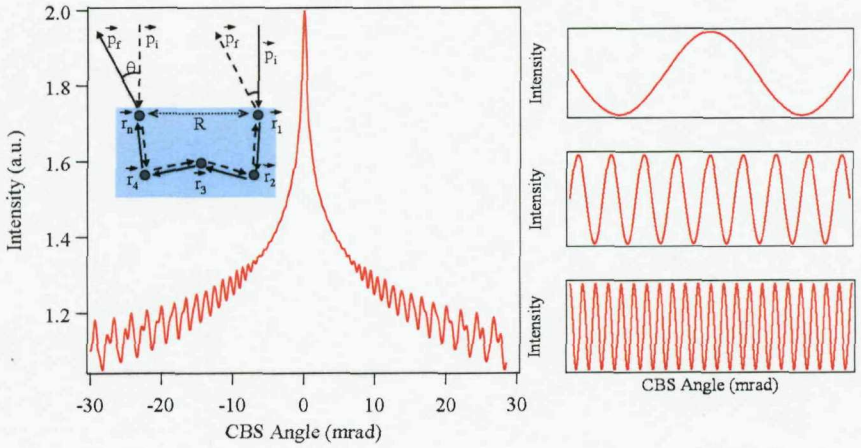

FIGURE 7.3: Total CBS signal (left) is a coherent envelope sum of different scattering contributions due to short (top left), intermediate (middle left) and long (bottom left) path length contributions. Inset at right: Reminder of the CBS mechanism.

where we have used the real part of (7.9) for the intensity and R refers to the first and last scatterer separation (cf. Fig. 7.3). On average the more scattering events give longer R and thus (7.10) can be used to model the contributions of different length paths, i.e. the number of scattering events. This has been done in the traces of Fig. 7.3, right, where the traces correspond to short ($\sim 10\mu$m, top), intermediate (middle), and long ($\sim 200\mu$m, bottom) scattering paths. The overall cone is achieved by an infinite sum of the different scattering path contributions and is given in Fig. 7.3, left. The termination of long scattering loops (e.g. absorption, or light leakage due to thin sample) would change the weighting in the sum (7.9) towards shorter loop contributions and this would result in the rounding of the top of the cusp because of the missing "sharp" or rapidly varying contribution of (7.10) [132].

Another interesting result can be derived from (7.7). The maximum critical cone angle corresponds to the smallest possible scattering path which is defined by two scattering events. In this case the photon enters the structure, scatters once, travels the distance s and is scattered out of the structure. We see that in this case $s = l^*$ and (7.7) becomes:

$$\theta_{max} \approx \frac{\lambda}{\sqrt{2}l^*}. \tag{7.11}$$

This is a very useful results since it directly relates the transport mean free path and the maximum CBS cone width. It also tells us that the shorter the mean free path the broader the angular cone width, so in other words scattery materials have wider CBS cones than less-scattery materials. The CBS cone FWHM $\Delta\theta_{CBS}$ is usually related to the transport mean free path for scalar waves by a similar expression [140, 141, 142]:

$$\Delta\theta_{CBS} \approx \frac{0.7\lambda}{2\pi l^*}. \tag{7.12}$$

Eq. 7.12 can then be used directly with the measured scattering cone width FWHM in translating them to distance units. Moreover, the CBS measurement can now be used as a direct characterization tool between doped and undoped polymer opals to see how the doping effects the scattering features. Finally, the CBS measurement yields an input parameter for the model framework proposed in Section 6.4.

7.1.1 Scattering and Transport Mean Free Paths

In the derivation of (7.11) a parameter called the transport mean free path was used. The transport mean free path l^* is defined as the length over which the information about the initial photon direction or momentum is completely lost [140, 143]. The scrambling of the initial direction is essential for the CBS interference phenomenon. The scattering mean free path, on the other hand, is the statistical mean distance between two consecutive scattering events in the material. The transport mean free path can be related to the scattering mean free path l_{mfp} through the mathematical expression given below:

$$l^* = \frac{l_{mfp}}{1 - \langle \cos \theta_{is} \rangle}, \tag{7.13}$$

where θ_{is} is the angle between the incident and scattered light and an ensemble average is taken over the cosine of this angle. This expression is a quite intuitive way of looking at the difference between the two paths given the written descriptions above. It follows directly from (7.13) that only in case of $\langle \cos \theta_{is} \rangle = 0$ the two length scales are the same. An example of this would be scattering with an isotropic spherical radiation pattern. However, the condition $l^* = l_{mfp}$ might be fulfilled also for anisotropic scattering, e.g. for dipole-like scattering patterns or Rayleigh scattering. The important fact here is that while the transport mean free path can be estimated from the CBS cone through (7.12) in order to determine the actual scattering path step l_{mfp} the scattering environment and the scatterer size needs to be carefully considered to determine the cosine of the average scattering angle θ_{is}. Their influence can then be estimated through (7.13).

7.1.2 Coherent Backscattering and Polarization

The theory outlined in Section 7.1 dealt with scalar waves and thus no polarization effects were taken into account. In reality the polarization has important effects on the detected CBS cone lineshapes. The addition of the vector nature of light into the consideration adds some complexity but also provides some means of background reduction when conducting the CBS measurements. The importance of polarization has been dealt with in Refs. [132, 136, 140, 144] and rigorous treatment on the scatterer shape-induced effects is given in [145, 146]. Here the background reduction technique

will be considered while other polarization-related features will be considered later on with CBS data analysis.

It is possible to record different polarization signals during the CBS measurement and the "correct" choice of the input and output channels enables one (at least for some scatterers) to exclude the singly-scattered portion of light from the detected light [140]. This singly-scattered portion contributes only to the incoherently scattered background level because of the absence of its reverse-path mate. With the use of a quarter-wave plate ($\lambda/4$) the single scattering contribution can be minimized. This is due to the fact that for circular polarization a single scattering event flips the polarization state. The method to exclude the singly-scattered (polarization-flipped) contribution is outlined in Fig. 7.4. The incoming light is first polarized vertically by the polarizer P. This polarization state is then converted to right-handed circular (RHC) by the $\lambda/4$ plate. The single scattering event is simulated by the mirror M reflection flipping the polarisation to left-handed circular (LHC), which is thereafter converted to horizontal polarization while traversing the $\lambda/4$ plate and thus rejected by the vertically oriented polariser P. Each polarization state is indicated by an arrow in the schematic. Also the incoming and reflected beams are shifted vertically for clarity. Single scattering events in Rayleigh regime (where the typical scattering size $d \ll \lambda$) act exactly as a mirror to the incoming spherical polarization [140] and thereby the incoherent single scattering background can be excluded by using this "optical diode" setup. If the single scattering contribution is included in the CBS signal the enhancement factor is reduced from 2 to lower values (cf. Fig. 7.1).

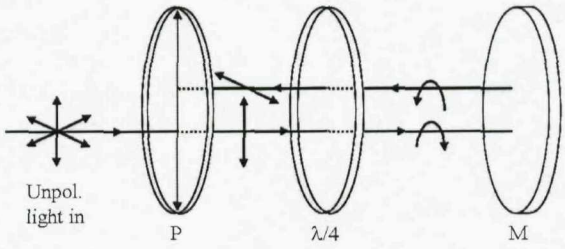

FIGURE 7.4: Setup to eliminate singly scattered contribution in the CBS signal. Incoming unpolarized light is vertically polarized by P and thereafter converted to right-handed circularly (RHC) polarized light by the $\lambda/4$ plate. At reflection (i.e. single scattering) from mirror M the RHC is flipped to left-handed circular (LHC) and this polarization state is thereafter converted to horizontal by the $\lambda/4$ plate and thus rejected by polarizer P. The states of polarization are indicated by arrows after each component. The incoming and reflected beams are shifted vertically for clarity.

The exact setup of Fig. 7.4 is used to align the polarisers with respect to the $\lambda/4$ plate in the CBS measurement setup presented later. By looking at the viewer's eye reflection through the polariser and the $\lambda/4$ plate one can rotate the $\lambda/4$ plate into such orientation that no light is reflected back through the system. At this mutual orientation the polariser and the $\lambda/4$ plate are correctly aligned.

7.1.3 Coherent Backscattering and Beam Quality

Another mechanism reducing the enhancement factor from 2 is the intensity imbalance between the two path-reversed partial waves. This mechanism is schematically illustrated in Fig. 7.5 [140]. CBS is a two-wave interference effect where the interference depends on the correlation of the fields at the first and last scatterers. Considering the Gaussian intensity profile in Fig. 7.5 a photon enters the material at the intensity maximum (upper red arrow) and undergoes scattering indicated by black arrows exiting the material at the location indicated by the lower red arrow. If the location of the entry and exit points of the photons is separated by more than the gaussian beam width w there is a significant intensity imbalance between the path-reversed photons leading to pronounced imbalance in the correlation of the two paths and thus lowering of the enhancement ratio from the theoretical maximum of 2. The incident beam needs to be carefully expanded and collimated (preferably ~4-6 -fold expansion) in order to minimize this intensity imbalance. This imbalance induced enhancement factor reduction is expected in materials with large l_{mfp}/w ratio.

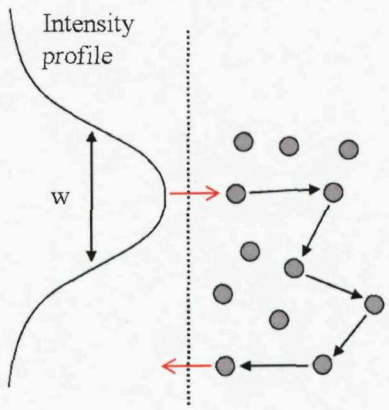

FIGURE 7.5: The effect of intensity imbalance on the CBS signal. The first photon (upper red arrow) undergoes scattering by the gray scatterers through the path marked with black arrows. At the exit point (lower red arrow) the Gaussian intensity is considerably lower creating an imbalance between these two interfering mates leading to the reduction of the enhancement factor. After [140].

7.2 Setup for Measuring the CBS Signal

The setup used for measuring the coherent backscattering is depicted in Fig. 7.6. Either a monochromatic source (Coherent Innova 90C Fred Ar-ion laser) or a supercontinuum source (Fianium SC450-4) can be used. The source beam is expanded 6-fold by a lens arrangement consisting of 50mm focal length focussing lens and a 300mm collimator lens. If the supercontinuum source is used the beam is additionally filtered first by a Schott KG5 colour glass filter cutting the IR contribution and then filtered into 8nm bandwidths

by a CRI Varispec liquid crystal filter. The additional filtering components related to the supercontinuum source are drawn in dashed boxes. The polarised output from either the Ar-ion laser or the Varispec filter is incident on a beamsplitter BS splitting the beam into two components. The reflected component is carefully dumped with a beam dump D and the transmitted part of the beam is retarded into RHC polarization by the quarter wave $\lambda/4$ plate before hitting the sample at an angle θ. The beam width can be controlled by the adjustable iris I. The backscattered contribution is again polarization retarded by the $\lambda/4$ plate and then reflected by BS towards a monochrome CCD camera (StarlightXpress SXV-H9). An achromatic doublet lens L (f=150mm) is used to focus the intensity contribution on the CCD. The lens is positioned on an X-Y-Z translation mount to enable accurate focussing. Before the camera there is a broadband polarizer P on a rotatable mount enabling the detection of the two orthogonally polarized components as was explained in Section 7.1.2. The multiply scattered CBS contribution is recorded by aligning the polariser P parallel to the original linear polarization leaving the Ar-ion laser or the liquid crystal filter. The singly-scattered (and thus polarization flipped from RHC to LHC) contribution is recorded by aligning the polariser perpendicularly to the original linear polarization.

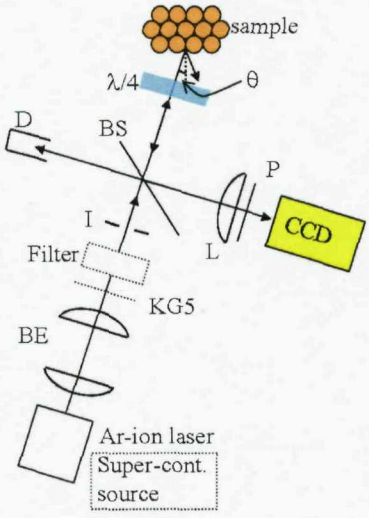

FIGURE 7.6: CBS measurement setup. Polarized light from the source (either Ar-ion laser or supercontinuum source) is expanded 6-fold before hitting the beamsplitter (BS). The reflected part of the beam is carefully dumped and the transmitted beam is converted into RHC polarization by the $\lambda/4$ plate and thereafter incident on the opal sample at the angle θ. The beam width can be controlled by the adjustable iris I. The backscattered contribution is again polarization flipped by the $\lambda/4$ plate and reflected (partially) towards the CCD camera. Lens L (f=150mm) on an X-Y-Z translation stage is used for focussing the scattered light onto the CCD surface. Before the lens there is a polarizer (P) on a rotation mount used for recording the singly or multiply scattered contributions differing in their polarization states. The path of the photons is indicated by arrows.

The CBS setup is very delicate to align. Due to the beam-splitting component, great care must be taken to dump the contributions that are not used thus minimizing the stray

light in the signal. For the reflected part of the incident beam, the light can be reflected from an ND filter at the Brewster angle into a beam dump. However, in this work better results were found using a black cloth as the beam dump. Secondly, the correct setting of the iris is important to minimize the $\lambda/4$ plate back surface stray reflection in the detected CBS signal. Finally, the $\lambda/4$ plate incident angle must be adjusted such that ghost reflections from its surfaces are not collected into the signal. Furthermore, the sample is mounted on a rapidly rotating fan to provide spatial ensemble averaging to reduce the speckle in the signal [140, 147].

7.3 CBS Using Single Line Source

In this section the results obtained using the setup of Fig. 7.6 with the Ar-ion laser source are considered. The measured samples were Mix1-Mix4 (cf. Table 3.4). The samples were mounted on the rotation fan at an incident angle of 30°. As the Ar-ion laser line of 514.5nm was used this means that the CBS response was measured off-resonance, i.e. below the Bragg resonance wavelength which for this incident angle would be about 570nm. Different polarization contributions were measured for the channels "vv" and "vh", where the "vv" means that the Ar-ion vertically polarized output is first converted to RHC and the multiply scattered (thus helicity/polarization preserving) signal is collected by aligning the polarizer P in Fig. 7.6 vertically. The channel "vh" corresponds to the polarization flipping channel and is recorded by aligning the polarizer P horizontally. Measurement results are given in Fig. 7.7. The panels from top to bottom correspond to the measurements made on Mix1 to Mix4, respectively. In each panel there are the inset images of the recorded intensities in the orthogonal polarization channels; left inset "vv", right inset "vh" channel. The bright spots superimposed on the gray background are the CBS intensity spots in each of the left inset images. The traces correspond to the horizontal cross-sections of the intensity distributions and they are plotted against the backscattering angle on the horizontal scale. Black (red) trace corresponds to the "vv" ("vh") channel in each panel. Each trace has been normalized to the background levels such that the comparison of the enhancement factors becomes straightforward.

The noise in the images in Fig. 7.7 seems to increase with the increasing C-black content making especially the measurements for Mix3 and Mix4 quite challenging to analyze. The reason for this increase in stray light noise is not entirely clear, but one reason is that due to increasing absorption with the increasing carbon black content and thus decreasing CBS signal levels the CCD integration time had to be increased and thus the amount of sample-independent ambient stray light has increased to worsen the signal. Another reason is that the increasing C-black content has increased the scattering cone width (as was explained in Chapter 6) and thus some of the scattering cone light is scattered to the backscattering direction thus possibly creating some of the noise in the

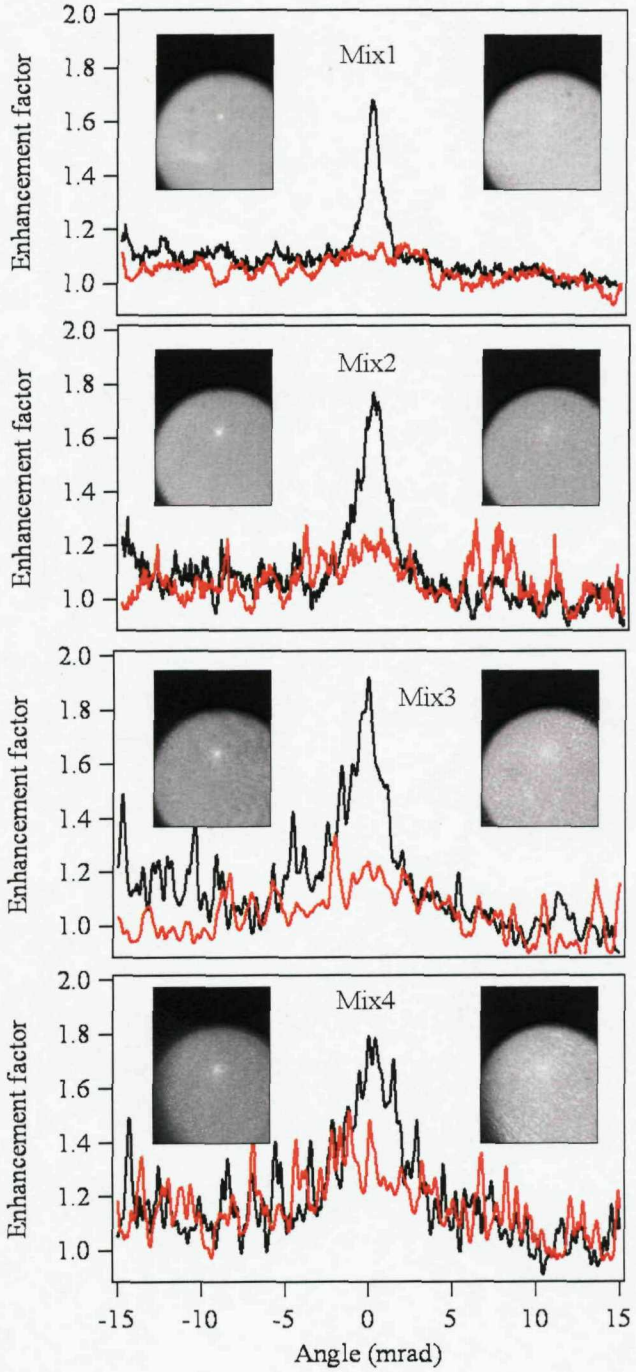

FIGURE 7.7: CBS results for samples Mix1-Mix4. The small bright dots superimposed on the gray background are the CBS intensity spots in the left inset (i.e. the "vv" channel) in each panel. Angular cross-sections of the CBS intensity cone were taken from the channel "vv" (left inset in each panel, black trace) and "vh" (right inset in each panel, red trace). The panels correspond to Mix1 to Mix4 from top to bottom. Ar-ion laser line λ=514.5nm was used.

images. However, the speckle-like appearance of the noise in the images of the Mix3-Mix4 panels would suggest that the major contribution is from the ghost reflections from the beam splitter or the $\lambda/4$ plate. This further illustrates the point that in the CBS measurement extreme care must be taken to minimize the effect of stray light.

Nevertheless, some conclusions can be drawn from the cross-sectional traces of Fig. 7.7. The enhancement factor E_{vv} seems to be around 1.7-1.8 for the "vv" channel and relatively unaffected by the inclusion of C-black absorber. In the case of Mix3 the apparent increase in the enhancement factor is attributed to a partially overlapping stray light speckle. Generally the peak shape seems to change from a cusp-like pointy cone to a more rounded non-cusped profile (although noise has obscured some of this behaviour) and this is understood by the absorption-terminated long scattering paths that only contribute to the very peak of the cone. Furthermore the "vv" channel peak increases in width with increasing C-black content. This is a direct proof of the increased scattering, because it means that the transport mean free path has decreased, cf. (7.12). This trend has been depicted previously in Fig. 6.20 where we have neglected the possible angular dependence of the l_{mfp} on l^* described in (7.13) and set $l_{mfp} = l^*$. This figure is re-presented in Fig. 7.8 together with the "vv" channel peak widths (FWHM). The FWHM is seen to double from 1.5mrad to about 3.2 mrad when the C-black content increases from 0 (Mix1) to 0.2 (Mix4) wt-%. This increase is accompanied by the decreasing l_{mfp} calculated with (7.12), when neglecting the angle effect of (7.13). The l_{mfp} decreases from about 27 to 12 μm with the increasing doping. This is a very significant result because it proves that by doping the opals we are directly affecting the scattering properties which is crucial to the structural colour formation ideas presented in Chapter 6.

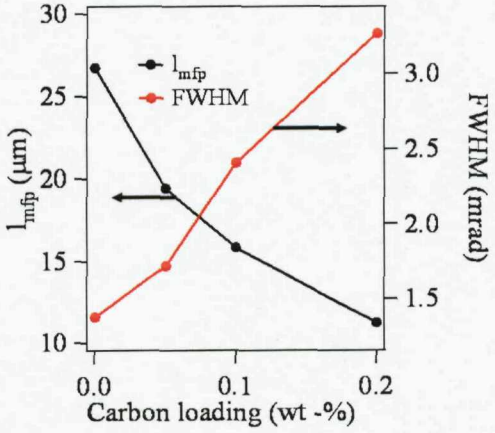

FIGURE 7.8: Scattering mean free path l_{mfp} (left axis) and CBS cone FWHM (right axis) plotted against the C-black loading. Measurements were conducted on the samples Mix1-Mix4 using Ar-ion laser ($\lambda = 514.5$nm) as the source in the setup of Fig. 7.6.

The fact that the enhancement factor is below 2 is partially attributed to experimental non-idealities such as the beam profile (cf. Section 7.1.3) and possibly to inadequate

experimental angular resolution. It should be pointed out that the decrease (increase) in the l_{mfp} (FWHM) does not give us any indication of the nature of the scatterer. The dopants could well be acting as scattering centers themselves and in this case the scattering could be described in Rayleigh regime, i.e. the $\langle \cos\theta_{is} \rangle$ is zero. On the other hand the dopants might introduce additional scattering through large scale lattice deformations (dislocated spheres, cracks) in which case the scattering should be treated in the Mie regime and thus angularly anisotropic. Strictly speaking without prior knowledge of the exact nature of the scattering regime a slight error is committed by ignoring the scattering angle effect of (7.13). This is done to enable the comparison between the mean free scattering paths, and should be treated as a first approximation of the scattering phenomenon.

The analysis of the "vh" channel cross-sections is more challenging due to noise in the signal in Fig. 7.7. From the red trace of the uppermost panel we see that the polarization-flipped channel has no CBS signal in the case of Mix1. However, it certainly seems that the inclusion of the dopants brings out slight peak in the "vh" channel. This is very difficult to distinguish because of the stray light but seems to apply for all of the doped samples Mix2-Mix4. This is a very interesting feature and it will be further discussed later on when considering the results also from the CBS measurements using the super-continuum source.

7.4 CBS Using Super-Continuum Source

A detailed set of measurements using the Fianium supercontinuum source on the setup of Fig. 7.6 were conducted on samples Mix1-Mix3. The advantage of using the continuum source is that with the help of the liquid crystal filter the incident photon wavelength (or more precisely the center wavelength of the 8nm bandwidth) can be controlled and tuned across the photonic crystal bandgap. In other words this technique enabled us first to compare the CBS characteristics on- and off-bandgap and furthermore directly compare the results between the differently doped samples Mix1-Mix3. Furthermore, the CBS measurements were repeated on a thick piece of paper simulating a white scatterer response.

All measurements were conducted on the setup of Fig. 7.6 with a slight modification in form of an additional half-wave plate ($\lambda/2$ plate) located directly after the iris I. With the $\lambda/2$ plate the incoming polarization could be changed between horizontal and vertical thus enabling us to investigate the difference of polarization flipping when the incoming beam is RHC or LHC polarized. We found no difference in the CBS behaviour and thus only the data for vertical polarization incident on the $\lambda/4$ plate is presented below. The incoming wavelengths were scanned from 500 to 670nm, i.e. over a wide range of wavelengths below, on and above the bandgap. The incident angle was $\theta = 30°$

shifting the (111) plane bandgap to 570nm. For each wavelength band the images were taken with two different polariser P orientations. First, the CCD was exposed with the polariser aligned parallel to the incoming polarization (i.e. polarization after the filter), and subsequently the orthogonal polarization channel was also recorded into a separate image through rotating the polarizer 90° and exposing the CCD again. Typical intensity images for the orthogonal polarization channels for Mix1 and paper at source wavelength of $\lambda = 500nm$ are presented in Fig. 7.9.

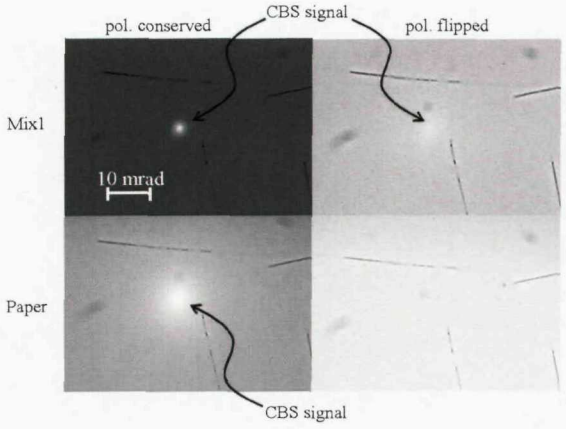

FIGURE 7.9: CBS intensity images from Mix1 (top) and paper (bottom) at wavelength $\lambda = 500nm$. The left (right) images correspond to the polarization conserving (flipping) channels. The CBS intensity dots are marked with arrows, dark lines on the images are CCD cover glass impurities.

In the CBS intensity images of Fig. 7.9 there are several interesting features that can be first pointed out from the images[2]. First of all in the polarization conserving channels we have the typical bright spots corresponding to the backscattered signal. Closer inspection shows that the distribution is wider for paper indicating a larger amount of scattering and thus shorter scattering mean free path. It is very interesting to point out that the polarization flipping channel has a peak in the case of Mix1 but for paper this peak is missing. Also there seems to be quite a big difference in the background levels between the preserving and flipping channels especially for Mix1.

Similar images as in Fig. 7.9 were taken at the wavelength range of 500-670nm for Mix1-Mix3 and paper with a step of 10nm. In order to build a set of normalized data the polarization crossing channel for paper at each wavelength was taken as a reference image, i.e. all other images were normalized with this image after having been normalized with corresponding exposure times. Horizontal cross-sections were then taken from each normalized image and this cross-sectional CBS cone data was analyzed further. The normalization procedure can be justified by considering the following intensities incident on the CCD camera when the CBS signal is measured with originally (after the filter in Fig. 7.6) vertically polarized light with sample Mix1 and paper:

[2]The dark stripes in the images are artificial impurities on the CCD cover glass.

$$
\begin{aligned}
I_{vv_1} &= R_v \sigma_{vv_1} T_v I_0, \quad \text{Mix1 "vv" channel} \\
I_{vh_w} &= R_h \sigma_{vh_w} T_v I_0, \quad \text{white paper "vh" channel,}
\end{aligned}
$$

where I_{vv_1} (I_{vh_w}) is the measured intensity for the polarization conserving (flipping) channel "vv" ("vh") for Mix1 (white paper), R_v (R_h) is the beamsplitter reflectivity for vertically (horizontally) polarized light, σ_{vv_1} (σ_{vh_w}) is the polarization conserving (flipping) scattering strength of Mix1 (white paper), T_v is the beamsplitter transmission for vertically polarized light, and I_0 is the input intensity at a particular wavelength. Now dividing the the two intensities yields parameter Q:

$$
Q_{vv_1} = \frac{R_v \sigma_{vv_1}}{R_h \sigma_{vh_w}}, \tag{7.14}
$$

and by calibrating this parameter with manufacturer-supplied and independently checked beamsplitter reflectivities for different polarization channels, a setup-independent parameter is extracted. This procedure is repeated for all samples and wavelengths in both polarization channels and thus the CBS cross-sections can be directly compared through the polarization calibrated parameter Q.

A typical CBS cross-section with relevant parameters used in the following analysis are identified in Fig. 7.10 for Mix1. The wavelength was 520nm and both polarization conserving and flipping channel CBS cross-sections are presented after normalizing them with the corresponding exposure times and the paper polarization flipping channel image for the same wavelength. Mix2 and Mix3 show similar features in their cross sections, and detailed analysis of the differences will be given later in the text. The different parameters identified are the background values: BG_{vh} and BG_{vv} for polarization flipping and conserving channels; Peak_{vh} and Peak_{vv} for the peak values; enhancement ratios E_{vh} and E_{vv} are defined as the ratio of the peak to the background for both channels. The background values are extracted as a mean of 50 pixels at angular distance of 20 mrad away from the CBS peak direction.

Before looking at the CBS data closer for the samples Mix1-Mix3 it is informative to consider the corresponding CBS data for the paper reference sample. This data is given in Fig. 7.11 for the polarization conserving channel and normalization is done by dividing the images by the exposure time and the polarization flipping channel image. The figure shows the normalized peak and background values for the polarization conserving channel ("vv") across the wavelength range and confirms that the paper response is fairly flat with the enhancement ratio (Peak/BG) around 1.68.

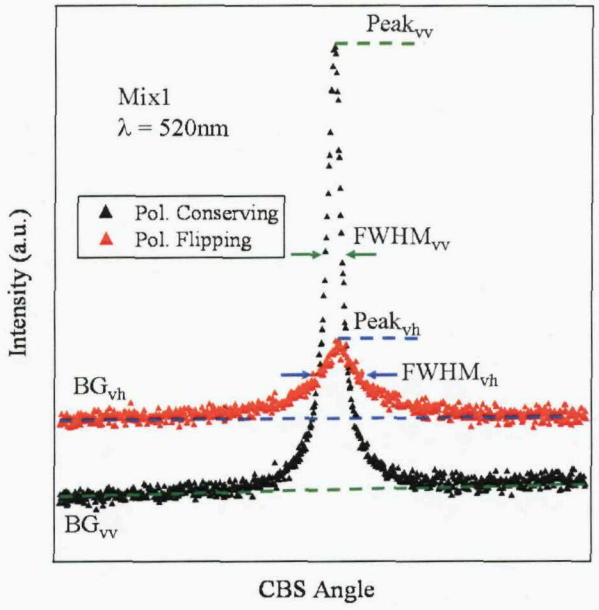

FIGURE 7.10: Typical CBS cross sections taken with sample Mix1 at $\lambda = 520nm$ for polarization conserving (black) and polarization flipping (red) channels. The images were first normalized with the relevant exposure times and then with the paper CBS image from the polarization flipping channel at the same wavelength. The relevant parameters for the future analysis are analysed in the figure: BG_{vh} and $Peak_{vh}$ are the background and peak values, respectively, for the polarization flipping channel. BG_{vv} and $Peak_{vv}$ are the corresponding values for the polarization preserving channel.

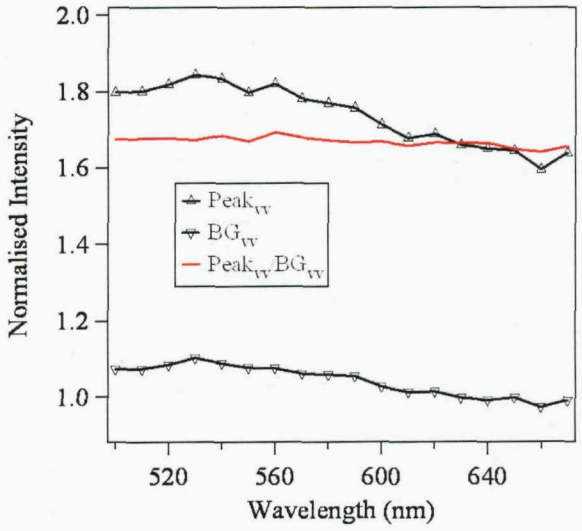

FIGURE 7.11: Normalized background and peak values (in black) for the polarization conserving ("vv") channel measured with paper. Also the enhancement ratio is shown to be constant around 1.68 (red trace).

7.4.1 Broadband CBS Results

CBS results for the samples Mix1-Mix3 (top to bottom) are presented in Fig. 7.13. In the figure normalized CBS cross-section peak values for both polarization channels together with the cross-section background values have been extracted from the CCD camera images. Furthermore the enhancement ratios E_{vv} and E_{vh} which are calculated as the ratio Peak/BG are given. First a quick comparison in the CBS cross-section lineshapes is given in Fig. 7.12.

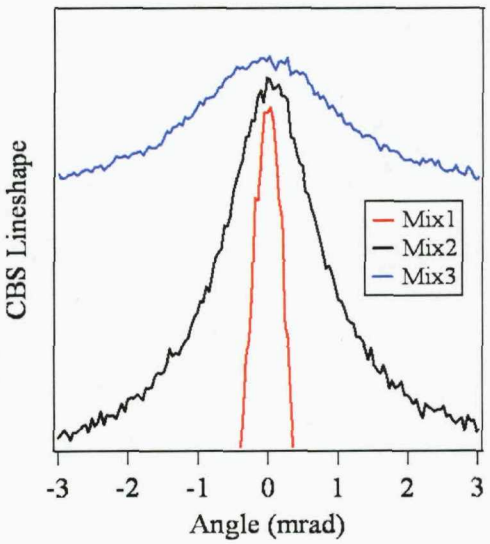

FIGURE 7.12: The top parts of the CBS cross-sections around the exact backscattering direction for Mix1 (red), Mix2 (black) and Mix3 (blue).

The effect of the increasing amount of absorbing C-black is clearly visible in the traces of Fig. 7.12. For Mix1 (undoped) the CBS cusp is very sharp indicating the presence of high-order scattering (cf. Fig. 7.3). The cusp is increasingly rounded due to C-black induced absorption in the case of Mix2 and Mix3, because the long scattering paths are more likely to be absorbed [140].

In Fig. 7.13 the cross-sectional CBS peak values are plotted in black for the "vv" (solid line) and "vh" (dashed line) channels. The CBS cross-section background values are plotted in red. The peak and background values intensity values can be read from the left axis while the enhancement ratios (in blue) are read from the right axis. Several very interesting features can be pointed out from the data of Fig. 7.13. One general feature is the overall intensity drop in each of the peak and background traces when moving from Mix1 to Mix3 which can be understood by considering the increasing absorption due to the increasing C-black doping from Mix1 to Mix3. A very interesting feature is that a CBS peak is observed also in the polarization flipping channel i.e. in the "vh" channel. This is a characteristic of the opal which was absent in case of the flat white paper scatterer. In other words the constructive CBS interference phenomenon is observed

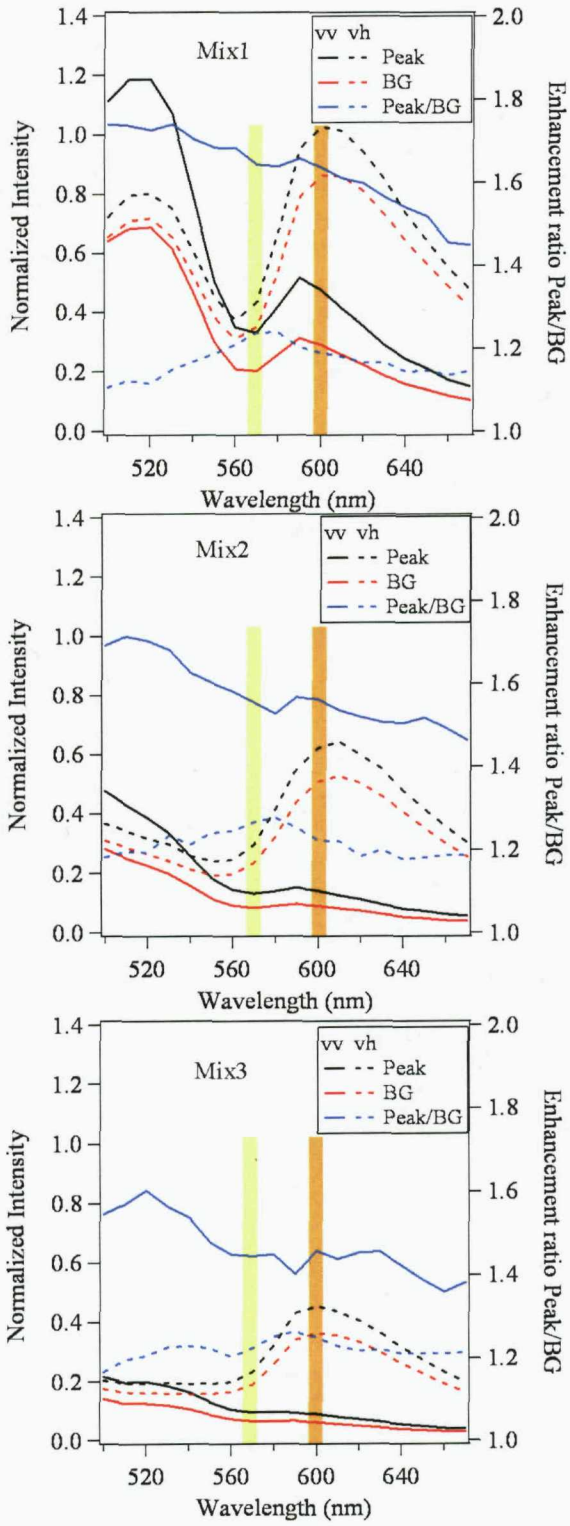

FIGURE 7.13: CBS cross-sectional peak (black, left axis) and background (red, left axis) intensities together with the enhancement factors E_{vv} and E_{vh} (blue, right axis) for samples Mix1-Mix3 (from top to bottom) at polarization channels "vv" (solid lines) and "vh" (dashed lines). Bandgaps for the 30° and 0° angle of incidence are highlighted in yellow and orange, respectively.

in both polarization channels. Furthermore, the peak values have *minima* close to the bandgap location of 570nm for this angle of incidence (highlighted in Fig. 7.13 in light yellow). This is the case for all samples although one major effect of the increasing C-black content especially in the "vv" channel is to smear out the features of these traces. Also unexpectedly the background values which correspond to the CBS cross-sections at wide angles are minimized at the bandgap location. Moreover, the background seems to be maximized at the normal incidence (111) plane Bragg resonance wavelength which is around 600nm for these samples. This region is highlighted in Fig. 7.13 in orange. This indicates that the "incoherent" background scattering is most enhanced at the wavelength corresponding to the (111) plane perpendicular resonance.

7.4.2 Background and Peak Values - Enhancement Ratio

Various features of the enhancement ratios (right axes) can be highlighted in Fig. 7.13. First of all, the enhancement ratios decrease as a function of the CBS wavelength in the "vv" channel starting from around E_{vv}=1.75 at λ=500nm and ending at E_{vv}=1.45 at λ=670nm with sample Mix1. Samples Mix2 and Mix3 show similar features with the declines from E_{vv}=1.7 to E_{vv}=1.45 and from E_{vv}=1.6 to E_{vv}=1.35, respectively. In the orthogonal "vh" polarization channel the behaviour is considerably different. The enhancement ratio has its maximum of E_{vh}=1.25 for both Mix1 and Mix2 at approximately 10nm above the bandgap at λ=580nm. For Mix3 the maximum seems to have been pushed to even higher wavelengths, the maximum E_{vh}=1.2 is reached at λ=590nm.

The background and the peak level evolution with wavelength is very puzzling. One way to look at the peak intensity profile is that it is a monotonically decreasing function with increasing wavelength with an additional minimum at the bandgap location. This relatively wide minimum can tentatively be related to the very scattering nature of these opals; the tendency of these opals to scatter resonantly near the band gap into wide angular cone around the resonant direction (as was described in Chapter 6) removes the intensity from the backscattering cone and results in a minimum when compared to the other non-resonant wavelengths. For the same reason also the background intensities are minimized. The background maximum at the normal incidence bandgap wavelength for all the samples and both polarization channels also requires attention. This contribution corresponds to multiply scattered light into wide angles where the interference is washed away by the rapid phase modulation of multiple path contributions. It is not entirely clear why this contribution should be maximized at the normal incidence band gap wavelength for each opal. This possible relation of this background maximum wavelength to the incident angle and normal incidence wavelength should be studied further in future measurements taken on different angles of incidence.

Comparison of the polymer opal to the existing theories in the literature provides no immediate explanation for the features of the enhancement factor. The polarization

conserving channel enhancement ratio E_{vv} changes have been studied by Dlugach et al. [145]. They have theoretically examined the dependence of the helicity preserving channel enhancement ratio on scatterer sphericity, absorption and size. The authors define an effective size parameter $x_{eff} = \frac{2\pi r_{eff}}{\lambda}$, where r_{eff} is the scatterer radius, and also a parameter ϵ which is a ratio of a spheroid scatterer long axis to short axis. When $\epsilon = 1$ (i.e. spherical scatterer) $E_{vv} = 2$ and independent of x_{eff} i.e. independent on the CBS wavelength. This is also confirmed by Labeyrie et al. [140]. They find that increasing non-sphericity results in the decrease of E_{vv}, but this does not explain the wavelength dependence. The drop in the enhancement factor with increasing wavelength cannot be explained by simply the normalised scatterer size x_{eff} since Dlugach et al. report the opposite effect, i.e. decreasing E_{vv} with increasing x_{eff} (i.e. decreasing λ). It should be noted that measurement setup resolution cannot explain the decreasing enhancement factor either. According to (7.12) the CBS cone becomes wider with increasing wavelength so system resolution cannot be limiting the signal throughput and thereby resulting in E_{vv} decrease. Thus the decreasing E_{vv} with increasing λ cannot be explained at this point. However, in their data there seems to be a general trend that absorption decreases the enhancement factor for non-spherical scatterers, which is also the case in the data of Fig. 7.13.

The fact that there is a peak in the CBS measurement in the polarization flipping channel ("vh") (cf. Fig. 7.7 and 7.10) is also very interesting. This is the channel where the RHC polarization of the incoming photon has been affected by the scattering and after passing through the $\lambda/4$ plate non-zero component in the horizontal polarizer direction exists. This could be due to birefringence effects in the scattering in the opal. The incident RHC polarization is converted to elliptic polarization by multiple scattering and the same thing happens for the path-reversed counterpart. These two elliptically polarized photons then interfere to create the peak also in the "hv" channel. This would mean that the effective scatterer shape distribution is dominantly non-spherical, so the RHC polarization could be converted to elliptic. Also in this mechanism the CBS enhancement factor in the "vv" channel would also be reduced from 2 to smaller values, which is also in unison with the findings of Dlugach et al. [145], who report strong decrease in the E_{vv} with increasing scatterer non-sphericity. Finally, the enhancement E_{hv} is relatively insensitive to the amount of doping which suggests that this type of polarization-flipping scattering is related to the inherent polymer structure rather than to the doping itself.

7.4.3 CBS Peak Widths

The CBS cross-section peak widths have also been analysed for the two orthogonal scattering channels "vv" and "vh". These widths yield direct information on the transport mean free path l^* (at least for "vv" channel) through the use of (7.12) and can be related

to the average scattering step l_{mfp} through (7.13). The FWHMs and the corresponding scattering steps are presented in Fig. 7.14 for samples Mix1-Mix3 as functions of the CBS center wavelength.

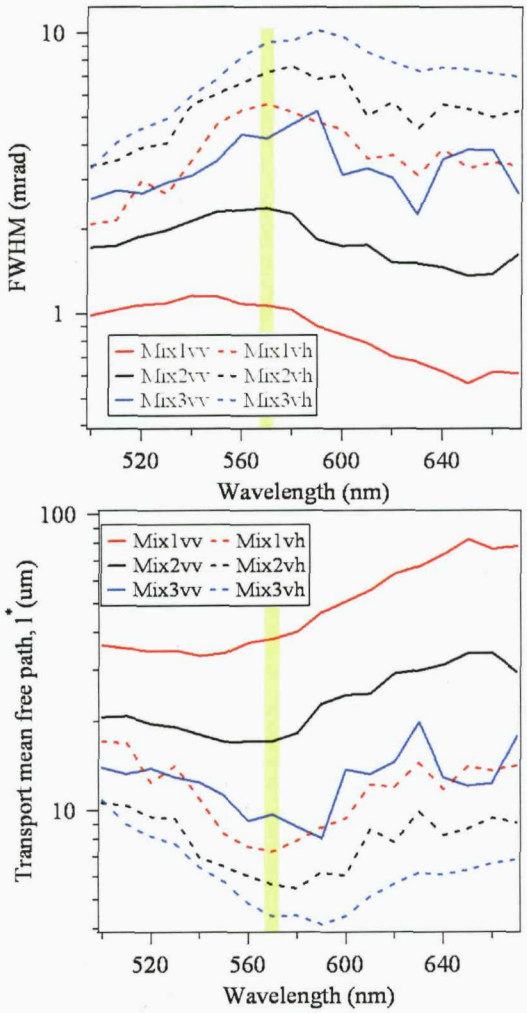

FIGURE 7.14: The FWHMs of the CBS cross-sections (top) and the calculated transport mean free paths (bottom) for samples Mix1-Mix3 for both polarization channels. Solid (dashed) lines "vv" ("vh") channel.

The top part if Fig. 7.14 depicts the FWHMs of the CBS horizontal cross-sections as a function of the center wavelengths measured with the supercontinuum source for samples Mix1-Mix3. Polarization conserving (flipping) channel "vv" ("vh") is represented by solid (dashed) lines. The bottom part of the figure illustrates the corresponding scattering mean free paths (l^*) obtained from the FWHMs. The effect of the C-black doping is to increase the FWHMs thus decreasing the l^*. Looking at the wavelength dependence especially the doped samples Mix2 and Mix3 show dependence of the l^* on wavelength. The maximum (minimum) of the FWHM (l^*) is found in the vicinity of the bandgap wavelength for the "vv" channel. The l^*s range from 35 to 80 μm (Mix1, no clear minimum), from 17 to 35 μm (Mix2, minimum 17 μm at 570nm), and from 8

to 20 μm Mix3, minimum 8 μm at 590nm). The clear effect of the doping is thus the decrease the transport mean free path. This is intuitively easy to understand, the more scatterers the shorter the scattering step. Furthermore the enhanced scattering in the bandgap region can qualitatively be understood by the increased scattering cross-section due to the standing wave pattern essential for the bandgap generation. The effect of the bandgap has been studied by Koenderink et al. [119]. They develop a model combining the effects Bragg scattering and photonic crystal band structure into the CBS calculation but fail to show any definite experimental data on the effect of the band gap on the transport mean free paths in case of PS opals.

Similar behaviour is observed in the orthogonal channel. In the "vh" channel the FWHMs are much larger than in the "vv" channel. The FWHMs increase by about 33% between the samples and again the maximum value is found in the vicinity of the bandgap or slightly above it. It is interesting that the scattering maximum (FWHM maximum) for the "vh" channel seems to be above the bandgap wavelength for Mix2 and Mix3. In the simple analysis of the electric field location around the bandgap (Section 5.5) it was shown that the electric field is in the PEA material when $\lambda < \lambda_{BG}$. The scattering dopants cannot enter the PS-PMMA spheres and reside in the surrounding material and thus more scattering would be expected when $\lambda < \lambda_{BG}$. However there exists another possibility to explain this behaviour. It is possible that the increasing scattering disturbs the lattice slightly dislocating the PS-PMMA spheres. Therefore in the wavelength regime just above the bandgap the scattering would increase because the electric field is concentrated on the slightly dislocated PS-PMMA spheres. The shifting of the minimum of the l^* towards higher wavelengths is especially strong between samples Mix2 and Mix3 at both channels "vv" and "vh" indicating that in fact the 0.1 wt% doping of Mix3 already disturbs the lattice ordering significantly.

7.4.4 Depolarization

Finally it is interesting to see the effect of the doping on the depolarization of the light in the CBS signal. This depolarization parameter is calculated as the ratio of the background signal in the "vv" to the "vh" channel an is depicted in Fig. 7.15. The bandgap location is highlighted in light yellow.

In multiple scattering the polarization of the incident wave is (at least partially) depolarized [140]. The wavelength dependence of this background "incoherent" depolarization is observed to have three regions in Fig. 7.15. First the ratio values start at a plateau level around 0.5 (Mix1) or 0.55 (Mix2, Mix3) from wavelengths 500nm to 540nm before increasing superlinearly between 540nm and 630nm to another plateau level of around 0.8 (Mix1) or 0.85 (Mix2, Mix3). The depolarization bandgap values are 0.65 (Mix1) and 0.75 (Mix2, Mix3). The introduction of doping increases depolarization but the increase in the doping levels seems to do little if anything to further strengthen the

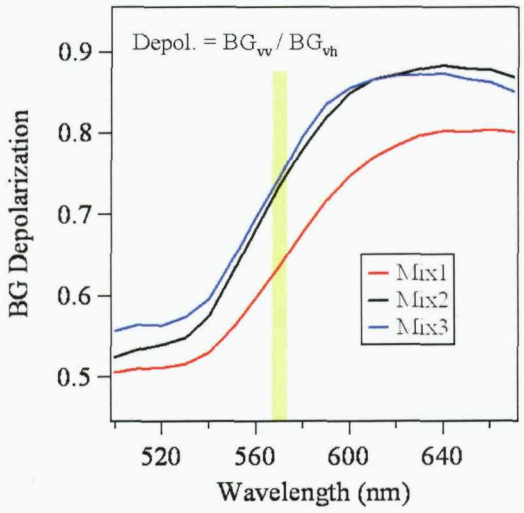

FIGURE 7.15: CBS depolarization calculated as the ratio of the background intensity of "vv" to "vh" channel for samples Mix1-Mix3. Bandgap location highlighted in light yellow.

phenomenon. Moreover, the depolarization is not complete at any wavelengths so a "polarization memory effect" exists throughout the wavelength range. This is contrary to the findings of Labeyrie et al. [140] who find that for a suspension of TiO_2 spheres the incoming light is completely depolarized even for very low optical thicknesses. Optical thickness is defined as the ratio of the samples thickness d to l^* and it is reasonable to assume in our case that the polymer opal samples are optically thick (d$\sim$500μm and $l^* \leq 80\mu$m). The non-complete depolarization could be due to the different material system used. The higher refractive-index TiO_2 is a stronger scatterer than a polymer [91], thus possibly enabling the complete depolarization. On the other hand, the CBS takes place *inside* the crystal and it is by no means clear that depolarization in constant and periodically modulating refractive index host material should yield similar depolarization results. Furthermore, the shape of the depolarization curves of Fig. 7.15 is not well understood. It is possible that the different depolarization values result from the scattering regimes (e.g. different Mie-resonances) when changing the wavelength in CBS.

7.5 Rayleigh or Mie Scattering?

It is a challenge to characterize the actual nature of the scattering process in the polymer opal. This can be done by considering the scattering cross-section of the scatterer. Scattering cross-section σ describes the tendency of particles to scatter light. It is a function of wavelength, refractive index and scatterer size and has the units of area. Basically two possible regimes can be distinguished in the opal scattering at hand, Rayleigh and

Mie scattering. In Rayleigh scattering the typical scatterer size is much smaller than the wavelength while Mie scattering is the prevailing mechanism when the scatterer size is close to or greater than the wavelength. Rayleigh scattering manifests itself in radiation patterns where forward and backward scattering are equal [78]. Furthermore in the Rayleigh regime the scattering and transport mean free paths would be equal, cf. (7.13) where the average cosine value equals zero. On the other hand Mie scattering is also possible. In this case the scattering cross-section is dependent on the scatterer size and the wavelength. Basically this stems from the fact that the scatterer experiences a non-constant electric field distribution due to its size and the wavelength being comparable and thus the scattered light distribution has non-symmetric distribution. Fig. 7.16 presents calculated normalized scattering cross-sections using different dielectric spherical scatterer sizes [78] in vacuum. The refractive index used in the calculations was 1.59. The sizes correspond roughly to 1/10 (blue trace), 1/1 (red trace), and 3/1 (black trace) ratios to the Mix1-Mix3 sphere sizes. Also presented is the scattering cross-section for a scatterer of diameter 1/10*ϕ (ϕ is the PS-PMMA sphere diameter) in the Rayleigh regime where the scattering cross-section is given by [91]:

$$\sigma_R = \frac{2\pi^5}{3}\frac{d^6}{\lambda^4}\left(\frac{n^2-1}{n^2+2}\right)^2 \tag{7.15}$$

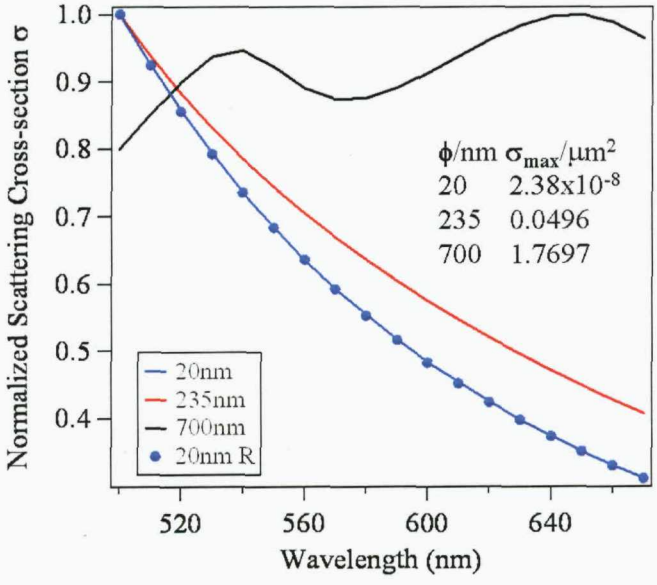

FIGURE 7.16: Mie scattering cross-sections as a function of wavelength for three different dielectric spherical scatterer diameters: 20nm (blue), 235nm (red), and 700nm (black). Also presented normalized Rayleigh scattering cross-section σ_R (blue solid circles), scatterer diameter = 20nm. Inset: maximum values used for normalization for each Mie scatterer.

We see in Fig. 7.16 that by decreasing the scatterer diameter we move from the Mie - regime characterized by an alternating cross-section towards the familiar Rayleigh regime

characterized by the $1/\lambda^4$ dependence. Finally at 20nm scatterer diameter the traces are equal indicating that the scatterer is small enough to be treated as a point scatterer. This data indicates that for example a missing sphere in the lattice would scatter light in a manner that decreases monotonically with wavelength. A line defect consisting of several spheres would have more complex scattering cross sections, as can be verified by observing the black trace in Fig. 7.16. The dopants could be acting as scattering centers themselves. As can be observed in Fig. 3.8 the mixing of the dopants is relatively homogeneous and larger clusters are not formed. Thus the induced scattering would then be most likely obey the characteristics outlined by the red or blue traces in Fig. 7.16, and scattering cross-section would be monotonically decreasing function of wavelength. Another possibility is that the dopants are disrupting the lattice order (although this is not observed in Fig. 3.8), creating larger scattering centers and thus the scattering should be treated in the Mie regime. At this point, it is very interesting to look at the background intensity data of Fig. 7.13 for Mix1-Mix3 and compare it with the typical Rayleigh $1/\lambda^4$ scattering dependence. This is done in Fig. 7.17.

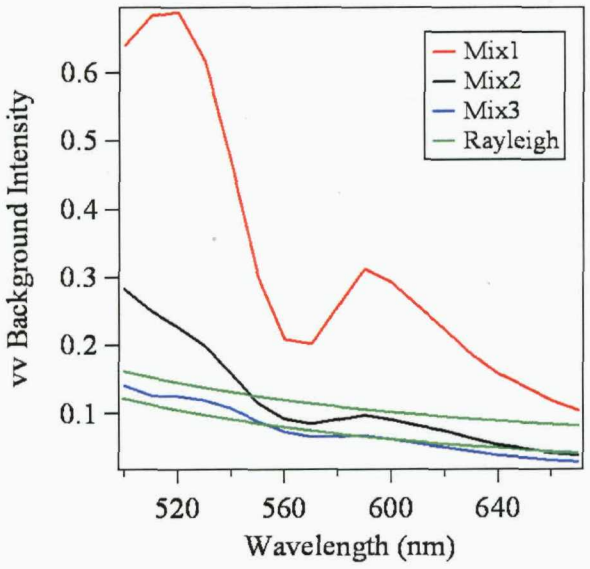

FIGURE 7.17: Background CBS intensities for Mix1 (black), Mix2 (red) and Mix3 (blue) together with the Rayleigh $1/\lambda^4$ scattering cross-section (two green lines). The green lines have been scaled to accommodate for the comparison between Mix2, Mix3 and Rayleigh.

We see that Rayleigh scattering describes the background CBS intensity best for the sample Mix3 although the agreement is by no means perfect. The fit (scaled Rayleigh line) fits even worse the background intensity of Mix2 and is in complete disagreement with Mix3 (the fit not shown). In other words by doping the sample the background scattering intensity is shifted from a more complicated scattering regime towards the Rayleigh regime. This in turn means that the nano-dopants act increasingly as scattering centers and for undoped samples (like Mix1) the scattering is much more complicated.

One explanation is that the dopant-induced Rayleigh scattering in heavily doped samples like Mix3 is overwhelmingly strong compared to the intrinsic scattering that is present in samples Mix1 and Mix2. It is very difficult to characterize the nature of scattering in samples Mix1 and Mix2. If we assume it to be Mie-like we can in turn discuss some consequences in terms of the actual scattering step or the scattering mean free path l_{mfp}. We use (7.13) to calculate the scattering mean free path l_{mfp} assuming a spherical scatterer with $n = 1.59$ and $\phi = 235nm$ (corresponding to Mix1-Mix3 sphere diameters) in vacuum. At λ =570nm we get $\langle \cos\theta_{is} \rangle = 0.382$. This in turn yields for the l_{mfp} by (7.13) and Fig. 7.16:

$$\begin{aligned} l_{mfp} &= 22\mu m \text{ Mix1} \\ l_{mfp} &= 10\mu m \text{ Mix2} \\ l_{mfp} &= 6\mu m \text{ Mix3.} \end{aligned}$$

The model for the polymer opal structural colour in Section 6.4 discussed the importance of the scattering mean free path length l_{mfp} in comparison to the Bragg length L_B. While L_B was calculated to be around 6μm the l_{mfp} is around 10μm by the above analysis. These two length scales are now comparable and the scattering is taking place *inside* the material even though we are at the bandgap wavelength. The scenario outlined in Fig. 6.21 is thus entirely possible and thus the proposal for the structural colour formation plausible.

The reality is, once again, more complicated than described above. For the Mie scattering calculations several assumptions were made. First of all the cross-sections were calculated in vacuum conditions whereas the real situation is more complicated due to the periodic photonic crystal environment where clearly the scattering is affected by the density of optical states which is different from vacuum. Nonetheless, the refractive index contrast is very low in the polymer opal and the vacuum calculation approach can thus be justified as a starting point for the modelling. Secondly, sphericity of the scatterers could be disputed. The enhancement ratio E_{vv} in the CBS measurements did not reach the theoretical maximum value of 2. This can be partially due to experimental error, but at least partially most likely due to non-spherical scatterers, for which the enhancement is less than 2 [145].

7.6 Chapter Summary

In this section the photon weak localization phenomenon called Coherent Backscattering and a novel technique to measure this was discussed. Techniques using both single line as well as broadband source were used revealing that the scattering and more precisely

the scattering mean free path can be controlled by doping of the opal. A very interesting characteristic of the appearance of a CBS peak in the helicity non-preserving channel in the polymer opal CBS signal was found, and while not completely understood it was tentatively attributed to birefringence. Moreover, the background scattering responsible for the CBS signal in the helicity preserving channel was found to change towards Rayleigh regime in the heavily doped opal. The precise nature of the scattering in the undoped or lightly doped opals is not clear but if Mie type scattering was assumed the conclusion that the polymer opal Bragg length and scattering mean free path are comparable was reached. This in turn would indicate that the scattering is a very important feature in the the structural colour formation in the low refractive index contrast polymer opal. Finally, although the theory of CBS for *disordered* material was outlined with care in the beginning of this chapter it is by no means obligatory that the CBS scattering from *ordered* polymer opals should obey the theory. Some features could be explained in terms of the existing theory but sufficient theories to describe coherent backscattering from ordered materials around the bandgap regime do not, to the best of my knowledge, exist.

Chapter 8

Conclusions and Future

This thesis has explored the world of the low refractive index contrast polymer opals using different optical spectroscopic techniques. The polymer opal is a very versatile material system with some characteristics that can be understood within the existing framework of photonic crystal theories. On the other hand some features presented in this thesis require a whole new theoretical approach combining the theory of periodic materials with scattering and absorption.

Chapter 2 presented the conventional approach to the theory of photonic crystals based on Maxwell's equations the underlying symmetry. It was discussed that due to symmetry it suffices to restrict the photon - lattice interaction considerations to the 1st Brillouin zone in the reciprocal lattice. Examples of photonic crystals in one, two and three dimensions were given and the photonic band gap formation was discussed in the 1D case. Band diagrams were also discussed relating them to the group velocity and the density of states, and finally topics related to the properties of the *fcc* -lattice were described.

8.1 Polymer Opal Fabrication

The manufacturing techniques of different types of opal based periodic material systems including sedimentation, vertical deposition, spin-coating and shearing of colloids were described in Chapter 3. Especially sedimentation and vertical sedimentation methods often yield opals with excellent short-range ordering but are plagued by cracks or multiple domains resulting in the deterioration of the long-range quality of the opal. Fabrication steps towards the further functionalization of the opals were described; these include among other things the inversion procedure of the opal yielding higher RIC photonic crystals or doping of the interstities by e.g. semiconductor materials. As a contrary method to the above mentioned fabrication sequences the uniaxial compression of polymer melts was introduced as a powerful manufacturing method yielding high quality thin

film photonic crystals. A polymerization reaction technique is first utilized producing very monodisperse core-interlayer-shell (PS-PMMA-PEA) polymer particles which self-assemble into a predominantly *fcc* -lattice with the hard PS-PMMA cores at the lattice sites and the PEA filling the interstitial sites. The planes parallel to the compression plates form the (111) planes of the resulting crystal. The refractive index contrast is very low (0.06), owing to the different polymers of the lattice. These opals can be doped with nanomaterials straightforwardly by introducing the nanoparticles into the polymer melt before the compression or by going through an additional mixing phase with an extruder. The opals studied in this thesis have been mostly doped with carbon black nanoparticles. Additionally, subsequent manufacturing steps can include PEA polymer cross-linking making the thin film opals flexible. The polymer opals can also be manufactured in extrusion mode enabling large-scale continuous manufacturing of photonic crystal films (cf. Fig. 1.4).

8.2 Ordering of the Polymer Opal

Structural order (mainly in 2D) was discussed in detail in Chapter 4. The key for achieving large-scale ordering in polymer opals is to create a suitable shearing profile in the melt through compression. Basically the opals studied in this thesis can be divided in three regions in the [111] direction based on the ordering properties. Roughly the top and bottom thirds are well-ordered regions and in between there is a disordered middle third region. These findings are mostly based on the extensive TEM studies conducted at the DKI, Darmstadt. In this thesis a straightforward measurement system was developed based on UV-laser diffraction from the polymer opal. Due to the opal absorption, the UV photons probe only the surface layer of the thin film opal and the surface properties can be calculated from the 2D surface diffraction patterns. The most important finding is that the lattice orientation in the compression-manufactured opals can be fully characterised by a radially oriented director vector, see Fig. 4.7. In other words these opals show deterministic ordering over tens of squared-centimeters! This radial ordering has to be accommodated by some point or line dislocations, which were not further analysed. Furthermore we analysed the full characteristics of the strain-induced polymer opal unit cell change by combining the surface diffraction measurement with the changes in the thickness direction analysed by measuring the (111) plane reflection resonance. These unit cell changes show significant anisotropy depending on the mutual orientation of the strain vector vs. the opal lattice director (cf. Fig. 4.12). The opal elastic limit is reached at relative strains around 10%, due to the strain being exlusively distributed in the PEA interstitial material.

8.3 Spectroscopic Characteristics

The remainder of the thesis was dedicated to the simulations and spectroscopic study of the low refractive index contrast polymer opals. Chapter 5 presented the results from 1D multilayer simulations of a PEA/PS polymer system with and without absorbing dopants. Basic reflectivity and transmission properties can be understood through this simplified model although the model does not take scattering into account which is the major shortcoming of this multilayer simulation approach. A theoretical expression for angle-dependent reflectivity based on the optical equivalent of the Laue condition was outlined resulting in the optical Bragg law. Its validity was verified by both multilayer simulations and experimental data from actual polymer opals. Spectroscopic analysis of the changes in the (111) plane spacing due to lateral strain was conducted. The results yield a Poisson ratio value of 0.39 for the hard-soft polymer opal composite that is surprisingly close to the bulk PS value of 0.34. Properties of different dopants were briefly introduced and the interaction between the bandgap and the dopant described. 1D multilayer simulation shows that the nanoparticle interacts with the band gap about 5 times stronger at the short wavelength side of the bandgap than on the long wavelength side. Furthermore, the effect of carbon black doping on the reflection and transmission properties of the opals was discussed, and the most significant finding was the dependence of the reflection/scattering contribution on the collection aperture. The results show that specular reflection is at its *minimum* at the bandgap whereas the wide angular scattering around the specular direction is maximised. A multilayer model was developed to explain the reflection minimum and the conclusion is that energy is removed from the reflection contribution into the wide scattering pattern at bandgap. This makes the complete understanding of the reflection transmission and scattering features very challenging; depending on the location with respect to the bandgap these characteristics have features stemming from both periodic structures and bulk-like material.

The structural colour features of the polymer opals were discussed in more detail in Chapter 6. These opals show interesting colour features when the PS-PMMA sphere diameter is in the range of 180-280nm. The major findings of this experimental research is that the colour can be tuned by the inclusion of nanoparticles. We experimented with C-black, and the results show that moderate dopings (0.05wt-%) enhance the appearance of the opals remarkably. The inclusion of the dopant prunes the non-resonant colours and thereby enhances the relative contrasts of the resonant colour. The resonant colour also is spread into wider viewing angles by the doping thus changing the perceived colour. Whereas the undoped samples have milkish appearance outside the bandgap viewing angle, the doped ones scatter the bandgap colour also to off-bandgap viewing angles. The angular features of this resonant colour scattering were studied in detail and these characteristics cannot be understood by any theoretical model in the existing literature. While it is clear that the foundation of the polymer opal structural colour lies in the scattering inside the photonic crystal it cannot be understood as a combination

of diffuse light and Bragg diffraction. These features relate to the scattering features *within* the interaction length of the photon and the opal at bandgap frequency. This length is called the Bragg length and its magnitude in comparison with the characteristic scattering mean free path need to be understood in order to build a theoretical model for the polymer opal scattering, see Fig. 6.21.

Coherent backscattering (CBS) measurements were conducted in order to characterise the scattering in the polymer opal further. CBS data of Chapter 7 shows indeed, that the scattering mean free path can be adjusted with the inclusion of dopants. This verifies the finding of the previous chapter that the colour can be tuned through doping-induced scattering. Wavelength dependent measurements were conducted to describe effects of the band gap on the scattering mean free path. While some of the features can be understood in the traditional CBS framework based on the theory for completely disordered structures others cannot be understood by these models. One of the most interesting findings was the appearance of the CBS peak also in the polarization flipping channel. Furthermore, both Rayleigh and Mie scattering regimes were considered to understand the CBS features. On one hand the shorter scattering length in the polarization preserving channel (cf. Fig. 7.14) especially in the heavily doped samples was tentatively attributed to the disrupted lattice and thereby resulting Mie-scattering by polymer spheres. On the other hand the background values of the CBS signal seem to indicate that the Rayleigh scattering is enhanced by the increasing doping and outweighs any other background scattering features in the heavily doped opals. On the whole it seems plausible that there are two different origins for the scattering; one relating to the intrinsic properties of the polymers, and another related to the doping. It remains a challenge to build a concise model describing the CBS in a periodic (not random!) environment.

The major finding in this thesis is that by introducing additional scatterers in form of *black* carbon nanoparticles we are able to turn the appearance of the polymer opal from milkish white into strikingly coloured. Clearly this type of scatter induced colour cannot be a result of single scattering in a bulk-like medium. If on the other hand we would have a single scattering event (assume for simplicity Rayleigh scattering) combined with a Bragg reflection we would expect the scattered colours still more or less obey the directionality set by the Bragg law of (5.4). The next step is to consider a double scattering event combined with a (Bragg) mirror. This type of scattering has also been studied by Jakeman et al. [148, 149], who report that in certain conditions the mirror presence can lead to backscattering enhancement ratios exceeding 2. We have not witnessed enhancement ratios exceeding 2 but it is imaginable that the colour scattering measured in this thesis could be brought about by a mechanism involving multiple scattering with a Bragg mirror where number of scattering events $N_{scatt} \geq 2$. The simplest case would be a scattering event followed by Bragg reflection and subsequent scattering possibly even by the same scatterer. This scenario could indeed yield the

measured colour-scattering dependence presented in Chapter 6. Finally it is interesting to consider the possibility of higher order scattering combined with a Bragg mirror interaction. The typical scattering field localization length was calculated to be around 2μm in Chapter 6. This compares relatively well with the results for the scattering mean free path, which for the same sample BV02 are expected to be $\leq 8\mu m$ in resonance, cf. Fig. 7.8 and Fig. 7.14. Also the Bragg interaction length was found to be $L_B = 7\mu m$. Thus it is likely that photons undergo multiple scattering ($N_{scatt} \geq 2$) in the structure before being scattered out of the opal. The hypothesis of multiple scattering into a wide angular cone is further supported by the attenuation of the reflected peak along the Bragg direction, cf. Fig. 5.24. Next, we can find an upper limit to N_{scatt} by considering the depolarization curves of Fig. 7.15. In multiple scattering the incoming polarization is depolarized by the scattering events [118, 150, 151]. The incomplete depolarization at the resonance in Fig. 7.15 is an indication that photons are Bragg-reflected out of the structure before sufficient amount of scatterings for complete depolarization is achieved. Based on the depolarization ratio of 0.75 of Fig. 7.15 for the doped samples and on the calculations reported in Ref. [151] we can estimate N_{scatt} to be about 3-4 for point like scatterers or 5-6 for Mie -type scattering from a sphere size of 240m corresponding to the sphere size of MIx1-Mix3. Although these estimates are for linearly polarised light they are in fair agreement with $N_{scatt} \geq 6$ required for complete depolarization with strong scatteres (TiO_2) as reported by Labeyrie et al. [118]. In order to understand the full complexity of the scattering the photon density of states needs to be taken into account, as was mentioned earlier. As a summary it is argued that low-order multiple scattering in the polymer opal is most likely the prevailing mechanism responsible for the colourful scattering reported in this thesis.

8.4 Future

8.4.1 Future Measurements

Some future challenges and ideas of the possible future experiments are presented in the following. From the data of Chapters 5 - 7 it is concluded that the most interesting features in the doped polymer opals are already present at moderate doping levels. This would suggest concentrating the future studies on opals with doping levels between 0 and 0.05wt-%.

Dopant effects on the polymer opal properties were briefly touched upon in this thesis. A thorough study of the effect of different dopants (e.g. Au, QDs) on the lineshape and width and the overall colour-scattering appearance could prove extremely interesting. Also the use of different dopants would serve to distinguish further the effects of increasing absorption and increasing amount of scatterers.

The elastomeric properties of the opals should be further explored. It would be very interesting to explore in more detail the strain-induced changes in the UV-diffraction spots of the LS02 sample including strain-director orientations from 0 to 120° analyzing both the surface cell change and the spot width change. This would provide further insight into the radial ordering of the opal but also to the possible strain-improved ordering briefly discussed in Section 4.4.2. Also the strain-related changes in the colour-scattering cones and the CBS features would provide valuable information on the details of the scattering process and further inputs into the future theoretical model of the polymer opal scattering.

The CBS measurements should be conducted with a range of incident angles in the future work. This would shed more light into the effect of the normal incidence and the actual incident angle bandgap on the CBS signal. The possible effects of these different angles were outlined in Fig. 7.13 and in the discussion thereafter.

Finally major efforts should be made to build a model describing scattering in a 3D periodic environment. Currently this topic is not very well understood and would definitely provide interesting challenges for theorists and new physics to be explored.

8.4.2 Outlook

The polymer opal material system has wide ranging potential in both future applications. The traditional difficulties in the world of photonic crystals were discussed in Chapter 1 and can be largely overcome by the polymer opal manufacturing techniques discussed in this thesis. The polymer opal material system offers a robust, industrially-scalable manufacturing sequence yielding high-quality thin film photonic crystals. One of the most interesting possible applications is presented in Fig. 8.1 (a). This is a picture of an extruded colourful polymer fibre with the dimensions in millimeters. The outer organised layer giving off the scattered colour is indicated by the black arrow while the inner disordered region is indicated by the white arrow. The latest extrusion test runs show that these fibres can be created in diameters around a few hundred micrometers thus opening up potential applications e.g. in clothing industry. Fig. 8.1 (b) shows a more straightforward way towards applications in the form of a polymer opal coated miniature car. This picture clearly indicates the polymer opal potential in high value coatings. Furthermore, we can speculate on the potential of the opal for different security applications such as bank notes and credit cards. Due to its flexibility the thin film opal could also in the near future be used e.g. in the food industry as a food wrapper. If the foodstuff wrapped in the polymer opal film starts decomposing, it releases molecules which make the opal swell and change its colour. Thus the true condition of the pork pie is immediately revealed to the customer. These are just a couple of visions on the possible future applications.

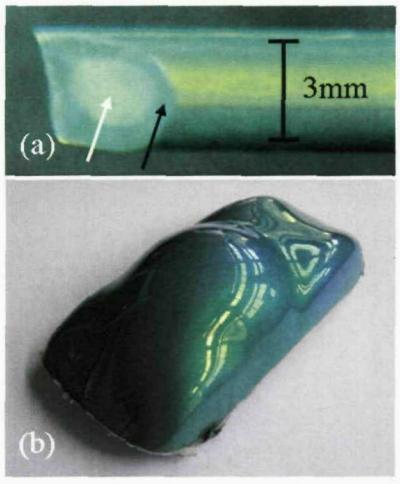

FIGURE 8.1: (a) An extruded colourful polymer opal fibre showing the outer ordered (black arrow) and the inner disordered region (white arrow). (b) A miniature automobile coated with a polymer opal thin film.

While the rest of the 3D photonic crystal industry is still deep in the search of the real-value functionality, the polymer opal, despite its relatively young age, is already plunging ahead with a plethora of applications!

Appendix A

Fresnel Coefficients for Reflection and Transmission

A.1 Amplitude

The Fresnel amplitude bulk reflection r and transmission t coefficients between two dielectric materials with refractive indices n_i and n_t for s- and p-polarizations are described through A.1-A.4 [16]:

$$r_s = -\frac{\sin(\theta_i - \theta_t)}{\sin(\theta_i + \theta_t)} \tag{A.1}$$

$$t_s = \frac{2\sin\theta_t \cos\theta_i}{\sin(\theta_i + \theta_t)} \tag{A.2}$$

$$r_p = \frac{\tan(\theta_i - \theta_t)}{\tan(\theta_i + \theta_t)} \tag{A.3}$$

$$t_p = \frac{2\sin\theta_t \cos\theta_i}{\sin(\theta_i + \theta_t)\cos(\theta_i - \theta_t)}, \tag{A.4}$$

where θ_i and θ_t correspond to the incident and transmitted angles, respectively, and the incident and transmitted angles are related through Snell's law:

$$n_i \sin\theta_i = n_t \sin\theta_t. \tag{A.5}$$

Fig. A.1 (a) presents the calculated values for r_{s01}, r_{p01}, t_{s01}, and t_{p01} for a dielectric interface with $n_1 = 1$ and $n_2 = 1.49$. Fig. A.1 (b) presents the calculated values for r_{s12}

and r_{p12}, when $n_1 = 1.49$ and $n_2 = 1.56$ as well as t_{s10}, and t_{p10}. The critical angles for the sign change are also identified.

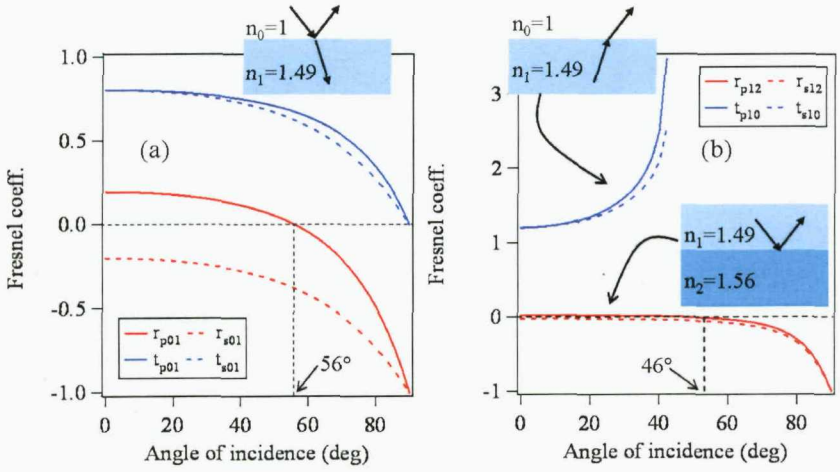

FIGURE A.1: (a) The calculated values for r_{s01}, r_{p01}, t_{s01}, and t_{p01} for a dielectric interface with $n_1 = 1$ and $n_2 = 1.49$. (b) The calculated values for r_{s12} and r_{p12}, when $n_1 = 1.49$ and $n_2 = 1.56$ as well as t_{s10}, and t_{p10}. The critical angles for the sign change are also identified.

A.2 Intensity

The Fresnel intensity reflection R_{sp} and transmission T_{sp} coefficients are defined through (A.6)-(A.7):

$$R_{sp} = r_{sp}^2 \tag{A.6}$$

$$T_{sp} = \frac{n_t \cos\theta_t}{n_i \cos\theta_i} t_{sp}^2. \tag{A.7}$$

Appendix B

Photon Diffusion

In the diffusion approximation the photon is undergoing Brownian motion or random walk with an average step size of l^*. In 1D the probability $p(x,t)$ that the photon has travelled an average total path length x after random walk time of t can be shown to have Gaussian distribution [138]:

$$p(x,t) = \frac{1}{\sqrt{4\pi Dt}} \exp\left(-\frac{x^2}{4Dt}\right), \tag{B.1}$$

where D is the photon diffusion constant. Distribution $p(x,t)$ satisfies the 1D diffusion equation:

$$\frac{\partial p}{\partial t} = D\frac{\partial^2 p}{\partial x^2}, \tag{B.2}$$

and for the average displacement $\langle x \rangle$ it applies:

$$\langle x^2 \rangle = 2Dt. \tag{B.3}$$

This can be extended to the 3D case and (B.3) then reads:

$$\langle r^2 \rangle = 6Dt. \tag{B.4}$$

Finally the photon diffusion constant D is defined by [139]:

$$D = \frac{cl^*}{3}. \tag{B.5}$$

Bibliography

[1] Yablonovitch, E. Inhibited spontaneous emission in solid-state physics and electronics. *Phys. Rev. Lett.* **58**, 2059 (1987).

[2] John, S. Strong localization of photons in certain disordered dielectric superlattices. *Phys. Rev. Lett.* **58**, 2486 (1987).

[3] Bykov, V. P. Spontaneous emission in a periodic structure. *Sov. Phys. JETP* **35**, 269 (1972).

[4] Joannopoulos, J. D., Villeneuve, P. R. & Fan, S. Photonic crystals: putting a new twist on light. *Nature* **386**, 143 (1997).

[5] Vlasov, Y. A., O'Boyle, M., Hamann, H. F. & McNab, S. J. Active control of slow light on a chip with photonic crystal waveguides. *Nature* **438**, 65 (2005).

[6] Perney, N. M. B. *et al.* Tuning localized plasmons in nanostructured substrates for surface-enhanced Raman scattering. *Opt Exp.* **14**, 847 (2005).

[7] Koenderink, A. F., Lagendijk, A. & Vos, W. L. Optical extintion due to intrinsic structural variations of photonic crystals. *Phys. Rev. B* **72**, 153102 (2005).

[8] Knight, J. C., Broeng, J., Birks, T. A. & Russell, P. S. J. Photonic band gap guidance in optical fibers. *Science* **282**, 1476 (1998).

[9] Russell, P. Photonic crystal fibers. *Science* **299**, 358 (2003).

[10] Sazio, P. J. A. *et al.* Microstructured optical fibers as high-pressure microfluidic reactors. *Science* **311**, 1583 (2006).

[11] Arsenault, A. C. *et al.* From colour fingerprinting to the control of photoluminescence in elastic photonic crystals. *Nature Mater.* **5**, 179 (2006).

[12] Tian, E. *et al.* Colorful humidity sensitive photonic crystal hydrogel. *J. Mater. Chem.* doi=10.1039/b717368g (2008).

[13] Pursiainen, O. L. J. *et al.* Nanoparticle-tuned structural color from polymer opals. *Opt. Exp.* **15**, 9553 (2007).

[14] Brillouin, L. *Wave Propagation in Periodic Structures* (Dover Publications, 1946).

[15] Bykov, V. P. Spontaneous emission from a medium with a band spectrum. *Sov. J. Quant. Electron.* **4**, 861 (1975).

[16] Hecht, E. *Optics* (Addison Wesley, 2002).

[17] Boroditsky, M., Krauss, T. F., Coccioli, R., Bhat, R. & Yablonovitch, E. Light extraction from optically pumped light-emitting diode by thin-slab photonic crystals. *Appl. Phys. Lett.* **75**, 1036 (1999).

[18] Wijnhoven, J. E. G. J. & Vos, W. L. Preparation of photonic crystals made of air spheres in titania. *Science* **281**, 802 (1998).

[19] Sakoda, K. *Optical Properties of Photonic Crystals* (Springer Verlag, 2005).

[20] Joannopoulos, J. D., Meade, R. D. & Winn, J. N. *Photonic Crystals, Molding the Flow of Light* (Princeton University Press, 1995).

[21] Leung, K. M. & Liu, Y. F. Full vector wave calculation of photonic band structures in face-centered-cubic dielectric media. *Phys. Rev. Lett.* **65**, 2646 (1990).

[22] Zhang, Z. & Satpathy, S. Electromagnetic wave propagation in periodic structures: Bloch wave solution of Maxwell's equations. *Phys. Rev. Lett.* **65**, 2650 (1990).

[23] Ho, K. M., Chan, C. T. & Soukoulis, C. M. Existence of a photonic gap in periodic dielectric structures. *Phys. Rev. Lett.* **65**, 3152 (1990).

[24] Satpathy, S., Zhang, Z. & Salehpour, M. R. Theory of photon bands in three-dimensional periodic dielectric structures. *Phys. Rev. Lett.* **64**, 1239 (1990).

[25] Shung, K. W. K. & Tsai, Y. C. Surface effects and band measurements in photonic crystals. *Phys. Rev. B* **48**, 11265 (1993).

[26] Bertone, J. F., Jiang, P., Hwang, K. S., Mittleman, D. M. & Colvin, V. L. Thickness dependence of the optical properties of ordered silica-air and air-polymer photonic crystals. *Phys. Rev. Lett.* **83**, 300 (1999).

[27] Johnson, S. G. & Joannopoulos, J. D. Introduction to Photonic Crystals: Bloch's Theorem, Band Diagrams, and Gaps (But No Defects). MIT, USA (2003).

[28] Kittel, C. *Introduction to Solid State Physics* (John Wiley & Sons, 1996).

[29] Pavarini, E. *et al.* Band structure and optical properties of opal photonic crystals. *Phys. Rev. B* **72**, 045102 (2005).

[30] van Driel, H. M. & Vos, W. L. Multiple bragg wave coupling in photonic band-gap crystals. *Phys. Rev. B* **62**, 9872 (2000).

[31] Romanov, S. G. *et al.* Diffraction of light from thin-film polymethymethacrylate opaline photonic crystals. *Phys Rev. E* **63**, 056603 (2001).

[32] Biswas, R., Sigalas, M. M., Subramania, G. & Ho, K. Photonic band gaps in colloidal systems. *Phys. Rev. B* **57**, 3701 (1998).

[33] Fan, S., Villeneuve, P. R., Joannopoulos, J. D. & Schubert, E. F. High extraction efficiency of spontaneous emission from slabs of photonic crystals. *Phys. Rev. Lett.* **78**, 3294 (1997).

[34] Iler, R. K. Formation of precious opal. *Nature* **207**, 472 (1965).

[35] Darragh, P. J., Gaskin, A. J., Terrell, B. C. & Sanders, J. V. Origin of precious opal. *Nature* **209**, 13 (1966).

[36] Fritsch, E. *et al.* The nanostructure of fire opal. *J. Non-Cryst. Solids* **352**, 3957 (2006).

[37] van Blaaderen, A. Opals in a new light. *Science* **282**, 887 (1998).

[38] Oxtoby, D. W. Crystallization: Diversity suppresses growth. *Nature* **413**, 694 (2001).

[39] McComb, D. W., Treble, B. M., Smith, C. J., Rue, R. M. D. L. & Johnson, N. P. Synthesis and characterisation of photonic crystals. *J. Mater. Chem.* **1**, 142 (2001).

[40] Jiang, P., Bertone, J. F., Hwang, K. S. & Colvin, V. L. Single-crystal colloidal multilayers of controlled thickness. *Chem. Mater* **11**, 2132 (1999).

[41] Tarhan, I. I. & Watson, G. H. Photonic band structure of fcc colloidal crystals. *Phys. Rev. Lett.* **76**, 315 (1996).

[42] Mueller, M., Zentel, R., Maka, T., Romanov, S. G. & Torres, C. M. S. Dye-containing polymer beads as photonic crystals. *Chem. Mater.* **12**, 2508 (2000).

[43] Miguez, H. *et al.* Control of the photonic crystal properties of fcc-packed submicrometer SiO_2 spheres by sintering. *Adv. Mater.* **10**, 480 (1998).

[44] Fukuda, K., Sun, H., Matsuo, S. & Misawa, H. Self-organizing three-dimensional colloidal photonic crystal structure with augmented dielectric contrast. *Jpn. J. Appl. Phys.* **37**, 508 (1998).

[45] Ni, P., Dong, P., Cheng, B., Li, X. & Zhang, D. Synthetic SiO_2 opals. *Adv. Mater.* **16**, 437 (2001).

[46] Fujikawa, R., Baryshev, A. V., Nishimura, K., Uchida, H. & Inoue, M. Optical study on opaline thin films grown by vertical deposition. *J. Porous Mater.* **13**, 287 (2006).

[47] Gu, Z., Fujishima, A. & Sato, O. Fabrication of high-quality opal films with controllable thickness. *Chem. Mater.* **14**, 760 (2002).

[48] http://www.ics.mq.edu.au/~lstew/research/outline.html.

[49] Ruhl, T., Spahn, P. & Hellman, G. P. Artificial opals prepared by melt compression. *Polymer* **44**, 7625 (2003).

[50] Jiang, P. & McFarland, M. J. Large-scale fabrication of wafer-size colloidal crystals, macroporous polymers and nanocomposites by spin-coating. *J. Am. Chem. Soc.* **126**, 13778 (2004).

[51] Lopez, C. Three-dimensional photonic bandgap materials: semiconductors for light. *J. Opt. A: Pure Appl. Opt.* **8**, R1 (2006).

[52] Ackerson, B. J. & Pusey, P. N. Shear-induced order in suspensions of hard spheres. *Phys. Rev. Lett.* **61**, 1033 (1988).

[53] Ackerson, B. J. Shear induced order of hard sphere suspensions. *J. Phys.: Condens. Matter* **2**, SA389 (1990).

[54] Haw, M. D., Poon, W. C. K. & Pusey, P. N. Direct obervation of oscillatory-shear-induced order in colloidal suspension. *Phys. Rev. E* **57**, 6859 (1998).

[55] Haw, M. D., Poon, W. C. K., Pusey, P. N., Hebraud, P. & Lequeux, F. Colloidal glasses under strain. *Phys. Rev. E* **58**, 4673 (1998).

[56] Amos, R. M., Rarity, J. G., Tepster, P. R., Shepherd, T. J. & Kitson, S. C. Fabrication of large-area face-centered-cubic hard-sphere colloidal crystals by shear alignment. *Phys. Rev. E* **61**, 2929 (2000).

[57] Liu, J., Weitz, D. A. & Ackerson, B. J. Coherent crystallography of shear-aligned crystals of hard-sphere colloids. *Phys. Rev. E* **48**, 1106 (1993).

[58] Lodahl, P. *et al.* Controlling the dynamics of spontaneous emission from quantum dots by photonic crystals. *Nature* **430**, 654 (2004).

[59] Vlasov, Y. A. *et al.* Existence of a photonic pseudogap for visible light in synthetic opals. *Phys. Rev. B* **55**, R13357 (1997).

[60] Astratov, V. N. *et al.* Photonic band gaps in 3d ordered fcc silica matrices. *Nature* **222**, 349 (1996).

[61] Ruhl, T. & Hellman, G. P. Colloidal crystals in latex films: rubbery opals. *Macromol. Chem. Phys.* **202**, 3502 (2001).

[62] Harkins, W. D. A general theory of the mechanism of emulsion polymerization. *J. Am. Chem. Soc.* **69**, 1428 (1947).

[63] Smith, W. V. & Ewart, R. H. Kinetics of emulsion polymerization. *J. Chem. Phys.* **16**, 592 (1948).

[64] Ruhl, T. *Elastomere kolloidale Kristalle aus hart-weichen Kern-Mantel-Latices.* Ph.D. thesis, Technische Universitaet Darmstadt (2003).

[65] www.dukescientific.com.

[66] Private discussion with Dr. Tilmann Ruhl at Deutsches Kunststoff Institut, Germany, 2006.

[67] Ashcroft, N. W. & Mermin, N. D. *Solid State Physics* (Holt-Saunders International Editions, 1976).

[68] Yablonovitch, E. & Gmitter, T. J. Photonic band structure: The face-centered-cubic case. *Phys. Rev. Lett.* **63**, 1950 (1989).

[69] http://www.carbon-black.org/what_is.html.

[70] Vickereva, O., Kalinina, O. & Kumacheva, E. Colloid crystal growth under oscillatory shear. *Adv. Mater.* **12**, 110 (2000).

[71] Pursiainen, O. L. J. *et al.* Shear-induced organization in flexible polymer opals. *Adv. Mater.* **accepted** (2007).

[72] Lamb, H. *Hydrodynamics* (Dover, 1945).

[73] Baryshev, A. V., Kosobukin, V. A., Samusev, K. B., Usvyat, D. E. & Limonov, M. F. Light diffraction from opal-based photonic crystals with growth-induced disorder: Experiment and theory. *Phys. Rev. B* **73**, 205118 (2006).

[74] Lazare, S. & Granier, V. Excimer laser light induced ablation and reactions at polymer surfaces as measured with a quartz-crystal microbalance. *J. Appl. Phys.* **63**, 2110 (1988).

[75] Astratov, V. N. *et al.* Interplay of order and disorder in the optical properties of opal photonic crystals. *Phys. Rev. B* **66**, 165215 (2002).

[76] McLachlan, M. A., Johnson, N. P., Rueb, R. M. D. L. & McComb, D. W. Manifestation of intrinsic defects in optical properties of self-organized opal photonic crystals. *J. Mater. Chem.* **14**, 144 (2004).

[77] Avrutsky, I., Li, B. & Zhao, Y. Characterization of two-dimensional colloidal polycrystalline materials using optical diffraction. *J. Opt. Soc Am. B* **17**, 904 (2000).

[78] Born, M. & Wolf, E. *Principles of Optics* (Cambridge University Press, 1999).

[79] Ma, X. *et al.* Determination of complex refractive index of polystyrene microspheres from 370 to 1610 nm. *Phys. Med. Biol.* **48**, 4165 (2003).

[80] Pursiainen, O. L. J. *et al.* Compact strain-sensitive flexible photonic crystals for sensors. *Appl. Phys. Lett.* **87**, 101902 (2005).

[81] Feynman, R. P., Leighton, R. B. & Sands, M. *The Feynman Lectures on Physics, vol.II* (Addison-Wesley Publishing Company, 1965).

[82] Nielsen, L. E. *Mechanical Properties of Polymers* (Reinhold, 1967).

[83] Vlasov, Y. A. *et al.* Manifestation of intrinsic defects in optical properties of self-organized opal photonic crystals. *Phys. Rev. E* **61**, 5784 (2000).

[84] Rengarajan, R., Mittleman, D., Reich, C. & Colvin, V. Effect of disorder on the optical properties of colloidal crystals. *Phys. Rev. E* **71**, 016615–1 (2005).

[85] Vos, W. L. *et al.* Strong effects of photonic band structures on the diffraction of colloidal crystals. *Phys. Rev. B* **53**, 16231 (1996).

[86] Vos, W. L., Megens, M., van Kats, C. M. & Boesecke, P. Transmission and diffraction by photonic colloidal crystals. *J. Phys.: Condens. Matter* **8**, 9503 (1996).

[87] Kaliteevski, M. A., Martinez, J. M., Cassagne, D. & Albert, J. P. Disorder-induced modification of the transmission of light in a two-dimensional photonic crystal. *Phys. Rev. B* **66**, 113101 (2002).

[88] Stefanou, N., Yannopapàs, V. & Modinos, A. Heterostructures of photonic crystals: frequency bands and transmission coefficients. *Comput. Phys. Commun.* **132**, 189 (1998).

[89] Stefanou, N., Yannopapas, V. & Modinos, A. Multem 2: A new version of the program for transmission and band-structure calculations of photonic crystals. *Comput. Phys. Commun.* **132**, 189 (2000).

[90] Private discussion with Dr. Tilmann Ruhl at Deutsches Kunststoff Institut, Germany, 2006.

[91] Bohren, C. F. & Huffman, D. R. *Absorption and Scattering of Light by Small Particles* (John Wiley & Sons, 1998).

[92] Bremell, P., Rodriquez, A., Joannopoulos, J. D. & Soljacic, M. Tailoring optical nonlinearities via the Purcell effect. *Phys. Rev. Lett.* **99**, 053601 (2007).

[93] Coen, S. *et al.* Supercontinuum generation by stimulated raman scattering and parametric four-wave mixing in photonic crystal fibers. *J. Opt. Soc. Am. B* **19**, 753 (2002).

[94] Reeves, W. H. *et al.* Transformation and control of ultra-short pulses in dispersion-engineered photonic crystal fibres. *Nature* **424**, 511 (2003).

[95] Miguez, H., Meseguer, F., Lopez, C., Lopez-Tejeira, F. & Sanchez-Dehesa, J. Synthesis and photonic bandgap characterization of polymer inverse opals. *Adv. Mater.* **13**, 393 (2001).

[96] Galisteo-Lopez, J. F. *et al.* Design of photonic bands for opal-based photonic crystals. *Photonics and Nanostructures - Fundamentals and Applications* **2**, 117 (2004).

[97] Palacios-Lidon, E., Juarez, B. H., Castillo-Martinez, E. & Lopez, C. Optical and morphological study of disorder in opals. *J. Appl. Phys.* **97**, 06352–1 (2005).

[98] Garcia, P. D. & Lopez, C. Optical study of ΓL high energy pseudogaps in ZnO inverted opals. *J. Appl. Phys.* **99**, 046103–1 (2006).

[99] Galisteo-Lopez, J. F., Galli, M., Balestreri, A., Andreani, L. C. & Lopez, C. Optical response of artificial opals oriented along the ΓX direction. *Appl. Phys. Lett.* **90**, 231112–1 (2007).

[100] Solovyev, V. G., Romanov, S. G., Chigrin, D. N. & Torres, C. M. S. Light extinction in bulk and thin film opal photonic crystals. *Synth. Met.* **139**, 601 (2003).

[101] Romanov, S. G. & Torres, C. M. S. Forward scattering of light in thin opal films. *Phys. Rev. E* **69**, 046611 (2004).

[102] Sanders, J. V. & Murray, M. J. Ordered arrangements of spheres of two different sizes in opal. *Nature* **275**, 201 (1978).

[103] Vukusic, P. & Sambles, J. R. Photonic structures in biology. *Nature* **424**, 852 (2003).

[104] Ghiradella, H., Aneshansley, D., Eisner, T., Silberglied, R. E. & Hinton, H. E. Ultraviolet reflection of a male butterfly: Interference color caused by thin-layer elaboration of wing scales. *Science* **178**, 1214 (1972).

[105] Jenkins, A. Photonics: Winged light. *Nature* **438**, 436 (2005).

[106] Vukusic, P. & Hooper, I. Directionally controlled fluorescence emission in butterflies. *Science* **310**, 1151 (2005).

[107] Koenderink, A. F. & Vos, W. L. Optical properties of real photonic crystals: anomalous diffuse transmission. *J. Opt. Soc. Am. B* **22**, 1075 (2005).

[108] Hughes, S., Ramunno, L., Young, J. F. & Sipe, J. E. Extrinsic optical scattering loss in photonic crystal waveguides: Role of fabrication disorder and photon group velocity. *Phys. Rev. Lett.* **94**, 033903 (2005).

[109] Guinier, A. *X-ray Diffraction* (W.H. Freeman and Company, 1963).

[110] Kreyszig, E. *Advanced Engineering Mathematics* (John Wiley & Sons Inc., 1999).

[111] Zhao, Y., Avrutsky, I. & Li, B. Optical coupling between monocrystalline colloidal crystals and a planar waveguide. *Appl. Phys. Lett.* **75**, 3596 (1999).

[112] Sanders, J. V. Diffraction of light by opals. *Acta Cryst.* **A24**, 427 (1967).

[113] Vlasov, Y. A., Kaliteevski, M. A. & Nikolaev, V. V. Different regimes of light localization in a disordered photonic crystal. *Phys. Rev. B* **60**, 1555 (1999).

[114] Baryshev, A. V. *et al.* Light diffraction from opal-based photonic crystals with growth-induced disorder: Experiment and theory. *Physica E* **17**, 426 (2003).

[115] Medhat, M., El-Zaiat, S. Y., Radi, A. & Omar, M. F. Diffraction of light by opals. *J. Opt A: Pure Appl. Opt.* **4**, 174 (2002).

[116] Neve-Oz, Y., Golosovsky, M., Davidov, D. & Frenkel, A. Bragg attenuation length in metallo-dielectric photonic band gap materials. *J. Appl. Phys.* **95**, 5989 (2004).

[117] Romanov, S. G., Maka, T., Torres, C. M. S., Mueller, M. & Zentel, R. Suppression of spontaneous emission in incomplete opaline photonic crystal. *J. Appl. Phys.* **91**, 9426 (2002).

[118] Labeyrie, G., Muller, C. A., Wiersma, D. S., Miniatura, C. & Kaiser, R. Observation of coherent backscattering of light by cold atoms. *J. Opt. B: Quantum Semiclass. Opt.* **2**, 672 (2000).

[119] Koenderink, A. F., Megens, M., van Soest, G., Vos, W. L. & Lagendijk, A. Enhanced backscattering from photonic crystals. *Phys. Lett. A* **268**, 104 (2000).

[120] Hermann, C. & Hess, O. Modified spontaneous-emission rate in an inverted-opal structure with complete photonic bandgap. *J. Opt. Soc. Am. B* **19**, 3013 (2002).

[121] McPhedran, R. C. *et al.* Density of states functions for photonic crystals. *Phys. Rev. E* **69**, 16609 (2004).

[122] Meade, R. D., Brommer, K. D., Rappe, A. M. & Joannopoulos, J. D. Photonic bound states in periodic dielectric materials. *Phys. Rev. B* **44**, 13772 (1991).

[123] Busch, K. & John, S. Photonic band gap formation in certain self-organizing systems. *Phys. Rev. E* **58**, 3896 (1998).

[124] Biswas, R., Sigalas, M. M., Subramania, G. & Ho, K. Photonic band gaps in colloidal systems. *Phys. Rev. B* **57**, 3701 (1998).

[125] Discussions with referees during peer-reviewing process.

[126] Krokhin, A. A. & Halevi, P. Influence of weak dissipation on the photonic band gap structure of periodic composites. *Phys. Rev. B* **53**, 1205 (1996).

[127] Boedecker, G. & Henkel, C. All-frequency effective medium theory of a photonic crystal. *Opt. Exp.* **11**, 1590 (2003).

[128] Gajiev, G. M. *et al.* Bragg reflection spectroscopy of opal-like photonic crystals. *Phys. Rev. B* **72**, 205115 (2005).

[129] Velikov, K. P., van Dillen, T., Polman, A. & van Blaaderen, A. Photonic crystals of shape-anisotropic colloidal particles. *Phys. Rev. B* **81**, 838 (2002).

[130] Yoshiyama, T., Sogami, I. & Ise, N. Kossel line analysis on colloidal crystals in semidilute aqueous solutions. *Phys. Rev. Lett.* **53**, 2153 (1984).

[131] Asher, S. A., Weissman, J. M., Tikhonov, A., Coalson, R. D. & Kesavamoorthy, R. Kossel line analysis on colloidal crystals in semidilute aqueous solutions. *Phys. Rev. E* **69**, 066619 (2004).

[132] Akkermans, E., Wolf, P. E. & Maynard, R. Coherent backscattering of light by disordered media: Analysis of the peak line shape. *Phys. Rev. Lett.* **56**, 1471 (1986).

[133] Corey, R., Kissner, M. & Saulnier, P. Coherent backscattering of light. *Am. J. Phys.* **63**, 560 (1995).

[134] Kuga, Y. & Ishimaru, A. Retroreflectance from a dense distribution of spherical particles. *J. Opt. Soc. Am. A* **1**, 831 (1984).

[135] van Albada, M. P. & Lagendijk, A. Observation of weak localization of light in a random medium. *Phys. Rev. Lett.* **55**, 2692 (1985).

[136] Wolf, P. & Maret, G. Weak localization and coherent backscattering of photons in disordered media. *Phys. Rev. Lett.* **55**, 2696 (1985).

[137] Wiersma, D. S., van Albada, M. P., van Tiggelen, B. A. & Lagendijk, A. Experimental evidence for recurrent multple scattering events of light disordered media. *Phys. Rev. Lett.* **74**, 4193 (1995).

[138] http://www.pma.caltech.edu/~mcc/ph127/b/lecture15.pdf.

[139] OLeary, M. A., Boas, D. A., Chance, B., & Yodh, A. G. Refraction of diffuse photon density waves. *Phys. Rev. Lett.* **69**, 2658 (1992).

[140] Labeyrie, G., Mueller, C. A., Wiersma, D. S., Miniatura, C. & Kaiser, R. Observation of coherent backscattering of light by cold atoms. *J. Opt. B: Quantum Semiclass. Opt.* **2**, 672 (2000).

[141] Akkermans, E. & Maynard, R. Weak localization of waves. *J. Phys. Lett.* **46**, 1045 (1985).

[142] van Albada, M. P., van der Mark, M. B. & Lagendijk, A. Observation of weak localization of light in a finite slab: Anisotropy effects and light-path classification. *Phys. Rev. Lett.* **58**, 361 (1987).

[143] Busch, K., Soukolis, C. M. & Economou, E. N. Transport and scattering mean free paths of classical waves. *Phys. Rev. B* **50**, 93 (1994).

[144] van Albada, M. P., van der Mark, M. B. & Lagendijk, A. Polarisation effects in weak localisation of light. *J. Phys. D: Appl. Phys.* **21**, S28 (1988).

[145] Dlugach, J. M. & Mishchenko, M. I. Enhanced backscattering of polarized light: Effect of particle nonsphericity on the helicity-preserving enhancement factor. *JQSRT* **100**, 115 (2006).

[146] Dlugach, J. M. & Mishchenko, M. I. Diffuse and coherent backscattering of polarized light: Polarization ratios for a discrete random medium composed of nonspherical particles. *JQSRT* **106**, 21 (2007).

[147] Huang, J. *et al.* Anomalous coherent backscattering of light from opal photonic crystals. *Phys. Rev. Lett.* **86**, 4815 (2001).

[148] Jakeman, E., Tapster, P. R. & Weeks, A. R. Enhanced backscattering through a deep random phase screen. *J. Phys. D: Appl. Phys.* **21**, S32 (1988).

[149] Jakeman, E. Enhanced backscattering through a deep random phase screen. *J. Opt. Soc. Am. A* **5**, 1638 (1988).

[150] Akkermans, E., Wolf, P. E., Maynard, R. & Maret, G. Theoretical study of the coherent backscattering of light by disordered media. *J. Phys. (Paris)* **49**, 77 (1988).

[151] Rojas-Ochoa, L. F., Lacoste, D., Lenke, R., Schurtenberger, P. & Scheffold, F. Depolarization of backscattered linearly polarized light. *J. Opt. Soc. Am. A* **21**, 1799 (2004).